

PICKING A FIGHT WITH WATER, AND WATER LOST ...

AN ELECTRON

by

Jonathan D. Herr

A dissertation submitted to the faculty of
The University of Utah
in partial fulfillment of the requirements for the degree of

Doctor of Philosophy

Department of Chemistry

The University of Utah

May 2017

Copyright © Jonathan D. Herr 2017

All Rights Reserved

The University of Utah Graduate School

STATEMENT OF DISSERTATION APPROVAL

The dissertation of Jonathan D. Herr

has been approved by the following supervisory committee members:

Ryan P. Steele, Chair 12/12/2016
Date Approved

Valeria Molinero, Member 12/12/2016
Date Approved

Peter B. Armentrout, Member 12/12/2016
Date Approved

Shelley D. Minter, Member 12/12/2016
Date Approved

Thomas E. Cheatham, Member 12/12/2016
Date Approved

and by Cynthia Burrows, Chair/Dean of

the Department/College/School of Chemistry

and by David B. Kieda, Dean of The Graduate School.

ABSTRACT

The global need for energy is increasing, as is the importance of producing energy by green and renewable methodologies. This document outlines a research program dedicated to investigating a possible source for this form of energy generation and storage: solar fuels. The photon-induced splitting of water into molecular hydrogen and oxygen is currently hindered by large overpotentials from the oxidation half-reaction of water-splitting. This study concentrated on fundamental models of water-splitting chemistry, using a physical and computational chemistry analysis. The oxidation was first explored via ab initio electronic structure calculations of bare cationic water clusters, comprised of 2 to 21 molecules, in order to determine key electronic interactions that facilitate oxidation. Deeper understanding of these interactions could serve as guides for the development of viable water oxidation catalysts (WOC) designed to reduce overpotentials. The cationic water cluster study was followed by an investigation into hydrated copper (I) clusters, which acted as precursor models for real WOCs. Analyzing how the copper ion perturbed the properties of water clusters led to important electronic considerations for the development of WOCs, such as copper-water interactions that go beyond simple electrostatics. The importance of diagnostic thermodynamic properties, as well as anharmonic characteristics being persistent throughout oxidized water clusters, necessitated the use of quantum and classical molecular dynamics (MD) routines. Therefore, two new methods for accelerating computationally demanding classical and

quantum MD methods were developed to increase their accessibility. The first method utilized a new form of electronic extrapolation – a linear prediction routine incorporating a Burg minimization – to decrease the iterations required for solving the electronic equations throughout the dynamics. The second method utilized a multiple-timestepping description of the potential energy term in the path integral molecular dynamics (PIMD) formalism. This method led to reductions of computational time by allowing the use of less computationally laborious methods for portions of the simulation and resulted in negligible increase of error. The determination of the fundamental driving forces within water oxidation and the development of acceleration techniques for important electronic structure methods will help drive progress into fully solar-initiated water oxidation.

To Alex, Mom, Dad, and Caitlin for their complete and unwavering support

Water is the most important element in life... because without it you cannot make coffee.

- Carrie Bradshaw

TABLE OF CONTENTS

ABSTRACT.....	iii
LIST OF TABLES.....	ix
ACKNOWLEDGMENTS.....	x
Chapters	
1 INTRODUCTION.....	1
1.1 Overview.....	1
1.2 Fossil Fuel Dependence and Damage.....	2
1.3 Renewable and Green Energy Alternatives and Solutions.....	5
1.4 Water Oxidation Catalysts and Overpotentials.....	9
1.5 Summary of Methods.....	12
1.6 Cationic Water Clusters.....	14
1.7 Solvated Copper: A Model Catalyst System.....	17
1.8 Quantum and Classical Molecular Dynamics Acceleration.....	19
1.9 References.....	22
2 STRUCTURAL PROGRESSION IN CLUSTERS OF IONIZED WATER, $(\text{H}_2\text{O})_{n=1-5}^+$	29
2.1 Introduction.....	30
2.2 Methods.....	31
2.3 Results and Discussion.....	31
2.4 Conclusions.....	41
2.5 Associated Content.....	41
2.6 Author Information.....	41
2.7 Acknowledgements.....	41
2.8 References.....	41
3 ION-RADICAL PAIR SEPARATION IN LARGER IONIZED CLUSTERS, $(\text{H}_2\text{O})_{n=6-21}^+$	45
3.1 Introduction.....	46
3.2 Methods.....	47
3.3 Results.....	48

3.4	Conclusions.....	57
3.5	Associated Content.....	58
3.6	Author Information.....	58
3.7	Acknowledgments.....	58
3.8	References.....	58
4	SIGNATURES OF SIZE-DEPENDENT STRUCTURAL PATTERNS IN HYDRATED COPPER (I) CLUSTERS, $\text{Cu}^+(\text{H}_2\text{O})_{n=1-10}$	60
4.1	Introduction.....	61
4.2	Methods.....	62
4.3	Results and Discussion.....	63
4.4	Conclusions.....	69
4.5	Associated Content.....	69
4.6	Author Information.....	69
4.7	Acknowledgments.....	70
4.8	References.....	70
5	ACCELERATING <i>AB INITIO</i> MOLECULAR DYNAMICS BY LINEAR PREDICTION METHODS.....	73
5.1	Introduction.....	74
5.2	Methods.....	75
5.3	Results.....	76
5.4	Conclusions.....	79
5.5	Acknowledgements.....	79
5.6	Supplementary Material.....	79
5.7	References.....	79
6	ACCELERATING <i>AB INITIO</i> PATH INTEGRALS VIA IMAGINARY MULTIPLE-TIMESTEPPING.....	80
6.1	Introduction.....	81
6.2	Methods.....	82
6.3	Results.....	84
6.4	Discussion and Conclusions.....	89
6.5	Author Information.....	89
6.6	Acknowledgements.....	89
6.7	References.....	89
7	CONCLUSION.....	93
7.1	Summary of Research and Future Prospects.....	93
7.2	References.....	95

LIST OF TABLES

Tables

2.1 Benchmark Methodology Comparisons for H_2O^+	32
2.2 Benchmark Methodology Comparisons for $(\text{H}_2\text{O})_2^+$	33
2.3 Relative Isomer Energies for $(\text{H}_2\text{O})_{n=2-5}^+$	35
2.4 n -Body Decomposition of Isomer Interaction Energies (kcal/mol).....	36
2.5 DFT (MPW1K/aTZ) Results for $(\text{H}_2\text{O})_4^+$ and $(\text{H}_2\text{O})_5^+$	40
3.1 Two-Body Decomposition of the $(\text{H}_2\text{O})_{21}^+$ Structural Evolution.....	57
5.1 SCF Cycles, Averaged Over 5-ps AIMD Trajectories with HF/6-31G(d,p).....	77
5.2 SCF Cycles, Averaged Over 5-ps AIMD Trajectories with HF/6-31G(d,p).....	77
5.3 SCF Cycles, Averaged Over 5-ps AIMD Trajectories with HF/6-31G(d,p).....	77
5.4 SCF Cycles, Averaged Over 5-ps AIMD Trajectories with HF/6-31G(d,p), Δt 20 a.u. and SCF Convergence of 10^{-8} a.u.	78
6.1 Computational Cost Analysis for $(\text{H}_2\text{O})_8$ Using B3LYP/6-31G**	88
6.2 Computational Cost Analysis for GlyH^+ Using RI-MP2/cc-pVTZ.....	88

ACKNOWLEDGEMENTS

The author expresses deep gratitude towards Ryan Steele for his mentorship over the course of this program. Also, the committee members Valeria Molinero, Peter Armentrout, Shelley Minter, and Thomas Cheatham are thanked for their helpful input throughout this program. The entire Steele group, all current and past members, are also greatly thanked for their helpfulness and teachings. The support and resources of the Center for High-Performance Computing at The University of Utah and the Extreme Science and Engineering Discovery Environment (XSEDE) are gratefully acknowledged as well.

I would like to extend a special thanks to Alex Leahy for her patience and inspiring motivation throughout this program. I would like to thank Elam, Patti, and Caitlin Herr for their support and optimism. Lastly, I greatly appreciate Steve Werst, Michael Scheidler, and Justin Koch for sitting through many discussions and presentations that may not have resonated with them – the author is very grateful for their help and suggestions during my dissertation practice.

CHAPTER 1

INTRODUCTION

1.1 Overview

Fossil fuels have many advantageous properties, including high-energy density, low acquisition cost, and long-term storage potential. New green and renewable energy sources need to meet these same criteria in order to be considered viable alternatives. Meeting these conditions is an arduous requirement for current renewable methods, because most renewable-energy technologies are still in development for better efficacy. The goal of this research program was to investigate the properties of fundamental models of renewable energy chemistry, in order to understand the underlying chemical physics.

The alternative energy target for this research program was solar fuels. The generation of solar fuels requires the use of a catalyst in order for the requisite water-splitting redox chemistry to be energetically practical, due to large activation barriers present in the oxidation half-reaction. The underlying, inner-sphere, fundamental driving forces within the oxidation of water are discussed throughout this research study. This fundamental information is intended to enable the continued developments of green, water-splitting systems for energy generation, resulting from a deeper understanding of the oxidation chemistry.

1.2 Fossil Fuel Dependence and Damage

Escalating environmental, political, and economic pressure is being placed on countries around the world to enact more environmentally friendly methods for energy production and storage. The impact the fossil fuel-reliant energy economy is having on the environment, from the global to the local scale, is becoming harder to dismiss.¹⁻⁸ Monthly global average temperatures are routinely being broken.⁹ The melting rate of polar ice deposits is increasing yearly.¹⁰ Droughts are occurring more frequently and for longer durations.¹¹ Air quality of major metropolitan areas is considered a major health concern.¹²

In addition to the environmental impact presented by the combustion of fossil fuels, a more pragmatic concern stems from the fact that the supply of fossil fuels is finite.¹² The global need for energy is increasing while the reserves of fossil fuels are steadily decreasing.¹³ Fossil fuels are not a readily renewable source of energy; geological lengths of time are required for the natural formation of coal, crude oil, and other carbon-based deposits. This relationship will ultimately lead to an inescapable energy crisis, likely on the human timescale. To mitigate the severity of the transition from current fuel sources to renewable methodologies, the development of new, clean, alternative energy approaches is required.

The negative impact of fossil fuels, as well as their prolific use in society, highlights an important dichotomy: If fossil fuel deposits are running out and their use is damaging the environment, what properties of fossil fuels make them too advantageous to transition to an alternative source? The answer is 3-fold; fossil fuels are relatively inexpensive, easy to store and transport, and have high energy densities.¹⁴ These

characteristics are required of any form of energy to be universally accepted and implemented.

The dominant reason fossil fuels are cheap is that they only need to be extracted and processed. These procedures can be a laborious endeavor, depending on the location of the deposit within the earth. But society possesses the infrastructure to perform these extractions at large enough scales to make the process economically viable. Unfortunately, the extraction process itself can induce environmental hazards, such as earthquakes initiated by hydraulic fracturing.¹⁵ Once the fuel source has been collected and processed, however, only simple combustion is required to release the stored energy.

The method of extracting energy from fossil fuel sources at the commercial scale has largely been unchanged throughout their use. The raw materials are incinerated to increase the temperature of a surrounding heat sink, typically a water bath. The water evaporates and expands, driving the rotation of a turbine for generating electrical energy. In the late 1700s, John Fitch harnessed the core concept of this process when he constructed a coal-fired steam engine connected to a paddle wheel, thus inventing the steamboat.¹⁴ Robert Fulton, who is typically associated with inventing the steamboat, later took the idea founded by Fitch and further refined it. More than 200 years later, the overwhelming majority of global electrical energy generation is virtually identical, aside from some advancements in higher efficiency machinery and combustion techniques. At the smaller scale, internal combustion engines work in a similar manner as the turbine setup; combustion is used to extract the chemical energy from the fuel. The resulting increase in pressure, from the production of carbon dioxide and other gasses, is harnessed to drive the oscillations of pistons and turn a central drive shaft. The first modern internal

combustion engine was also developed in the late 1700s, by John Stevens; however, it did not use any form of electrical spark for ignition.¹⁶ As with the steam engine, the core concept invented hundreds of years ago is still in use with virtually no critical changes. Improvements have been made to the internal combustion engine, such as more efficient engine assemblies and better use of thermodynamics (such as the Atkinson's cycle¹⁷), but at its core, a liquid fossil fuel is combusted in order to generate energy. Combustion is a very simple and cost-effective method of energy extraction.

Fossil fuels are also attractive for long-term energy storage, due to their simple and stable molecular structure.¹⁸ Aside from forming millions of years ago, once the fuel is extracted from the ground, the energy yield does not have an expiration date. Coal can be piled, and natural gas and oil can be contained. When needs arise, they can be transported and utilized with no energetic loss. The long shelf life of fossil fuels consequently results in less money being diverted to costly storage apparatuses.

One other beneficial aspect of fossil fuels is their comparably high-energy density, including 35 MJ/L for gasoline,¹⁹ 20 MJ/L for coal,¹⁹ and 22 MJ/L for natural gas (compressed to a liquid).²⁰ Compared to compressed molecular hydrogen, which has an energy density of approximately 6 MJ/L,¹⁹ fossil fuels carry substantially more chemical energy per unit volume. The higher energy density results in less required fossil fuel in order to produce the same amount of energy, when compared to hydrogen or other alternatives.

These benefits of fossil fuels are what retain them as the primary source of global energy, even given their environmental drawbacks. Fossil fuels have set the proverbial bar for the adoption of other fuel sources. To be considered a viable alternative, any

green or renewable form of energy must meet or exceed the advantages of fossil fuels. However, because nonrenewable energy sources are being outgrown by global energy demand, a reliable, scalable, clean energy alternative will need to be developed in the near future.

1.3 Renewable and Green Energy Alternatives and Solutions

Renewable and green methods of energy production and storage do not currently comprise a majority of global energy generation techniques. Only 10 % of the energy consumed in the U.S. is from renewable sources.²¹ Of this small fraction, 5 % comes from solar energy, 19 % from wind energy, 25 % from hydro-electric energy, 2 % from geothermal energy, and 49 % from biomass energy.²¹ Renewables may not count for a majority the global energy output, but what they lack in overall output, they make up in variety. Consistently, new methods are put forth to harness a force to capture energy. For example, a Japanese firm, Challengery, has recently been researching and developing wind turbines capable of withstanding and harnessing the forces created by the many typhoons Japan experiences every year.²² A company from Indiana, Solar Roadway, is scheduled to install a solar road at the welcome center of Route 66 and eventually into a small section of the road itself.²³ In addition to harnessing solar energy, the road surface can use the energy to melt snow and ice that accumulates in the winter. A sustainable-energy dance club in the Netherlands, aptly named Watt, harnesses the bodily movement of bar patrons. The floor converts the motion of dancers to electrical energy and allocates it to power the establishment's audio and lighting system.²⁴ Clearly, no shortage of ideas and methodologies are present for generating energy renewably.

Unfortunately, many of these renewable and green approaches have substantial

drawbacks. Wind relies on discontinuous air currents. Hydroelectric power needs large reservoirs to ensure energy supplies. Solar energy necessitates incident sunlight and is inhibited by weather and day and night cycles. Wind needs a rowdy nightlife. The common problem with these methods is discontinuous energy production.²⁵

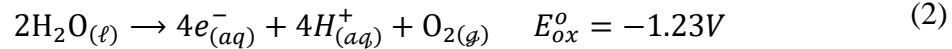
Development of energy storage is an equal and parallel problem to the development of green and renewable energy generation. A fundamental issue is that even if green energy production is possible, how is the energy going to be retained until it is required? Currently, no large-scale, clean, commercially viable method of storing electrical energy for future use is available. Elon Musk is currently employing lithium-ion battery technology installed in large banks in California. However, these banks are, at present, costly to manufacture and maintain;²⁶ lower energy density is typically associated with using the redox states of a material to store energy compared to that of chemical bonds. To provide enough storage at the community scale, large battery volumes are required, thereby further complicating implementation. Another method is using rotating flywheels, in which the energy is stored in the rotational momentum of a wheel under vacuum.²⁷ The commercial practicality of this method is suspect and has not been tested for longevity. Hydroelectric reservoirs are another system for storing energy by using excess energy to pump water into a containment basin. Unfortunately, hydroelectric power generation only encompasses a small fraction of global energy generation, limiting the impact of this method. One last example is using compressed air. Excess power can be diverted for compressing air into storage tanks. The stored energy can later be released by discharging and heating the air to rotate a turbine.²⁸ A small number of power plants throughout the world do use this technology, but the necessity

for large specialized equipment and environments has limited the adoption of this method.²⁹ However, ongoing and very promising research is currently being performed to make it a more globally accessible energy storage system. Although some technology does exist for the storage of a minimum amount of electrical energy, the requirement for equal or even greater efficiency in energy-storage capabilities becomes increasingly paramount as the efficiency of energy generation methods also continue to increase.

Water-splitting is one possible solution to both clean energy generation, as well as energy storage. The method comprises a means to store energy within the chemical bonds of molecular hydrogen and oxygen.



The oxidation and reduction half reactions are shown in equations 2 and 3, respectively, and redox potentials are listed with respect to the standard hydrogen electrode.



Ideally, the splitting is initiated by solar energy, which motivates the molecular gasses to be termed “solar fuels”. Extraction of electrical energy from this water-splitting method is completed by performing the water-splitting reaction in reverse, using the molecular hydrogen and oxygen and a proton-exchange membrane (PEM) fuel cell. The outputs from this process are electrical energy, water vapor, and minimal heat. Clear advantages to this methodology exist beyond being renewable and green. The stored energy has a long lifespan. Other methods, such as batteries, slowly bleed chemical potential and are highly affected by temperature. The storage of the gasses will persist indefinitely if the containment vessels remain intact. Furthermore, the chemical potential of the gasses will

not be permanently affected by large fluctuations in temperature, as can occur with lithium-ion batteries.³⁰

The storage of these solar fuels can be performed on the large scale for electrical grid supply or at the small scale for home and vehicle power. Even with setbacks in establishing a hydrogen economy via Department of Energy mandates, various companies are constantly trying to harness this clean energy source for transportation.³¹ Chevrolet has recently unveiled a prototype hydrogen-fueled military vehicle.³² Hydrogen fuel cells enable the vehicle to be much quieter and possess a smaller thermal signature than if powered by a conventional internal combustion engine. These properties provide unique advantages in military operations. Another company, Riversimple (United Kingdom), is developing a hydrogen fuel cell car to take advantage of England's growing hydrogen economy.³³ Although an uphill battle for the widespread utilization of hydrogen as an energy source exists, research and development in this field is growing.

Water-spitting chemistry has certainly not yet been perfected and is not without drawbacks. The dominant shortfall – the one on which this research program was mainly focused – is that the oxidation half of the water-splitting redox reaction requires an impractical amount of energy input. Accordingly, photo-catalysts have not been refined to an extent that their longevity and efficiency enable large-scale commercialization. The seemingly simple water-splitting reaction belies its complicated redox chemistry and accordant kinetic bottlenecks. In water-splitting, a 4-electron redox reaction occurs, promoting the formation of molecular oxygen and hydrogen from water molecules. The energy storage resides in the interatom chemical bonds within molecular hydrogen and molecular oxygen and is released via a PEM fuel cell. The water-splitting redox reaction

is highly endothermic. The breaking of 4 hydrogen-oxygen bonds and the creation of 1 oxygen-oxygen bond and 2 hydrogen-hydrogen bonds requires 4.92 eV, in a completely efficient and reversible system.³⁴ This free energy results in 1.23 V per electron required for water oxidation.³⁴ In solar water-splitting processes, the energy of the sun is intended to supply this redox potential, thereby storing the sun's energy in the chemical bonds of the molecules – this is not yet feasible due to overpotentials.

1.4 Water Oxidation Catalysts and Overpotentials

Water oxidation overpotentials cause a further increase to the already large activation energy required to practically split water. Catalyst development is most concerned with the lowering of these overpotentials to keep the required activation energy as close to 1.23 V as possible, because, at this range, 10,000-cm⁻¹ photons can activate the reaction. Many WOCs (water oxidation catalysts) have been developed and studied,³⁵⁻⁴² but none yet have sufficient efficiency for use outside the laboratory setting for energy storage.⁴³⁻⁴⁵ Both homogenous WOCs, such as ruthenium polypyridine-based catalysts,⁴⁶⁻⁴⁹ and heterogeneous WOCs, such as hematite photoanodes,⁵⁰⁻⁵³ are being analyzed for their efficacy in solving the water-splitting overpotential problem. Even with novel approaches to enhancing the catalysts by decreasing electron-recombination probabilities,^{54, 55} manipulating band gaps,^{56, 57} and increasing the kinetics of evolving molecular oxygen,^{58, 59} a clear solution has not yet been found. The key hurdle to overcoming these technological barriers is a molecular-level understanding of water oxidation mechanisms. The research performed in this study was designed to accelerate the advancements for creating a viable WOC by examining these mechanisms computationally.

The reduction of overpotentials is the reason for incorporating a catalyst into an electrochemical system, because overpotentials can manifest as increased activation energies. In water oxidation, an overpotential is created by numerous mechanisms. Some overpotentials cannot be circumvented by the incorporation of a catalyst, such as electrical (ohm) resistance within an electrolytic cell's circuitry or the electrical resistance resulting from poor conductivity of the solvent inside the cell.⁶⁰ Other overpotentials are due to the shape and size of electrodes, the distance between electrodes, or the composition of the semipermeable membrane between electrodes that could impede electrical and mass transfer.⁶¹ Overpotentials that can be reduced by catalysis in water-splitting, concentrate on the inner-sphere effects of the oxidation reaction. Full 4-electron water oxidation requires the movement of molecules, protons, and electrons, which can incur a kinetics penalty due to slow mass transfer. Stable, or even terminal, intermediates can occur, such as hydrogen peroxide evolution instead of oxygen evolution, as well as competing oxidation of other molecules within the reaction cell. Both of these outcomes slow the kinetics of the reaction and increase the energetic cost for initiation.⁶² Poor electronic overlap between the catalysts and the surrounding water will prevent favorable proton-coupled electron transfer (PCET) reactions that otherwise could lead to the greatest efficiencies.⁶³ An efficient WOC needs to expunge, or at least reduce, these shortcomings in order to lower the energy input required to split water by a solar source.

Many proposed and developed WOCs do reduce activation barriers. However, none currently have been manufactured on a large commercial scale. This lack of commercialization is because fundamental issues associated with WOCs have not been

resolved. Some catalysts are not long-term stable and deteriorate under the extremely harsh oxidizing environmental working conditions. The pH required by many WOCs to perform at peak efficiency ranges from neutral to highly alkaline and presents an exceedingly oxidative environment^{64, 65} Often a catalyst may have appreciably lowered activation barriers, but, unfortunately, after only a handful of reaction cycles, the catalyst has denatured. Catalyst examples that suffer from this breakdown are a cobalt picolinate complex, a cobalt carbonate bipyridine cubane type complex, and a sodium cobalt pyridinyl cubane type complex.⁶⁶ Large-scale WOC development is also inhibited by the expensive materials and/or laborious synthesis methods. Many proposed WOCs contain rare and expensive elements. The WOCs may be stable and have terrific effects on activation barriers but the presence rare elements make the commercialization of such catalysts difficult, if not unfeasible, due to cost. However, other WOCs contain cheap and easily obtainable elements but require highly specialized environments and laborious procedures for synthesis. The cost associated with bringing these procedures and methodologies to the large commercial scale would be substantial and, in most cases, be prohibitive. One such catalyst with this drawback is a multiple ruthenium-centered catalyst. This catalyst has minimum overpotential but requires many molecular pieces and synthesis steps for its assembly.⁶⁷⁻⁶⁹ Other such examples are an iridium bis-pyridine complex⁷⁰ and a large gallium boric acid system⁷¹, both containing rare and expensive elements and difficult synthesis mechanisms. Lastly, and most importantly, the catalyst may not lower the activation energy for water oxidation enough to warrant further large scale development.⁶⁶ An example of a catalyst containing this flaw is a copper dipyrindyl ketone complex. Despite an easy synthesis and great stability, it has very little impact on

the reaction barrier. The present study was designed to help rectify this last trait of poor activity in decreasing overpotentials. By developing a robust understanding of the electronic environment of a WOC will interact with, a deeper insight obtained into how a WOC can be modified in order to have an increased effect on the activation energies and produce a viable WOC.

1.5 Summary of Methods

The investigation into the fundamental driving forces present within water oxidation involved computational quantum chemistry methods that could accurately represent open-shell ions. This form of chemical analysis enabled the dissection of the highly intricate electronic characteristics present in cationic water and generated diagnostic data that would be challenging to obtain experimentally. Computational methods allowed for the analysis of orbital interactions, various forms of bonding, and the role of the quantum nature of electrons and nuclei, all of which are discussed for their contributions to deciphering water oxidation. The information gathered from these theoretical methods was meant to be complementary to experimental data, as well as offer insight for deciphering anomalous experimental spectra.

Many different electronic structure methods were used for this study, and each chapter describes the specific procedures used within it. Overall, accurate methods for calculating the electronic potential were required in order to obtain reliable electronic information. Therefore, robust benchmarking of ab initio electronic structure procedures was performed with a variety of different methods in order to find an accurate approach that could reproduce experimental standards. The methods required for a high degree of accuracy incorporated a large amount of electron correlation and were computationally

demanding. Carefully chosen hybrid density functionals, determined to yield results sufficiently consistent with demanding highly correlated methods, were then used in order to save calculation time. From these accurate methods, configuration space searches were conducted throughout this study, and relative energies were obtained for stable isomers for the specific cluster sizes. Obtaining the isomer energy ordering offered insight to not only what kinds of structures are more prevalent, and, therefore, the properties that stabilize these low-energy forms, but also the thermal distribution of the isomers. These distributions are especially important when comparing to experimental data because many isomers may be thermally accessible at the experimentally sampled temperature. Many-body expansions of the electronic energies within the isomers, as well as energy decompositions of bonding energies, were conducted on specific isomers. From these analyses, driving forces were isolated, and highlighting the origin of size-dependent characteristics. In-depth harmonic and anharmonic analyses were also conducted and provided diagnostic information into how bond strengths are affected within the clusters and in what manner the vibrations deviate from a harmonic approximation. Analysis of the orbital manifold of the water cluster cations and the changes of electron densities from ionization, unveiled important electronic considerations for structural properties and demonstrated the effect that charged species can have on solvating water molecules. The aggregate of all of the isomer studies, energy and structural decompositions, and vibrational analyses, enabled an accurate in-depth analysis of water clusters perturbed by the removal of an electron.

The following introductory sections provide background and summary knowledge for the study of water oxidation. Each section focuses on an individual step within the

larger study, each building to larger and more complicated chemical systems. The layout of the remaining introductory sections mirrors the remaining chapters in the manuscript – all but one of which have been published in peer-reviewed journals, the other being accepted and to-be published – and form an anchor for these chapters to big-picture WOC research ramifications.

1.6 Cationic Water Clusters

The aim of this research study was to understand the underlying driving forces involved in water oxidation. The foundation of this investigation was built upon a study of bare water cluster oxidation, the energy-demanding, coupled 4-electron, 4-proton half-reaction responsible for generating molecular oxygen from water. As a first step, toward fundamental understanding of this 4-electron oxidation process, the first oxidation step – removal of a single electron from water – was examined in this series of studies. However, the removal of 1 electron transitions the problem from closed-shell to open-shell, thereby severely complicating system's electronic structure. Therefore, initiating the study at this simplified water oxidation model enabled easier deconvolution of the complicated inner-sphere electronics and dynamics involved in the oxidation of water, as well as determination of the driving forces that could provide insight into how to reduce the influence of undermining oxidation overpotentials.

The drawbacks listed in section 1.4 comprise the motivations for pursuing the study into oxidized water clusters that *do not* contain any catalyst. The perspective of this investigation was atypical, compared to many WOC development studies. Rather than finding a molecule and exploring its water-oxidation ability, the purpose of this study was to alternatively determine the key electronic signatures in oxidized water that could be

utilized as the targeted interactions for a WOC to either promote or impede. The determination of these targets would lead to more precise and refined studies to be performed on WOCs as a result of having a clearer idea of the key interactions that must take place for efficient water oxidation, thus possibly accelerating their development.

The bottom-up study began at small oxidized water cluster sizes containing only 2 to 5 molecules (Chapter 2). The low-energy configuration space was investigated at the selected size regimes as well as incorporated anharmonic vibrational analyses (Chapter 3). In a relaxed neutral state, the dimer was comprised of a hydrogen-bond donor and acceptor. Upon single ionization, a proton is shuttled from donor to acceptor, forming a stable hydronium and hydroxyl radical contact pair. This species was stable until 3 additional solvating water molecules were added to the ionized cluster. At this size regime, the solvation energy of the hydronium by water molecules outcompeted the attraction between the contact pair, and an interleaving water migrated between the hydronium and hydroxyl radical. An increase in the cationic cluster size to 21 waters (Chapter 4), where multiple solvation shells were possible, led to an accentuation of the separation between the hydronium and hydroxyl radical. At this size regime, the two species migrated to opposite sides of the cluster, via a Grotthus-type mechanism,^{72, 73} where any driving force to reform a contact-pair was largely outcompeted by the favorable solvation of the hydronium. These gas-phase calculations contained very few waters compared to a condensed-phase environment. But even with this model, favorable properties for an efficient catalytic cell were recognized – driven charge separation. In chemistry involving a homogeneous WOC, the hydroxyl unit is typically bound to the WOC's active center, forming a hydroxyl ligand. One such characteristic was that the

ligands in the WOC cannot sterically prohibit the migration of water molecules near the location of the activated waters. Sterically inhibiting this movement would decrease the driving force for the separation of charge. The ligands ideally should promote water molecules into the activated water complex, increasing the driving force to separate the contact pair. Secondly, the catalyst should encourage the localization of the radical electron away from the hydronium and towards the hydroxyl species. In a contact-pair structure, the radical electron was shared between both the hydroxyl and hydronium units. After a separation of just one interstitial water molecule, the radical electron becomes highly localized only on the hydroxyl species. Therefore, a WOC promoting these behaviors could decrease the overpotential associated with the localization of charge in the water oxidation mechanism and with the movement involved with the separation of the hydroxyl radical and hydronium.

A second achievement of the investigation into cationic water clusters was the resolution and characterization of experimental spectra. By using high-accuracy anharmonic models (Chapter 3), as well as thermally weighted normal mode data (Chapter 4), computational vibrational spectra were generated for various cluster sizes. The spectra were developed to confirm the accuracy of theoretical models, as well as interpret noisy experimental spectra. Infrared spectra were also generated for cluster sizes for which experimental data was available. This information, as well as the knowledge of diagnostic peaks within spectra, such as free hydroxyl radical stretches, will prove valuable for resolving future physical experiments.

1.7 Solvated Copper: A Model Catalyst System

The study of cationic bare water clusters provided insight into the effects that ionization incurs upon water. The true utility of this information comes from observing how water clusters are perturbed by inclusion of a WOC. As an intermediate step, a model WOC – a copper (I) ion – was chosen. Copper is the active center in experimental WOCs,^{74, 75} and has well understood redox properties.⁶² The copper atoms in WOCs are at higher oxidation states than +1, but beginning the study at closed-shell copper (I) provided an important testing ground for the competition between electrostatic and chemical effects. The model copper catalyst continued the bottom-up approach that had been the foundation of this entire study. Hydrated copper (I) (Chapter 5) was a first step to understanding how a real WOC will interact with water without introducing an extremely complicated metal complex. A copper (I) provides the potential for unique chemical interactions beyond simple electrostatic considerations, because it contains chemically available d orbitals. Understanding how, and to what extent, the extra d orbitals of a non-standard cation chemically perturbed a water cluster established a clear reference point for analyzing the properties of the water and catalyst systems.

This project was meant to answer two overall questions: what is the isomer progression in solvated copper (I) systems at sizes that have not been studied, and how far does the electronic influence of the metal atom extend into a solvation network? In order to answer these questions, a configuration-space search was performed on hydrated copper (I) clusters containing 1 to 10 water molecules. As in the cationic water cluster studies, an understanding of the isomer landscape, when combined with quantum chemistry analyses, yielded clues to what properties and driving forces that stabilize the dominant isomers. The relative energies of the stable isomers, as well as harmonic zero-

point energies and vibrational modes, were calculated for all cluster sizes. Harmonic frequencies were helpful in understanding the extent of the copper's perturbation to a water cluster by analyzing the deviation of O-H vibrational frequencies away from their inherent frequencies in neutral water. Decomposition of the electronic interactions of the numerous isomers into the approximate contributions of electrostatic, polarization, and charge transfer effects was also performed, and the contributions were tracked with cluster size. The data collected from these analyses enabled the observation of copper (I)'s spatial range of influence with increasing solvation. The interaction between the copper cation and the surrounding water molecules, unlike solvated alkali metal cations, was found to be decidedly chemical in nature. This effect was found to be notably size-dependent, with more electrostatic character in larger clusters. The resulting perturbation of the characteristic water stretch frequencies was also found to extend into at least the third solvation shell, suggesting that the influence of strong ions can partially activate water over a reasonably long distance.

The information acquired from the copper (I) study portrayed a much more electronically complicated system than was originally believed to be responsible for the cation's interactions with solvating water molecules. Polarization of the water's electron density as well as electrostatic interactions, comprised most of the molecular interactions within the clusters, but also a significant amount of charge transfer was present. The chemical bonding, due in part from hybridization of copper orbitals, was confirmed by substituting the copper atom with lithium, sodium, and potassium cations. The incorporation of these copper substitutes resulted in significant differences in spectroscopic signatures in small clusters, where charge transfer plays a more significant

role. This property also affected the geometries of copper-containing clusters, most notably in the 3-coordinate trimer cation where one of the copper-oxygen bonds is longer than the other two. The chemical interaction also influenced different binding energies for sequential additions of the last 2 water molecules in the trimer to make a 3-coordinated copper (I) system. The second water's binding energy was dominated by polarization while the third water's binding energy was highly influenced by electrostatics.

At smaller clusters sizes, copper has been shown⁷⁶ to favor a 2-coordinate system, and this coordination was thought to continue with cluster growth. In this study, cluster sizes around 5 to 6 solvating waters displayed a growing driving force manifesting to increase the coordination of the copper (I) center and, by 10 waters, low-energy 4-coordinate copper (I) conformers became stable. This stepwise progression in coordination originated from a combination of the extreme polarization the copper (I) atom enacted upon multiple solvation shells. This strong interaction also affected the strength of hydrogen bonds, resulting in significant red shifts of O-H stretches within the solvated copper clusters. The beginning signatures of water-cluster activation (oxidation) were detected within these solvated copper (I) systems. These results provide a small-model glimpse into the manner in which water is chemically activated and demonstrate how the interactions within a hydrated nonstandard cation system differs from that of a solvated "noble-ion" behavior.

1.8 Quantum and Classical Molecular Dynamics Acceleration

Dynamics simulations provide indispensable information in many theoretical chemical investigations, including the study of WOCs. These kinds of simulations can

provide diagnostic kinetic and thermodynamic data, as well as vibrational spectra. Oxidized water is very anharmonic and contains a complicated open-shell ion electronic structure, which necessitates the use of computationally laborious methods, such as ab initio molecular dynamics (MD). Path integral methodology, such as path integral molecular dynamics (PIMD), can incorporate nuclear quantum effects into dynamics simulations. These quantum properties manifest as zero-point energies, tunneling, and anharmonic effects. These properties can also result in peak shifts, the appearance of new peaks, intensity changes, and resonances in vibrational spectra. Unfortunately, first principles classical and quantum dynamics are computationally demanding. This computational bottleneck limits the accuracy, as well as the sizes of chemical systems that can be practically studied via these methods. Because of the importance of classical and quantum dynamics to chemical systems in this study, as well as larger oxidized systems in the future, new methodologies were developed in parallel with the WOC study to accelerate dynamics trajectories.

The first enhancement developed was a new way to perform an extrapolation of the self-consistent field (SCF) equations in Born Oppenheimer MD (BOMD).⁷⁷ The SCF procedure is iteratively converged at each timestep in an MD simulation and constitutes the dominant computational bottleneck. A simple polynomial least-squares regression (PLSR) is able to be applied to the previous timesteps' solutions to the SCF equations and extrapolate the approximately converged value.⁷⁸ On average, only minor changes to the system occur from one dynamics step to the next due to small timesteps. This concept enables fairly accurate extrapolations to occur. The extrapolated guess can then be used to initiate the SCF iterations and typically results in less iterations being necessary for

convergence.

Motivated by the observation that this electronic information forms an oscillatory signal, a linear prediction routine incorporating a Burg minimization (BLP), was integrated into BOMD simulations as an alternative to PLSR extrapolation (Chapter 6). This change is a result of BLP having the potential to produce higher-quality extrapolated values in comparison to PLSR for this form of data.⁷⁹ BLP is similar to PLSR in that it performs a minimization of the chi-squared (χ^2) function, but the construction and implementation is unique and more powerful. The extrapolated data point generated from BLP is comprised of a weighted linear combination of previous data points, unlike in PLSR where a polynomial is fit to the data, from which the extrapolated value is calculated. BLP noticeably decreased the number of iterations per timestep, as well as decreased the instability incurred from utilizing any algorithm that is not strictly time-reversible. BLP proved to be a very easy and user-friendly methodology to accelerate MD trajectories.

A second method, designed to accelerate PIMD simulations, decreased computational overhead in PIMD by enabling the use of faster, less accurate electronic structure methods instead of accelerating existing MD machinery, as was performed with BLP. This acceleration was achieved by applying a multiple-timestep approach to PIMD, specifically to the potential energy term (Chapter 7). In PIMD, multiple trajectory instances occur simultaneously, and this collection of trajectories is colloquially termed path integral “beads”. The beads are connected by harmonic springs, forming a ring polymer that is responsible for capturing the delocalized quantum properties. Unfortunately, the number of beads used in a simulation multiplies the cost of running a

classical MD trajectory by that same number (e.g., 32 beads are typically required to converge water at 300K). This increase in computational expense can make even relatively small systems computationally prohibitive. By applying multiple-timestepping techniques to the potential energy, the new method enabled the application of the desired high-level quantum calculations on only a few beads of the ring polymer, whereas the balance can be characterized by much simpler, cost-effective quantum chemistry methods. Standard implementations of PIMD require all beads to be computed at the same level of theory. This new simplification of the electronic structure methods for the beads led to a significant computational speedup with only negligible error accumulation.

The following chapters within the document are comprised of the publications obtained for the topics discussed thus far and in the same order. They collectively represent an investigation into the fundamental electronic and structural behaviors of the cationic water systems as precursors to WOCs, as well as methodologies to accelerate MD for computational accessibility for larger water-oxidation studies. The information and tools developed throughout this research study will help enable investigations beyond the cationic water analysis presented in this manuscript.

1.9 References

1. Wigley, T. M. L.; Richels, R.; Edmonds, J. A. Economic and Environmental Choices in the Stabilization of Atmospheric CO₂ Concentrations. *Nature* **1996**, 379 (6562), 240-243.
2. Hoffert, M. I.; Caldeira, K.; Jain, A. K.; Haites, E. F.; Harvey, L. D. D.; Potter, S. D.; Schlesinger, M. E.; Schneider, S. H.; Watts, R. G.; Wigley, T. M. L.; Wuebbles, D. J. Energy Implications of Future Stabilization of Atmospheric CO₂ Content. *Nature* **1998**, 395 (6705), 881-884.
3. Haines, A.; Kovats, R. S.; Campbell-Lendrum, D.; Corvalan, C. Climate Change and Human Health: Impacts, Vulnerability and Public Health. *Public Health* **2006**, 120

(7), 585-596.

4. Hoel, M.; Kverndokk, S. Depletion of Fossil Fuels and the Impacts of Global Warming. *Resour. Energy Econ.* **1996**, *18* (2), 115-136.
5. Olah, G. A.; Goeppert, A.; Prakash, G. K. S. Fossil Fuels and Climate Change. *Beyond Oil and Gas: The Methanol Economy*; Wiley-VCH Verlag GmbH & Co. KGaA: 2009; pp 77-89.
6. Höök, M.; Tang, X. Depletion of Fossil Fuels and Anthropogenic Climate Change—A Review. *Energy Policy* **2013**, *52*, 797-809.
7. Davis, S. J.; Caldeira, K.; Matthews, H. D. Emissions and Climate Change from Existing Energy Infrastructure. *Science* **2010**, *329* (5997), 1330-1333.
8. Wuebbles, D. J.; Jain, A. K. Concerns About Climate Change and the Role of Fossil Fuel Use. *Fuel Process. Technol.* **2001**, *71* (1–3), 99-119.
9. Hansen, J.; Ruedy, R.; Sato, M.; Lo, K. Global Surface Temperature Change. *Rev. Geophys.* **2010**, *48* (4), 1-29.
10. Mercer, J. H. West Antarctic Ice Sheet and CO₂ Greenhouse Effect- A Threat of Disaster. *Nature* **1978**, *271* (5643), 321-325.
11. Gagnon, L.; Bélanger, C.; Uchiyama, Y. Life-Cycle Assessment of Electricity Generation Options: The Status of Research in Year 2001. *Energy Policy* **2002**, *30* (14), 1267-1278.
12. Kampa, M.; Castanas, E. Human Health Effects of Air Pollution. *Environ. Pollut.* **2008**, *151* (2), 362-367.
13. Suganthi, L.; Samuel, A. A. Energy Models for Demand Forecasting—A Review. *Renew. Sust. Energy Rev.* **2012**, *16* (2), 1223-1240.
14. Crabtree, G. W.; Dresselhaus, M. S.; Buchanan, M. V. The Hydrogen Economy. *Phys. Today* **2004**, *57* (12), 39-44.
15. Ellsworth, W. L. Injection-Induced Earthquakes. *Science* **2013**, *341* (6142), 1-7.
16. Turnbull, A. D. *John Stevens: An American Record*; Beaufort Books: New York, 1928.
17. Boggs, D. L.; Hilbert, H. S.; Schechter, M. M. *The Otto-Atkinson Cycle Engine-Fuel Economy and Emissions Results and Hardware Design*; SAE International: 1995.
18. Mango, F. D. The Stability of Hydrocarbons Under the Time-Temperature

Conditions of Petroleum Genesis. *Nature* **1991**, 352 (6331), 146-148.

19. Fischer, M.; Werber, M.; Schwartz, P. V. Batteries: Higher Energy Density than Gasoline? *Energy Policy* **2009**, 37 (7), 2639-2641.
20. Dresselhaus, M.; Thomas, I. Alternative Energy Technologies. *Nature* **2001**, 414 (6861), 332-337.
21. Renewable Energy. *Monthly Energy Review*; EIA-0035(2016/9) Department of Energy U.S. Energy Information Administration, Washington, DC, 2016; pp 151-170.
22. Ogura, J.; Marsh, J. Storm Chasers: The Typhoon Turbine that Could Power Japan for 50 Years, <http://www.cnn.com/2016/09/27/asia/typhoon-catchers-japan-challenergy>, (accessed Nov 17, 2016).
23. Eisensein, P. A. Missouri Plans to Build Solar Panels into Road Along Old Route 66, <http://www.nbcnews.com/business/autos/missouri-plans-build-solar-panels-road-along-old-route-66-n608676>, (accessed Nov 17, 2016).
24. Rosenthal, E. Partying Helps Power a Dutch Nightclub, <http://www.nytimes.com/2008/10/24/world/europe/24rotterdam.html>, (accessed Nov 17, 2016).
25. Inganäs, O.; Sundström, V. Solar Energy for Electricity and Fuels. *Ambio* **2016**, 45 (Suppl 1), 15-23.
26. Ferris, R. Tesla tackles California Energy Woes with Massive Energy-Storage Deal, <http://www.cnbc.com/2016/09/15/tesla-tackles-california-energy-woes-with-massive-energy-storage-deal.html>, (accessed Nov 17, 2016).
27. Ahrens, M.; Kucera, L.; Larsonneur, R. Performance of a Magnetically Suspended Flywheel Energy Storage Device. *IEEE Trans. Control Syst. Technol.* **1996**, 4 (5), 494-502.
28. Lund, H.; Salgi, G. The Role of Compressed Air Energy Storage (CAES) in Future Sustainable Energy Systems. *Energ. Convers. Manage.* **2009**, 50 (5), 1172-1179.
29. Vosburgh, K. G. Compressed Air Energy Storage. *J. Energy* **1978**, 2 (2), 106-112.
30. van Schalkwijk, W.; Scrosati, B. *Advances in Lithium-Ion Batteries*; Springer Science & Business Media: New York, 2007.
31. Hoffmann, P.; Dorgan, B. *Tomorrow's Energy: Hydrogen, Fuel Cells, and the Prospects for a Cleaner Planet*; MIT press: Sabon, 2012.
32. Burden, M. GM, Army Debut Chevrolet Colorado ZH2 Fuel-cell Vehicle,

<http://www.detroitnews.com/story/business/autos/general-motors/2016/10/03/army-colorado-fuel-cell/91462260>, (accessed Nov 17, 2016).

33. Taylor, A. Riversimple Rasa Review: Is this Hydrogen Car the Future—or Just a Gimmick?, <http://arstechnica.com/cars/2016/04/riversimple-rasa-hydrogen-car-review>, (accessed Nov 17, 2016).
34. Walter, M. G.; Warren, E. L.; McKone, J. R.; Boettcher, S. W.; Mi, Q.; Santori, E. A.; Lewis, N. S. Solar Water Splitting Cells. *Chem. Rev.* **2010**, *110* (11), 6446-6473.
35. Li, Y.-F.; Selloni, A. Mechanism and Activity of Water Oxidation on Selected Surfaces of Pure and Fe-Doped NiOx. *ACS Catal.* **2014**, *4* (4), 1148-1153.
36. Cady, C. W.; Gardner, G.; Maron, Z. O.; Retuerto, M.; Go, Y. B.; Segan, S.; Greenblatt, M.; Dismukes, G. C. Tuning the Electrocatalytic Water Oxidation Properties of AB₂O₄ Spinel Nanocrystals: A (Li, Mg, Zn) and B (Mn, Co) Site Variants of LiMn₂O₄. *ACS Catal.* **2015**, *5* (6), 3403-3410.
37. Kwapien, K.; Piccinin, S.; Fabris, S. Energetics of Water Oxidation Catalyzed by Cobalt Oxide Nanoparticles: Assessing the Accuracy of DFT and DFT+U Approaches Against Coupled Cluster Methods. *J. Phys. Chem. Lett.* **2013**, *4* (24), 4223-4230.
38. Ronconi, F.; Syrgiannis, Z.; Bonasera, A.; Prato, M.; Argazzi, R.; Caramori, S.; Cristino, V.; Bignozzi, C. A. Modification of Nanocrystalline WO₃ with a Dicationic Perylene Bisimide: Applications to Molecular Level Solar Water Splitting. *J. Am. Chem. Soc.* **2015**, *137* (14), 4630-4633.
39. Butchosa, C.; Guiglion, P.; Zwijnenburg, M. A. Carbon Nitride Photocatalysts for Water Splitting: A Computational Perspective. *J. Phys. Chem. C.* **2014**, *118* (43), 24833-24842.
40. Pokhrel, R.; Goetz, M. K.; Shaner, S. E.; Wu, X.; Stahl, S. S. The “Best Catalyst” for Water Oxidation Depends on the Oxidation Method Employed: A Case Study of Manganese Oxides. *J. Am. Chem. Soc.* **2015**, *137* (26), 8384-8387.
41. Mirzakułova, E.; Khatmullin, R.; Walpita, J.; Corrigan, T.; Vargas-Barbosa, N. M.; Vyas, S.; Oottikkal, S.; Manzer, S. F.; Hadad, C. M.; Glusac, K. D. Electrode-Assisted Catalytic Water Oxidation by a Flavin Derivative. *Nat. Chem.* **2012**, *4* (10), 794-801.
42. Morawski, O.; Izdebska, K.; Karpiuk, E.; Suchocki, A.; Zhydachevskyy, Y.; Sobolewski, A. L. Titanyl Phthalocyanine as a Water Photooxidation Agent. *J. Phys. Chem. C.* **2015**, *119* (25), 14085-14093.
43. Liu, G.; Hall, J.; Nasiri, N.; Gengenbach, T.; Spiccia, L.; Cheah, M. H.; Tricoli, A. Scalable Synthesis of Efficient Water Oxidation Catalysts: Insights into the Activity of

Flame-Made Manganese Oxide Nanocrystals. *ChemSusChem*. **2015**, 8 (24), 4162-4171.

44. Suib, S. L. *New and Future Developments in Catalysis: Solar Photocatalysis*; Newnes: Oxford, 2013.

45. Fillol, J. L.; Codolà, Z.; Garcia-Bosch, I.; Gómez, L.; Pla, J. J.; Costas, M. Efficient Water Oxidation Catalysts Based on Readily Available Iron Coordination Complexes. *Nat. Chem.* **2011**, 3 (10), 807-813.

46. Duan, L.; Bozoglian, F.; Mandal, S.; Stewart, B.; Privalov, T.; Llobet, A.; Sun, L. A Molecular Ruthenium Catalyst with Water-Oxidation Activity Comparable to that of Photosystem II. *Nat. Chem.* **2012**, 4 (5), 418-423.

47. Sheridan, M. V.; Sherman, B. D.; Marquard, S. L.; Fang, Z.; Ashford, D. L.; Wee, K.-R.; Gold, A. S.; Alibabaei, L.; Rudd, J. A.; Coggins, M. K.; Meyer, T. J. Electron Transfer Mediator Effects in Water Oxidation Catalysis by Solution and Surface-Bound Ruthenium Bpy-Dicarboxylate Complexes. *J. Phys. Chem. C* **2015**, 119 (45), 25420-25428.

48. Duffy, E. M.; Marsh, B. M.; Garand, E. Probing the Hydrogen-Bonded Water Network at the Active Site of a Water Oxidation Catalyst: $[\text{Ru}(\text{bpy})(\text{tpy})(\text{H}_2\text{O})]^{2+} \cdot (\text{H}_2\text{O})_{0-4}$. *J. Phys. Chem. A* **2015**, 119 (24), 6326-6332.

49. Wang, L.-P.; Wu, Q.; Van Voorhis, T. Acid-Base Mechanism for Ruthenium Water Oxidation Catalysts. *Inorg. Chem.* **2010**, 49 (10), 4543-4553.

50. Erogbogbo, F.; Lin, T.; Tucciarone, P. M.; LaJoie, K. M.; Lai, L.; Patki, G. D.; Prasad, P. N.; Swihart, M. T. On-Demand Hydrogen Generation using Nanosilicon: Splitting Water without Light, Heat, or Electricity. *Nano Lett.* **2013**, 13 (2), 451-456.

51. Annamalai, A.; Subramanian, A.; Kang, U.; Park, H.; Choi, S. H.; Jang, J. S. Activation of Hematite Photoanodes for Solar Water Splitting: Effect of FTO Deformation. *J. Phys. Chem. C* **2015**, 119 (7), 3810-3817.

52. Le Formal, F.; Pastor, E.; Tilley, S. D.; Mesa, C. A.; Pendlebury, S. R.; Grätzel, M.; Durrant, J. R. Rate Law Analysis of Water Oxidation on a Hematite Surface. *J. Am. Chem. Soc.* **2015**, 137 (20), 6629-6637.

53. Sivula, K.; Le Formal, F.; Grätzel, M. Solar Water Splitting: Progress Using Hematite ($\alpha\text{-Fe}_2\text{O}_3$) Photoelectrodes. *ChemSusChem*. **2011**, 4 (4), 432-449.

54. Park, J. H.; Kim, S.; Bard, A. J., Novel Carbon-Doped TiO_2 Nanotube Arrays with High Aspect Ratios for Efficient Solar Water Splitting. *Nano Lett.* **2005**, 6 (1), 24-28.

55. Zhong, D. K.; Sun, J.; Inumaru, H.; Gamelin, D. R. Solar Water Oxidation by

- Composite Catalyst/ α -Fe₂O₃ Photoanodes. *J. Am. Chem. Soc.* **2009**, *131* (17), 6086-6087.
56. Hu, S.; Shaner, M. R.; Beardslee, J. A.; Lichterman, M.; Brunschwig, B. S.; Lewis, N. S. Amorphous TiO₂ Coatings Stabilize Si, GaAs, and GaP Photoanodes for Efficient Water Oxidation. *Science* **2014**, *344* (6187), 1005-1009.
57. Ohno, T.; Tanigawa, F.; Fujihara, K.; Izumi, S.; Matsumura, M. Photocatalytic Oxidation of Water by Visible Light Using Ruthenium-Doped Titanium Dioxide Powder. *J. Photochem. Photobiol. A* **1999**, *127* (1-3), 107-110.
58. Zhong, D. K.; Gamelin, D. R. Photoelectrochemical Water Oxidation by Cobalt Catalyst ("Co-Pi")/ α -Fe₂O₃ Composite Photoanodes: Oxygen Evolution and Resolution of a Kinetic Bottleneck. *J. Am. Chem. Soc.* **2010**, *132* (12), 4202-4207.
59. Suntivich, J.; May, K. J.; Gasteiger, H. A.; Goodenough, J. B.; Shao-Horn, Y. A Perovskite Oxide Optimized for Oxygen Evolution Catalysis from Molecular Orbital Principles. *Science* **2011**, *334* (6061), 1383-1385.
60. Shuo, W.; Minghuan, L.; Yaming, D. Understanding the Stability of Surface Nanobubbles. *J. Phys. Condens. Matter* **2013**, *25* (18), 184007.
61. Mazloomi, S. K.; Sulaiman, N. Influencing Factors of Water Electrolysis Electrical Efficiency. *Renew. Sust. Energ. Rev.* **2012**, *16* (6), 4257-4263.
62. Chen, Z.; Meyer, T. J. Copper(II) Catalysis of Water Oxidation. *Angew. Chem. Int. Ed.* **2013**, *52* (2), 700-703.
63. Tamaki, Y.; Vannucci, A. K.; Dares, C. J.; Binstead, R. A.; Meyer, T. J. One-Electron Activation of Water Oxidation Catalysis. *J. Am. Chem. Soc.* **2014**, *136* (19), 6854-6857.
64. Roger, I.; Symes, M. D. Efficient Electrocatalytic Water Oxidation at Neutral and High pH by Adventitious Nickel at Nanomolar Concentrations. *J. Am. Chem. Soc.* **2015**, *137* (43), 13980-13988.
65. Takashima, T.; Hashimoto, K.; Nakamura, R. Mechanisms of pH-Dependent Activity for Water Oxidation to Molecular Oxygen by MnO₂ Electrocatalysts. *J. Am. Chem. Soc.* **2012**, *134* (3), 1519-1527.
66. Zhao, Y.; Lin, J.; Liu, Y.; Ma, B.; Ding, Y.; Chen, M. Efficient Light-Driven Water Oxidation Catalyzed by a Mononuclear Cobalt(III) Complex. *Chem. Commun.* **2015**, *51* (97), 17309-17312.
67. Sherman, B. D.; Ashford, D. L.; Lapides, A. M.; Sheridan, M. V.; Wee, K.-R.; Meyer, T. J. Light-Driven Water Splitting with a Molecular Electroassembly-Based Core/Shell Photoanode. *J. Phys. Chem. Lett.* **2015**, *6* (16), 3213-3217.

68. Gao, Y.; Ding, X.; Liu, J.; Wang, L.; Lu, Z.; Li, L.; Sun, L. Visible Light Driven Water Splitting in a Molecular Device with Unprecedentedly High Photocurrent Density. *J. Am. Chem. Soc.* **2013**, *135* (11), 4219-4222.
69. Duan, L.; Fischer, A.; Xu, Y.; Sun, L. Isolated Seven-Coordinate Ru(IV) Dimer Complex with [HOHOH]⁻ Bridging Ligand as an Intermediate for Catalytic Water Oxidation. *J. Am. Chem. Soc.* **2009**, *131* (30), 10397-10399.
70. Li, M.; Takada, K.; Goldsmith, J. I.; Bernhard, S. Iridium(III) Bis-Pyridine-2-Sulfonamide Complexes as Efficient and Durable Catalysts for Homogeneous Water Oxidation. *Inorg. Chem.* **2016**, *55* (2), 518-526.
71. Gao, W.; Jing, Y.; Yang, J.; Zhou, Z.; Yang, D.; Sun, J.; Lin, J.; Cong, R.; Yang, T. Open-Framework Gallium Borate with Boric and Metaboric Acid Molecules inside Structural Channels Showing Photocatalysis to Water Splitting. *Inorg. Chem.* **2014**, *53* (5), 2364-2366.
72. Peighambardoust, S. J.; Rowshanzamir, S.; Amjadi, M. Review of the Proton Exchange Membranes for Fuel Cell Applications. *Int. J. Hydrogen Energy.* **2010**, *35* (17), 9349-9384.
73. Agmon, N. The Grotthuss Mechanism. *Chem. Phys. Lett.* **1995**, *244* (5), 456-462.
74. Coggins, M. K.; Zhang, M.-T.; Chen, Z.; Song, N.; Meyer, T. J. Single-Site Copper(II) Water Oxidation Electrocatalysis: Rate Enhancements with HPO₄²⁻ as a Proton Acceptor at pH 8. *Angew. Chem.* **2014**, *126* (45), 12422-12426.
75. Barnett, S. M.; Goldberg, K. I.; Mayer, J. M. A Soluble Copper-Bipyridine Water-Oxidation Electrocatalyst. *Nat. Chem.* **2012**, *4* (6), 498-502.
76. Iino, T.; Ohashi, K.; Inoue, K.; Judai, K.; Nishi, N.; Sekiya, H. Infrared Spectroscopy of Cu⁺ (H₂O)_(n) and Ag⁺ (H₂O)_(n): Coordination and Solvation of Noble-Metal Ions. *J. Chem. Phys.* **2007**, *126* (19), 194302-194302.
77. Pulay, P.; Fogarasi, G. Fock Matrix Dynamics. *Chem. Phys. Lett.* **2004**, *386* (4-6), 272-278.
78. John M. Herbert, M. H.-G. Accelerated, Energy-Conserving Born-Oppenheimer Molecular Dynamics via Fock Matrix Extrapolation. *Phys. Chem. Chem. Phys.* **2005**, *7*, 3269-3275.
79. Press, W. H.; Teukolsky, S. A.; Vetterling, W. T.; Flannery, B. P. *Numerical Recipes 3rd Edition: The Art of Scientific Computing*; Cambridge University Press: New York, 2007.

CHAPTER 2

STRUCTURAL PROGRESSION IN CLUSTERS

OF IONIZED WATER $(\text{H}_2\text{O})_{n=1-5}^+$

Reprinted with permission from Herr, J. D.; Talbot, J.; Steele, R. P. Structural Progression in Clusters of Ionized Water, $(\text{H}_2\text{O})_{n=1-5}^+$. *J. Phys. Chem. A* **2015**, *119* (4), 752-766. Copyright 2015 American Chemical Society.

Structural Progression in Clusters of Ionized Water, $(\text{H}_2\text{O})_{n=1-5}^+$

Jonathan D. Herr, Justin Talbot, and Ryan P. Steele*

Henry Eyring Center for Theoretical Chemistry, Thatcher Building for Biological and Biophysical Chemistry, University of Utah, 315 South 1400 East, Salt Lake City, Utah 84112, United States

Supporting Information

ABSTRACT: Ionized water clusters serve as a model of water-splitting chemistry for energetic purposes, as well as postradiolytic events in condensed-phase systems. Structures, properties, and relative energies are presented for oxidized water clusters, $(\text{H}_2\text{O})_{n=1-5}^+$, using equation-of-motion coupled-cluster theory approaches. In small clusters, an ion–radical contact pair $\text{OH}\cdots\text{H}_3\text{O}^+$ is known to form upon ionization. The transition from $n = 4$ to $n = 5$ molecules in the cluster, however, is found to demarcate a size regime in which a propensity for the ion and radical to separate exists. This trend is consistent with recent experimental vibrational analyses. Decomposition of the cluster energetics reveals that preferential solvation of the hydronium cation by water serves as the dominant driving force for this pair separation, which should persist in larger clusters and bulk water ionization.



I. INTRODUCTION

The discovery of clean, secure, renewable, and widely distributed sources of energy remains a long-sought societal and scientific goal.^{1–6} Forecasted energy appetites challenge known reserves⁷ and rely on fuel sources with non-negligible environmental impacts.⁴ One alternative is the storage of solar energy in chemical bonds. In particular, the electrochemical splitting of water into molecular hydrogen and oxygen has the potential for environmentally friendly solar fuel storage. To become practical, this process requires catalysts, and indeed, several potentially viable catalysts have been developed in recent years.^{8–38} However, although many of these catalysts have known redox properties, discerning the molecular-level, inner-sphere chemistry remains challenging, which hampers further catalyst development.³⁹ In this work, simplified models of the *uncatalyzed* oxidation chemistry [ionized water clusters, $(\text{H}_2\text{O})_n^+$] are examined via *ab initio* electronic structure calculations to establish a reference point for catalytic chemistry and to examine the unknown, molecular-level details of the water ionization process.⁴⁰

This ionized cluster model also has significant relevance for radiation chemistry. Ionizing radiation in bulk water is known to generate solvated electrons,⁴⁰ and this reductive product of the ionization process is now reasonably well characterized on experimental and theoretical fronts.^{41,42} The ionized hole left behind (the water cation) has received relatively less study, and mechanistic details remain unsolved. Textbook presentations⁴³ and more recent experiments⁴⁴ suggest that this hole is the source of hydroxyl radicals, OH^\bullet , in the condensed phase, whereas gas-phase studies of the prototypical water dimer cation nominally suggest a rapidly formed hydronium–hydroxyl ion–radical contact pair, $\text{H}_3\text{O}^+\cdots\text{OH}^\bullet$.^{45–56} This work demonstrates a critical size-dependent structural transition that connects these two regimes and discusses the driving force underlying their difference.

Previous computational studies of ionized water have ranged from detailed examinations of the dimer^{46–54,57,58} to density functional theory (DFT)-based examinations of the short-time, post-ionization dynamics in clusters^{53,59–62} and bulk water.⁶³ One of the major challenges to understanding water ionization, however, is the lack of reliable methodological mileposts beyond the dimer prototype.⁵⁸ Early DFT studies,⁵⁸ for example, erroneously assigned the structure of the dimer, and only after careful wavefunction-based analysis,^{47–52} in concert with vibrational spectroscopy experiments,⁵⁵ was the dimer structure definitively determined. Similar benchmark data for the behavior in larger clusters are needed, especially because recent experiments^{64,65} suggest qualitatively different behavior in these regimes.

The purpose of this study is to examine the size-dependent structural trends exhibited by equilibrium, oxidized water clusters, $(\text{H}_2\text{O})_n^+$. In short, how do the initially formed ion and radical behave in the presence of additional water molecules? What are the driving forces for the observed behavior? In spite of the model nature of these cluster systems, the answers to these questions are critically important for water-splitting chemistry. The varied behavior scenarios (including contact-pair diffusion, pair separation, or processes intermediate to these two limiting cases) constitute very different electronic environments for potential catalysts. The energy scales and natural behavior of ionized water, in the absence of other chemical species, establish reference points for catalyst design and understanding of radiolysis events.

To examine such structural trends, this study first generates a library of relevant isomers of water cluster ions, $(\text{H}_2\text{O})_{1-5}^+$. Structures and properties are optimized and benchmarked at a

Received: September 25, 2014

Revised: January 6, 2015

Published: January 7, 2015

hierarchy of levels of electronic structure theory, culminating in a reliable set of isomer reference data for this open-shell cation. This set also serves to establish a computational reference point for subsequent studies of larger clusters, as well as future explorations of the efficacy of alternative methodology. Similar past studies of protonated water clusters, $\text{H}^+(\text{H}_2\text{O})_n$ have provided key structural and methodological information.⁶⁶ The distinguishing characteristic of the current study is the presence of the hydroxyl radical, which challenges current methodology; comparison to these previous protonated-water benchmark studies will also be provided.

The main portion of this investigation examines the structural evolution trends and their driving forces in the water cation monomer through pentamer. As will be shown, the pentamer marks a critical qualitative juncture in the cation cluster anatomy, and the electronic source of this transition is investigated. The pentamer is sufficient to demonstrate a *propensity for the ion and radical to separate*, spurred by the preferential solvation of the hydronium cation by water. The computed trends are consistent with the interpretation of recent experimental studies,^{64,65} and we are here able to provide accurate quantitative support for such trends, as well as an explanation for the driving forces underlying them.

II. METHODS

Oxidized water is an open-shell cation and has been shown to require accurate electronic structure theory.^{47–52,54,63,67,68} Computational approaches based on equation-of-motion coupled-cluster theory^{69–75} circumvent the inherent spin imbalance in these open-shell states and have demonstrated remarkable accuracy in computing ionization potentials and structural properties.⁷⁶ In fact, equation-of-motion approaches have been used previously to benchmark relative energies of the water dimer cation,⁴⁸ as well as generate an analytic potential energy surface for this reference system.⁵¹ Therefore, geometry optimizations and harmonic frequency calculations for $(\text{H}_2\text{O})_{n=1-5}^+$ were performed with equation-of-motion coupled-cluster theory with single and double excitations for ionized states (EOM-IP-CCSD), and further refinement of relative energies was performed with single-point energy calculations using a perturbative treatment of triple excitations [EOM-IP-CCSD(dT)]. Structures were optimized with the atom-centered aug-cc-pVDZ basis set, after aug-cc-pVTZ validation on the $n = 1-3$ structures (section IIIA). Single-point energy calculations for the dimer and trimer were performed with aug-cc-pVDZ, aug-cc-pVTZ, and aug-cc-pVQZ,⁷⁷ hereafter denoted aDZ, aTZ, and aQZ, respectively. On the basis of this small-cluster testing, single-point energy calculations for the four- and five-water clusters were performed with aDZ and aTZ. In all cases, an extrapolated⁷⁸ estimate of complete basis set (CBS) energies was also performed. The core electrons of oxygen were frozen in all correlation calculations.

To compare to previous analyses, as well as test whether less computationally demanding approaches are viable for this system, several lower-level methods were also examined. Computations utilizing Hartree–Fock (HF), resolution-of-the-identity second-order Møller–Plesset perturbation theory (RI-MP2),^{79–84} and coupled-cluster theory^{85,86} with single, double, and perturbative triple excitations [CCSD and CCSD(T)] were performed for comparison. Kohn–Sham density-functional theory (DFT)^{87,88} analyses will be discussed in context in section III E. For the MP2 calculations, the

6-31++G(d,p) basis set^{89,90} was also tested. Analytic Hessians were utilized for HF, whereas MP2 and all coupled-cluster frequencies were computed by finite-difference of analytic first derivatives, using a step size of 0.0005 Å. All calculations were performed with a development version of the Q-Chem 4.2 quantum chemistry software package,⁹¹ and molecular structures are displayed using images generated with VMD.⁹²

Even a five-water cluster accesses sufficient configuration space that a search for isomers is nontrivial. Early manual exploration of this space exhibited trends consistent with lessons learned from the solvated hydroxyl radical, where the lowest-energy isomer is often the “hydrogen-deleted” analogue of known neutral water cluster isomers.^{93–97} A dangling O–H bond is simply removed, with little (relative) energetic penalty, to generate the analogous $\text{OH}(\text{H}_2\text{O})_n$ cluster; only subtle subsequent structural relaxation occurs. The studies of the current work observed a similar trend in the transition from $\text{H}^+(\text{H}_2\text{O})_n$ to $(\text{H}_2\text{O})_n^+$. By selective deletion of each unique hydrogenic moiety in the parent protonated-water complexes, for which a database of known structures exists,^{98,99} a reasonably sampled population of cationic isomers was generated. The resulting ion–radical structures were relaxed via geometry optimization, and unique low-energy isomers are presented here. As a check of this somewhat limited sampling procedure, a thermal ensemble of neutral water clusters was sampled via 330 ps of molecular dynamics using the OPLS-AA molecular mechanics force field¹⁰⁰ and a Langevin thermostat at 300 K. Structures were randomly selected from this ensemble, ionized, and then structurally relaxed via the *ab initio* procedures outlined above. This procedure discovered additional high-energy isomers and transition states, but the low-energy isomers generated by the “H-deletion” procedure were shown to be robust. These isomers are presented in the following data and discussion, with the intent of focusing on the equilibrium structural evolution.

To benchmark the electronic structure and further examine the source of the structural trends, spin densities ($\rho^{\text{spin}} = \rho^\alpha - \rho^\beta$) and density-difference ($\Delta\rho = \rho^0 - \rho^+$) plots were generated throughout. The latter are defined as the total electron density difference between the neutral and cation electronic states, fixed in the complex geometry. These two analyses serve to identify the character and location of the radical and cationic hole in ionized water. These analyses were performed in both the neutral and cationic geometries to examine the relaxation of these ionization effects as the structural progression occurs.

III. RESULTS AND DISCUSSION

A. *Ab Initio* Benchmarking. A preliminary requirement for a reliable analysis of structural data is the establishment of a baseline level of theory for these complexes. One of the aims of this study is to provide a benchmark set of accurate relative energy data, and this aim is the justification for the use of EOM methods. Common density functionals, without empirical self-interaction corrections,^{101–103} have been shown to fail qualitatively for this problem,⁴⁷ as it is essentially a larger-scale incarnation of the infamous H_2^+ problem.¹⁰⁴ Recent developments in range-separated hybrids show promise in this regard,^{105,106} however, and the MPW1K functional^{107,108} also has demonstrated accuracy in small clusters. Although the current analysis focuses mainly on wavefunction-based approaches, this set of reference data will hopefully facilitate examination of these alternative methodologies. A comparison

Table 1. Benchmark Methodology Comparisons for H₂O⁺

energy		geometry		ionization potential (eV)	
method	basis	method	basis	vertical	adiabatic
HF	aDZ	HF	aDZ	11.074	10.970
	aTZ		aDZ	11.038	10.939
	aQZ			11.032	10.938
	aTZ		aTZ	11.047	10.939
	aQZ			11.041	10.939
MPW1K	aQZ	MPW1K	aQZ	11.046	10.939
	aDZ		aDZ	12.549	12.445
	aTZ			12.519	12.423
	aQZ			12.519	12.426
	aTZ		aTZ	12.530	12.423
RI-MP2	aQZ	RI-MP2	aQZ	12.529	12.427
	aDZ		aDZ	12.534	12.427
	aTZ			12.696	12.612
	aQZ			12.844	12.770
	aTZ		aTZ	12.910	12.843
CCSD	aQZ	CCSD		12.859	12.770
	aDZ			12.933	12.844
	aTZ			12.934	12.844
	aQZ		aQZ	12.447	12.354
	aTZ		aDZ	12.556	12.477
CCSD(T)	aQZ	CCSD		12.608	12.538
	aDZ			12.577	12.478
	aTZ		aTZ	12.629	12.539
	aQZ			12.639	12.539
	aTZ		aDZ	12.513	12.415
EOM-IP-CCSD	aTZ	EOM-IP-CCSD (CCSD) ^a		12.657	12.572
	aQZ			12.715	12.639
	aDZ			12.715	12.639
	aTZ		aTZ	12.677	12.572
	aQZ			12.735	12.639
EOM-IP-CCSD(dT)	aQZ	EOM-IP-CCSD (CCSD) ^a		12.745	12.639
	aDZ			12.745	12.639
	aTZ		aDZ	12.365	12.270
	aQZ			12.573	12.494
	aTZ		aTZ	12.653	12.584
	aQZ			12.594	12.494
	aDZ			12.674	12.585
	aTZ			12.684	12.585
	aQZ		aQZ	12.684	12.585
	aTZ		aDZ	12.544	12.444
	aQZ			12.722	12.638
	aDZ			12.722	12.722
	aTZ			12.797	12.722
	aQZ		aTZ	12.742	12.637
	aTZ		aQZ	12.817	12.722
				12.827	12.721

^aParenthetical listings denote paired methodologies for neutral species optimizations.

of these benchmark results to MPW1K will follow in section III E.

The water monomer and dimer cations serve as demonstrative test cases for the underlying computational methodology. The molecular orbital details of this ionization process were presented in depth in ref 48. The results of our systematic benchmarking tests for these systems are shown in Tables 1 and 2, including vertical and adiabatic ionization potentials (IPs).

Monomer. The water monomer cation exhibits a vertical ionization potential of 12.827 eV using EOM-IP-CCSD(dT)/aQZ (with the EOM-IP-CCSD/aQZ geometry), with 0.105 eV of geometric relaxation toward the adiabatic IP; these numbers are taken to be the reference point for subsequent comparisons. The monomer's structure relaxes via lengthening of the O–H

bond (0.956–0.997 Å) and opening of the H–O–H bond angle (104.6–109.4°). Due to the role of differential electron correlation, HF underestimates the monomer's ionization potential by more than 1.5 eV. At the same basis set, the CCSD and CCSD(T) methods also differ from the EOM-IP-CCSD(dT) vertical IP result by –0.188 and –0.082 eV, respectively. The perturbative triples correction adds a nontrivial shift to the EOM results, accounting for 0.142 eV of the vertical IP. A simplified approach (not shown in Table 1), in which the aDZ triples correction is added to the aQZ EOM-IP-CCSD results (the EOM analogue of the ΔCCSD(T) correction^{109–111}) is able to recover this target value to within 0.036 eV. Interestingly, the RI-MP2 method, which is known to exhibit difficulty with such radical systems,¹¹² is able to accurately reproduce these relative energies; RI-MP2/aTZ, for

Table 2. Benchmark Methodology Comparisons for $(\text{H}_2\text{O})_2^+$

energy		geometry		ionization potential (eV)		PT-HB gap ^b (kcal/mol)
method	basis	method	basis	vertical	adiabatic	
HF	aDZ	HF	aDZ	10.263	9.178	23.16
	aTZ		aDZ	10.228	9.132	23.83
	aQZ		aDZ	10.223	9.137	23.73
	aTZ		aTZ	10.238	9.132	27.79
	aQZ		aTZ	10.233	9.138	27.73
MPW1K	aDZ	MPW1K	aDZ	11.610	10.537	6.59
	aTZ		aDZ	11.580	10.503	7.47
	aQZ		aDZ	11.579	10.510	7.39
	aTZ		aTZ	11.600	10.510	7.31
	aQZ		aTZ	11.600	10.519	7.19
RI-MP2	aDZ	RI-MP2	aDZ	11.802	10.849	5.24
	aTZ		aDZ	11.950	10.980	6.07
	CBS _{DT} ^c		aDZ	12.028	11.058	5.83
	aQZ		aDZ	12.016	11.050	6.00
	CBS _{TQ}		aDZ	12.067	11.096	5.99
	aTZ		aTZ	11.963	10.979	6.08
	aQZ		aTZ	12.028	11.050	5.99
	CBS _{TQ}		aTZ	12.080	11.097	5.97
	aDZ		aDZ	11.587	10.592	8.11
	aTZ		aDZ	11.696	10.680	9.49
CCSD	CBS _{DT}	CCSD	aDZ	11.757	10.739	9.49
	aQZ		aDZ	11.748	10.737	9.50
	CBS _{TQ}		aDZ	11.789	10.775	9.56
	aTZ		aTZ	11.712	10.680	9.49
	aQZ		aTZ	11.764	10.738	9.48
	CBS _{TQ}		aTZ	11.806	10.775	9.52
	aDZ		aDZ	11.655	10.654	6.44
	aTZ		aDZ	11.799	10.777	7.19
	CBS _{DT}		aDZ	11.875	10.850	6.94
	aQZ		aDZ	11.857	10.839	7.08
CCSD(T)	CBS _{TQ}	CCSD	aDZ	11.902	10.880	7.05
	aTZ		aTZ	11.815	10.775	7.24
	aQZ		aTZ	11.872	10.838	7.11
	CBS _{TQ}		aTZ	11.918	10.879	7.07
	aDZ		aDZ	11.545	10.609	3.35
	aTZ		(CCSD) ^d	11.752	10.790	4.64
	CBS _{DT}		(CCSD) ^d	11.840	10.871	4.90
	aQZ		(CCSD) ^d	11.832	10.876	4.65
	CBS _{TQ}		(CCSD) ^d	11.890	10.930	4.72
	aTZ		(CCSD) ^d	11.768	10.789	4.64
EOM-IP-CCSD	aQZ	EOM-IP-CCSD	aDZ	11.848	10.876	4.63
	CBS _{TQ}		aDZ	11.907	10.931	4.70
	aDZ		aDZ	11.845	10.855	5.34
	aTZ		(CCSD) ^d	12.106	11.100	6.03
	CBS _{DT}		(CCSD) ^d	12.215	11.208	6.04
	aQZ		(CCSD) ^d	12.190	11.192	5.82
	CBS _{TQ}		(CCSD) ^d	12.251	11.252	5.73
	aTZ		(CCSD) ^d	12.120	11.099	5.99
	aQZ		(CCSD) ^d	12.204	11.191	5.79
	CBS _{TQ}		(CCSD) ^d	12.265	11.251	5.71

^aParentetical listings denote paired methodologies for neutral species optimizations. ^bEnergy gap between the proton-transferred (PT) and hemibonded (HB) isomers, defined as $E_{\text{HB}} - E_{\text{PT}}$. ^cComplete basis set estimates based on a two-point extrapolation scheme,⁷⁸ using either aDZ/aTZ (CBS_{DT}) or aTZ/aQZ (CBS_{TQ}).

example, exhibits a vertical IP error of only 0.032 eV. As expected for the correlated methods, the ionization potentials are sensitive to the basis set. However, the aTZ basis set on the aDZ geometry is sufficient to obtain the IP's within ≈ 0.1 eV in all cases. The adiabatic IP's are less sensitive to basis set, which,

for the purpose of the present study, suggests that geometrically relaxed properties of the ion do not require prohibitive basis set sizes.

Dimer. The prototypical water dimer cation has been studied extensively as a model of the water-oxidation process.^{46–54,57,58}

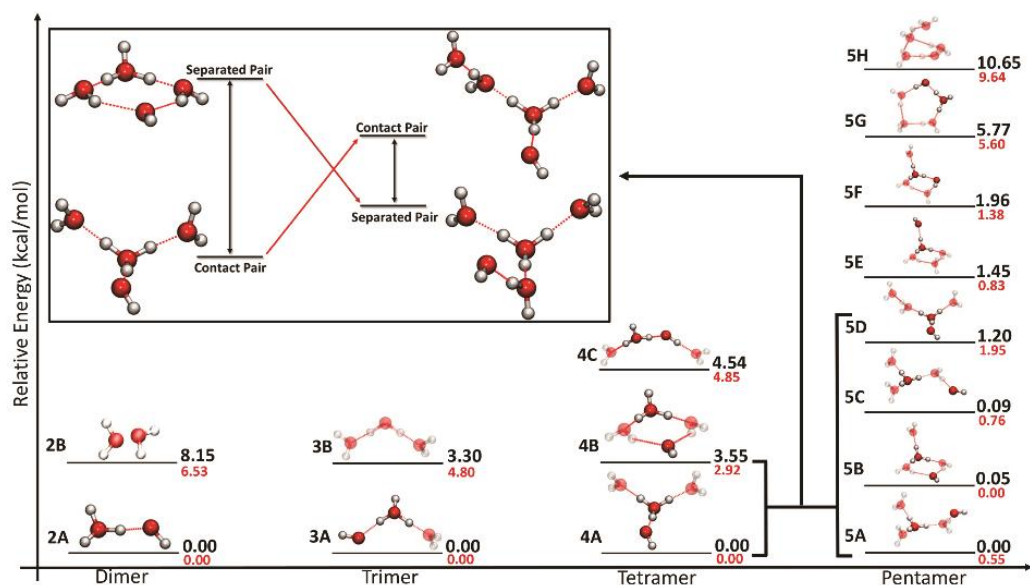


Figure 1. Summary of $(\text{H}_2\text{O})_{2-5}^+$ structures and relative energies, in kcal/mol. Structures have been optimized at the EOM-IP-CCSD/aDZ level of theory; relative energies were computed with EOM-IP-CCSD(dT)/CBS_{DT}. Relative energies (ΔE_0) include harmonic zero-point energy corrections and are shown in black numbers. For reference, the bare electronic energies (ΔE_e) are shown in red. The hydroxyl radical and hydronium cation are emphasized in all structures in which they exist as distinct fragments. The inset highlights the contact-pair separation which is the focus of this analysis.

Two geometric minima are known to exist, which include a proton-transferred (PT) configuration (the ion–radical contact pair discussed at length in this work) and a hemibonded (HB) arrangement. Much computational work has been devoted to the energy gap between these configurations because this quantity poses a severe challenge to electron correlation methods. Wavefunction-based electronic structure approaches have reached consensus that the PT structure is the more stable structure,⁴⁸ and the aforementioned analytic EOM-IP-CCSD/aug-cc-pVTZ potential energy surface confirmed this qualitative behavior. The current results are consistent with these studies, as well as experimental analyses, and provide further quantitative benchmarks of the energy gap. The EOM-IP-CCSD(dT)/CBS estimate of the bare electronic vertical IP is 12.265 eV. This value is notably lower than the IP of the monomer, a trend which has been shown to continue toward bulk water.¹¹³ Due to the large structural rearrangement upon ionization—and the concomitantly abysmal Franck–Condon overlap—comparison to experimental values¹¹⁴ is somewhat dubious. Proton transfer to form the ion–radical pair serves as the driving force for approximately 1 eV of structural relaxation upon ionization. At the same level of theory, the relative electronic energy of the PT and HB structures is 5.71 kcal/mol; this quantity is notably sensitive to the treatment of electron correlation. Previous values using EOM-IP-CCSD/6-311G** and EOM-IP-CC(2,3)/6-311G** are 5.3 and 7.4 kcal/mol, respectively. These results are consistent with the present benchmarks, in the sense that the EOM-IP-CCSD isomer energy gap is notably smaller than the gap computed by CCSD or CCSD(T) alone, although the present results more accurately approach the basis set limit. The triples correlation correction partially restores some of this gap, but it remains more than a full kcal/mol lower than even CCSD(T). The

shared-proton O–H distance in the dimer is 1.054 Å (more than 0.08 Å longer than the remaining two hydronium O–H bonds) whereas the hydrogen-bonded O···H distance is 1.426 Å. The O–H and O···H bonds in the dimer change by -0.005 and $+0.046$ Å between EOM-IP-CCSD and CCSD structures at aug-cc-pVTZ. Therefore, inclusion of the EOM correlation provides subtle but nontrivial effects beyond more standard methodologies.

The RI-MP2 method with a double- ζ basis set is once again sufficient to obtain the correct isomer structures, as well as surprising accuracy in the relative isomer ordering, compared to EOM-IP-CCSD(dT). The RI-MP2 ionization potentials are more accurate, compared to EOM benchmarks, than CCSD or CCSD(T), and the PT–HB gap is nearly quantitative. For benchmarking purposes, EOM-CC theory with large basis sets introduces further refinement of relative isomer and binding energies, but no qualitative change in isomer ordering is observed with MP2. Whether this effect reflects the ability of MP2 to capture the essential physics of the problem or, instead, involves a cancellation of errors, remains unclear. The fact that CCSD and CCSD(T) exhibit nontrivial differences from the EOM results suggests that the latter effect may be dominant. Given the lower relative cost (and scaling) of the perturbative treatment, the RI-MP2 method is likely sufficient for semiquantitative studies of larger clusters. The lone exception to this statement involves the vibrational frequencies in the HB structures, which are known to exhibit erratic behavior ($\bar{\nu} > 6000$ cm^{-1}) in this configuration. This behavior was confirmed in our studies, and the EOM-CC approaches rectify this problem.

Finally, the data in Tables 1 and 2 provide sufficient evidence for a well-defined protocol for reliably benchmarking the larger clusters without prohibitive computational cost. In particular,

Table 3. Relative Isomer Energies for $(\text{H}_2\text{O})_{n=2-5}^+$

species ^a	ΔE_e (kcal/mol) ^b	ΔE_0 (kcal/mol) ^c	$\Delta G_{298\text{K}}$ (kcal/mol) ^d	r_{OH} (Å) ^e	$r_{\text{O}\cdots\text{H}}$ (Å) ^e	r_{OO} (Å) ^f
2A	0.00	0.00	0.00	1.048	1.429	2.473
2B	6.53	8.15	8.33			2.025
3A	0.00	0.00	0.00	1.000	1.574	2.570
3B	4.80	3.30	3.28			
4A	0.00	0.00	0.00	0.994	1.653	2.644
4B	2.92	3.55	5.03			3.754
4C	4.85	4.54	3.96	1.049	1.444	2.492
5A	0.55	0.00	0.10			4.495
5B	0.00	0.05	1.58			3.878
5C	0.76	0.09	0.00			4.365
5D	1.95	1.20	1.34	0.988	1.687	2.671
5E	0.83	1.45	3.59	0.992	1.675	2.666
5F	1.38	1.96	3.99	1.001	1.626	2.611
5G	5.60	5.77	7.82	1.049	1.445	2.493
5H	9.64	10.65	13.20			

^aSpecies labeling follows the structure ordering in Figure 1. ^bRelative bare electronic energy using EOM-IP-CCSD(dT)/CBS_{DT} on EOM-IP-CCSD/aDZ structures. The (dT) correction was computed using aDZ. ^cRelative isomer energy including harmonic EOM-IP-CCSD/aDZ zero-point energy contributions. ^dRelative isomer Gibbs free energy at 298 K using the RRHO approximation. ^eFor the contact-pair structures, the H-bond-participating hydronium O–H bond length (r_{OH}) and H-bond length to the hydroxyl radical ($r_{\text{O}\cdots\text{H}}$) are listed. ^fFor all structures, the distance from the hydronium O to the hydroxyl O (r_{OO}) is also listed.

results are reasonably insensitive to the basis set used for structure optimization. The aDZ basis set provides sufficient accuracy, provided that more accurate basis sets are used for subsequent single-point energy refinement. The PT-HB gap, for example, varies less than 0.02 kcal/mol between aDZ and aTZ structures. For reliable energetics, the CBS_{DT} basis set extrapolation⁷⁸ is employed, where the notation signifies extrapolation to the complete basis set limit, based on aDZ and aTZ values. (For EOM energies, both the reference CC correlation energy and ionization potential have been extrapolated.) A comparison of CBS_{DT} and CBS_{TQ} in Table 2 shows that only a few hundredths of a kcal/mol separate the two approaches in the PT-HB gap, which is one of the most difficult quantities to compute accurately in this analysis. For practical computations on large clusters, even the aTZ basis set calculations are cost-prohibitive. The $\Delta(\text{dT})/\text{aDZ}$ corrections on top of EOM-IP-CCSD/CBS_{TQ} values (not shown in Table 2), however, are sufficiently accurate to obtain the vertical IP to within 0.07 eV of actual EOM-IP-CCSD(dT)/CBS_{TQ} values; the vertical-to-adiabatic relaxation is also captured to within 1% of reference values. These results are consistent with behavior observed in the monomer cation. Therefore, this protocol provides a reliable but computationally tractable approach to benchmarking behavior in the larger clusters.

B. Structural Evolution. The $n = 2-5$ structures are shown in Figure 1, and their key geometric parameters and relative energies are listed in Table 3. A complete listing of isomer energies and structures at each level of theory can be found in the Supporting Information. All methods and basis sets tested here generated the same qualitative set of isomers, so only the structures computed with EOM-IP-CCSD/aug-cc-pVDZ are shown in Figure 1.

With optimized, benchmarked structures available, the size-dependent structural evolution of the ionized clusters can now be analyzed. In particular, a critical size regime is reached for $n = 5$, at which ion–radical contact-pair separation becomes favorable. To highlight the structural trends observed, each cluster size is discussed in turn below and is followed by an analysis of the source of this qualitative trend.

$(\text{H}_2\text{O})_3^+$. Addition of a water molecule to the ion–radical contact pair leads to two plausible bonding arrangements involving solvation of the radical or hydronium moieties. Because of its charge, the latter wins the competition for the third water molecule, forming a complex in which the hydroxyl radical and the neutral water both act as solvation partners of the central hydronium [3A]. An additional isomer [3B] exhibits a solvated- H_2O^+ structure and lies 3.30 kcal/mol above the minimum-energy structure. The hemibonding structure was not pursued in this work because past studies⁵⁸ have shown it to be notably higher in energy.

The lowest-energy isomer can be envisioned as $\text{OH}^+\cdots\text{H}_3\text{O}^+\cdots\text{H}_2\text{O}$, and this arrangement highlights the fact that the contact pair remains intact at $n = 3$. Geometric parameters and harmonic frequency analyses (section IIID) suggest that this species may be better interpreted as a hydroxyl-perturbed H_3O_2^+ complex, however. Unlike in the dimer complex, in which the stretch of the proton shared between the radical and ion is strongly red-shifted, the O–H stretch of the hydronium unit toward the *water* molecule is now the dominantly red-shifted vibrational signature. Accordingly, the O–H bond in the hydronium unit, which points toward the radical, shifts from 1.048 Å back to 1.007 Å. The long hydronium O–H bond in the trimer now instead points toward the solvating H_2O and possesses a bond length of 1.041 Å. This result is also a harbinger of behavior in larger complexes. The large-amplitude shuttling of the partially shared proton in the $\text{H}_3\text{O}^+\cdots\text{H}_2\text{O}$ moiety hints at an increasing propensity of the complex toward ion–radical separation. At the outer turning point of this stretch, a nominally $\text{OH}^+\cdots\text{H}_2\text{O}\cdots\text{H}_3\text{O}^+$ complex begins to form, which is the first inkling of contact-pair separation. Such separation has *not* yet fully occurred at $n = 3$, but the geometric and vibrational signatures of this complex suggest an increasing stabilization of such a putative state.

$(\text{H}_2\text{O})_4^+$. At $n = 4$, the complexes now have the flexibility to expand the solvation shell of the hydronium ion. The lowest-energy isomer [4A] is found to complete the first solvation shell via hydrogen-bond donation to the hydroxyl unit and to the two water molecules, thereby keeping the ion–radical

Table 4. *n*-Body Decomposition of Isomer Interaction Energies (kcal/mol)

species ^a	pair type	$E^{(1)}$			$E^{(2)}$			
		H ₂ O ^b	OH	H ₃ O ⁺	H ₂ O–H ₂ O	H ₂ O–OH	H ₃ O ⁺ –OH	H ₃ O ⁺ –H ₂ O
4A	contact	0.23	0.05	1.39	0.85	0.51	–17.81	–62.66
4B	separated	0.56	0.05	2.96	0.51	–4.14	–3.36	–64.21
<i>isomer difference</i>		–0.33	0.00	–1.57	0.34	4.65	–14.45	1.55
5B	separated	0.52	0.04	1.52	2.82	–4.17	–2.86	–90.45
5E	contact	0.68	0.05	1.95	–6.37	1.11	–17.73	–70.58
<i>isomer difference</i>		–0.16	–0.01	–0.43	9.19	–5.28	14.87	–19.87

^aShown are one- and two-body interaction terms for two isomers—a contact-pair isomer [4A and 5E] and a separated-pair isomer [4B and 5B]—of the water tetramer and pentamer cations. Results are computed using EOM-IP-CCSD/aTZ energies in the EOM-IP-CCSD/aDZ structures. ^bEntries represent the total contribution from each type of interaction, with the sign convention that negative entries are stable with respect to (*n*–1)-body constituents.

contact pair intact, whereas structures 4B (+3.55 kcal/mol) and 4C (+4.54 kcal/mol) expand to a second solvation shell. Structure 4B is particularly critical to the current analysis. Although it lies higher in energy than the global minimum structure, it is the first stable isomer exhibiting signs of ion–radical pair separation. A ring structure is formed in this complex, which is reminiscent of bonding motifs in other ion–molecule complexes, such as Li⁺(H₂O)_{*n*} and NO⁺(H₂O)_{*n*}.^{115,116} The two water molecules comprise the pair-separating entities in this configuration, and their ability to donate hydrogen bonds to the hydroxyl radical provides further stabilization.

A higher-energy contact-pair isomer [4C] was also found, in which the two water molecules individually solvate the hydronium and hydroxyl moieties. Interestingly, the shared-proton O–H bond of the hydronium (pointing toward OH[•]) is particularly long in this species (1.049 Å), suggesting that it has the most contact-pair character of these tetramer isomers. Most relevant to the structural progression analysis, however, is the fact that isomer 4B has now worked its way into the manifold of contact-pair isomers. Solvation of the H₃O⁺ favors structure 4A over 4C, but ring structure 4B is now intermediate to these two reference points.

(H₂O)₅⁺. The water pentamer cation exhibits significantly enhanced configurational flexibility. It also establishes a critical demarcation point at which separation of the ion–radical contact pair is energetically favorable. Whereas the separated species [4B] was 3.55 kcal/mol higher in energy at *n* = 4, three pair-separated species [5A–5C] are now the lowest-energy isomers at *n* = 5, and all exist within 0.1 kcal/mol of one another in relative energy. In each of these complexes, the first solvation shell of the hydronium is completed entirely by water molecules, whereas the OH[•] radical receives one of the dangling hydrogen bonds of the solvating water molecules. Four contact-pair complexes, in contrast, are now 1.20–5.77 kcal/mol higher in energy [5D–5G]. (A hemibonding complex [5H] is included for reference and is still found to be 10.65 kcal/mol above the minimum-energy structure; solvation, therefore, does not increase its relevance.) This structural progression is highlighted in the inset of Figure 1. The relative ordering of these isomers is sensitive to the level of theory, and the role of low-frequency and anharmonic motions in such floppy complexes makes harmonic vibrational corrections somewhat dubious, regardless of the treatment of electron correlation. Indeed, the ordering of the isomers changes upon inclusion of these vibrational corrections. However, the bare electronic energies, also shown in red in Figure 1, demonstrate that the ordering of *classes* of isomers remains robust. The three pair-separated isomers [5A–5C] remain lowest in energy with

or without ZPE corrections; only the ordering *within* this pair-separated class changes. Similarly, the contact-pair class of isomers exhibits ZPE-dependent reordering, but the class, as a whole, remains higher in energy than the pair-separated isomers and lower in energy than the HB isomer.

Entropic considerations favor branched species 5A/5C at nonzero temperatures, where the increased availability of terminal-rotor motions competes with the electronic energy preference. Ring structures, such as 5B, become higher in free energy by 1.58 kcal/mol upon inclusion of thermal and entropic effects at room temperature. The same trend applies to the contact-pair isomers, where the branched structure 5D remains relatively low in free energy and ring structures 5 × 10^{–5} SE–5G are shifted upward upon inclusion of entropic factors.

All three of the low-energy (ΔE_0) pentamer isomers exhibit contact-pair separation. Intact water molecules comprise the first complete solvation shell of the hydronium ion, and the OH radical acts mainly as a hydrogen bond-accepting spectator in the second shell. This result is consistent with the experimental vibrational spectrum interpretation of Fujii,^{64,65} which suggested a migration toward a protonated water cluster spectrum,⁶⁶ dressed by an OH stretch peak. At low temperatures, the 5A isomer is found to be lowest in relative energy in the current study. This isomer differs slightly from the one reported in by Fujii (5C), although the differences between these isomers—mainly a water rotation in the first solvation shell, are likely insignificant. The lack of observation of isomer 5B, however, requires further consideration, which will be presented in section IIID below.

Driving Force. Critical to the current analysis is the fact that our isomer searches can reliably identify structures that are *not* readily available in these cold experiments, simply due to energetic separation. The computations provide additional isomers that highlight the changing proportion of physical contributions to the interaction energies of these species and, therefore, help explain the presence of the observed isomers. To unravel such effects, a many-body analysis has been performed, in which the complexes are decomposed into fragments of OH[•], H₃O⁺, and H₂O. The total interaction energy, truncated at the two-body term, is

$$E^{\text{tot}} = \sum_{i=1} E_i^{(0)} + \sum_{i=i} E_i^{(1)} + \sum_{i<j} E_{ij}^{(2)}$$

where summation indices run over fragments. The “zero-body” energy is here defined as the optimized energy of the noninteracting fragment monomers, whereas the first-order energy accounts for the structural change of the noninteracting

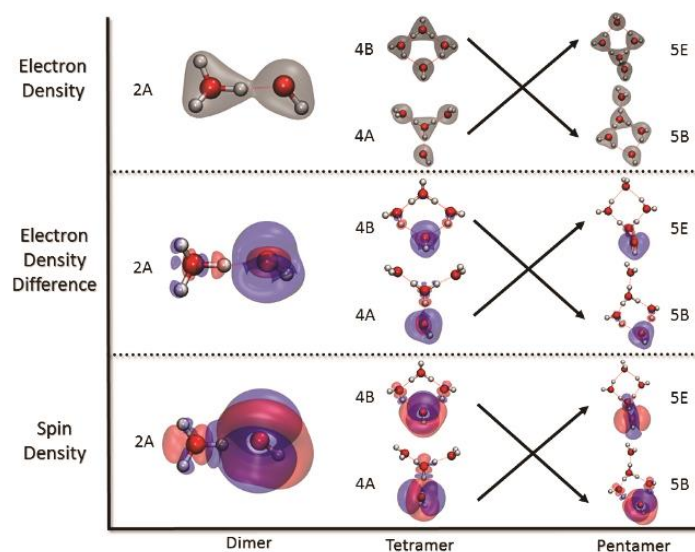


Figure 2. Analysis of electronic contributions to structural progression. Shown are the total electronic densities (upper panel), electronic density differences (middle panel, defined in Methods), and spin densities (lower panel) using EOM-IP-CCSD/aDZ. Contact-pair and pair-separated isomers are shown for the tetramer and pentamer species; the contact-pair isomer of the dimer is shown for reference. Each set of densities uses a consistent isovalue across species. In the spin density plots, blue represents excess α density, whereas red represents a depletion in this quantity. In the density-difference plots, blue represents excess charge in the neutral species, relative to the ion, at a given point in space; red again represents depletion in this quantity.

monomers in the cluster geometry. The leading-order contribution to the cluster binding energy, therefore, occurs at the two-body term, and this term is sufficient to qualitatively describe the propensity for contact-pair separation at $n = 5$.

Shown in Table 4 are the n -body components of this analysis for selected isomers at $n = 4$ and $n = 5$, using the EOM-IP-CCSD/aTZ method on EOM-IP-CCSD/aDZ structures (CCSD was used for neutral species); similar trends are found with other methods. The pentamer isomers are chosen as the isomers in each structural class with the lowest bare electronic energy, although the trends are similar in other isomers. In the table, entries represent the total contribution from each type of interaction. The expansion, up to two-body terms, accounts for roughly 70% of the total interaction energy in each of these systems. The one-body terms make minor contributions and show little difference between the isomers. The two-body terms show larger interactions and highlight the distinct structural progression that occurs at the four- to five-water transition.

Preferential solvation of the hydronium by water, as opposed to the hydroxyl radical, is revealed to be the main driving force for contact-pair separation in larger clusters. At $n = 4$, the cluster stability is dominated by the hydronium–water interaction. However, the strength of this interaction is roughly constant between the isomers because both configurations include two direct hydrogen-bonding interactions between H_3O^+ and H_2O . Instead, the main difference stems from the hydronium–hydroxyl interaction. In the contact-pair isomer [4A], the large hydrogen-bonding interaction between these species leads to more than 14 kcal/mol of preferential stability. The H_2O –OH interactions in the separated-pair isomer [4B] only partially make up for this difference, and these interactions are not sufficient to lead to a lower overall energy. In contrast, at $n = 5$, the H_3O^+ – H_2O interaction overwhelmingly

dominates the relative isomer energy difference. The water–hydroxyl and hydronium–hydroxyl interactions show behavior similar to that of the $n = 4$ isomers, whereas the ion–water interaction is now qualitatively distinct. The pair-separated isomer [5B] exhibits nearly 20 kcal/mol of additional stability in this term, owing to the first solvation shell of H_3O^+ , which has been exclusively completed by water. This difference accounts for the lion's share of the isomer ordering difference upon increasing cluster size from tetramer to pentamer. Although the increased solvating ability of water over the hydroxyl radical is certainly not a novel concept, the relative contribution of all of these pairwise terms in the expansion, including the accurate representation of the ion–radical interaction, is required to definitively assign the dominant role of solvation of the ion.

The separation of charged species in solvent is a well-established phenomenon in condensed-phase chemistry. The solvating ability of surrounding water molecules, for example, can stabilize effectively zwitterionic states,¹¹⁷ and condensed-phase examples of independently solvated ions abound. The fact that such a separation occurs in this *ion–radical complex* is fairly unique, especially given the strong interaction between the ion and the radical in the dimer structure. The fact that this separation occurs upon completion of the *first* solvation shell of hydronium further emphasizes the dominant role of ion solvation in the structural progression. The ability of the OH^\bullet radical to act as a strong hydrogen-bond acceptor further stabilizes separation, but this effect is minor compared to the ion–water interaction.

C. Electronic Considerations. Experimental observation of the post-ionization dynamics in oxidized water has proven to be challenging.^{54,63,113} Electronic structure theory computations, therefore, provide the unique ability to examine the electronic constitution of these structures during the structural

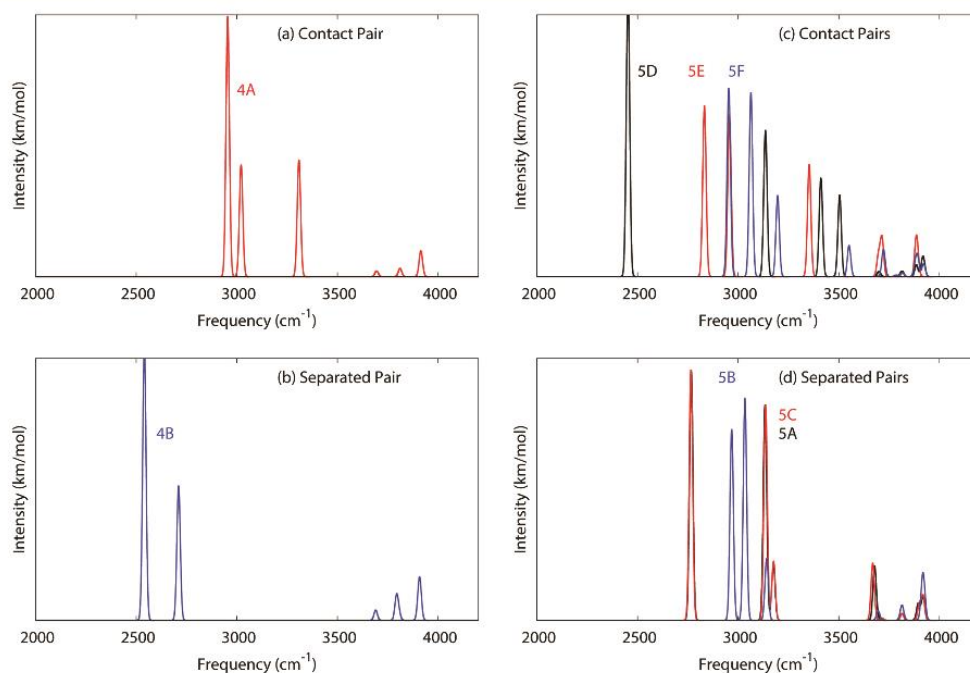


Figure 3. Harmonic infrared absorption spectra. Shown are harmonic frequencies and intensities, computed with the EOM-IP-CCSD/aDZ method, and broadened with a Gaussian of width 20 cm^{-1} . Panels a and b show the vibrational spectrum for contact-pair and pair-separated tetramer isomers, respectively. Panel c shows spectra for three of the contact-pair pentamer isomers [5D (black), 5E (red), 5F (blue)]. Panel d shows analogous spectra for pair-separated pentamer isomers [5A (black), 5B (blue), 5C (red)]. In (d), isomers 5A and 5C exhibit nearly overlapping spectra.

progression which is the focus of this study. Shown in Figure 2 are the total electronic densities, spin densities, and density-difference plots for selected pairs of isomers involved in the titular progression. A constant isovalue has been used within each set of densities. An examination of these densities across the sequence of methods in this work (Supporting Information) shows that the qualitative behavior is retained in all methods, whereas subtle density relaxation details are unique to EOM approaches. The following discussion will focus on the EOM-based results shown in Figure 2.

The spin density plots (lower panel of Figure 2) illustrate that the radical character of ionized water is delocalized over the contact pair in small clusters. This qualitative behavior is consistent with the strongly red-shifted signatures in the vibrational spectrum of the dimer, which suggest an electronic structure intermediate to $\text{H}_3\text{O}^+\cdots\text{OH}^\bullet$ and $\text{H}_2\text{O}^+\cdots\text{H}_2\text{O}$.⁵⁵ (A full analysis of these anharmonic vibrational features and the role of electronic coupling will be presented in a separate study.) As the cluster size increases, however, the spin density of the cationic complex becomes localized on the nominally OH^\bullet fragment. This spin localization is also isomer-specific and is consistent with the structural progression analyzed in the previous section. The separated-pair isomers [4B, 5B], for example, display no spin density on the hydronium at this isovalue. The interleaving water molecules are sufficient to arrest the interaction between the ion and the radical, thereby stabilizing a localized spin on the hydroxyl radical moiety.

The density-difference plots (middle panel) provide further evidence of this electronic localization. In the cationic structures, the neutral reference point is more akin to autoionized water ($\text{H}_3\text{O}^+\cdots\text{OH}^-$). In a localized radical, the

density difference would also be expected to localize on the OH moiety. In the dimer and in the larger contact-pair species [4A, 5E], however, nontrivial participation of the hydronium unit is observed, once again suggesting a moderately delocalized electronic interaction in these isomers. The separated-pair species, on the contrary, exhibit nearly complete localization of the density difference on the OH unit, with only minor contributions from the solvating water molecules. No contribution from the hydronium is observed. Therefore, with the completion of only a single hydration shell of the hydronium, the strong interaction between ion and radical has been effectively silenced. This effect appears to be an inherent property of large, ionized water clusters and stands in stark contrast to the dimer prototype.

These clusters are, unfortunately, not large enough to answer the important question concerning the number of water molecules involved in the initial neutral-water ionization process, as has been studied by others.⁶⁷ They are, however, sufficiently large to demonstrate ion–radical pair separation behavior in the relaxed ion region of configuration space.

D. Harmonic Vibrational Signatures. Vibrational spectroscopy provides a key link between computational isomer benchmarks and experimental observation of ionized clusters. From the outset, the inherently floppy, anharmonic nature of these complexes suggests that harmonic computations of vibrational spectra should be used with caution. However, these results do provide (a) a necessary reference point, off of which subsequent anharmonic computations could be performed and (b) a semiquantitative analysis of the shifting bonding patterns among the isomers.

Figure 3 displays the vibrational spectra of the isomers involved in the four- to five-water structural progression. Shown are EOM-IP-CCSD/aDZ harmonic spectra for the most relevant tetramer (panels a and b) and pentamer (panels c and d) species. For the pentamer spectra, three isomers within the contact-pair and pair-separated classes of species are overlaid in the same plot, with distinguishing colors. Because of expected inhomogeneity in the anharmonicity of free O–H and shared-proton stretches, no empirical scaling has been applied to these spectra.

The low-energy tetramer species (4A, panel 3a) exhibits three extremely bright O–H stretches in the 3000–3300 cm^{-1} region of the spectrum, corresponding to the three stretches of the central hydronium unit. The most intense transition (2955 cm^{-1}) corresponds to the asymmetric stretch of the two O–H bonds participating in hydrogen bonds to the flanking waters, and the highest-frequency member of this triplet (3309 cm^{-1}) corresponds to the hydronium stretch toward the hydroxyl radical. The (relatively) weaker and higher-frequency free O–H stretches exhibit a distinctive pattern, corresponding to the water asymmetric stretches (3912 and 3916 cm^{-1}), symmetric stretches (3809 and 3812 cm^{-1}), and characteristic hydroxyl radical stretch (3694 cm^{-1}). This pattern is confirmed in the known experimental spectrum of this isomer,^{64,65} although the harmonic frequencies are roughly 100 cm^{-1} too high. The higher-energy (and likely not observed) separated-pair isomer [4B] exhibits similar (but red-shifted) free O–H stretches but notably more red-shifted hydrogen-bonded stretches. Because this isomer exhibits more solvated-hydronium structural characteristics, such shifts are to be expected.

As shown above, the pentamer exhibits a new structural motif, in which the ion and radical moieties are separated by solvating water molecules. The three isomers corresponding to this motif [5A, 5B, 5C] exhibit spectra shown in Figure 3d. Because the structures of 5A and 5C differ only by the orientation of the bridging water molecule, their spectra are nearly overlapping. The ring-type 5B isomer, however, exhibits a distinct spectrum. In particular, the stretch of the bridging water molecule toward its hydrogen-bonded hydroxyl radical partner in 5A displays a strong intensity at 3678 cm^{-1} ; because of its ring structure, isomer 5B's analogous modes (3807 and 3813 cm^{-1}) involve stretches of the ring waters and display less intensity. Importantly, in the latter isomer, these stretches sit to the blue to the hydroxyl stretch (3695 cm^{-1}), in contrast to the pattern for 5A/5C. Isomers 5B and 5A/5C also display very different hydrogen-bonded stretches in the 2750–3250 cm^{-1} region. Whereas 5A/5C possess harmonic spectra in this region similar to that of the *eigen* cation [$\text{H}_3\text{O}^+(\text{H}_2\text{O})_3$], the ring constraint in 5B notably alters the vibrational pattern. In 5A, the lowest-frequency stretch of the hydronium unit (an O–H stretch toward the $\text{H}_2\text{O}/\text{OH}$ pair) shows a strong intensity at 2767 cm^{-1} . The asymmetric (3133 cm^{-1}) and symmetric (3175 cm^{-1}) stretches are split strongly from this most intense stretch. In contrast, analogous motions are split by only 174 cm^{-1} in 5B, with the two most intense modes sitting between the bands in 5A. All of the contact-pair isomers, previously shown to be higher in energy, exhibit distinct spectral signatures, owing to the variety of structural patterns.

With these harmonic spectra in-hand, congruency of the present results may be checked against the experimental pentamer spectra of refs 64 and 65. The hydronium-stretch region of the spectrum is likely not reliable in this harmonic treatment, where strong anharmonicity and mode coupling are

expected. The remaining O–H stretches provide critical structural information, however. First, none of the contact-pair pentamer isomers provides fidelity with the experimental spectrum, whereas the low-lying isomers 5A/5C are consistent with the experimental band pattern in this region. The ordering of the hydroxyl and (bridging) water stretches, in particular, suggests that isomer 5A and/or 5C is the structure observed in these spectra. Therefore, the propensity of the ion and radical to separate appears consistent between the current benchmarks and the experimental analysis.

This comparison can also possibly help resolve the closely lying 5A/5C and 5B isomers, the ordering of which was entirely dependent on the estimate of the zero-point energy. The energies computed in the present analysis suggest that 5B should be relevant at low temperatures. No evidence of this isomer appears in the experimental spectrum, however, except in the unlikely event that the bridging water stretches within the ring exhibit surprisingly large anharmonicity. The spectrum in ref 64 was taken at ≈ 180 K, so entropic considerations would favor 5A/5C. The much colder Ar-tagged spectra of ref 65 exhibit nearly identical (albeit narrower) features, though. The presence of the rare gas atom could potentially shift the isomer ordering. More likely, however, is the possibility that anharmonic contributions to the zero-point energy of these clusters is sufficient to bias the isomer population toward 5A/5C. Because of the closely lying energies involved, even subtle shifts in the relative zero-point energies (100 cm^{-1} or less) could bias the population distribution. The high-level electronic benchmarks in this analysis are likely robust, but the treatment of the nuclear motion requires refinement in the context of this dense manifold of isomers. Encouragingly, the hydrogen-bonded region of the pentamer spectrum is notably different for these two isomers, so if a mixture of these two isomers could be prepared under properly chosen experimental conditions, double-resonance/hole-burning experiments¹¹⁸ could be employed to isolate properties of the two isomers individually.

E. DFT Comparisons. Although the EOM-based results in this work provide reliable benchmarks, their computational cost far exceeds the cost of DFT-based approaches. These reference data provide a test suite for the examination of DFT approaches, however. The MPW1K functional has demonstrated success for smaller ionized clusters, and it was employed as computational support for the interpretation of vibrational spectra in refs 64 and 65. In this section, the accuracy of the MPW1K functional is examined in the context of the size-dependent pair separation, and an analysis of the source of its accuracy is provided.

The qualitative structures of the isomers presented in this work are preserved by MPW1K and are not shown again. The relative energies for this functional, using the original EOM-based structure labeling, are presented in Table 5. This functional correctly captures the isomer ordering change upon increasing cluster size from $n = 4$ to $n = 5$. In particular, $E_{4A} < E_{4B}$ and $E_{5A-5C} < E_{5D-5H}$, which reproduces the qualitative trend that is the focus of this analysis. The doubly solvated contact-pair isomer of the tetramer [4C] is incorrectly degenerate with the separated-pair isomer [4B] when zero-point corrections are included. The MPW1K bare electronic relative energies are in error by up to 1.14 kcal/mol for the low-lying isomers of the pentamer, but the relative ordering of the two classes of isomers is still well reproduced. The ionization potentials (Tables 1 and 2) and relative isomer energies (Table

Table 5. DFT (MPW1K/aTZ) Results for $(\text{H}_2\text{O})_4^+$ and $(\text{H}_2\text{O})_5^+$

species ^a	ΔE_0 (kcal/mol) ^b		ΔE_e (kcal/mol) ^c	
	EOM-IP-CCSD(dT)	MPW1K	EOM-IP-CCSD(dT)	MPW1K
4A	0.00	0.00	0.00	0.00
4B	3.55	3.39	2.92	3.35
4C	4.54	3.38	4.85	3.92
5A	0.00	0.00	0.55	0.00
5B	0.05	1.13	0.00	0.38
5C	0.09	0.16	0.76	0.15
5D	1.20	1.20	1.95	1.35
5E	1.45	3.06	0.83	1.97
5F	1.96	2.94	1.38	1.85
5G	5.77	6.37	5.60	5.71
5H	10.65	12.91	9.64	11.25

^aSpecies are labeled according to EOM-based results from Figure 1.

^bRelative isomer energies, including harmonic zero-point energy corrections. The MPW1K results use the aTZ basis for both energies and harmonic frequencies. ^cRelative bare electronic isomer energies.

5), therefore, are not of benchmark quality but are sufficiently accurate to capture the structural progression.

The unique characteristic of the MPW1K functional is the relative partitioning of HF and MPW91 exchange, which has been optimized for kinetic barriers in reactive systems.¹⁰⁷

Figure 4 displays the relative PT/HB isomer energy of $(\text{H}_2\text{O})_2^+$

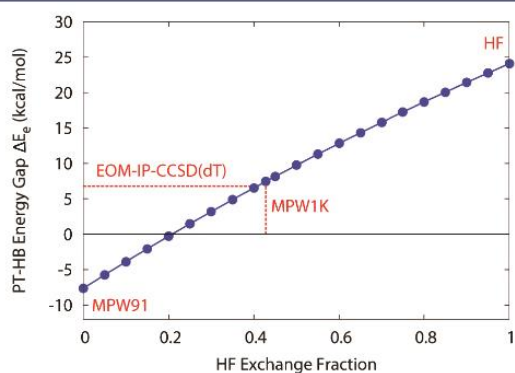


Figure 4. Analysis of the HF exchange contribution to MPW1K accuracy. Displayed is the PT-HB electronic energy gap, in kcal/mol, as a function of HF exchange fraction. The EOM-IP-CCSD(dT)/CBS_{TQ} benchmark (on aTZ geometries) is highlighted. The MPW1K result at 42.8% HF exchange is also denoted.

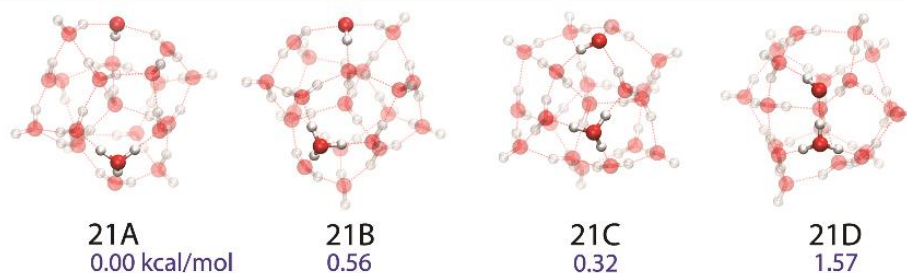


Figure 5. Representative optimized isomers of $(\text{H}_2\text{O})_{21}^+$, computed with RI-MP2/6-31++G(d,p). The ion and radical are emphasized in the plots, with the remaining water network semitransparent.

as a function of this partitioning fraction, with the PW91 correlation functional and aTZ basis set used throughout. Pure HF exchange (100%) overstabilizes the PT structure, whereas pure MPW91 exchange (0%) leads to the qualitatively incorrect overstabilization of the HB structure, as has been observed in previous studies using “pure” density functionals. The intermediate behavior is nearly linear, and the MPW1K fraction of HF exchange (42.8%) is found to be almost ideal for this isomer energy gap, compared to the EOM-IP-CCSD(dT) results presented in this work.

This agreement is fortuitous, and it begs the question of whether this parameter is transferable to larger systems. Given the results of Table 5, this accuracy does appear to reasonably persist across clusters up to $n = 5$. The ZPE-corrected relative energy gap of isomers 4A and 4B, for example, is 3.55 kcal/mol with MPW1K and 3.39 kcal/mol in the present benchmarks. Similarly, the 5A–5D gap is 1.27 kcal/mol with MPW1K, compared to 1.20 kcal/mol with the benchmark EOM method, although other isomers exhibit larger errors. Whether this accuracy continues in much larger systems, where the optimal fraction of HF exchange in density functionals is known to vary,¹¹⁹ remains to be determined. The method, therefore, is not sufficient for numerical benchmark accuracy (and may not be sufficient to distinguish isomers which are close in energy) but the overall energy landscape for small clusters is reproduced nicely. The role of anharmonicity, for example, in ZPE-corrected relative energies and free energies, is likely larger than the MPW1K error compared to reference values. Therefore, its use for this open-shell cation system appears to be robust within the size regime considered in this work, and its use in the interpretation of the vibrational experiments of refs 64 and 65 is justified.

F. Outlook for Larger Complexes and Generality of Separation Trend. A remaining question concerns the generality of this ion–radical separation trend in larger clusters and bulk water. Is, for example, the water pentamer a special case in which forces balance to separate the pair, or does the preferential solvation of the ion continue to drive the two apart when additional solvent molecules are present? A general answer to this question will be addressed in a separate, forthcoming analysis, but in the present context, preliminary results for a 21-water cluster serve to illustrate the general trend. This cluster size was chosen to represent a regime in which internal solvation of neutral water is known to be viable in a cluster environment.¹²⁰

Figure 5 presents a quartet of optimized isomers for $(\text{H}_2\text{O})_{21}^+$ using the RI-MP2/6-31++G(d,p) method. The data provided in Tables 1 and 2 and in the Supporting Information

suggest that this less computationally demanding methodology is also accurate compared to EOM benchmarks, and it has been used in this large cluster analysis as a reasonable compromise of accuracy and efficiency. The structures and relative energies show that the separation trend *does* continue. A contact-pair isomer [21D] is still a stable, but high-energy, form of ionized water, whereas ion–radical pair separation by one [21C], two [21B], and three [21A] water molecules is more stable. This result is partially an artifact of the cluster environment because the ion and radical adopt cluster-surface morphologies analogous to the known structure¹²¹ of $\text{H}^+(\text{H}_2\text{O})_{21}$, and future analyses will require an assessment of this trend in condensed-phase contexts. Interestingly, the driving force for separation beyond the first solvation shell appears to be small, as the energy gap among isomers 21A–21C is relatively small. Whether $n = 5$ definitively demarcates this structural transition, or whether size-dependent alternation occurs, as has been observed in the behavior neutral water clusters,¹²⁰ remains to be examined. The present results, however, when combined with the fact that the ion–water interaction dominates the stability trend (section IIIC), suggest that the generality of this trend in large clusters (and, possibly, bulk water) should be expected.

IV. CONCLUSIONS

A size-dependent structural evolution was observed in benchmark-quality computations of ionized water clusters, $(\text{H}_2\text{O})_n^+$. The ion–radical contact pair, which dominates the configuration space of the prototypical dimer species, is prone to separation in the presence of additional, solvating water molecules. Independent localization of the charge and radical moieties was confirmed in the electronic structure of the complexes, as well. A two-body decomposition of the cluster stability revealed that preferential solvation of the hydronium cation by water molecules serves as the dominant driving force for this separation trend.

Given this driving force for separation, the continuation of the trend in larger clusters and in bulk water is likely. Further solvation of the hydronium cation, beyond a single solvent shell, will only provide additional relative stabilization. Known experimental vibrational spectra^{64,65} appear to be consistent with an interpretation of independently solvated H_3O^+ and OH^\bullet , and although direct observation of these features beyond $n = 11$ is challenging, the driving forces computed in this work are predicted to continue into the bulk.

This result carries special significance for water oxidation in the context of renewable-energy chemistry. In the current work, the ionization process is assumed to be efficient and complete, as no recombination dynamics are considered. In such a regime, a definitive driving force exists for separation of the nascent contact pair. If the initially ionized water molecule was, instead, attached to a catalytic transition metal center or electrode, the propensity of the hydronium ion to relocate away from the remnant hydroxyl *ligand* is exactly the driving force required for fast diffusion toward a proton-exchange membrane and the balancing of charge in an electrolytic cell. Therefore, this driving force is expected to be an inherent property of a successful water-oxidation process, and the manner in which catalysts affect this behavior will be of critical importance in the design of improved technologies. Previous computational studies of water-oxidation catalysts, for example, have required explicit waters beyond the activated water species, to provide a reliable assessment of mechanistic energies.^{122–126} The rather

nuanced interactions underlying the structural evolution in this work are suspected to be the source of this requirement. Implicit solvent models simply do not include the detailed electrostatic and chemical interactions required to properly separate the initially formed contact pair. Therefore, the structural progression highlighted in this work is likely to be general, even in the highly inhomogeneous environment in the immediate vicinity of water-oxidation catalysts.

■ ASSOCIATED CONTENT

Supporting Information

Cartesian coordinates of optimized isomer structures at all discussed levels of theory, energies, harmonic frequencies and intensities. This material is available free of charge via the Internet at <http://pubs.acs.org>.

■ AUTHOR INFORMATION

Corresponding Author

*R. P. Steele. E-mail: ryan.steele@utah.edu

Notes

The authors declare no competing financial interest.

■ ACKNOWLEDGMENTS

The support and resources from the Center for High-Performance Computing at the University of Utah are gratefully acknowledged. This work also used the Extreme Science and Engineering Discovery Environment (XSEDE), which is supported by National Science Foundation grant number ACI-1053575. This work was supported by startup funds from the University of Utah. The authors also thank Evgeny Epifanovsky of Q-Chem, Inc., for identifying and correcting a parallelization bug in the OpenMP coupled-cluster gradient code, without which these calculations would not have been feasible.

■ REFERENCES

- (1) Barber, J.; Tran, P. D. From Natural to Artificial Photosynthesis. *J. R. Soc. Interface* **2013**, *10*, 20120984.
- (2) Cook, T. R.; Dogutan, D. K.; Reece, S. Y.; Surendranath, Y.; Teets, T. S.; Nocera, D. G. Solar Energy Supply and Storage for the Legacy and Nonlegacy Worlds. *Chem. Rev.* **2010**, *110*, 6474–6502.
- (3) Harriman, A. Prospects for Conversion of Solar Energy into Chemical Fuels: The Concept of a Solar Fuels Industry. *Philos. Trans. R. Soc. A: Math., Phys. Eng. Sci.* **2013**, *371*, 20110415.
- (4) Hoffert, M. I.; Caldeira, K.; Jain, A. K.; Haites, E. F.; Harvey, L. D. D.; Potter, S. D.; Schlesinger, M. E.; Schneider, S. H.; Watts, R. G.; Wigley, T. M. L.; et al. Energy Implications of Future Stabilization of Atmospheric CO_2 Content. *Nature* **1998**, *395*, 881–884.
- (5) Nocera, D. G. Great Challenges Ahead. *ChemSusChem* **2008**, *1*, 8.
- (6) Nocera, D. G. Chemistry of Personalized Solar Energy. *Inorg. Chem.* **2009**, *48*, 10001–10017.
- (7) Lewis, N. S.; Nocera, D. G. Powering the Planet: Chemical Challenges in Solar Energy Utilization. *Proc. Natl. Acad. Sci.* **2006**, *103*, 15729–15735.
- (8) Barber, J. Photosystem II: The Water-Splitting Enzyme of Photosynthesis. *Cold Spring Harbor Symp. Quant. Biol.* **2012**, *77*, 295–307.
- (9) Barnett, S. M.; Goldberg, K. I.; Mayer, J. M. A Soluble Copper–Bipyridine Water-Oxidation Electrocatalyst. *Nat. Chem.* **2012**, *4*, 498–502.
- (10) Bediako, D. K.; Costentin, C.; Jones, E. C.; Nocera, D. G.; Saveant, J.-M. Proton-Electron Transport and Transfer in Electrocatalytic Films. Application to a Cobalt-Based O_2 -Evolution Catalyst. *J. Am. Chem. Soc.* **2013**, *135*, 10492–10502.

- (11) Bediako, D. K.; Surendranath, Y.; Nocera, D. G. Mechanistic Studies of the Oxygen Evolution Reaction Mediated by a Nickel–Borate Thin Film Electrocatalyst. *J. Am. Chem. Soc.* **2013**, *135*, 3662–3674.
- (12) Chen, Z.; Concepcion, J. J.; Luo, H.; Hull, J. F.; Paul, A.; Meyer, T. J. Nonaqueous Catalytic Water Oxidation. *J. Am. Chem. Soc.* **2010**, *132*, 17670–17673.
- (13) Concepcion, J. J.; Jurss, J. W.; Norris, M. R.; Chen, Z.; Templeton, J. L.; Meyer, T. J. Catalytic Water Oxidation by Single-Site Ruthenium Catalysts. *Inorg. Chem.* **2010**, *49*, 1277–1279.
- (14) Costi, R.; Young, E. R.; Bulović, V.; Nocera, D. G. Stabilized CdSe–CoPi Composite Photoanode for Light-Assisted Water Oxidation by Transformation of a CdSe/Cobalt Metal Thin Film. *ACS Appl. Mater. Interfaces* **2013**, *5*, 2364–2367.
- (15) Dogutan, D. K.; McGuire, R.; Nocera, D. G. Electrocatalytic Water Oxidation by Cobalt(III) Hangman β -Octafluoro Corroles. *J. Am. Chem. Soc.* **2011**, *133*, 9178–9180.
- (16) Gagliardi, C. J.; Vannucci, A. K.; Concepcion, J. J.; Chen, Z.; Meyer, T. J. The Role of Proton Coupled Electron Transfer in Water Oxidation. *Energy Environ. Sci.* **2012**, *5*, 7704–7717.
- (17) Hull, J. F.; Balcells, D.; Blakemore, J. D.; Incarvito, C. D.; Eisenstein, O.; Brudvig, G. W.; Crabtree, R. H. Highly Active and Robust Cp* Iridium Complexes for Catalytic Water Oxidation. *J. Am. Chem. Soc.* **2009**, *131*, 8730–8731.
- (18) Jurss, J. W.; Concepcion, J. C.; Norris, M. R.; Templeton, J. L.; Meyer, T. J. Surface Catalysis of Water Oxidation by the Blue Ruthenium Dimer. *Inorg. Chem.* **2010**, *49*, 3980–3982.
- (19) Kanan, M. W.; Nocera, D. G. In Situ Formation of an Oxygen-Evolving Catalyst in Neutral Water Containing Phosphate and Co^{2+} . *Science* **2008**, *321*, 1072–1075.
- (20) Karunadasa, H. I.; Chang, C. J.; Long, J. R. A Molecular Molybdenum–Oxo Catalyst for Generating Hydrogen from Water. *Nature* **2010**, *464*, 1329–1333.
- (21) Luttermann, D. A.; Surendranath, Y.; Nocera, D. G. A Self-Healing Oxygen-Evolving Catalyst. *J. Am. Chem. Soc.* **2009**, *131*, 3838–3839.
- (22) McAlpin, J. G.; Stich, T. A.; Ohlin, C. A.; Surendranath, Y.; Nocera, D. G.; Casey, W. H.; Britt, R. D. Electronic Structure Description of a $[\text{Co(III)}_3\text{Co(IV)O}_4]$ Cluster: A Model for the Paramagnetic Intermediate in Cobalt-Catalyzed Water Oxidation. *J. Am. Chem. Soc.* **2011**, *133*, 15444–15452.
- (23) McAlpin, J. G.; Surendranath, Y.; Dincă, M.; Stich, T. A.; Stoian, S. A.; Casey, W. H.; Nocera, D. G.; Britt, R. D. EPR Evidence for Co(IV) Species Produced During Water Oxidation at Neutral pH. *J. Am. Chem. Soc.* **2010**, *132*, 6882–6883.
- (24) Meyer, T. J. Catalysis: The Art of Splitting Water. *Nature* **2008**, *451*, 778–779.
- (25) Meyer, T. J. Catalysis: Oxidizing Water Two Ways. *Nat. Chem.* **2011**, *3*, 757–758.
- (26) Moonshiram, D.; Jurss, J. W.; Concepcion, J. J.; Zakharova, T.; Alperovich, I.; Meyer, T. J.; Pushkar, Y. Structure and Electronic Configurations of the Intermediates of Water Oxidation in Blue Ruthenium Dimer Catalysis. *J. Am. Chem. Soc.* **2012**, *134*, 4625–4636.
- (27) Nocera, D. G. “Fast Food” Energy. *Energy Environ. Sci.* **2010**, *3*, 993–995.
- (28) Pijpers, J. J. H.; Winkler, M. T.; Surendranath, Y.; Buonassisi, T.; Nocera, D. G. Light-Induced Water Oxidation at Silicon Electrodes Functionalized with a Cobalt Oxygen-Evolving Catalyst. *Proc. Natl. Acad. Sci.* **2011**, *108*, 10056–10061.
- (29) Reece, S. Y.; Hamel, J. A.; Sung, K.; Jarvi, T. D.; Esswein, A. J.; Pijpers, J. J. H.; Nocera, D. G. Wireless Solar Water Splitting Using Silicon-Based Semiconductors and Earth-Abundant Catalysts. *Science* **2011**, *334*, 645–648.
- (30) Schley, N. D.; Blakemore, J. D.; Subbaiyan, N. K.; Incarvito, C. D.; D’Souza, F.; Crabtree, R. H.; Brudvig, G. W. Distinguishing Homogeneous from Heterogeneous Catalysis in Electrode-Driven Water Oxidation with Molecular Iridium Complexes. *J. Am. Chem. Soc.* **2011**, *133*, 10473–10481.
- (31) Sundstrom, E. J.; Yang, X.; Thoi, V. S.; Karunadasa, H. I.; Chang, C. J.; Long, J. R.; Head-Gordon, M. Computational and Experimental Study of the Mechanism of Hydrogen Generation from Water by a Molecular Molybdenum–Oxo Electrocatalyst. *J. Am. Chem. Soc.* **2012**, *134*, 5233–5242.
- (32) Surendranath, Y.; Dincă, M.; Nocera, D. G. Electrolyte-Dependent Electrosynthesis and Activity of Cobalt-Based Water Oxidation Catalysts. *J. Am. Chem. Soc.* **2009**, *131*, 2615–2620.
- (33) Surendranath, Y.; Kanan, M. W.; Nocera, D. G. Mechanistic Studies of the Oxygen Evolution Reaction by a Cobalt-Phosphate Catalyst at Neutral pH. *J. Am. Chem. Soc.* **2010**, *132*, 16501–16509.
- (34) Young, E. R.; Costi, R.; Paydavosi, S.; Nocera, D. G.; Bulović, V. Photo-Assisted Water Oxidation with Cobalt-Based Catalyst Formed from Thin-Film Cobalt Metal on Silicon Photoanodes. *Energy Environ. Sci.* **2011**, *4*, 2058–2061.
- (35) Young, E. R.; Nocera, D. G.; Bulović, V. Direct Formation of a Water Oxidation Catalyst from Thin-Film Cobalt. *Energy Environ. Sci.* **2010**, *3*, 1726–1728.
- (36) Woods, J. A.; Bernhard, S.; Albrecht, M. Recent Advances in the Field of Iridium-Catalyzed Molecular Water Oxidation. *Molecular Water Oxidation Catalysis*; John Wiley & Sons, Ltd.: New York, 2014; pp 113–133.
- (37) Chadwick Ellis, W.; McDaniel, N. D.; Bernhard, S. Molecular Water Oxidation Catalysts from Iron. *Molecular Water Oxidation Catalysis*; John Wiley & Sons, Ltd.: New York, 2014; pp 153–162.
- (38) Barnett, S. M.; Waidmann, C. R.; Scheuermann, M. L.; Nesvet, J. C.; Goldberg, K.; Mayer, J. M. Developing Molecular Copper Complexes for Water Oxidation. *Molecular Water Oxidation Catalysis*; John Wiley & Sons, Ltd.: New York, 2014; pp 187–210.
- (39) Bard, A. J. Inner-Sphere Heterogeneous Electrode Reactions. *Electrocatalysis and Photocatalysis: The Challenge*. *J. Am. Chem. Soc.* **2010**, *132*, 7559–7567.
- (40) Garrett, B. C.; Dixon, D. A.; Camaioni, D. M.; Chipman, D. M.; Johnson, M. A.; Jonah, C. D.; Kimmel, G. A.; Miller, J. H.; Rescigno, T. N.; Rossky, P. J.; et al. Role of Water in Electron-Initiated Processes and Radical Chemistry: Issues and Scientific Advances. *Chem. Rev.* **2004**, *105*, 355–390.
- (41) Abel, B.; Buck, U.; Sobolewski, A. L.; Domcke, W. On the Nature and Signatures of the Solvated Electron in Water. *Phys. Chem. Chem. Phys.* **2012**, *14*, 22–34.
- (42) Herbert, J. M.; Jacobson, L. D. Nature’s Most Squishy Ion: The Important Role of Solvent Polarization in the Description of the Hydrated Electron. *Int. Rev. Phys. Chem.* **2011**, *30*, 1–48.
- (43) Mozumder, A. *Fundamentals of Radiation Chemistry*, 1st ed.; Academic Press: New York, 1999.
- (44) Elles, C. G.; Jailaubekov, A. E.; Crowell, R. A.; Bradforth, S. E. Excitation-Energy Dependence of the Mechanism for Two-Photon Ionization of Liquid H_2O and D_2O from 8.3 to 12.4 eV. *J. Chem. Phys.* **2006**, *125*, 044515.
- (45) Gardenier, G. H.; Johnson, M. A.; McCoy, A. B. Correction to “Spectroscopic Study of the Ion–Radical H-Bond in H_4O_2^+ ”. *J. Phys. Chem. A* **2012**, *116*, 8797.
- (46) Gill, P. M. W.; Radom, L. Structures and Stabilities of Singly Charged Three-Electron Hemibonded Systems and Their Hydrogen-Bonded Isomers. *J. Am. Chem. Soc.* **1988**, *110*, 4931–4941.
- (47) Sodupe, M.; Bertran, J.; Rodríguez-Santiago, L.; Baerends, E. J. Ground State of the $(\text{H}_2\text{O})_2^+$ Radical Cation: DFT versus Post-Hartree–Fock Methods. *J. Phys. Chem. A* **1998**, *103*, 166–170.
- (48) Pieniazek, P. A.; VandeVondele, J.; Jungwirth, P.; Krylov, A. I.; Bradforth, S. E. Electronic Structure of the Water Dimer Cation. *J. Phys. Chem. A* **2008**, *112*, 6159–6170.
- (49) Cheng, Q.; Evangelista, F. A.; Simmonett, A. C.; Yamaguchi, Y.; Schaefer, H. F. Water Dimer Radical Cation: Structures, Vibrational Frequencies, and Energetics. *J. Phys. Chem. A* **2009**, *113*, 13779–13789.
- (50) Lee, H. M.; Kim, K. S. Water Dimer Cation: Density Functional Theory vs Ab Initio Theory. *J. Chem. Theory Comput.* **2009**, *5*, 976–981.

- (51) Kamarchik, E.; Kostko, O.; Bowman, J. M.; Ahmed, M.; Krylov, A. I. Spectroscopic Signatures of Proton Transfer Dynamics in the Water Dimer Cation. *J. Chem. Phys.* **2010**, *132*, 194311.
- (52) Do, H.; Besley, N. A. Proton Transfer or Hemibonding? The Structure and Stability of Radical Cation Clusters. *Phys. Chem. Chem. Phys.* **2013**, *15*, 16214–16219.
- (53) Lee, H. M.; Kim, K. S. Dynamics and Structural Changes of Small Water Clusters on Ionization. *J. Comput. Chem.* **2013**, *34*, 1589–1597.
- (54) Svoboda, O.; Hollas, D.; Oncak, M.; Slavicek, P. Reaction Selectivity in an Ionized Water Dimer: Nonadiabatic Ab Initio Dynamics Simulations. *Phys. Chem. Chem. Phys.* **2013**, *15*, 11531–11542.
- (55) Gardener, G. H.; Johnson, M. A.; McCoy, A. B. Spectroscopic Study of the Ion–Radical H-Bond in H_4O_2^+ . *J. Phys. Chem. A* **2009**, *113*, 4772–4779.
- (56) Shinohara, H.; Nishi, N.; Washida, N. Photoionization of Water Clusters at 11.83 eV: Observation of Unprotonated Cluster Ions $(\text{H}_2\text{O})_n^+$ ($2 \leq n \leq 10$). *J. Chem. Phys.* **1986**, *84*, 5561–5567.
- (57) Sodupe, M.; Oliva, A.; Bertran, J. Theoretical Study of the Ionization of the $\text{H}_2\text{O}\text{-H}_2\text{O}$, $\text{NH}_3\text{-H}_2\text{O}$, and $\text{FH}\text{-H}_2\text{O}$ Hydrogen-Bonded Molecules. *J. Am. Chem. Soc.* **1994**, *116*, 8249–8258.
- (58) Barnett, R. N.; Landman, U. Pathways and Dynamics of Dissociation of Ionized $(\text{H}_2\text{O})_2$. *J. Phys. Chem.* **1995**, *99*, 17305–17310.
- (59) Tachikawa, H. A Direct ab-Initio Trajectory Study on the Ionization Dynamics of the Water Dimer. *J. Phys. Chem. A* **2002**, *106*, 6915–6921.
- (60) Tachikawa, H. Ionization Dynamics of the Small-Sized Water Clusters: A Direct Ab Initio Trajectory Study. *J. Phys. Chem. A* **2004**, *108*, 7853–7862.
- (61) Furuhashi, A.; Dupuis, M.; Hirao, K. Reactions Associated with Ionization in Water: A Direct Ab Initio Dynamics Study of Ionization in $(\text{H}_2\text{O})_{17}$. *J. Chem. Phys.* **2006**, *124*, -.
- (62) Furuhashi, A.; Dupuis, M.; Hirao, K. Application of a Kinetic Energy Partitioning Scheme for ab Initio Molecular Dynamics to Reactions Associated with Ionization in Water Tetramers. *Phys. Chem. Chem. Phys.* **2008**, *10*, 2033–2042.
- (63) Marsalek, O.; Elles, C. G.; Pieniazek, P. A.; Pluhařová, E.; VandeVondele, J.; Bradforth, S. E.; Jungwirth, P. Chasing Charge Localization and Chemical Reactivity Following Photoionization in Liquid Water. *J. Chem. Phys.* **2011**, *135*, 224510.
- (64) Mizuse, K.; Kuo, J.-L.; Fujii, A. Structural Trends of Ionized Water Networks: Infrared Spectroscopy of Water Cluster Radical Cations $(\text{H}_2\text{O})_n^+$ ($n = 3\text{--}11$). *Chem. Sci.* **2011**, *2*, 868–876.
- (65) Mizuse, K.; Fujii, A. Characterization of a Solvent-Separated Ion-Radical Pair in Cationized Water Networks: Infrared Photodissociation and Ar-Attachment Experiments for Water Cluster Radical Cations $(\text{H}_2\text{O})_n^+$ ($n = 3\text{--}8$). *J. Phys. Chem. A* **2013**, *117*, 929–938.
- (66) Headrick, J. M.; Diken, E. G.; Walters, R. S.; Hammer, N. I.; Christie, R. A.; Cui, J.; Myshakin, E. M.; Duncan, M. A.; Johnson, M. A.; Jordan, K. D. Spectral Signatures of Hydrated Proton Vibrations in Water Clusters. *Science* **2005**, *308*, 1765–1769.
- (67) Pieniazek, P. A.; Sundstrom, E. J.; Bradforth, S. E.; Krylov, A. I. Degree of Initial Hole Localization/Delocalization in Ionized Water Clusters. *J. Phys. Chem. A* **2009**, *113*, 4423–4429.
- (68) Lee, H.; Kim, K. Water Trimer Cation. *Theor. Chem. Acta* **2011**, *130*, 543–548.
- (69) Krylov, A. I. Equation-of-Motion Coupled-Cluster Methods for Open-Shell and Electronically Excited Species: The Hitchhiker's Guide to Fock Space. *Annu. Rev. Phys. Chem.* **2008**, *59*, 433–462.
- (70) Rowe, D. J. Equations-of-Motion Method and the Extended Shell Model. *Rev. Mod. Phys.* **1968**, *40*, 153–166.
- (71) Emrich, K. An Extension of the Coupled Cluster Formalism to Excited States (I). *Nucl. Phys. A* **1981**, *351*, 379–396.
- (72) Geertsens, J.; Rittby, M.; Bartlett, R. J. The Equation-of-Motion Coupled-Cluster Method: Excitation Energies of Be and CO. *Chem. Phys. Lett.* **1989**, *164*, 57–62.
- (73) Stanton, J. F.; Bartlett, R. J. The Equation of Motion Coupled-Cluster Method. A Systematic Biorthogonal Approach to Molecular Excitation Energies, Transition Probabilities, and Excited State Properties. *J. Chem. Phys.* **1993**, *98*, 7029–7039.
- (74) Stanton, J. F.; Gauss, J. Analytic Energy Derivatives for Ionized States Described by the Equation-of-Motion Coupled Cluster Method. *J. Chem. Phys.* **1994**, *101*, 8938–8944.
- (75) Mukherjee, D.; Pal, S. Use of Cluster Expansion Methods in the Open-Shell Correlation Problem. In *Advances in Quantum Chemistry*; Per-Olov, L., Ed.; Academic Press: New York, 1989; Vol. 20, pp 291–373.
- (76) Pieniazek, P. A.; Arnstein, S. A.; Bradforth, S. E.; Krylov, A. I.; Sherrill, C. D. Benchmark Full Configuration Interaction and Equation-of-Motion Coupled-Cluster Model with Single and Double Substitutions for Ionized Systems Results for Prototypical Charge Transfer Systems: Noncovalent Ionized Dimers. *J. Chem. Phys.* **2007**, *127*, 164110.
- (77) Dunning, T. H. Gaussian Basis Sets for Use in Correlated Molecular Calculations. I. The atoms boron through neon and hydrogen. *J. Chem. Phys.* **1989**, *90*, 1007–1023.
- (78) Halkier, A.; Helgaker, T.; Jørgensen, P.; Klopper, W.; Koch, H.; Olsen, J.; Wilson, A. K. Basis-Set Convergence in Correlated Calculations on Ne, N_2 , and H_2O . *Chem. Phys. Lett.* **1998**, *286*, 243–252.
- (79) Møller, C.; Plesset, M. S. Note on an Approximation Treatment for Many-Electron Systems. *Phys. Rev.* **1934**, *46*, 618–622.
- (80) Feyereisen, M.; Fitzgerald, G.; Komornicki, A. Use of Approximate Integrals in Ab Initio Theory. An Application in MP2 Energy Calculations. *Chem. Phys. Lett.* **1993**, *208*, 359–363.
- (81) Vahtras, O.; Almlöf, J.; Feyereisen, M. W. Integral Approximations for LCAO-SCF Calculations. *Chem. Phys. Lett.* **1993**, *213*, 514–518.
- (82) Eichkorn, K.; Treutler, O.; Öhm, H.; Häser, M.; Ahlrichs, R. Auxiliary Basis Sets to Approximate Coulomb Potentials. *Chem. Phys. Lett.* **1995**, *240*, 283–290.
- (83) Weigend, F.; Häser, M.; Patzelt, H.; Ahlrichs, R. RI-MP2: Optimized Auxiliary Basis Sets and Demonstration of Efficiency. *Chem. Phys. Lett.* **1998**, *294*, 143–152.
- (84) Jung, Y.; Sodt, A.; Gill, P. M. W.; Head-Gordon, M. Auxiliary Basis Expansions for Large-Scale Electronic Structure Calculations. *Proc. Natl. Acad. Sci.* **2005**, *102*, 6692–6697.
- (85) Čížek, J. On the Correlation Problem in Atomic and Molecular Systems. Calculation of Wavefunction Components in Ursell-Type Expansion Using Quantum-Field Theoretical Methods. *J. Chem. Phys.* **1966**, *45*, 4256–4266.
- (86) Bartlett, R. J.; Musiał, M. Coupled-Cluster Theory in Quantum Chemistry. *Rev. Mod. Phys.* **2007**, *79*, 291–352.
- (87) Kohn, W.; Sham, L. J. Self-Consistent Equations Including Exchange and Correlation Effects. *Phys. Rev.* **1965**, *140*, A1133–A1138.
- (88) Yang, R. G. P. W. *Density-Functional Theory of Atoms and Molecules*; Oxford University Press: Oxford, U.K., 1994.
- (89) Hehre, W. J.; Ditchfield, R.; Pople, J. A. Self-Consistent Molecular Orbital Methods. XII. Further Extensions of Gaussian-Type Basis Sets for Use in Molecular Orbital Studies of Organic Molecules. *J. Chem. Phys.* **1972**, *56*, 2257–2261.
- (90) Clark, T.; Chandrasekhar, J.; Spitznagel, G. W.; Schleyer, P. V. R. Efficient Diffuse Function-Augmented Basis Sets for Anion Calculations. III. The 3-21+G basis set for first-row elements, Li–F. *J. Comput. Chem.* **1983**, *4*, 294–301.
- (91) Shao, Y.; Molnar, L. F.; Jung, Y.; Kussmann, J.; Ochsenfeld, C.; Brown, S. T.; Gilbert, A. T. B.; Slipchenko, L. V.; Levchenko, S. V.; O'Neill, D. P.; et al. Advances in Methods and Algorithms in a Modern Quantum Chemistry Program Package. *Phys. Chem. Chem. Phys.* **2006**, *8*, 3172–3191.
- (92) Humphrey, W.; Dalke, A.; Schulten, K. VMD: Visual Molecular Dynamics. *J. Mol. Graphics* **1996**, *14*, 33–38.

- (93) Xie, Y.; Schaefer, H. F. Hydrogen Bonding Between the Water Molecule and the Hydroxyl Radical ($\text{H}_2\text{O}\text{-HO}\cdot$): The Global Minimum. *J. Chem. Phys.* **1993**, *98*, 8829–8834.
- (94) Chipman, D. M. Absorption Spectrum of OH Radical in Water. *J. Phys. Chem. A* **2008**, *112*, 13372–13381.
- (95) Hamad, S.; Lago, S.; Mejías, J. A. A Computational Study of the Hydration of the OH Radical. *J. Phys. Chem. A* **2002**, *106*, 9104–9113.
- (96) Du, S.; Francisco, J. S.; Schenter, G. K.; Garrett, B. C. Many-Body Decomposition of the Binding Energies for $\text{OH}\cdot(\text{H}_2\text{O})_2$ and $\text{OH}\cdot(\text{H}_2\text{O})_3$ Complexes. *J. Chem. Phys.* **2008**, *128*, 084307.
- (97) Hoffman, G. J.; Gurunathan, P. K.; Francisco, J. S.; Slipchenko, L. V. Excited States of $\text{OH}\cdot(\text{H}_2\text{O})_n$ Clusters for $n = 1\text{--}4$: An Ab Initio Study. *J. Chem. Phys.* **2014**, *141*, 104315.
- (98) Hodges, M. P.; Wales, D. J. Global Minima of Protonated Water Clusters. *Chem. Phys. Lett.* **2000**, *324*, 279–288.
- (99) Wales, D. J.; Doye, J. P. K.; Dullweber, A.; Hodges, M. P.; Naumkin, F. Y.; Calvo, F.; Hernández-Rojas, J.; Middleton, T. F. The Cambridge Cluster Database. <http://www-wales.ch.cam.ac.uk/CCD.html>.
- (100) Jorgensen, W. L.; Maxwell, D. S.; Tirado-Rives, J. Development and Testing of the OPLS All-Atom Force Field on Conformational Energetics and Properties of Organic Liquids. *J. Am. Chem. Soc.* **1996**, *118*, 11225–11236.
- (101) VandeVondele, J.; Sprik, M. A Molecular Dynamics Study of the Hydroxyl Radical in Solution Applying Self-Interaction-Corrected Density Functional Methods. *Phys. Chem. Chem. Phys.* **2005**, *7*, 1363–1367.
- (102) d’Avezac, M.; Calandra, M.; Mauri, F. Density Functional Theory Description of Hole-Trapping in SiO_2 : A Self-Interaction-Corrected Approach. *Phys. Rev. B* **2005**, *71*, 205210.
- (103) Mantz, Y. A.; Gervasio, F. L.; Laino, T.; Parrinello, M. Charge Localization in Stacked Radical Cation DNA Base Pairs and the Benzene Dimer Studied by Self-Interaction Corrected Density-Functional Theory. *J. Phys. Chem. A* **2006**, *111*, 105–112.
- (104) Zhang, Y.; Yang, W. A Challenge for Density Functionals: Self-Interaction Error Increases for Systems with a Noninteger Number of Electrons. *J. Chem. Phys.* **1998**, *109*, 2604–2608.
- (105) Livshits, E.; Baer, R. A Density Functional Theory for Symmetric Radical Cations from Bonding to Dissociation. *J. Phys. Chem. A* **2008**, *112*, 12789–12791.
- (106) Livshits, E.; Granot, R. S.; Baer, R. A Density Functional Theory for Studying Ionization Processes in Water Clusters. *J. Phys. Chem. A* **2010**, *115*, 5735–5744.
- (107) Lynch, B. J.; Fast, P. L.; Harris, M.; Truhlar, D. G. Adiabatic Connection for Kinetics. *J. Phys. Chem. A* **2000**, *104*, 4811–4815.
- (108) Adamo, C.; Barone, V. Exchange Functionals with Improved Long-Range Behavior and Adiabatic Connection Methods Without Adjustable Parameters: The mPW and mPWIPW Models. *J. Chem. Phys.* **1998**, *108*, 664–675.
- (109) Jurečka, P.; Hobza, P. On the Convergence of the $(\Delta\text{ECCSD}(\text{T})-\Delta\text{EMP2})$ Term for Complexes with Multiple H-bonds. *Chem. Phys. Lett.* **2002**, *365*, 89–94.
- (110) Leininger, M. L.; Nielsen, I. M. B.; Colvin, M. E.; Janssen, C. L. Accurate Structures and Binding Energies for Stacked Uracil Dimers. *J. Phys. Chem. A* **2002**, *106*, 3850–3854.
- (111) Tsuzuki, S.; Honda, K.; Uchimaru, T.; Mikami, M.; Tanabe, K. High-Level ab Initio Calculations of Interaction Energies of $\text{C}_2\text{H}_4\text{-CH}_4$ and $\text{C}_2\text{H}_6\text{-CH}_4$ Dimers: A Model Study of CH/π Interaction. *J. Phys. Chem. A* **1999**, *103*, 8265–8271.
- (112) Byrd, E. F. C.; Sherrill, C. D.; Head-Gordon, M. The Theoretical Prediction of Molecular Radical Species: A Systematic Study of Equilibrium Geometries and Harmonic Vibrational Frequencies. *J. Phys. Chem. A* **2001**, *105*, 9736–9747.
- (113) Svoboda, O.; OnCak, M.; SlaviCek, P. Simulations of Light Induced Processes in Water Based on ab Initio Path Integrals Molecular Dynamics. II. Photoionization. *J. Chem. Phys.* **2011**, *135*, 154302.
- (114) Ng, C. Y.; Trevor, D. J.; Tiedemann, P. W.; Ceyer, S. T.; Kronebusch, P. L.; Mahan, B. H.; Lee, Y. T. Photoionization of Dimeric Polyatomic Molecules: Proton Affinities of H_2O and HF. *J. Chem. Phys.* **1977**, *67*, 4235–4237.
- (115) Miller, D. J.; Lisy, J. M. Hydrated Alkali-Metal Cations: Infrared Spectroscopy and ab Initio Calculations of $\text{M}^+(\text{H}_2\text{O})_{n=2-5}\text{Ar}$ cluster ions for $\text{M} = \text{Li}, \text{Na}, \text{K}$, and Cs . *J. Am. Chem. Soc.* **2008**, *130*, 15381–15392.
- (116) Relph, R. A.; Guasco, T. L.; Elliott, B. M.; Kamrath, M. Z.; McCoy, A. B.; Steele, R. P.; Schofield, D. P.; Jordan, K. D.; Viggiano, A. A.; Ferguson, E. E.; et al. How the Shape of an H-Bonded Network Controls Proton-Coupled Water Activation in HONO Formation. *Science* **2010**, *327*, 308–312.
- (117) Jensen, J. H.; Gordon, M. S. On the Number of Water Molecules Necessary to Stabilize the Glycine Zwitterion. *J. Am. Chem. Soc.* **1995**, *117*, 8159–8170.
- (118) Elliott, B. M.; Relph, R. A.; Roscioli, J. R.; Bopp, J. C.; Gardenier, G. H.; Guasco, T. L.; Johnson, M. A. Isolating the Spectra of Cluster Ion Isomers Using Ar-“tag” -Mediated IR-IR Double Resonance within the Vibrational Manifolds: Application to $\text{NO}_2^-\text{H}_2\text{O}$. *J. Chem. Phys.* **2008**, *129*, 094303.
- (119) Garrett, K.; Sosa Vazquez, X.; Egri, S. B.; Wilmer, J.; Johnson, L. E.; Robinson, B. H.; Isborn, C. M. Optimum Exchange for Calculation of Excitation Energies and Hyperpolarizabilities of Organic Electro-optic Chromophores. *J. Chem. Theory Comput.* **2014**, *10*, 3821–3831.
- (120) Lagutschenkov, A.; Fanourgakis, G. S.; Niedner-Schatteburg, G.; Xantheas, S. S. The Spectroscopic Signature of the “All-Surface” to “Internally Solvated” Structural Transition in Water Clusters in the $n=17\text{--}21$ Size Regime. *J. Chem. Phys.* **2005**, *122*, 194310.
- (121) Fournier, J. A.; Johnson, C. J.; Wolke, C. T.; Weddle, G. H.; Wolk, A. B.; Johnson, M. A. Vibrational Spectral Signature of the Proton Defect in the Three-Dimensional $\text{H}^+(\text{H}_2\text{O})_{21}$ Cluster. *Science* **2014**, *344*, 1009–1012.
- (122) Ertem, M. Z.; Gagliardi, L.; Cramer, C. J. Quantum Chemical Characterization of the Mechanism of an Iron-Based Water Oxidation Catalyst. *Chem. Sci.* **2012**, *3*, 1293–1299.
- (123) Ertem, M. Z.; Cramer, C. J. Quantum Chemical Characterization of the Mechanism of a Supported Cobalt-Based Water Oxidation Catalyst. *Dalton Trans.* **2012**, *41*, 12213–12219.
- (124) Bozoglian, F.; Romain, S.; Ertem, M. Z.; Todorova, T. K.; Sens, C.; Mola, J.; Rodríguez, M.; Romero, I.; Benet-Buchholz, J.; Fontrodona, X.; et al. The Ru-Hbpp Water Oxidation Catalyst. *J. Am. Chem. Soc.* **2009**, *131*, 15176–15187.
- (125) Li, X.; Chen, G.; Schinzel, S.; Siegbahn, P. E. M. A Comparison Between Artificial and Natural Water Oxidation. *Dalton Trans.* **2011**, *40*, 11296–11307.
- (126) Wang, L.-P.; Wu, Q.; Van Voorhis, T. Acid-Base Mechanism for Ruthenium Water Oxidation Catalysts. *Inorg. Chem.* **2010**, *49*, 4543–4553.

CHAPTER 3

ION-RADICAL PAIR SEPARATION IN LARGE OXIDIZED WATER CLUSTERS, $(\text{H}_2\text{O})^+_{n=6-21}$

Reprinted with permission from Herr, J. D.; Steele, R. P. Ion–Radical Pair Separation in Larger Oxidized Water Clusters, $(\text{H}_2\text{O})^+_{n=6-21}$. *J. Phys. Chem. A* **2016**, *120* (36), 7225-7239. Copyright 2016 American Chemical Society.

Ion–Radical Pair Separation in Larger Oxidized Water Clusters, $(\text{H}_2\text{O})^+_{n=6-21}$

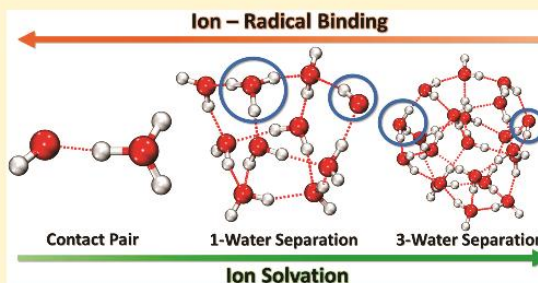
Jonathan D. Herr and Ryan P. Steele*

Department of Chemistry and Henry Eyring Center for Theoretical Chemistry, University of Utah, 315 South 1400 East, Salt Lake City, Utah 84112, United States

Supporting Information

ABSTRACT: The structures, properties, and spectroscopic signatures of oxidized water clusters, $(\text{H}_2\text{O})^+_{n=6-21}$, are examined in this work, to provide fundamental insight into renewable energy and radiological processes. Computational quantum chemistry approaches are employed to sample cluster morphologies, yielding hundreds of low-lying isomers with low barriers to interconversion. The ion–radical pair-separation trend, however, which was observed in previous computational studies and in small-cluster spectroscopy experiments, is shown to continue in this larger cluster size regime. The source of this trend is preferential solvation of the hydronium ion by water, including effects beyond the first solvation shell.

The fundamental conclusion of this work, therefore, is that the initially formed ion–radical dimer, which has served as a prototypical model of oxidized water, is a nascent species in large, oxidized water clusters and, very likely, bulk water.



INTRODUCTION

Storage of solar energy in the chemical bonds of molecules remains a propitious—yet daunting—aim for the field of energy science. The electrochemical splitting of water into molecular hydrogen and oxygen holds particular promise, and many potentially viable catalysts have been developed in recent years for this purpose.^{1–22} Water oxidation has proven to be the more difficult half of the redox couple, and progress in the development of oxidation catalysts continues. A central impediment to the development of new catalyst technology, however, is the challenge of discerning mechanistic details. In particular, the molecular-level, inner-sphere motions involved in the activation of condensed-phase water as a chemical species remain inaccessible to many electrochemical and spectroscopic techniques,²³ although recent progress in gas-phase spectroscopic techniques is encouraging.²⁴ A detailed analysis of the properties of oxidized water is required to fully understand the driving forces involved in the water oxidation process, as well as the inherent properties that may be amenable to catalytic control.

To this end, we recently published a computational analysis²⁵ of the simplest model of oxidized water, which consists of small, uncatalyzed cationic water clusters, $(\text{H}_2\text{O})^+_{n=1-5}$. This work confirmed and clarified the trend observed in recent gas-phase infrared spectroscopy experiments,^{26–28} suggesting a structural progression toward separation of the initially formed ion–radical pair, $\text{H}_3\text{O}^+\cdots\text{OH}$, which had long served as the prototypical model for gas-phase, oxidized water.^{28–34} The $(\text{H}_2\text{O})^+_5$ species, in particular, demarcated a critical structural transition in which the insertion of a solvating water molecule

between the ion and radical moieties became energetically favored (Figure 1). Independently, three investigations have

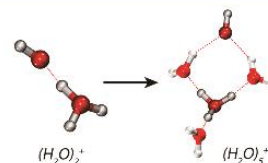


Figure 1. Lowest-energy isomers of the water dimer and pentamer cations, showing the hydronium–hydroxyl separation in the pentamer.²⁵

examined the $n = 3–9$,³⁵ $n = 5$,³⁶ and $n = 5–8$ ³⁷ size regimes, each using slightly different computational approaches. These analyses have shown that the low-energy isomers do, indeed, involve ion–radical pair separation beyond $n = 5$, thereby ruling out the possibility that $n = 5$ represents a size regime akin to “magic number” clusters^{38–42} in other systems. The clusters in these studies were also still small enough that only a single water molecule separated the two key subunits. This result leaves open the question of whether the pair-separation trend continues in larger clusters, or whether the solvated $\text{H}_3\text{O}^+\cdots\text{H}_2\text{O}\cdots\text{OH}^+$ subunit somehow exhibits special stability. In the present study, these benchmark analyses will be used to

Received: July 25, 2016

Revised: August 16, 2016

Published: August 17, 2016

assess the isomer-search methodology and to calibrate our approach for larger clusters. Our investigation is extended toward large clusters, up to $n = 21$, where internal solvation in a cluster environment is possible.⁴³ Throughout this study, focus will be placed on identifying driving forces for the observed structural and energetic trends. Is, for example, the electronic driving force for the native structure in a large cluster the same as in small clusters? Computational approaches also exhibit the unique ability to decompose such trends into physically meaningful pieces. The sources underlying these structural trends will be examined, with the intent of elucidating fundamental properties of oxidized water.

METHODS

The investigations in this work are guided by three fundamental questions:

1. What is the structural and energetic landscape of larger water cluster cations ($n \leq 21$)?
2. Does the ion–radical pair separation trend continue beyond a single-water separation in these large clusters?
3. What is the driving force for the observed structural trend, and how is it influenced by the local electronic environment of the ion and radical?

The overall approach taken to answer these questions involves the generation of a set of representative cluster isomer structures and relative energies. To generate this set, methods for the accurate treatment of the electronic structure of this open-shell ion are required, as are methods to sufficiently sample the space of relevant isomers. The preponderance of nearly degenerate structures—with low interconnecting barriers—suggests that an ensemble-based approach will begin to become more appropriate for large clusters. Extensive isomer sampling is performed in this work to provide a reasonable assessment of key structures within this ensemble. This approach also allows for the identification of isomers that would be minor species in a thermal ensemble and, therefore, a challenge for spectroscopic analysis. In the previous study, the presence of these isomers was critical information for the identification of the pair-separation trend.²⁵ The pair-separated isomer, for example, was a high-energy, yet stable, species prior to the $n = 5$ transition. Its progressing stability throughout the considered size range was indicative of a solvation-induced stabilization of the separated pair. Such higher-energy isomers will also be considered in the present context, with the intent of tracking the final fate of the ion–radical pair.

The properties of this open-shell ion require careful consideration of the electronic structure method. Our past analysis showed that the equation-of-motion coupled-cluster theory for ionized states (EOM-IP-CCSD) method^{44–48} and its perturbative-triples analogue [EOM-IP-CCSD(dT)] are well-suited for benchmark-quality results on this system. With large, atom-centered basis sets, the $n = 5$ species also, unfortunately, marked the current feasibility limit for these accurate methods. One of the ancillary goals of the previous study was to generate such benchmarks for the smaller clusters, to identify more computationally expedient methodologies with sufficient accuracy. The results of that study indicated that second-order perturbation theory (MP2⁴⁹) is surprisingly accurate for these systems, even when the CCSD method^{50,51} differs appreciably from benchmarks. The lone exception to this assessment occurred during a frequency analysis of the hemibonded (HB) species of the dimer. Because this isomer

has now been well established as a high-energy isomer^{25,29,31,32}—a trend that was shown to continue as more solvating waters were added—such concerns are irrelevant for the present analysis. Furthermore, although the applicability of density functional theory (DFT⁵²) methods without empirical corrections^{53–55} has been somewhat dubious for this system, due to spurious self-interaction effects,^{29,56–58} the MPW1K functional^{59,60} showed excellent accuracy. In fact, the fraction of Hartree–Fock exchange⁶¹ was shown in ref 25 to be nearly optimal for consistency with equation-of-motion benchmarks. Although this fraction is not guaranteed to remain optimal for larger systems,⁶² its accuracy across the set of $n = 1–5$ isomers confirms that it is at least accurate in both contact-pair and separated-pair regimes, which is the focus of the present study. Modest basis sets were also shown to be adequate for structural and energetic trends. Therefore, the MP2/6-31++G**^{63–67} and MPW1K/6-31++G** (with the SG-1 quadrature grid⁶⁸) methods will both be used in the current work to generate structures and relative energies. The MPW1K results will be the focus of much of the ensuing discussion; comparison to MP2 will be made when appropriate.

Using these underlying potentials, the representative isomers were first generated according to a scheme that was also presented in ref 25 and, independently, used in ref 37. The approach involved selective deletion of H atoms from known protonated water cluster structures.^{69,70} The observation was made early in our studies that the nominally $(\text{H}_3\text{O}^+)(\text{OH})(\text{H}_2\text{O})_{n-2}$ clusters bore significant structural similarity to known $(\text{H}_3\text{O}^+)(\text{H}_2\text{O})_{n-1}$ cluster structures, with the only modification being the elimination of a “dangling” O–H bond and subtle relaxation effects. Such a result is quite reasonable because these dangling bonds do not participate in the stabilizing hydrogen-bonding network. Using published results for larger protonated clusters, the same approach was employed in the present work. For an oxidized cluster of n original water molecules, $2n + 1$ possible H-deletion isomers were generated for $n = 6–21$.

Although this very simple H-deletion approach was previously shown to be robust for small clusters,³⁷ the available configuration space is significantly expanded for the larger clusters. Accordingly, it is compared to a more rigorous basin-hopping⁷¹ (BH) Monte Carlo approach for key size regimes ($n = 6, 10, 13, 21$), in which a Metropolis Monte Carlo⁷² search is performed in the space of optimized geometries. Displacements were alternately chosen to be bond (maximum ± 1 Å), angle (maximum $\pm 90^\circ$), or dihedral angle (maximum $\pm 90^\circ$) displacements in automatically generated z-matrix coordinates. For $n = 6$, the BH search was performed at 1000 K, and no additional isomers were found with subsequent searches at 3000 K. Seed structures for this size regime were five disparate isomer classes from known neutral water clusters.⁷³ For the larger clusters, 10 independent BH searches were performed at each of five temperatures, ranging from 1000 to 5000 K. Seed structures were selected randomly from long, thermostatted (300 K) neutral water trajectories using the empirical SPC potential. An initial BH search using HF/3-21G was subsequently refined with MPW1K/6-31++G(d,p) optimizations on unique structures. (For additional sampling purposes, all optimized structures were retained throughout the BH procedure.) Throughout the study, unique isomers were assigned automatically, using a root-mean-squared displacement (RMSD) criterion, after optimal alignment of structures with rigid-body translations and rotations. This code also

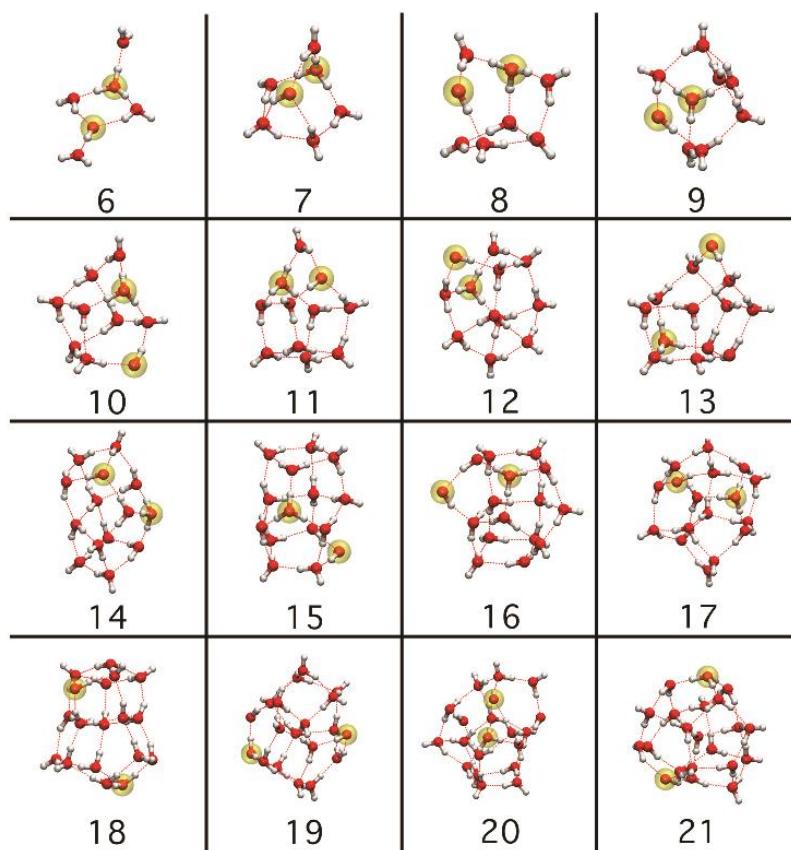


Figure 2. Isomers of $(\text{H}_2\text{O})_n^+$ with the lowest electronic energies, using MPW1K/6-31++G**. The full set of isomer structures is available from the author. The ion (H_3O^+) and radical (OH) are highlighted in each structure.

properly accounted for the possibility that hydrogenic moieties could switch oxygen partners during the optimizations. A 0.1 kcal/mol relative energy cutoff was employed, to accelerate the comparison of structures. An alternative molecular dynamics (MD) “quench” sampling approach, in which structures were sampled from long (≈ 1 ns) classical MD trajectories for the neutral cluster and used as initial structures for a cation geometry optimization, yielded similar results but with no obvious gain in sampling efficiency (aside from increased parallelizability). For this reason, only the BH results will be discussed in this work, with comparisons to H-deletion results where appropriate.

For the MPW1K results, harmonic zero-point energy (ZPE) and rigid-rotor/harmonic oscillator thermodynamic corrections were also applied to the relative energies. Past studies have shown that the relative isomer ordering can be impacted by ZPE corrections.^{35,37} Harmonic corrections should be interpreted with considerable caution, however, because the high-frequency stretches in these^{27,74} and other solvated-hydroxonium^{70,75–77} complexes are known to be strongly anharmonic, and the preponderance of frustrated rotations in the low-frequency region could nontrivially affect contributions to both ZPE and entropy corrections. For these reasons, the electronic trends and driving forces will remain the focus of this study, although the magnitude of these driving forces will be discussed

in detail in the context of the magnitudes of both ZPE and thermal corrections. Scaled harmonic vibrational spectra are presented in the high-frequency region to provide congruence with past experimental studies and qualitative guidance for future experiments. Previous experiments have been unable to access this larger cluster regime, and the trends observed may find use in guiding new experiments.

RESULTS

Using the methods described above, thousands of unique structural isomers of $(\text{H}_2\text{O})_n^+$ were obtained. The isomers with the lowest electronic energy, for each cluster size, are summarized in Figure 2. The full set of isomer coordinates and energies, using both electronic structure methods, is available from the author. The discussion in this section is designed as follows. The $n = 6$ isomer will be examined in detail, to provide a comparison to past computational and experimental studies. For this reference case, the efficacy of the isomer-search methodology will be analyzed. Subsequently, the $n = 10$ cluster will be examined because this cluster size has not been studied computationally and because experimental vibrational spectra are available. Thermally weighted harmonic spectra will be used to assess the consistency of the computed isomers. The $n = 13$ and $n = 21$ clusters will then be examined as representative size regimes for larger clusters, for which no experimental data

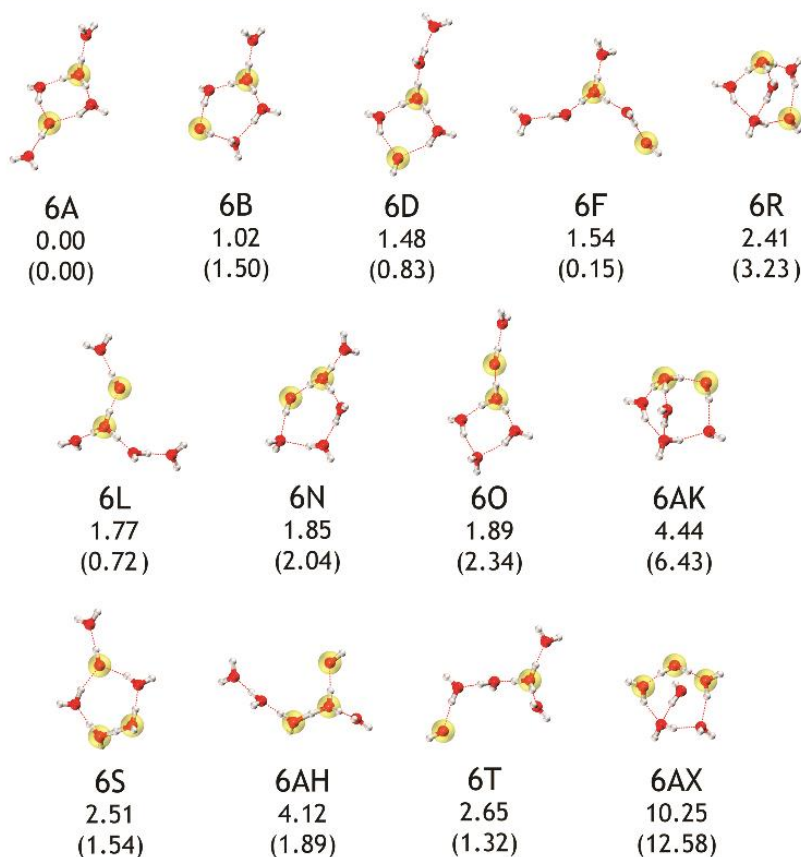


Figure 3. Representative stable isomers of $(\text{H}_2\text{O})_6^+$, using MPW1K/6-31++G**. (The full set of isomer structures and energies is available from the author.) Relative electronic energies are shown in kcal/mol. Harmonic ZPE-corrected relative energies are provided in parentheses. The oxygen atom of the ion (H_3O^+) and radical (OH) subunits are highlighted in yellow; the solvated trimer and Zundel subunits have been highlighted similarly. The first row of structures corresponds to structures with separation of the ion and radical by a single, intervening water molecule. The second row depicts contact-pair structures. The third row contains two Zundel structures, a two-water-separated ion and radical, and a solvated trimer structure.

currently exists. Using some of the simplified sampling techniques for the remaining isomer sizes, structural and energetic trends across the set will be discussed.

A. Isomers of $(\text{H}_2\text{O})_6^+$ and Isomer Search Efficacy. The smallest cluster considered in this work provides an accessible testing ground for methodology considerations. The basin-hopping search procedure was performed for the hexamer, starting with five diverse “seed” structures from known neutral water clusters.⁷³ After refinement with MPW1K/6-31++G** and the RMSD uniqueness protocol, 51 unique isomers were found. Structures and relative energies (MPW1K/6-31++G**) of 13 representative isomers, obtained from the basin-hopping procedure, are presented in Figure 3, and structures/energies of all isomers are available from the author. The ion (H_3O^+) and radical (OH) moieties’ oxygen atoms are highlighted for clarity in the figure. The isomer nomenclature used throughout this work follows the (n) (*isomer letter*) format, in which the isomer letter labeling corresponds to the electronic energy-ordered set of all unique isomers generated from the complete set of structures.

The lowest-energy isomer (6A) consists of a solvated ring structure, in which both the hydronium and hydroxyl units are

fully solvated by water. Importantly, this structure exhibits a hydronium and hydroxyl moiety that are separated by an intervening water molecule, which is consistent with the behavior observed previously for $n = 5$. The isomer with the lowest electronic energy (6A) is also consistent with the minimum-energy structure found in refs 35 and 37, although the present calculations agree only with ref 37 that this isomer continues to remain lowest in energy when ZPE corrections are included. (The use of the B3LYP functional for the harmonic frequencies in ref 35 is likely responsible for this difference. Such shifts are likely within the inherent error bars of harmonic ZPE’s and would require a detailed anharmonic analysis to clarify this subtle difference.) All of these studies agree that a one-water separation of the ion–radical pair occurs at $n = 6$, however.

The structures of the 51 unique isomers can be grouped into qualitative structural classes. The lowest-energy class of isomers, to which isomer 6A belongs, exhibits the aforementioned 1-water-separated ion–radical pair; this class of structures will hereafter be named “SP1-type” structures. The nuanced hydrogen-bonding possibilities lead to a spread of over 8 kcal/mol within this class, and several representative SP1

structures are shown in the first row of Figure 3. Solvated four-membered (6A and 6D) and five-membered (6B) rings are low-energy structures. A branched isomer (6F) is only slightly higher in energy and is nearly degenerate with 6A when harmonic ZPE corrections are included. A cage-like structure (6R) also exhibits ion–radical pair separation and sits only 2.41 kcal/mol above the minimum-energy structure. Due to symmetry, a Zundel-like, five-membered ring structure is observed for SP1-type isomer 6S (third row of Figure 3), which sits 2.51 kcal/mol above 6A.

The contact-pair (CP) isomers also exhibit a large spread in energies, and the manifold of CP structures overlaps the SP1 manifold. Many of the same hydrogen-bonding arrangements are observed for the low-energy CP structures as were found for SP1 (6O, four-membered ring; 6N, five-membered ring; 6L, branch; 6AK, cage; 6AH, Zundel). In fact, the CP structures can often be obtained by interchanging hydroxyl and water moieties in the SP1 structures, a process which incurs an electronic energy penalty of 0.15–2.03 kcal/mol for the structures shown. Interestingly, some of these contact-pair isomers are lower in (relative) energy than those found at $n = 5$, suggesting that intricate hydrogen-bonding effects dress the general trend toward contact-pair separation. Whether these effects are sufficient to counteract the trend in larger clusters, or whether they merely provide nuanced fluctuations to an otherwise-general driving force, will be examined in subsequent sections.

A third class of isomers consists of a solvated oxidized-trimer unit (6AX), the core of which was also found in our previous study. These structures, sitting 10.3–12.2 kcal/mol above the energy of 6A, constitute the highest-energy class of isomers found and would likely exhibit particularly unique vibrational spectra. Though these species could putatively be involved in the initial ionization dynamics^{34,78}—and have been implicated in recent MD analyses⁷⁹—they are likely too high in energy to be relevant for the present analysis. The fact that they are stable isomers, however, highlights the varied electronic landscape that the sampling procedure must be able to access in larger clusters. These solvated-trimer isomers were not found in any past computational studies of stable isomers in this size regime.

The extensive BH search results can be used to assess the much simpler H-deletion isomer search protocol. A graphical comparison of the results is shown in Figure 4. The H-deletion approach, starting from only a single protonated-water cluster, is sufficient to represent the distinct classes of structural isomers. It is not found to be sufficient to identify the lowest-energy isomer in each class, however. Performing such a search with multiple starting protonated-water isomers would likely provide appreciably enhanced sampling, as was suggested in the results of ref 37. The H-deletion isomers generated by the MPW1K and RI-MP2 methods, starting from the same protonated clusters, were generally consistent, although some of the more subtle isomer energy orderings differed. The consistency in the isomer structures, however, suggests that both methods are appropriate for structural information and trends.

The lowest-energy hexamer isomer found here is lower in energy than the branched isomer assigned in past experimental spectroscopic studies, which also used the MPW1K method.^{26,27} The previous analysis by Kuo³⁷ showed that these higher-energy branched isomers quickly begin to dominate at finite temperature when vibrational corrections are included. To more directly analyze this effect in the present analysis,

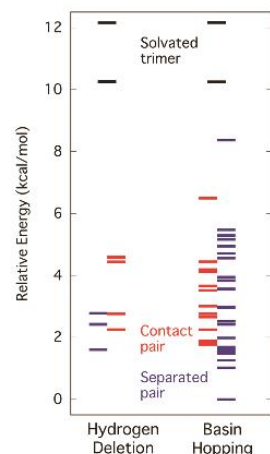


Figure 4. Isomer energies for $(\text{H}_2\text{O})_6^+$ using MPW1K/6-31++G**. Structural classes are color-coded. The left set of lines depicts the energies for the hydrogen-deletion search protocol, starting from a protonated water cluster, whereas the right set of lines shows the energies of unique isomers found by the basin-hopping sampling approach.

Gibbs free energies, based on the rigid-rotor/harmonic-oscillator (RRHO) approximation, were computed at temperatures from 0 to 300 K and a pressure of 1 atm, directly from the RRHO partition function. Using these free energies, Boltzmann-weighted isomer populations were computed; the results are presented in Figure 5 for all isomers exhibiting

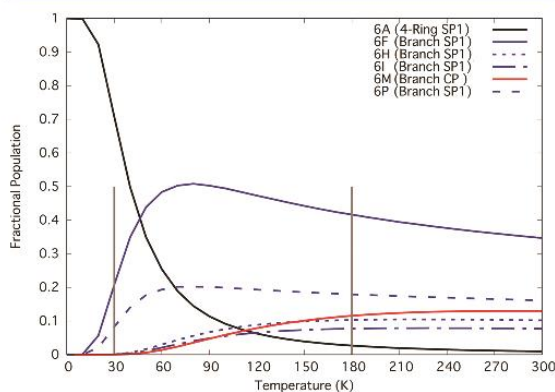


Figure 5. Thermal populations of $(\text{H}_2\text{O})_6^+$ isomers up to 300 K. Displayed are populations of the six isomers for which the population exceeds 5% at some point in this temperature range. The vertical gray lines denote temperatures at which experimental vibrational spectra have been obtained.

greater than 5% population at any temperature throughout this range. The four-membered ring structure 6A is found to be the dominant isomer at very low temperatures. However, beginning at around 50 K, several branch isomers—SP1 isomers 6F, 6H, and 6I, as well as CP isomer 6M—constitute the majority of the isomer population. The CP isomer is found to grow in population throughout the range and contributes a nontrivial fraction to the ensemble at 300 K.

On the basis of this observation, the thermally weighted, scaled (0.91524) harmonic vibrational spectra were computed for all isomers. The comparison between this spectrum and the 180 K experimental results of Fujii²⁶ is provided in the upper panel Figure 6. Overall, the agreement is quite good, given that

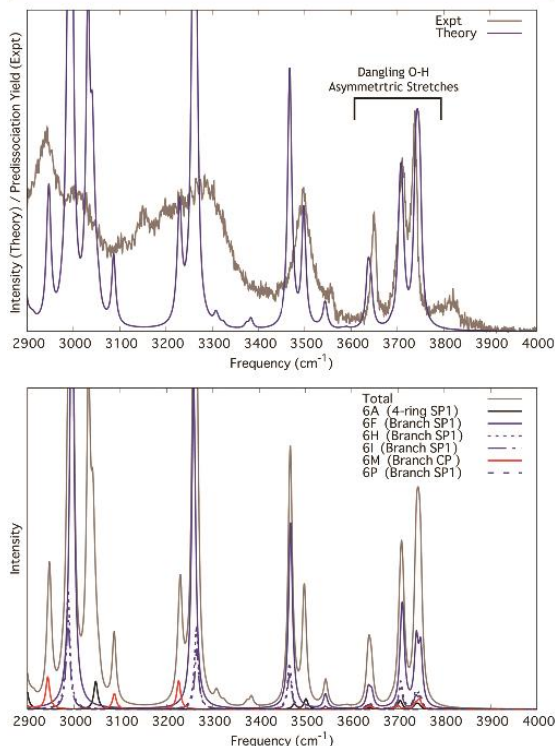


Figure 6. Vibrational spectra of $(\text{H}_2\text{O})_6^+$. [Upper panel] Thermally weighted harmonic spectra (scale factor, 0.91524; Lorentzian width, 10 cm^{-1}) of all unique isomers, using MPW1K/6-31++G**_s, are shown in blue; the experimental spectrum (180 K) of Fujii²⁶ is shown in gray. [Lower panel] Thermally weighted component spectra of the six isomers from Figure 5. Note that several additional isomers, which exhibit small populations but large intensities, also contribute to the total spectrum.

these results are only scaled harmonic spectra and are performed with a modest basis set. The strongly hydrogen-bonded transitions ($<3400\text{ cm}^{-1}$) show considerable broadening that is not captured by the purely fictitious 10 cm^{-1} Lorentzian broadening in the computed spectra. Although a portion of this experimental broadening is due to isomer populations, a non-negligible contribution is likely due to strong couplings of low-frequency modes to these bright transitions. A separate analysis of these anomalous effects in the spectrum of $(\text{H}_2\text{O})_2^+$ is forthcoming.⁸⁰ The assignments of most of the dominant experimental peaks have been discussed in past analyses and will not be repeated here; the portion of the spectrum shown in Figure 6 mainly represents O–H stretches of the water and hydroxyl units. For the present purposes, the good consistency of the relative intensities in the high-frequency dangling–OH stretch region (highlighted in Figure 6) suggests that the isomer ensemble is being adequately sampled by the basin-hopping approach. The weak, broad

transition near 3810 cm^{-1} is not reproduced by the current simulations. However, this peak also appears in the Ar-tagged (30 K) spectra,²⁷ which suggests that this transition is likely a combination band or overtone, rather than an isomer that is missing from the simulations.

The present computations suggest that the 180 K ensemble contains *both* SP1- and CP-type isomers in significant populations. Therefore, at this temperature (and above), the $n = 6$ region should be considered a transitional regime, in which the electronic driving force for CP separation is only sufficient to overcome entropic factors at low temperatures. The component spectra, shown in the lower panel of Figure 6, suggest that these isomeric contributions are sufficiently unique that double-resonance spectroscopy techniques^{81,82} could potentially be used to resolve the constituent spectra, however. On the basis of the computed spectra, such experiments are encouraged.

B. Detailed Analysis of $(\text{H}_2\text{O})_6^+$ and Competition of Driving Forces.

The 10-water oxidized cluster provides a size regime for which past computational studies have not been performed and for which experimental vibrational spectra are once again available. For this larger cluster, 571 unique isomers were obtained from the BH search. (In addition, 73 very high-energy isomers that contained dissociated H atoms and H_2 units were also obtained during the search; these isomers were excluded from the following analysis.) Representative structures and corresponding energies are shown in Figure 7; complete structures and energies are available from the author. The structure with the lowest electronic energy (10A) exhibits a globular configuration, in which all constituent species act as both a hydrogen-bond acceptor and donor. This structure consists of a five-membered ring, containing the ion and radical in an SP1 configuration. The remaining water molecules adopt a four-membered ring structure, with a single bridging water between the two halves. In this configuration, the ion is fully solvated, and the hydroxyl subunit acts as a single acceptor–donor species. Several additional isomers were obtained that contained similar qualitative behavior, with only subtle hydrogen-bonding differences. Structure 10F is the lowest-energy species when harmonic ZPE corrections are included. This structure is similar to 10A although the orientation of the hydroxyl radical, relative to the hydronium, differs (an effect that could potentially be observed spectroscopically). Both 10A and 10F display a one-water separation of the ion and the radical, although, via the H-bonding network, both 1-water and 2-water separation pathways are present, highlighting that additional separation of the ion and radical is becoming possible at this cluster size. In the first row of Figure 7, additional low-energy globular isomers are shown, including the lowest-energy CP isomer (10I), the lowest-energy Zundel isomer (10L), as well as a two-water-separated (SP2-type) isomer (10N). All of these structures exhibit ZPE-corrected energies within 2.32 kcal/mol of 10A.

Structures in the second row of Figure 7 exhibit single moieties acting only as H-bond acceptors. These configurations include SP1 (10P and 10AG) and SP2 (10S) structures in which a water molecule is the dangling species, as well as an SP2 species in which the radical is the dangling species (10Y). Zundel isomers (10AM) were also discovered; this particular form exhibits CP behavior. Interestingly, the harmonic ZPE corrections place several of these “+1” isomers (where the notation signifies a single dangling species), such as 10S and 10AG, low in the energy hierarchy even though they sit

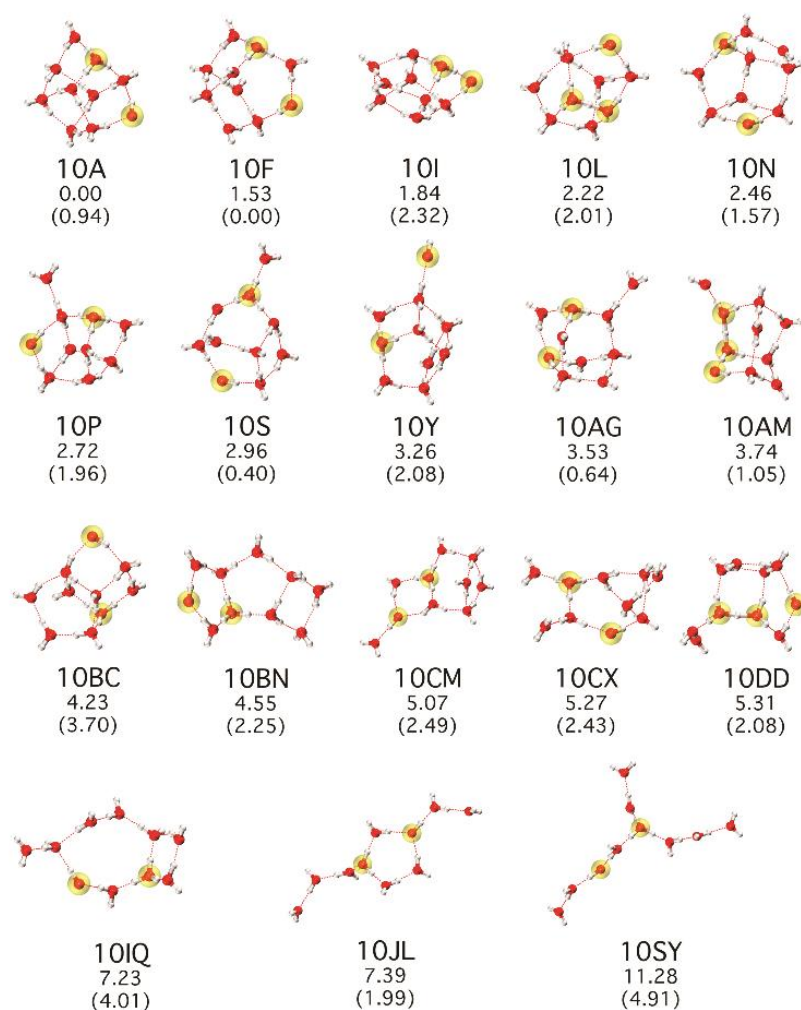


Figure 7. Representative stable isomers of $(\text{H}_2\text{O})_{10}^+$ using MPW1K/6-31++G**. (The full set of isomer structures and energies is available from the author.) Relative electronic energies are shown in kcal/mol. Harmonic ZPE-corrected relative energies are provided in parentheses. The oxygen atom of the ion (H_3O^+) and radical (OH) subunits are highlighted in yellow; the solvated trimer and Zundel subunits have been highlighted similarly.

2.8–3.8 kcal/mol above 10A electronically. The low energy of 10S is particularly noteworthy because it is an SP2 structure, suggesting that continued separation of the ion–radical pair is becoming nearly isoenergetic with SP1-type structures. This SP2 structure also sits *below* the lowest-energy CP isomer (10I).

Higher in energy, structures with more open character and broken H-bonds are observed. These structures are shown in the third row of Figure 7. Because of the available H-bonding patterns, most of the low-energy open structures still consist of fused four-, five-, and six-membered rings. Structure 10BN, for example, can be classified as fused five- and four-membered rings, forming an SP1 isomer. Structure 10CM is noteworthy because it contains the low-energy form of the hexamer (6A), H-bonded to an intact neutral water hexamer. Similarly, 10CX contains a branched form of the hexamer (6P), H-bonded to the neutral tetramer. Several open forms of the Zundel class of

isomers (10DD) were also obtained. Finally, more exotic species were also obtained through the BH search and are shown in the final row of Figure 7. A seven-membered ring structure (10IQ) is a stable isomer, sitting 7.2 kcal/mol above 10A. Partially (10JL) and fully (10SY) branched structures were also observed, with energies up to 11.3 kcal/mol. This latter structure defines an important open-structure bookend, which demonstrates that the full globular-to-open structural spectrum is spanned within about 11 kcal/mol.

For this cluster size, 10 isomers exhibit population contributions above 5% between 0 and 300 K, as shown in Figure 8. Isomer 10F, which exhibits the lowest ZPE-corrected energy, is the major conformer up to about 120 K. This isomer should be the dominant species in any future tagged (≤ 30 K) spectroscopy experiments of this size regime, provided that the tag atom/molecule does not alter the relative energies. Isomers 10S and 10AG, which possess “+1” water molecules,

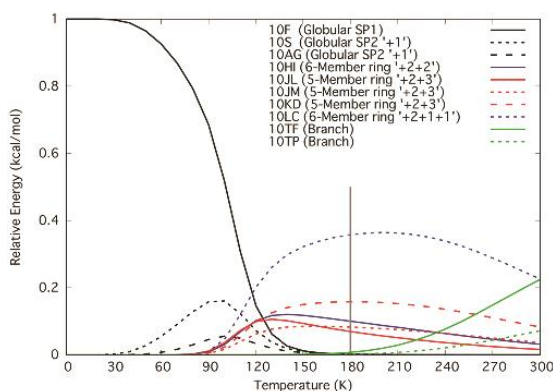


Figure 8. Thermal populations of $(\text{H}_2\text{O})_{10}^+$ isomers up to 300 K. Displayed are populations of the four isomers for which the population exceeds 5% across this temperature range. The vertical gray line denotes the temperature at which experimental vibrational spectra have been obtained.

appreciably contribute to the ensemble between roughly 60 and 120 K. At the 180 K experimental temperature, isomer 10LC—a six-membered-ring isomer with +2, +1, and +1 dangling water units—comprises the majority of the isomer population, due to an increased entropy term.

Using all 571 computed isomers, the thermally weighted vibrational spectrum shows some agreement with the experimental results, although the preponderance of highly coupled, broadened peaks in the experiment makes comparison rather difficult. The dangling O–H stretches ($3650\text{--}3750\text{ cm}^{-1}$) again provide the most diagnostic information because these stretches are indicative of the H-bonding environment, without the severe broadening of the lower-frequency bands. The thermally weighted, computed spectrum (upper panel of Figure 9) properly reproduces the four transitions corresponding to distinct dangling–OH asymmetric stretch environments, but the relative intensities are incorrect. Because the highest frequency of these transitions corresponds to the asymmetric stretch of a purely H-bond-accepting water molecule, the computed prediction of the presence of a slightly more open structure appears to be correct. A detailed temperature analysis (results not shown) exhibits a rapid change in relative intensities in the 90–120 K range, and the 110 K spectrum most closely represents the relative intensities (lower panel of Figure 9), particularly those of the “open” structures. This effect could be due to (a) incorrect intensities of the computed spectra, (b) errors in the computed relative free energies based on the RRHO model, (c) ambiguity in the assignment of the experimental temperature, or (d) kinetic trapping in the experimental cluster preparation. On the basis of the computed temperature dependence, small errors in any (or all) of these four effects could drastically shift the resulting spectral intensities, which highlights the continued need for cold trapping techniques. Nonetheless, the fact that the three dominant peaks are recovered by the thermally dominant isomers, using the same scaling factor as was used for $n = 6$, is particularly encouraging for the present search protocol.

To fully summarize the behavior of $(\text{H}_2\text{O})_{10}^+$, several competing effects must be considered. Some of these effects are germane to any H-bonded cluster, but they also provide an important backdrop to the observed trends in the present

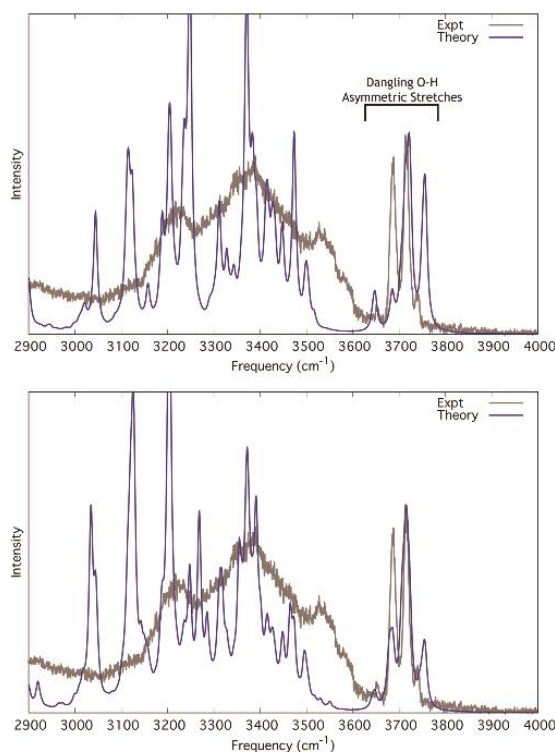


Figure 9. Vibrational spectra of $(\text{H}_2\text{O})_{10}^+$. Thermally weighted harmonic spectra (scale factor, 0.91524; Lorentzian width, 10 cm^{-1}), using MPWIK/6-31++G**, are shown in blue; the experimental spectrum of Fujii²⁶ is shown in gray. The upper panel depicts computed 180 K spectra; the lower panel depicts computed 110 K spectra.

analysis. From the electronic energy perspective, globular isomers dominate the low-energy structures, due to optimal H-bonding. This effect is somewhat tempered by the decreased zero-point energy of broken-H-bonded structures. Higher-frequency librational motions, for example, are traded for (nearly) free rotors, which lowers ZPE. Each broken H-bond contributes roughly the same amount to this trend, as shown in Figure S1. In addition to these energetic considerations, entropic factors favor the open structures. At temperatures still well below room temperature, the more branched isomers begin to appreciably contribute to the ensemble. Against this backdrop, trends among the ion–radical interaction can also be assigned. A bias toward SP1-type structures is observed, although SP2 and CP structures are energetically competitive. An electronic driving force for pair separation is observed *within each structural class*, but the magnitude of this electronic preference is small enough that ZPE and entropic terms can strongly modulate the relative energies. Such considerations would likely be less relevant in condensed-phase oxidized-water scenarios, where the free-rotor contributions to entropic factors would be mostly eliminated. These effects motivate the study of trends in larger clusters, therefore, where the collectively stronger effect of H-bonding provides more realistic models of oxidized water.

C. Structural Classes of $(\text{H}_2\text{O})_{13}^+$. To survey the structural landscape of larger oxidized clusters, selected isomer size

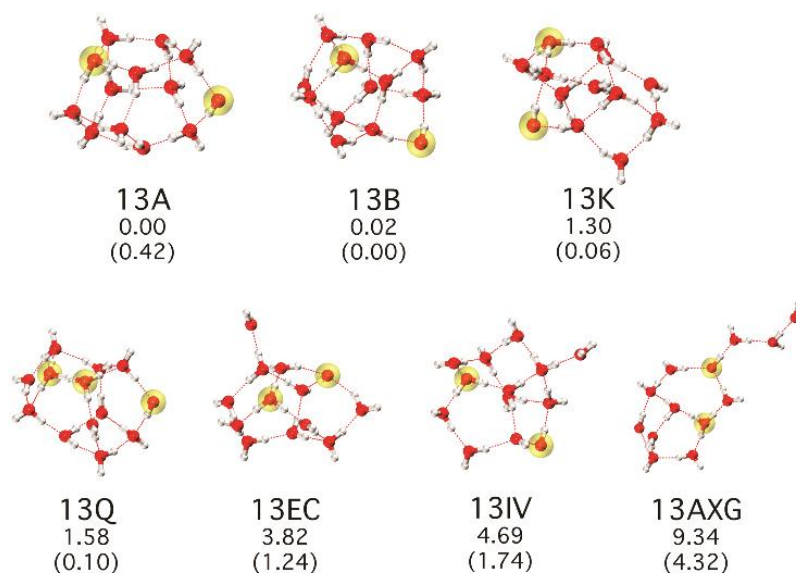


Figure 10. Representative stable isomers of $(\text{H}_2\text{O})_{13}^+$ using MPW1K/6-31++G**. Shown are isomers that exhibit appreciable ($\geq 10\%$) canonical ensemble population for 0–300 K, as well as the isomer (13A) with the lowest electronic energy. The full set of isomer structures and energies is available from the author. Relative electronic energies are shown in kcal/mol. Harmonic ZPE-corrected relative energies are provided in parentheses. The oxygen atom of the ion (H_3O^+) and radical (OH) subunits are highlighted in yellow; the solvated Zundel subunits have been highlighted similarly.

regimes will be examined in this and the subsequent subsection. The 13-water cluster provides the opportunity to expand solvation shells and exhibit new ion–radical behavior. It is not yet large enough to potentially stabilize an internally solvated species, however; this latter size regime ($n = 21$) is reserved for analysis in the following subsection. Because the backdrop of competing electronic and ZPE/entropic factors has now been established, hereafter the full set of structures will be discussed in less detail, and focus will be placed on the isomers that contribute most significantly to the low-temperature ensembles.

The BH search procedure yielded 2089 unique isomers (excluding high-energy isomers with isolated H atoms or H_2 units). Interestingly, the much simpler H-deletion protocol found the lowest-energy isomer, even when the preliminary round of BH searches did not. Subsequent BH sampling recovered this isomer, among many others. From the sampling perspective, therefore, BH searches initiated from H-deletion starting structures would appear to be a robust route to efficient ensemble exploration. Isomers of $(\text{H}_2\text{O})_{13}^+$ with appreciable computed ensemble population ($\geq 10\%$) for 0–300 K are shown in Figure 10, along with the isomer (13A) with the lowest electronic energy.

The lowest-energy isomer (with [13B] or without [13A] ZPE correction) once again exhibits separation of the ion–radical pair. In this case, however, *two* interleaving waters separate the pair (SP2 type), which is the first indication that the pair-separation trend is a genuine driving force, rather than a specific electronic interaction between the ion–radical pair and a single additional water molecule. The acceptor–donor (AD) hydroxyl radical is positioned most distant from the hydronium ion, even though a strong (23.5 kcal/mol with MPW1K/6-31++G**) attraction exists between these two species when in isolation. The SP1-type isomer 13K sits higher in energy electronically, but the ZPE correction makes it nearly

isoenergetic (0.06 kcal/mol) with 13B. Similarly, the SP1-type Zundel isomer 13Q remains low in energy (0.10 kcal/mol) with ZPE corrections. Isomers 13EC, 13IV, and 13AXG all contribute to the thermal ensemble at elevated temperatures, due to entropic factors.

The temperature-dependent populations of these isomers are shown in Figure 11. Because of the close competition between

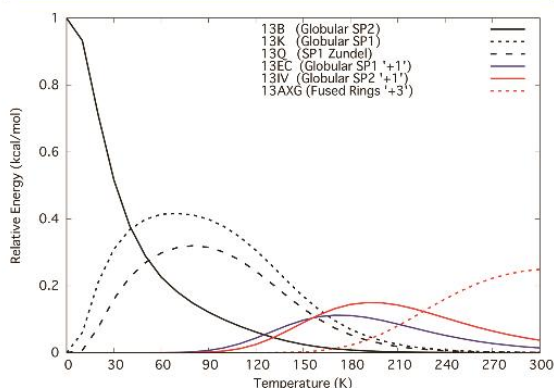


Figure 11. Thermal populations of $(\text{H}_2\text{O})_{13}^+$ isomers up to 300 K. Displayed are populations of the six isomers for which the population exceeds 10% across this temperature range.

electronic energy and ZPE in this case, multiple isomers—13B, 13K, and 13Q—are predicted to be present, even at cryogenic, tagged spectroscopy conditions (≤ 30 K). Lower temperatures would be required to isolate isomer 13B. Two additional “+1”-type isomers (13EC and 13IV) contribute near 200 K, and entropic contributions lead to population in “+3”-type isomer

13AXG by 300 K. All of these isomers are of either SP1- or SP2-type structures, however. Therefore, the $n = 13$ size regime is computed to be a transitional regime between SP1 and SP2 structures.

The presence of multiple isomers should be observable spectroscopically. Indeed, the predicted 30 K vibrational spectra, shown in Figure 12, exhibit isomer-specific signatures

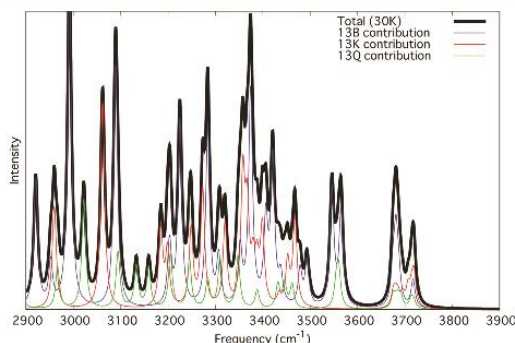


Figure 12. Computed vibrational spectrum of $(\text{H}_2\text{O})_{21}^+$ at 30 K. The thermally weighted harmonic spectrum (scale factor, 0.91524; Lorentzian width, 10 cm^{-1}), using MPW1K/6-31++G**, is shown in black. Component spectra from the three most populous isomers are shown as thin, colored traces.

from the three dominant isomers at this temperature. Many of these distinguishing bands occur in the strongly hydrogen-bonded region, and experimentally disentangling these transitions (where anharmonicity and combination bands/overtone are again likely) would be quite challenging. In fact, some of the bright hydronium O–H stretches are red-shifted to

the $1000\text{--}2000 \text{ cm}^{-1}$ range, even harmonically, which should be expected as the hydronium portion of the cluster transitions to a protonated-water cluster spectrum.^{26,27} The relative intensities of the terminal O–H stretches ($3600\text{--}3800 \text{ cm}^{-1}$) could, however, potentially be used to assign the isomers. The spectra in Figure 12 show that all three of the dominant isomers contribute differently to this spectral region. In none of the dominant isomers is the hydroxyl stretch intense enough to be clearly distinguishable from the remaining O–H stretches. The isomer dependence of these auxiliary stretches suggests that structural assignment should be possible, however.

D. Structural Classes of $(\text{H}_2\text{O})_{21}^+$. The neutral 21-water cluster internally self-solvates one of its water molecules in its lowest-energy structure.⁴³ Isomers were once again sampled in this size regime, to examine whether a caged ion, radical, or both were observed. Figure 13 depicts the seven isomers (of 404 unique) that contribute $\geq 5\%$ to the canonical ensemble in the 0–300 K temperature window. A clear preference for maximal separation of the ion and radical is observed, and the optimal H-bonding in globular isomers directs the stability of the low-energy structures. Isomer 21A, which exhibits an SP3 structural type, is lowest in energy with or without harmonic ZPE correction. Isomer 21B possesses a nearly identical structure, with only subtle reorientation of H-bonds and is nearly degenerate with 21A. These two structures also exhibit considerable structural homology with recently reported structures of $\text{H}^+(\text{H}_2\text{O})_{21}$,⁷⁰ including internal water solvation and an edge-bound hydronium. Four of the seven dominant isomers are of SP3 type; the remaining three (21D, G, and H) are of SP2 type. Somewhat surprisingly, none of the low-energy isomers exhibited an internally solvated species other than H_2O . Only two isomers (21T and 21V, not shown) possess an internally solvated OH. None possessed a truly internal H_3O^+ , although some of the higher-energy isomers—for which a

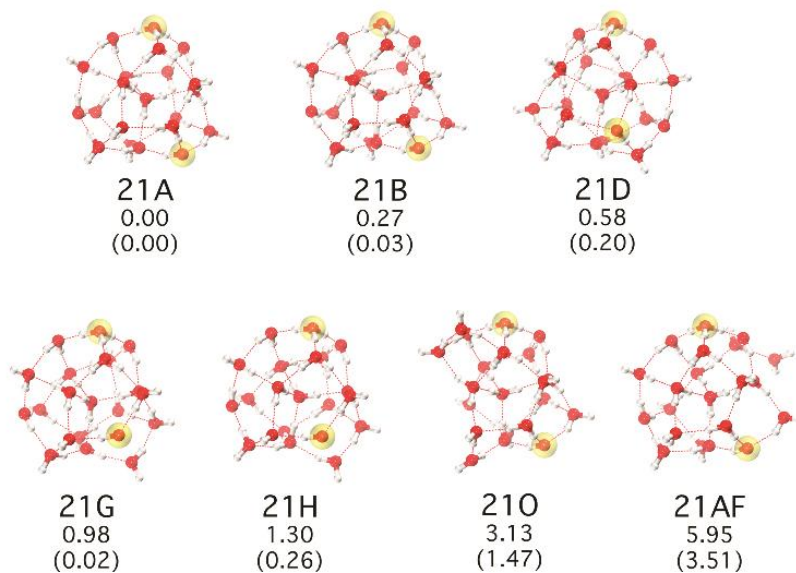


Figure 13. Representative stable isomers of $(\text{H}_2\text{O})_{21}^+$, using MPW1K/6-31++G**. Shown are isomers that exhibit appreciable ($\geq 5\%$) canonical ensemble population for 0–300 K. The full set of isomer structures and energies is available from the author. Relative electronic energies are shown in kcal/mol. Harmonic ZPE-corrected relative energies are provided in parentheses. The oxygen atom of the ion (H_3O^+) and radical (OH) subunits are highlighted in yellow. Depth cueing is used to aid in visualization; fainter atoms are more distant from the viewer.

cluster edge is somewhat ill-defined—could be classified as such.

The temperature-dependent populations and thermally weighted harmonic vibrational spectra are once again shown in Figures 14 and 15, respectively. As was observed for

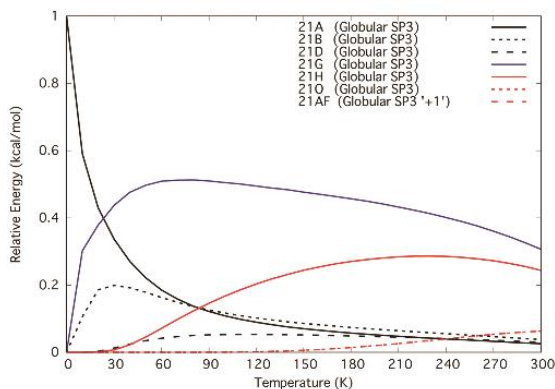


Figure 14. Thermal populations of $(\text{H}_2\text{O})_{21}^+$ isomers up to 300 K. Displayed are populations of the seven isomers for which the population exceeds 5% across this temperature range.

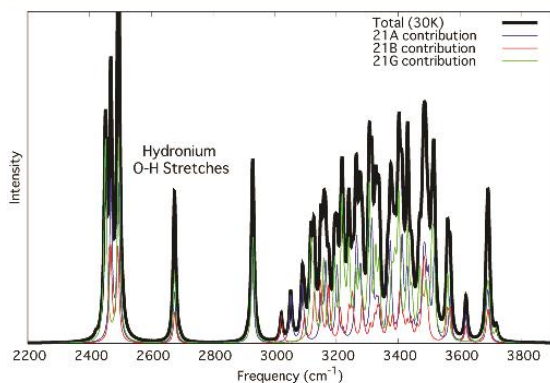


Figure 15. Thermally weighted, computed harmonic vibrational spectrum (scale factor, 0.91524; Lorentzian width, 10 cm^{-1}), using MPW1K/6-31++G** of $(\text{H}_2\text{O})_{21}^+$ at 30 K.

$(\text{H}_2\text{O})_{13}^+$, multiple isomers contribute to the low-temperature ensemble. Isomers 21A, B, and G (SP3 and SP2 types) dominate across a fairly large temperature range and are the main contributors to the low-temperature vibrational spectrum. The variety of strong H-bonding environments leads to a broad band between 3000 and 3600 cm^{-1} that is likely not resolvable experimentally. The O—H stretch of the hydroxyl unit sits at the red edge of this band and would probably be obscured by the water transitions. The analogous stretches of the hydronium subunit—which are also almost certainly more anharmonic than is captured by scaled harmonic frequencies—however, appear to remain distinct and would likely be the most indicative signature of the cluster structure.

With the largest of the clusters in this study now analyzed, comments regarding the trends across the set are now appropriate. Using the in-depth BH results for $n = 6, 10, 13,$ and 21, along with H-deletion data for intermediate cluster sizes

(Supporting Information), the driving force for pair separation is well established. The lowest-energy structures in each size regime seek to maximize the distance between the ion and the radical. A driving force must exist for the pair to separate upon sufficient solvation, although the driving force for further separation is weak enough that thermal fluctuations allow more closely spaced pairs to also contribute to the ensemble. On the basis of this trend, we conclude that the contact-pair species, although certainly involved in the initial ionization dynamics,⁷⁸ must be a low-population species at equilibrium in large clusters and, very likely, condensed-phase water.

E. Electronic Driving Forces for Pair Separation. Given the strong interaction between the hydroxyl radical and the hydronium ion—roughly 4 times the strength of the interaction of the water dimer, for example—the trend toward pair separation requires explanation. In our previous work, the interaction that drives the original, qualitative structural evolution was shown to be solvation of the hydronium ion by water. Put simply, water is a better solvent than hydroxyl, and the net result of these interactions was an independent solvation of the hydronium when enough water molecules are present. Whether this effect continues to be the driving force in larger clusters is examined in this subsection.

The quantum chemistry computations in this work allow for direct examination of the electronic anatomy of these clusters. Electronic spin densities ($\rho^{\text{spin}} = \rho^\alpha - \rho^\beta$) and density differences ($\Delta\rho = \rho^{\text{neutral}} - \rho^{\text{cation}}$) were computed to assess the spatial extent of these trends. For selected isomers of $(\text{H}_2\text{O})_{21}^+$, representing the lowest-energy isomers of each structural separation class, these electronic quantities are plotted in Figure 16. The MPW1K plots are shown in the figure; analogous quantities using MP2 relaxed densities are nearly identical. The difference densities demonstrate some slight interaction between the radical and the neighboring $\text{H}_3\text{O}^+/\text{H}_2\text{O}$ units in the contact-pair isomer, as well as the isomer with 1-water separation. However, the figure overwhelmingly shows radical spin densities corresponding to a localized OH electronic structure, especially compared to the equivalent properties computed in the lowest-energy configuration of the vertically ionized, neutral structure (lower panel of Figure 16). Although this result is consistent with past studies of the ionization process,³³ the equilibrium structures show little distinction among the isomers. A second analysis is, therefore, required to definitively assign the source of the pair-separation trend.

To assess the role of specific molecular interactions, a many-body expansion of the total cluster energy was computed. In this approach, hydronium, hydroxyl, and each water molecule are considered independent entities, and the total cluster energy is expanded as

$$E_{\text{tot}} = \sum_{i=1}^N E_i^{(1)} + \sum_{i=1}^N \sum_{j>i}^N \Delta E_{ij}^{(2)} + \dots$$

where ΔE_{ij} denotes the dimer interaction energy, relative to monomer energies in the same geometry, and N denotes the total number of monomers. In the present analysis, this expansion is truncated at second order, giving the composite 2-body contribution to the total cluster energy. As will be shown below, this approximation is sufficient to isolate the dominant contributions to the structural trends.

Results for representative low-energy isomers of $(\text{H}_2\text{O})_{21}^+$ are summarized in Table 1. Because the fluctuation in 1-body

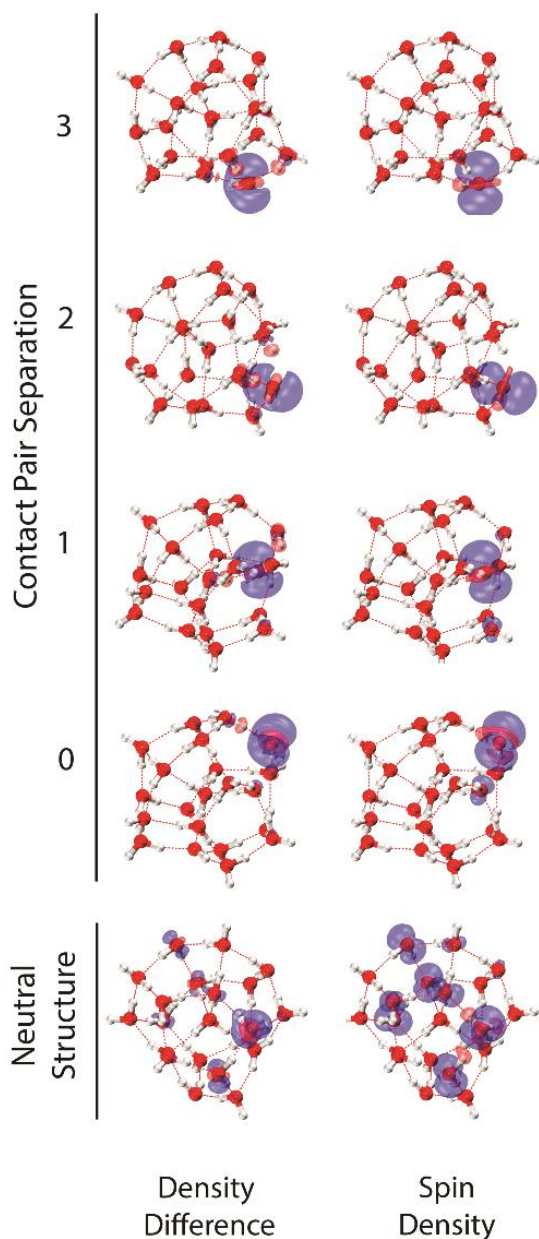


Figure 16. Electronic density plots for four selected isomers of $(\text{H}_2\text{O})_{21}^+$, using MPW1K/6-31++G**.

energies was found to be insignificant for isomer morphology trends, only the differential contribution of two-body effects ($\Delta E^{(2)}$) is shown here. The data in Table 1 indicate that solvation of the ion by water remains the dominant driving force for structural evolution. Increased distance between the ion and radical diminishes their favorable interaction; for example, this value changes from -19.7 kcal/mol in contact-pair isomer 2II to $+0.1$ kcal/mol in SP3-type isomer 21A. However, this penalty is insufficient to overcome the large, stabilizing effect of the ion–water interaction. Between limiting

Table 1. Two-Body Decomposition of the $(\text{H}_2\text{O})_{21}^+$ Structural Evolution

isomer	type	separation ^a	total relative energy ^b	$\text{H}_3\text{O}^+\cdots\text{OH}^c$	$\text{H}_2\text{O}\cdots\text{OH}^c$	$\text{H}_3\text{O}^+\cdots\text{H}_2\text{O}^c$
21A	SP3	7.2	0.0	0.1	-16.4	-144.5
21D	SP2	6.6	0.6	-1.5	-13.3	-142.5
21W	SP1	3.7	4.9	-6.2	-13.7	-137.7
21I	CP	2.7	1.9	-19.7	-8.3	-119.5

^aHydronium–hydroxyl distance (Å), measured between constituent oxygen atoms. ^bTotal relative electronic energy (kcal/mol), without many-body decomposition. ^cSummed two-body interactions (kcal/mol). The sign convention places favorable interactions less than zero. The water–water interactions show no structural trend and are omitted.

isomers 21I and 21A, the 19.8 kcal/mol penalty incurred by separation of the pair is more than offset by the -25.0 kcal/mol stabilization gained by solvation of the ion. Compared to previous results for smaller clusters,²⁵ the driving force is found to be notably enhanced by solvation effects beyond the first solvation shell. Solvation of the radical also provides an additional -8.1 kcal/mol of relative stability that serves to further drive separability. Therefore, this analysis conclusively shows that ion solvation serves as the dominant driving force for separation of the initially formed ion–radical contact pair, with an additional component from hydroxyl solvation. The backdrop of water–water interactions (of which many more exist in a given cluster) somewhat modulates this trend, as exemplified by the fact that CP isomer 21I is lower in electronic energy than SP1 isomer 21W. Overall, however, the clear correlation between hydronium/hydroxyl solvation and pair-separation distance is shown in the data of Table 1.

CONCLUSIONS

The preceding series of analyses has shown that the unique hydronium–hydroxyl contact pair, which has previously been studied extensively, must be a low-population species in the presence of sufficient solvation. Solvation of the ion and radical subunits serves as a subtle-yet-steady driving force for full separation of this pair. The magnitude of the driving force is large enough to cause separation at chemically relevant temperatures. It was also shown to be competitive with ZPE and thermal effects in certain cluster regimes, however, which highlights the need for added temperature control in cluster spectroscopy experiments. Nonetheless, in the largest cluster studied in this work, $(\text{H}_2\text{O})_{21}^+$, the ion and radical exhibited a clear propensity to stabilize at opposite edges of the cluster.

This edge stabilization requires brief comment, for the purpose of assessing future spectroscopic experiments. In all of the lowest-energy isomers discovered in this work, the hydronium ion is a 3-fold H-bond donor, sitting at the edge of the cluster. Because the commonly used tagging atoms (He, Ne, or Ar) or molecules (H_2 or D_2) in cryogenic cluster experiments are known to interact most strongly with charged species, such as hydronium,⁸³ a strong possibility exists that the tags could bias the structures observed. For example, because the ZPE and entropic effects were shown to be competitive with energetic driving forces, a slight bias of the tagging species to “grab” an H-bond of the ion could potentially alter the ensemble distribution. Such effects should be carefully considered in any future experiments.

The overall pair-separation results are consistent with established studies of radiolytic processes in condensed-phase water, and the present analysis unravels the source of this trend. Of course, ion solvation serves as the obvious driving force for many textbook chemical processes, such as ion-pair separation. For the hydronium half of the oxidized-water species, such a result is intuitive. The other half of this process—solvation of the hydroxyl radical and the radical's competition for the ion—was not *a priori* obvious. The results of this study clearly show that (1) ion solvation outcompetes the ion–radical effect to drive contact-pair separation, and (2) this solvation, through second- or third-shell effects, is strong enough to drive continued pair separation in large clusters and, likely, condensed-phase water.

This result is also encouraging for renewable energy processes involving the oxidation of water for solar fuels. The (first) oxidation has now been shown to lead to separation of the newly formed H_3O^+ unit, which must then migrate across a proton-exchange membrane.⁸⁴ The present analysis suggests that initial migration away from a putative hydroxyl ligand and out of the first solvation shell is electronically favorable. Motion thereafter is only slightly downhill, although preliminary molecular dynamics simulations (not presented here) suggest that rapid Grotthuss diffusion^{85–87} of the hydronium ion subsequently occurs. The extent to which the catalyst alters this landscape will, of course, be dependent on the details of the catalyst. This result highlights an important catalyst design consideration, however. The first oxidation of the surrounding water must occur with sufficient efficiency and with sufficient movement of the removed electron away from the oxidized water molecule that the hydronium unit bears no remnant attraction to the catalyst core. If the catalyst's ligand behaves akin to the hydroxyl radical considered here, without bias toward CP formation, then removal of the hydronium ion would be favorable. Even a small remnant electrostatic attraction could alter this behavior, however.

Future studies will need to address further oxidation steps, as well as the manner in which specific catalysts alter this energy landscape. This series of studies has established the critical uncatalyzed reference point and the electronic driving forces that are inherent to water and potentially amenable to catalytic control. They have also established methodologies that may serve as reliable tools for such future studies.

■ ASSOCIATED CONTENT

Supporting Information

The Supporting Information is available free of charge on the ACS Publications website at DOI: 10.1021/acs.jpca.6b07465.

Comparison of isomer energies and harmonic zero-point energies for $n = 10, 13,$ and 21 ; trends in relative isomer energies for H-deletion sampling for $n = 6–21$ (PDF)

■ AUTHOR INFORMATION

Corresponding Author

*R. P. Steele. Electronic mail address: ryan.steele@utah.edu. Telephone: 801-878-4312.

Notes

The authors declare no competing financial interest. Additional data are available from the authors: SuppInfo.combined.txt.zip contains basin-hopping MPW1K/6-31++G** isomer coordinates, basin-hopping MPW1K/6-31++G** isomer frequency outputs, and H-deletion MPW1K/6-31++G**

and RI-MP2/6-31++G** isomer coordinates. SuppInfo.Graphics.Combined.zip contains basin-hopping MPW1K/6-31++G** isomer structures, as TGA graphics. The ion and radical are highlighted in each structure.

■ ACKNOWLEDGMENTS

The authors thank Asuka Fujii for kindly providing the experimental vibrational spectra data. This material is based upon work supported by the National Science Foundation CAREER under CHE-1452596. The support and resources from the Center for High-Performance Computing at the University of Utah are gratefully acknowledged. This work also used the Extreme Science and Engineering Discovery Environment (XSEDE), which is supported by National Science Foundation grant number ACI-1053575.

■ REFERENCES

- (1) Kanan, M. W.; Nocera, D. G. In Situ Formation of an Oxygen-Evolving Catalyst in Neutral Water Containing Phosphate and Co^{2+} . *Science* **2008**, *321*, 1072–1075.
- (2) Meyer, T. J. Catalysis: The Art of Splitting Water. *Nature* **2008**, *451*, 778–779.
- (3) Hull, J. F.; Balcells, D.; Blakemore, J. D.; Incarvito, C. D.; Eisenstein, O.; Brudvig, G. W.; Crabtree, R. H. Highly Active and Robust Cp^* Iridium Complexes for Catalytic Water Oxidation. *J. Am. Chem. Soc.* **2009**, *131*, 8730–8731.
- (4) Lutterman, D. A.; Surendranath, Y.; Nocera, D. G. A Self-Healing Oxygen-Evolving Catalyst. *J. Am. Chem. Soc.* **2009**, *131*, 3838–3839.
- (5) Chen, Z.; Concepcion, J. J.; Luo, H.; Hull, J. F.; Paul, A.; Meyer, T. J. Nonaqueous Catalytic Water Oxidation. *J. Am. Chem. Soc.* **2010**, *132*, 17670–17673.
- (6) Concepcion, J. J.; Jurss, J. W.; Norris, M. R.; Chen, Z.; Templeton, J. L.; Meyer, T. J. Catalytic Water Oxidation by Single-Site Ruthenium Catalysts. *Inorg. Chem.* **2010**, *49*, 1277–1279.
- (7) Jurss, J. W.; Concepcion, J. C.; Norris, M. R.; Templeton, J. L.; Meyer, T. J. Surface Catalysis of Water Oxidation by the Blue Ruthenium Dimer. *Inorg. Chem.* **2010**, *49*, 3980–3982.
- (8) Karunadasa, H. I.; Chang, C. J.; Long, J. R. A Molecular Molybdenum-Oxo Catalyst for Generating Hydrogen from Water. *Nature* **2010**, *464*, 1329–1333.
- (9) Nocera, D. G. "Fast Food" Energy. *Energy Environ. Sci.* **2010**, *3*, 993–995.
- (10) Meyer, T. J. Catalysis: Oxidizing Water Two Ways. *Nat. Chem.* **2011**, *3*, 757–758.
- (11) Pijpers, J. J. H.; Winkler, M. T.; Surendranath, Y.; Buonassisi, T.; Nocera, D. G. Light-Induced Water Oxidation at Silicon Electrodes Functionalized with a Cobalt Oxygen-Evolving Catalyst. *Proc. Natl. Acad. Sci. U. S. A.* **2011**, *108*, 10056–10061.
- (12) Reece, S. Y.; Hamel, J. A.; Sung, K.; Jarvi, T. D.; Esswein, A. J.; Pijpers, J. J. H.; Nocera, D. G. Wireless Solar Water Splitting Using Silicon-Based Semiconductors and Earth-Abundant Catalysts. *Science* **2011**, *334*, 645–648.
- (13) Schley, N. D.; Blakemore, J. D.; Subbaiyan, N. K.; Incarvito, C. D.; D'Souza, F.; Crabtree, R. H.; Brudvig, G. W. Distinguishing Homogeneous from Heterogeneous Catalysis in Electrode-Driven Water Oxidation with Molecular Iridium Complexes. *J. Am. Chem. Soc.* **2011**, *133*, 10473–10481.
- (14) Barber, J.; Photosystem, I. I. The Water-Splitting Enzyme of Photosynthesis. *Cold Spring Harbor Symp. Quant. Biol.* **2012**, *77*, 295–307.
- (15) Barnett, S. M.; Goldberg, K. I.; Mayer, J. M. A Soluble Copper–Bipyridine Water-Oxidation Electrocatalyst. *Nat. Chem.* **2012**, *4*, 498–502.
- (16) Gagliardi, C. J.; Vannucci, A. K.; Concepcion, J. J.; Chen, Z.; Meyer, T. J. The Role of Proton Coupled Electron Transfer in Water Oxidation. *Energy Environ. Sci.* **2012**, *5*, 7704–7717.

- (17) Moonshiram, D.; Jurss, J. W.; Concepcion, J. J.; Zakharova, T.; Alperovich, I.; Meyer, T. J.; Pushkar, Y. Structure and Electronic Configurations of the Intermediates of Water Oxidation in Blue Ruthenium Dimer Catalysis. *J. Am. Chem. Soc.* **2012**, *134*, 4625–4636.
- (18) Sundstrom, E. J.; Yang, X.; Thoi, V. S.; Karunadasa, H. I.; Chang, C. J.; Long, J. R.; Head-Gordon, M. Computational and Experimental Study of the Mechanism of Hydrogen Generation from Water by a Molecular Molybdenum-Oxo Electrocatalyst. *J. Am. Chem. Soc.* **2012**, *134*, 5233–5242.
- (19) Bediako, D. K.; Surendranath, Y.; Nocera, D. G. Mechanistic Studies of the Oxygen Evolution Reaction Mediated by a Nickel–Borate Thin Film Electrocatalyst. *J. Am. Chem. Soc.* **2013**, *135*, 3662–3674.
- (20) Barnett, S. M.; Waidmann, C. R.; Scheuermann, M. L.; Nesvet, J. C.; Goldberg, K.; Mayer, J. M., Developing Molecular Copper Complexes for Water Oxidation. In *Molecular Water Oxidation Catalysis*; John Wiley & Sons, Ltd: 2014; pp 187–210.
- (21) Chadwick Ellis, W.; McDaniel, N. D.; Bernhard, S. Molecular Water Oxidation Catalysts from Iron. In *Molecular Water Oxidation Catalysis*; John Wiley & Sons, Ltd.: New York, 2014; pp 153–162.
- (22) Francàs, L.; Bofill, R.; García-Antón, J.; Escriche, L.; Sala, X.; Llobet, A. Ru-Based Water Oxidation Catalysts. In *Molecular Water Oxidation Catalysis*; John Wiley & Sons, Ltd.: New York, 2014; pp 29–50.
- (23) Bard, A. J. Inner-Sphere Heterogeneous Electrode Reactions. Electrocatalysis and Photocatalysis: The Challenge. *J. Am. Chem. Soc.* **2010**, *132*, 7559–7567.
- (24) Duffy, E. M.; Marsh, B. M.; Garand, E. Probing the Hydrogen-Bonded Water Network at the Active Site of a Water Oxidation Catalyst: $[\text{Ru}(\text{Bpy})(\text{Tpy})(\text{H}_2\text{O})]^{2+} \cdot (\text{H}_2\text{O})_{0-4}$. *J. Phys. Chem. A* **2015**, *119*, 6326–6332.
- (25) Herr, J. D.; Talbot, J.; Steele, R. P. Structural Progression in Clusters of Ionized Water, $(\text{H}_2\text{O})_{\text{N}=5}^+$. *J. Phys. Chem. A* **2015**, *119*, 752–766.
- (26) Mizuse, K.; Kuo, J.-L.; Fujii, A. Structural Trends of Ionized Water Networks: Infrared Spectroscopy of Water Cluster Radical Cations $(\text{H}_2\text{O})_{\text{N}}^+$ ($\text{N} = 3-11$). *Chem. Sci.* **2011**, *2*, 868–876.
- (27) Mizuse, K.; Fujii, A. Characterization of a Solvent-Separated Ion-Radical Pair in Cationized Water Networks: Infrared Photodissociation and Ar-Attachment Experiments for Water Cluster Radical Cations $(\text{H}_2\text{O})_{\text{N}}^+$ ($\text{N} = 3-8$). *J. Phys. Chem. A* **2013**, *117*, 929–938.
- (28) Gardener, G. H.; Johnson, M. A.; McCoy, A. B. Spectroscopic Study of the Ion–Radical H-Bond in H_4O_2^+ . *J. Phys. Chem. A* **2009**, *113*, 4772–4779.
- (29) Sodupe, M.; Bertran, J.; Rodríguez-Santiago, L.; Baerends, E. J. Ground State of the $(\text{H}_2\text{O})_2^+$ Radical Cation: DFT Versus Post-Hartree–Fock Methods. *J. Phys. Chem. A* **1999**, *103*, 166–170.
- (30) Livshits, E.; Baer, R. A Density Functional Theory for Symmetric Radical Cations from Bonding to Dissociation†. *J. Phys. Chem. A* **2008**, *112*, 12789–12791.
- (31) Pieniazek, P. A.; VandeVondele, J.; Jungwirth, P.; Krylov, A. I.; Bradforth, S. E. Electronic Structure of the Water Dimer Cation. *J. Phys. Chem. A* **2008**, *112*, 6159–6170.
- (32) Cheng, Q.; Evangelista, F. A.; Simmonett, A. C.; Yamaguchi, Y.; Schaefer, H. F. Water Dimer Radical Cation: Structures, Vibrational Frequencies, and Energetics. *J. Phys. Chem. A* **2009**, *113*, 13779–13789.
- (33) Pieniazek, P. A.; Sundstrom, E. J.; Bradforth, S. E.; Krylov, A. I. Degree of Initial Hole Localization/Delocalization in Ionized Water Clusters†. *J. Phys. Chem. A* **2009**, *113*, 4423–4429.
- (34) Kamarchik, E.; Kostko, O.; Bowman, J. M.; Ahmed, M.; Krylov, A. I. Spectroscopic Signatures of Proton Transfer Dynamics in the Water Dimer Cation. *J. Chem. Phys.* **2010**, *132*, 194311–11.
- (35) Do, H.; Besley, N. A. Structure and Bonding in Ionized Water Clusters. *J. Phys. Chem. A* **2013**, *117*, 5385–5391.
- (36) Lv, Z.-L.; Xu, K.; Cheng, Y.; Chen, X.-R.; Cai, L.-C. Ab Initio Investigation of the Lower Energy Candidate Structures for $(\text{H}_2\text{O})_5^+$ Water Cluster. *J. Chem. Phys.* **2014**, *141*, 054309.
- (37) Lu, E.-P.; Pan, P.-R.; Li, Y.-C.; Tsai, M.-K.; Kuo, J.-L. Structural Evolution and Solvation of the Oh Radical in Ionized Water Radical Cations $(\text{H}_2\text{O})_{\text{N}}^+$, $\text{N} = 5-8$. *Phys. Chem. Chem. Phys.* **2014**, *16*, 18888–18895.
- (38) Teo, B. K.; Sloane, N. J. A. Magic Numbers in Polygonal and Polyhedral Clusters. *Inorg. Chem.* **1985**, *24*, 4545–4558.
- (39) Harbola, M. K. Magic Numbers for Metallic Clusters and the Principle of Maximum Hardness. *Proc. Natl. Acad. Sci. U. S. A.* **1992**, *89*, 1036–1039.
- (40) Echt, O.; Kreisle, D.; Knapp, M.; Recknagel, E. Evolution of “Magic Numbers” in Mass Spectra of Water Clusters. *Chem. Phys. Lett.* **1984**, *108*, 401–407.
- (41) Iyengar, S. S.; Petersen, M. K.; Day, T. J. F.; Burnham, C. J.; Teige, V. E.; Voth, G. A. The Properties of Ion-Water Clusters. I. The Protonated 21-Water Cluster. *J. Chem. Phys.* **2005**, *123*, 084309.
- (42) Lee, H. M.; Suh, S. B.; Tarakeshwar, P.; Kim, K. S. Origin of the Magic Numbers of Water Clusters with an Excess Electron. *J. Chem. Phys.* **2005**, *122*, 044309.
- (43) Lagutschenkov, A.; Fanourgakis, G. S.; Niedner-Schatteburg, G.; Xantheas, S. S. The Spectroscopic Signature of the “All-Surface” to “Internally Solvated” Structural Transition in Water Clusters in the $\text{N} = 17-21$ Size Regime. *J. Chem. Phys.* **2005**, *122*, 194310.
- (44) Krylov, A. I. Equation-of-Motion Coupled-Cluster Methods for Open-Shell and Electronically Excited Species: The Hitchhiker’s Guide to Fock Space. *Annu. Rev. Phys. Chem.* **2008**, *59*, 433–462.
- (45) Rowe, D. J. Equations-of-Motion Method and the Extended Shell Model. *Rev. Mod. Phys.* **1968**, *40*, 153–166.
- (46) Emrich, K. An Extension of the Coupled Cluster Formalism to Excited States (I). *Nucl. Phys. A* **1981**, *351*, 379–396.
- (47) Geertsen, J.; Rittby, M.; Bartlett, R. J. The Equation-of-Motion Coupled-Cluster Method: Excitation Energies of Be and Co. *Chem. Phys. Lett.* **1989**, *164*, 57–62.
- (48) Stanton, J. F.; Bartlett, R. J. The Equation of Motion Coupled-Cluster Method. A Systematic Biorthogonal Approach to Molecular Excitation Energies, Transition Probabilities, and Excited State Properties. *J. Chem. Phys.* **1993**, *98*, 7029–7039.
- (49) Møller, C.; Plesset, M. S. Note on an Approximation Treatment for Many-Electron Systems. *Phys. Rev.* **1934**, *46*, 618–622.
- (50) Cizek, J. On the Correlation Problem in Atomic and Molecular Systems. Calculation of Wavefunction Components in Ursell-Type Expansion Using Quantum-Field Theoretical Methods. *J. Chem. Phys.* **1966**, *45*, 4256–4266.
- (51) Bartlett, R. J.; Musial, M. Coupled-Cluster Theory in Quantum Chemistry. *Rev. Mod. Phys.* **2007**, *79*, 291–352.
- (52) Sholl, D. S.; Steckel, J. A. *Density Functional Theory: A Practical Introduction*, 1st ed.; Wiley-Interscience: New York, 2009.
- (53) d’Avezac, M.; Calandra, M.; Mauri, F. Density Functional Theory Description of Hole-Trapping in SiO_2 : A Self-Interaction-Corrected Approach. *Phys. Rev. B: Condens. Matter Mater. Phys.* **2005**, *71*, 205210.
- (54) Mantz, Y. A.; Gervasio, F. L.; Laino, T.; Parrinello, M. Charge Localization in Stacked Radical Cation DNA Base Pairs and the Benzene Dimer Studied by Self-Interaction Corrected Density-Functional Theory. *J. Phys. Chem. A* **2007**, *111*, 105–112.
- (55) Perdew, J. P.; Zunger, A. Self-Interaction Correction to Density-Functional Approximations for Many-Electron Systems. *Phys. Rev. B: Condens. Matter Mater. Phys.* **1981**, *23*, 5048–5079.
- (56) Merkle, R.; Savin, A.; Preuss, H. Singly Ionized First-Row Dimers and Hydrides Calculated with the Fully-Numerical Density-Functional Program Numol. *J. Chem. Phys.* **1992**, *97*, 9216–9221.
- (57) Bally, T.; Sastry, G. N. Incorrect Dissociation Behavior of Radical Ions in Density Functional Calculations. *J. Phys. Chem. A* **1997**, *101*, 7923–7925.
- (58) Zhang, Y.; Yang, W. A Challenge for Density Functionals: Self-Interaction Error Increases for Systems with a Noninteger Number of Electrons. *J. Chem. Phys.* **1998**, *109*, 2604–2608.
- (59) Lynch, B. J.; Fast, P. L.; Harris, M.; Truhlar, D. G. Adiabatic Connection for Kinetics. *J. Phys. Chem. A* **2000**, *104*, 4811–4815.

CHAPTER 4

SIGNATURES OF SIZE-DEPENDENT STRUCTURAL

PATTERNS IN HYDRATED COPPER(I)

CLUSTERS, $\text{Cu}^+(\text{H}_2\text{O})_{n=1-10}$

Reprinted with permission from Herr, J. D.; Steele, R. P. Signatures of Size-Dependent Structural Patterns in Hydrated Copper(I) Clusters $\text{Cu}^+(\text{H}_2\text{O})_{n=1-10}$. *J. Phys. Chem. A* **2016**, *120* (51), 10252-10263. Copyright 2016 American Chemical Society.

Signatures of Size-Dependent Structural Patterns in Hydrated Copper(I) Clusters, $\text{Cu}^+(\text{H}_2\text{O})_{n=1-10}$

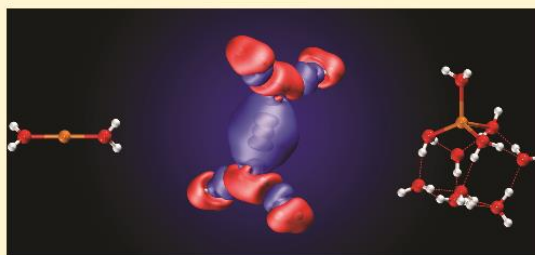
Published as part of *The Journal of Physical Chemistry virtual special issue "Mark S. Gordon Festschrift"*.

Jonathan D. Herr and Ryan P. Steele*[✉]

Department of Chemistry, University of Utah, 315 South 1400 East, Salt Lake City, Utah 84112, United States and
Henry Eyring Center for Theoretical Chemistry, University of Utah, 315 South 1400 East, Salt Lake City, Utah 84112, United States

 Supporting Information

ABSTRACT: The isomers of a hydrated Cu(I) ion with $n = 1-10$ water molecules were investigated by using *ab initio* quantum chemistry and an automated isomer-search algorithm. The electronic structure and vibrational spectra of the hundreds of resulting isomers were used to analyze the source of the observed bonding patterns. A structural evolution from dominantly two-coordinate structures ($n = 1-4$) toward a mixture of two- and three-coordinate structures was observed at $n = 5-6$, where the stability provided by expanded hydrogen-bonding was competitive with the dominantly electrostatic interaction between the water ligand and remaining binding sites of the metal ion. Further hydration ($n = 7-10$) led to a mixture of three- and four-coordinate structures. The metal ion was found, through spectroscopic signatures, to appreciably perturb the O–H bonds of even third-shell water molecules, which highlighted the ability of this nominally simple ion to partially activate the surrounding water network.



INTRODUCTION

The interaction of ions with water remains one of the key quantities of fundamental interest in both biological and energetic applications. In particular, the ability of strong ions to appreciably perturb the surrounding water network—chemically activating it in extreme cases^{1,2}—holds considerable significance for experimental applications, such as renewable-energy water-splitting chemistry and biological processes that either sense and regulate metal ions³⁻⁵ or exploit their chemistry for sensing other chemicals.⁶ The present computational study examines the size-dependent evolution of ion–water interactions during the hydration of a seemingly simple noble-metal cation, Cu(I), and examines the underlying electronic source of the observed bonding patterns.

Copper-based catalysts,⁷⁻⁹ including even simple copper salts,¹ have recently shown promise for water-splitting applications. The detailed, inner-sphere redox mechanisms¹⁰ of many of these catalysts remain experimental challenges, however, which hampers further catalyst development. Recently, our research group has provided detailed computational analyses of the first oxidation step in *bare* water, including structures and spectra of $(\text{H}_2\text{O})_2^+$,¹¹ $(\text{H}_2\text{O})_{1-5}^+$,¹² and $(\text{H}_2\text{O})_{6-21}^+$.¹³ In addition to explaining the unique vibrational signatures of the initially formed ion-radical contact pair ($\text{H}_3\text{O}^+\cdots\text{OH}^*$), these studies and others¹⁴⁻¹⁷ demonstrated a propensity for ion-radical pair separation for $n \geq 5$, which continues through $n = 21$ (and likely beyond¹⁸). These studies provide a backdrop for new studies of water clusters in the

presence of strong ions and simple oxidants. Open questions to be addressed include the electronic role of the ion in chemically activating the surrounding water, as well as the “depth” of this perturbation into the water network and spectroscopic signatures thereof. These questions will be examined in this analysis for Cu^+ , as a demonstrative case of seemingly simple ions yielding unique ion–water chemical and noncovalent interactions.

Small $\text{Cu}^+(\text{H}_2\text{O})_n$ clusters have previously been studied in detail, and discussion of many of these past works will be included in context in the ensuing discussion. Three studies provide key reference points for the present analysis, however. First, the binding energies of successive water molecules in $\text{Cu}^+(\text{H}_2\text{O})_{1-4}$ have most accurately been measured in the collision-induced dissociation (CID) experiments of Armentrout and co-workers.¹⁹ A noteworthy anomaly in these results, which was also discovered in earlier studies,^{20,21} is that the binding energy of the second water molecule is *larger* than the binding energy of the first. This effect clearly demonstrated that the interaction of this ion with water goes beyond simple electrostatic interactions and has previously been ascribed to unique 4s–3d hybridization effects in the nominally 4s⁰3d¹⁰ ion. The binding energy then dropped significantly for $n \geq 3$. Second, a computational study by Feller²² provided an analysis

Received: October 12, 2016

Revised: November 30, 2016

Published: December 1, 2016

of the electron correlation and basis set dependence of these binding energies (mainly for $n = 1, 2$) in quantum chemistry methods, including complete-basis-set limit estimates using the coupled-cluster singles and doubles method with perturbative triples [CCSD(T)]. These two studies will provide key benchmarks for calibration of the quantum chemistry methodology used in the present study. Finally, the most direct evidence for the structure of hydrated Cu^+ clusters stems from the cold (Ar-tagged) vibrational spectroscopy studies of Sekiya,^{23,24} in which density-functional theory (B3LYP)-based structures were used to provide reasonable congruence with the experimentally observed action spectra. The consensus among these reference studies is a propensity of hydrated Cu^+ to form two-coordinate structures, mainly due to the open 4s shell. Addition of water molecules beyond $n = 2$ preferentially opens a second solvation shell. The vibrational spectra of Sekiya suggested that this motif remains intact for $n = 5-7$,²⁴ although these larger clusters were also much warmer (nontagged), and the assignments relied on scaled harmonic frequencies. This propensity for two-coordinate binding has also been implicated as contributing to the condensed-phase redox potentials.²⁵

In the present study, three main items will be investigated in regard to Cu(I) hydration.

- Structures of Larger Clusters:** The available isomers for $n = 1-10$ will be examined, with the intent of assessing whether the two-coordinate motif remains favorable for larger clusters ($n \geq 7$). Neither computational nor experimental studies have examined this size regime.
- Isomeric Flexibility:** Although low-energy isomers and a few selected higher-energy forms have been examined in past studies,²⁶⁻³⁵ an exhaustive survey of the available structural space of $\text{Cu}^+(\text{H}_2\text{O})_n$ has not been performed. Using an automated isomer-search procedure, hundreds of isomers will be examined in this work. The energetic trends in higher-energy isomers of the small clusters will subsequently be used to explain the new trends observed in larger clusters.
- Water-Network Activation:** Past experimental studies have demonstrated nontrivial spectral shifts in the characteristic vibrations of first-shell water molecules.^{23,24,34} The present study seeks to examine whether this behavior persists in larger clusters, as well as the extent to which this spectral perturbation extends into the network of clusters with additional solvation shells. The motivating hypothesis of this study is that good water-oxidation catalysts can "preactivate" the surrounding water network for proton transfer. Certainly, simple Cu(I) ions cannot directly perform this redox chemistry, but a detailed investigation of the behavior of these ions should provide important fundamental insight for the manner in which copper-based catalysts interact with the surrounding solvent.

Finally, studies of the structural and energetic trends of "difficult" ions provide key reference points for new developments in computational methodology. Fragment-based and many-body methodologies have shown considerable promise for the simulation of solvated ions.³⁶⁻⁴⁴ Recent developments^{45,46} in near-exact fits to *ab initio* data also may provide transferable accuracy to large systems. However, the known behavior of $n \leq 4$ suggests that considerable collective effects may be at-play in hydrated Cu(I) , and a previous study³¹ has shown that the many-body decomposition of this system may

be qualitatively in error. Therefore, an ancillary aim of the present study is to provide reference structures and properties for the calibration of these *ab initio*-inspired potentials.

METHODS

The goal of this study was to investigate the structural trends—and the electronic source of these trends—in larger, hydrated clusters of Cu^+ . Such an investigation required the ability to rapidly, yet reliably, search the isomer space of moderately sized, fluxional clusters. Accordingly, the calibration of the electronic structure method, as well as the choice of the isomer-search protocol, requires discussion.

The aforementioned benchmark study by Feller²² showed that CCSD(T) with large basis sets was sufficient to accurately reproduce experimental binding energies in $\text{Cu}^+(\text{H}_2\text{O})_{1,2}$. Such an approach is well beyond current capabilities in the context of an exhaustive isomer-search procedure, however, in which tens of thousands of putative-structure optimizations were performed. Therefore, a careful benchmarking study was performed on $\text{Cu}^+(\text{H}_2\text{O})$ and $\text{Cu}^+(\text{H}_2\text{O})_2$ to find a suitable, computationally tractable method for these isomer searches. In addition to recomputed CCSD^{47,48} and CCSD(T) reference numbers, examined methodologies included Hartree–Fock (HF) and second-order Møller–Plesset perturbation theory⁴⁹ (MP2), as well as the MPW1K,^{50,51} B3LYP,^{52,53} and CAM-B3LYP⁵⁴ density functionals with the SG-1 quadrature grid.⁵⁵ Basis sets on the water ligand(s) included 6-31G(d,p),⁵⁶⁻⁵⁹ 6-31+G(d,p), cc-pVDZ, cc-pVTZ, aug-cc-pVDZ, and aug-cc-pVTZ.^{60,61} Basis sets on the copper ion included LANL2DZ,⁶² LANL2TZ,⁶³ LANL2TZ(f),⁶⁴ SBKJG,⁶⁵ and SRSG,⁶⁶ the matched effective core potential (ECP) for copper was used in each case, with frozen core orbitals for the wavefunction-based correlated methods. Only key energetic quantities will be discussed in context during the structural analyses below, but complete results for these analyses may be found in the Supporting Information. The MPW1K density functional performed particularly well in this analysis, which is consistent with our previous studies of $(\text{H}_2\text{O})_n^+$ and also allows for a direct comparison to properties in these ionized clusters. The LANL2DZ ECP and basis set (Cu) and the aug-cc-pVDZ basis set (O, H) were selected among these results as the most reliably accurate and cost-efficient method within the DFT framework. The electronic binding energy (D_e) of the first water molecule, for example, was found to be 40.13 kcal/mol with CCSD(T)/aug-cc-pVTZ(O,H)/LANL2TZ(f) (Cu) and 38.31 kcal/mol with MPW1K/aug-cc-pVDZ(O,H)/LANL2DZ(Cu). (For comparison, the CCSD(T)/aug-cc-pVTZ/LANL2DZ result was 38.56 kcal/mol.) Although this consistency is not fully quantitative, it is appreciably closer than the other density functionals tested and adequately reflected relative isomer-energy trends. Unless otherwise stated, all geometries, energies, and frequencies reported throughout this work are results from this methodology. A development version of the Q-Chem quantum chemistry package⁶⁷ was used for all calculations, and the VMD program⁶⁸ was used to visualize structures and electronic properties.

The search for available isomers was performed with the basin-hopping Monte Carlo procedure.⁶⁹ In this approach, a standard Metropolis Monte Carlo algorithm⁷⁰ was used to sample the space of optimized structures. After random displacement of the bonds, angles, and torsions (in automatically generated z-matrix coordinates), a standard geometry optimization was performed; the Metropolis procedure was

then applied only to the optimized structures. The only nonstandard modification to this protocol was the retention of *all* optimized geometries, rather than only the accepted structures. Several independent runs of 5000 Monte Carlo steps at 3000 K were performed for each cluster size. These initial searches were performed with the (qualitatively correct) HF/6-31G***(O,H)*/LANL2DZ(Cu) method, and unique isomers were subsequently refined with MPW1K/aug-cc-pVDZ(O,H)/LANL2DZ(Cu) for final structures, energies, and frequencies. The assignment of unique isomers was performed with an automated in-house code, in which each rigid structure was maximally aligned (through root-mean-square deviation minimization) with all previous structures; all possible permutations of like atoms were considered in this assignment because the basin-hopping protocol commonly led to interchange of hydrogen atoms. (Very high-energy isomers with dissociated H atoms were also occasionally found and were excluded from all subsequent analysis.) An RMSD cutoff of 1.0 Å was used for accelerating the pruning of structures. Convergence of the basin-hopping search was assessed by tracking the number of unique isomers obtained as a function of Monte Carlo steps; this convergence analysis is also included in the Supporting Information. Although this procedure is unlikely to find every available isomer for finite sampling, the results of this analysis suggest that the low-energy (<10 kcal/mol) isomer space was sufficiently sampled. The number of unique isomers in this energy window found through this procedure ranged from 1 at $n = 1$ to as many as 383 at $n = 8$.

To approximately assess the role of zero-point energy (ZPE) and rule out transition-state structures, analytic harmonic vibrational frequencies were computed for all unique isomers with the same MPW1K method. These frequencies were also used to assess the “depth” at which the ion perturbs the surrounding water network, by examining O–H stretch frequencies. Of course, such frequencies should be viewed with some caution because anharmonic effects are known to impact the spectra of strong ions. The spectral trends across the set of isomers should be reliable, however.

Finally, an analysis of the electronic structure of the various isomers was also performed. For this purpose, several techniques were employed. The energy decomposition analysis (EDA) of Khaliullin^{71–74} allowed for the decomposition of cluster interactions into electrostatic (frozen density), polarization, and charge-transfer components. Density difference plots, involving the difference in total electron densities between fragments and total complexes, also allowed for the visualization of polarization effects. An examination of molecular orbital (MO) coefficients and atomic partial charges was also performed. For relevant structures, comparison was also made to the analogous clusters of $\{\text{Li}^+, \text{Na}^+, \text{K}^+\}(\text{H}_2\text{O})_n$.

RESULTS AND DISCUSSION

Given the large amount of data generated through the isomer-search procedure, only key structures and trends will be discussed in this section. Optimized structures, energies, and harmonic frequencies for all species may be found in the Supporting Information. Nomenclature of the listed isomers is given as $[n][\text{letter}]$, where n corresponds to $\text{Cu}^+(\text{H}_2\text{O})_n$ and the letter corresponds to the electronic energy ordering of the isomers. Harmonic ZPE-corrected energies are also listed in each case. To avoid linguistic ambiguity, due to the presence of water ligands, the immediate coordination sphere of the ion will

be considered the first “solvation shell” of the ion throughout this discussion.

A. Reference Trends in $\text{Cu}^+(\text{H}_2\text{O})_{1-4}$. Several low-energy isomers for $n = 1-4$ are displayed in Figure 1. In this figure, the relative electronic energy (within a given n) is shown for each structure, and the harmonic ZPE-corrected relative energies are shown in parentheses. Although several aspects of this size regime have been examined in past studies, the structures are briefly reviewed in this section, along with two new pieces of information: (a) new electronic properties, illuminated through density-difference maps and energy decomposition analyses, and (b) higher-energy isomers that establish important reference energy scales for effects to be discussed in the larger clusters.

A1. Structures, Energies, and Electronic Properties. The only available isomer for $\text{Cu}^+(\text{H}_2\text{O})$ is the known structure, in which the water molecule’s oxygen binds directly to the metal center. In this configuration, the HOMO expansion coefficients reflect the well-known partial s–d hybridization effect in this complex. However, this hybridization contribution should not be considered the lone factor in the bond formation. In fact, the EDA results showed that the interaction is nearly evenly divided among electrostatic (32%), polarization (36%), and

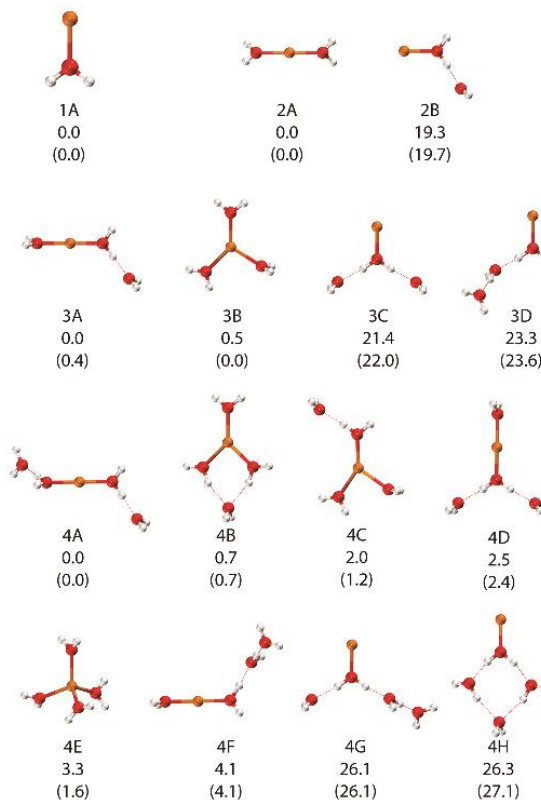


Figure 1. All discovered unique isomers of $\text{Cu}^+(\text{H}_2\text{O})_{1-4}$ using MPW1K/aug-cc-pVDZ(O,H)/LANL2DZ(Cu). Relative energies are listed for each isomer, in kcal/mol; ZPE-corrected relative energies are listed in parentheses. Coordinates, energies, and frequencies for the full set of isomer structures may be found in the Supporting Information.

charge-transfer (and higher-order relaxation) effects (32%). The latter component is reflected in the Cu Mulliken charge of only +0.85e. The density difference between the complex and the separate ion/water species is shown in Figure 2; an increase in density upon complexation is depicted in blue, whereas a decrease is shown in red. This analysis most directly depicts the fundamental nature of the interaction in the copper(I)–water system. At the lower isovalue ($\Delta\rho = 0.001$ au, Figure 2a), the strong polarization of the water molecule led to a shift in density that overlapped with the metal center. However, a decrease in electron density along the Cu–O axis (“inside” of the blue lobe) was also observed, which represents the partial loss of pure 3d character during bond formation. This behavior suggested that much of the bonding interaction actually involves the lone pair of the water ligand delocalizing to the sides of the metal ion as the 4s character is increased. At the higher isovalue ($\Delta\rho = 0.005$ au, Figure 2b), the bonding interaction was less obvious, but the response of the cation was more easily visualized. In particular, the increase in electron density on the ion was found to occur orthogonal to the bond axis, which is the result of this s–d hybridization effect. This image clearly demonstrates that the second water molecule should prefer to bind on the opposite (red) side of the ion, at the site where the first water molecule has polarized the metal and depleted the electron density.

Indeed, the computed isomers of $\text{Cu}^+(\text{H}_2\text{O})_2$ were found to be consistent with this $\Delta\rho$ analysis for $n = 1$ and were also consistent with past studies for the lowest-energy isomer. In 2A, the second water molecule bound directly to the metal center, opposite the metal to the first water and in a staggered configuration. A second isomer, 2B, which sits more than 19 kcal/mol above 2A, placed the second water molecule in a hydrogen-bonding configuration in the second solvation shell. Although this isomer is unlikely to be accessed in any cluster experiment, the energy of this species demarcates an important relative energy scale for metal and hydrogen bonding. Even though the water molecule in the H-bond configuration is bound appreciably stronger (18.7 kcal/mol) than a standard water–water H-bond (4.9 kcal/mol for the water dimer at this level of theory), the binding of this second water molecule directly to the metal is still heavily favored. Continued reduction in the Mulliken charge on the ion (+0.75e) suggested

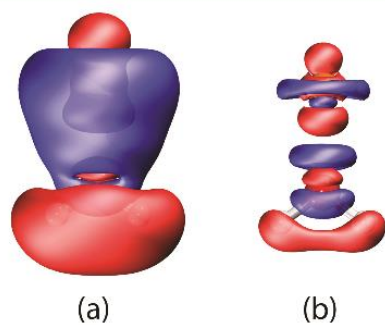


Figure 2. Total electron density difference upon complexation in $\text{Cu}^+(\text{H}_2\text{O})$, relative to ion/water fragments: $\Delta\rho = \rho(\text{Cu}^+\text{H}_2\text{O}) - [\rho(\text{Cu}^+) + \rho(\text{H}_2\text{O})]$. (a) Isovalue $\Delta\rho = 0.001$ au. (b) Isovalue $\Delta\rho = 0.005$ au. The orientation of the complex matches the orientation in Figure 1. Blue lobes correspond to an increase in density; red lobes correspond to a decrease in density.

that additional strong interactions affect the ion at $n = 2$. Relative to individual ion and water fragments, the density-difference response (Figure 3) reflected a symmetric, and slightly enhanced, polarization equivalent to the response seen at $n = 1$, including strong polarization of the water ligands and orthogonal polarization of the metal ion.

The $\text{Cu}^+(\text{H}_2\text{O})_3$ complex allowed for the direct examination of the role of a third binding site on the metal. Four unique isomers were observed for this complex, and these isomers set the stage for many of the bonding motifs observed in larger clusters. Isomers 3A and 3B were found to be nearly degenerate, with only subtle ZPE treatments separating the two forms. This result differs from known MP2-based benchmarks.²² To clarify this discrepancy, the present MPWIK structures were used to determine the single-point aug-cc-pVTZ/LANL2TZ(f) electronic energy gaps using CCSD (0.40 kcal/mol) and CCSD(T) (0.95 kcal/mol), which were much closer to our 0.47 kcal/mol result than the MP2 result of 2.7 kcal/mol. The BLYP functional^{75,76} further exacerbated this discrepancy, at 3.8 kcal/mol, which may suggest a method-dependent bias in previous claims that the two-coordinate form remains preferred in condensed-phase hydration.²⁵ The near-equivalence of the binding energies in these two forms (with appropriate underlying methodology) suggested that the strong H-bonding energy of a water molecule to the first-shell waters is comparable to the energy of the third metal binding site, when distortion of the original two waters was included. These structural motifs will hereafter be considered (2+1) and (3+0) configurations, reflecting the number of water molecules in the first and second solvation shells. These two low-energy forms were appreciably more stable than the set of remaining isomers. The latter isomers form either branched structures in the second solvation shell in a (1+2) form (3C, +21.4 kcal/mol) or water chains into the third shell in a (1+1+1) form (3D, +23.3 kcal/mol). On the basis of these two structures, the binding energy of a third-shell site is slightly diminished, compared to that for further second-shell solvation.

The two low-energy forms of $n = 3$ were investigated further, to understand the electronic origin of the competition between metal coordination and expanded solvation. In the (3+0) isomer 3B, the EDA results indicated that the interaction with the metal ion became more strongly electrostatic (42%), with

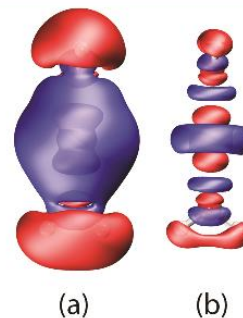


Figure 3. Total electron density difference upon complexation in $\text{Cu}^+(\text{H}_2\text{O})_2$, relative to individual ion/water fragments: $\Delta\rho = \rho(\text{Cu}^+(\text{H}_2\text{O})_2) - [\rho(\text{Cu}^+) + \rho(\text{H}_2\text{O}) + \rho(\text{H}_2\text{O})]$. (a) Isovalue $\Delta\rho = 0.001$ au. (b) Isovalue $\Delta\rho = 0.005$ au. Blue lobes correspond to an increase in density; red lobes correspond to a decrease in density.

lesser contributions from polarization (30%) and charge transfer (28%). The behavior of the (2+1) isomer **3A** was roughly reversed, with 26% electrostatics, 47% polarization, and 27% charge transfer. This effect can clearly be seen in the water-binding density-difference plots of Figure 4. At the same isovalue ($\Delta\rho = 0.005$ au), the third water molecule was notably more polarized in **3A** than in **3B**. (Because the bond lengths in **3B** of the “first” two water molecules are shorter, due to a pseudo-Jahn–Teller distortion, a “third” water molecule can uniquely be identified for this analysis.) The H-bond-donating water molecule in the coordination sphere of **3A** was also further polarized, and the spectroscopic implications of this many-body effect will be discussed below. The density response of the metal center was found to be larger in the (3+0) isomer, presumably due to the direct interaction of the water ligand in this case. Finally, a simple many-body decomposition, using ion/water fragments, was found to be slowly convergent. The one- and two-body contributions incorrectly assigned the order of the isomers, with the two-body relative energy in error by more than 23 kcal/mol. Three-body contributions restored the correct electronic energy ordering but overstabilized **3A** by a factor of 4. Therefore, at least four-body interactions appear to be required for quantitative representation of Cu(I) hydration.

The isomeric flexibility of $\text{Cu}^+(\text{H}_2\text{O})_4$ is also shown in Figure 1. Although the low-energy form is consistent with some^{22–24} (but not all^{29,31}) past studies, several additional, new isomers were uncovered through the basin-hopping procedure. In fact, seven isomers (of the eight total unique isomers) were found to exist below 6 kcal/mol. The low-energy structure **4A** is the (2+2) structure with each first-shell water donating a single H-bond to a second-shell water. The strong polarization of the second-shell waters continued in this complex and outweighed the metal-binding interactions. However, the (3+1) isomer **4B** was found to sit only 0.7 kcal/mol higher in energy. This structure adopted a form akin to known low-energy structures of other monovalent cations,^{77–81} with the lone second-shell water acting as a double-acceptor. Other low-energy forms included (3+1) isomer **4C**, branched (2+2) isomer **4D**, and even (4+0) isomer **4E** (+3.3 kcal/mol; +1.5 kcal/mol with ZPE). The latter isomer, which is only slightly more stable than (2+1+1) isomer **4F**, suggested that the fourth metal binding site is also comparable in binding energy with the third solvation-shell binding energy. The EDA analysis, using the separate ions and waters as fragments, suggested that this four-coordinate structure is now dominantly electrostatic (51%). Therefore, within the $n \leq 4$ size regime, several of the relative

energy scales were discerned from this isomer landscape. The observation that these varying structures are all of similar energy highlights the subtle electronic interactions that the quantum chemistry method (and any future force fields) must adequately explore.

A2. Vibrational Signatures of Structural Trends. Across this set of $n = 1–4$ isomers, the harmonic frequencies were indicative of the metal ion’s impact on the surrounding water molecules. With the same level of theory, the harmonic O–H stretch frequencies for an isolated water molecule were found to be 3968 cm^{-1} (symmetric) and 4080 cm^{-1} (asymmetric). In structures **1A** and **2A**, the asymmetric stretch was red-shifted to 3917 and 3931 cm^{-1} , respectively. This result is a clearly discernible spectroscopic signature that the electronic interaction goes well beyond electrostatic binding and electric field considerations. Standard anticooperativity arguments,⁸² for example, would suggest that the electrostatic contribution to the binding would be appreciably diminished in **2A**, compared to that in **1A**. Although a subtle manifestation of this effect (a 14 cm^{-1} blue shift) was found to occur, the strong chemical interaction in the two-coordinate species preserved the majority of the original spectral shift.

The $n = 3$ clusters provided the first testing ground for assessing the “depth” of the much stronger frequency perturbations, however. In the (2+1) isomer **3A**, the lowest-frequency asymmetric stretch, which naturally became more of a localized O–H stretch, was significantly red-shifted to 3335 cm^{-1} . The experimentally determined²³ position of this stretch is 2980 cm^{-1} for this isomer, which highlights the possible anharmonicity in these modes and the potential errors in harmonic ZPE-corrected energies. In fact, this anharmonicity may be sufficient to preferentially stabilize isomer **3A** over **3B** (which is suggested spectroscopically²³), in spite of the prediction of the harmonically corrected results. The close energy of these two forms may also explain the appearance of several additional transitions, as well.^{23,24} Isomer **3B**, with three first-shell water molecules, exhibited a lowest-frequency O–H stretch of 3939 cm^{-1} , which continued the subtle anticooperativity trend of first-shell complexation in **1A** and **2A**. The stark differences between these $n = 3$ configurations highlighted the utility of vibrational spectroscopy in assigning the structures. The high-energy isomer **3D** provided an assessment of the spectral modifications to the third solvation shell. In this structure, the harmonic asymmetric stretch of the first-shell water molecule continued the trend toward the red at 2925 cm^{-1} . Therefore, the presence of additional H-bonding interactions, even in the third solvation shell, further destabilizes the coordination-shell O–H bonds. The second-shell water molecule exhibited a 3562 cm^{-1} O–H stretch, and the terminal water molecule exhibited a symmetric stretch at 3955 cm^{-1} (asymmetric at 4058 cm^{-1}). The latter frequencies still deviate from the isolated water values, suggesting that even third-shell effects are nontrivial in these complexes. The second-shell effects were partially shared in the $n = 4$ complexes, with the lowest-frequency stretch of **4A** shifted slightly back to the blue at 3377 cm^{-1} . In **4B**, the two donating hydrogen bonds exhibited stretches intermediate to the $n = 3$ limiting regimes at 3795 cm^{-1} . Overall, the vibrational trends were consistent with the electronic analyses, and these vibrational signatures will be used as probes of perturbations to the water network in subsequent size regimes.

B. Expanding Structural Flexibility in $\text{Cu}^+(\text{H}_2\text{O})_{5,6}$. Representative structures for $\text{Cu}^+(\text{H}_2\text{O})_5$ and $\text{Cu}^+(\text{H}_2\text{O})_6$ are

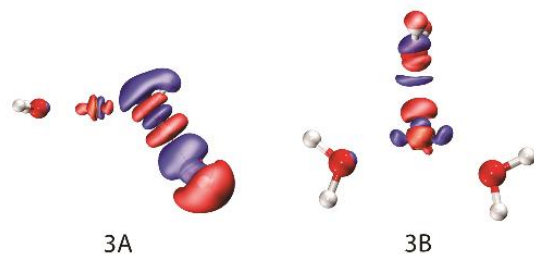


Figure 4. Total electron density difference upon complexation in two isomers of $\text{Cu}^+(\text{H}_2\text{O})_3$, relative to $\text{Cu}^+(\text{H}_2\text{O})_2$: $\Delta\rho = \rho(\text{Cu}^+(\text{H}_2\text{O})_3) - [\rho(\text{Cu}^+(\text{H}_2\text{O})_2) + \rho(\text{H}_2\text{O})]$. The isovalue is $\Delta\rho = 0.005$ au in both panels. Blue lobes correspond to an increase in density; red lobes correspond to a decrease in density.

shown in Figure 5; the complete list of isomer structures and properties can be found in the Supporting Information. The lowest-energy isomers of each cluster size, when ZPE corrections were included, were **5B** and **6C**, and these isomers shared structural similarity. The fifth and sixth water molecules were most stable in second-shell hydrogen-bonding configurations as single H-bond acceptors. The inner, two-coordinate metal–water core remained intact in both cases, and this low-energy isomer assignment is qualitatively consistent with structures conjectured from experimental vibrational spectra and limited B3LYP computations.²⁴

The more extensive isomer-search procedure employed in the present work highlighted that the variety of low-energy isomers was more significant than suggested by single structures alone. For $n = 5$, for example, 24 unique isomers were discovered, all of which exhibited relative energies below 9 kcal/mol. Even at the low-energy end of the isomer ensemble, the (3+2) isomer **5A** was less than 0.1 kcal/mol (ZPE-corrected) above the energy of (2+3) lowest-energy isomer **5B**. The experimental vibrational spectrum²⁴ exhibited several broad bands in the 3000–3400 cm^{-1} region that were not easily assigned to **5B** harmonic frequencies alone. Whether this

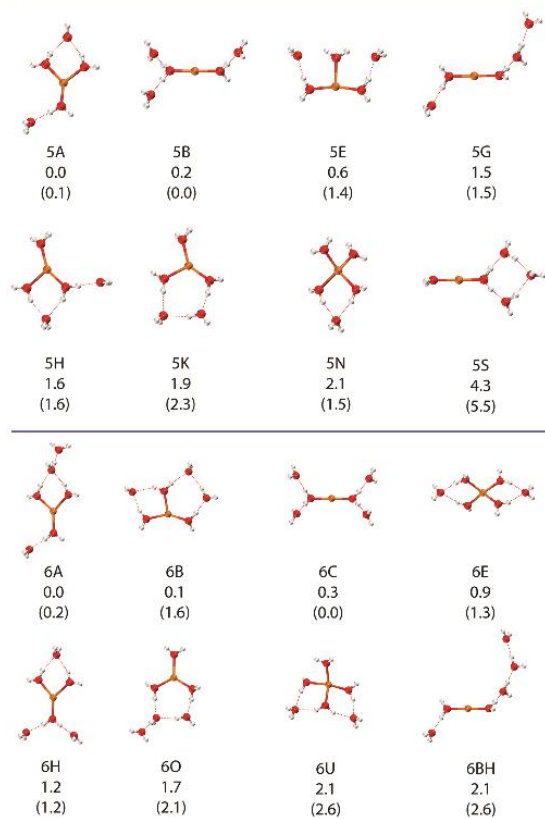


Figure 5. Representative unique isomers of $\text{Cu}^+(\text{H}_2\text{O})_{5,6}$ using MPW1K/aug-cc-pVDZ(O,H)/LANL2DZ(Cu). Relative energies are listed for each isomer, in kcal/mol; ZPE-corrected relative energies are listed in parentheses. Coordinates, energies, and frequencies for the full set of isomer structures may be found in the Supporting Information.

competition among the low-energy forms is responsible for this breadth is presently unclear and would require an in-depth anharmonic analysis and, likely, a colder, better-resolved investigation of the experimental high-frequency O–H stretches. The relatively hot existing spectra for these ions likely favored structure **5B**, however, which possesses more terminal rotors than **5A**. As was observed in our recent $(\text{H}_2\text{O})_n^+$ study,¹³ very modest changes in temperature can dramatically shift the isomer populations in these fluxional clusters. Regardless of the nuanced energy difference, which is likely within the error bars of the present quantum chemistry and vibrational treatments, the fact that structures with 2- and 3-fold coordination at the metal site were nearly degenerate was noteworthy and defined the behavior of the $n = 5, 6$ size regime. The presence of three second-shell water molecules (**5B**) is evidently of the same energy scale as two second-shell water molecules and a first-shell ligand (**5A**), provided that one of the second-shell waters is a double-acceptor. The remainder of the isomers accessed many of the expected binding motifs available to H-bonding water molecules and a coordinated core. Interestingly, a four-coordinate structure, **5N**, was found to be only 1.5 kcal/mol above **5B**. Even though additional H-bonding stability has been provided to **5B**, compared to the case for its $n = 4$ analogue, similar stability was imparted by the second-shell water molecule of **5N**. This effect rendered the four-coordinate energy gap nearly the same at $n = 4$ and $n = 5$. The remaining high-energy isomers of $n = 5$ (not shown in Figure 5) mainly formed “attached water clusters” to the two- and three-coordinate ion cores.

For $\text{Cu}^+(\text{H}_2\text{O})_6$, a total of 79 unique isomers were obtained, with the highest sitting 12.2 kcal/mol (ZPE-corrected) above **6C**. Similar to the behavior of $n = 5$, the lowest-energy (2+4) isomer is competitive in energy, within 0.22 kcal/mol, with (3+2+1)-type isomer **6A**, which is also the singly solvated analogue of **5A**. From an energetic standpoint, the bias toward two-coordinate species appears to be not nearly as strong as previously suggested. In fact, three-coordinate species comprise the majority of the low-energy isomer landscape, aside from the lowest-energy form, **6C**. Due to two second-shell water molecules acting in a double-acceptor capacity, the (4+2) species **6E** was further stabilized to only 1.3 kcal/mol.

Many of the remaining $n = 6$ isomers were logical extensions of structures observed at $n = 5$, so no additional insight is gained by further structural analysis. The remainder of this discussion will focus on the electronic properties at $n = 6$. In particular, the density-difference analyses were especially instructive at this cluster size. Focusing on **6C**, the $\Delta\rho$ plots (relative to the individual fragments, Figure 6a,b) displayed the same qualitative bonding behavior seen at $n = 2$, in the sense that the strongly polarized first-shell waters overlapped favorably with the s–d-hybridized Cu^+ ion. At the same isovalences, however, the first-shell water molecules were *more* strongly polarized at $n = 6$. This result is consistent with the vibrational response, in which the lowest-frequency harmonic O–H stretch (H-bond donor) appeared at 3570 cm^{-1} , compared to the 3931 cm^{-1} stretch observed for **2A**. The completed second-shell H-bonding environment further polarized the first-shell water molecules. Also shown in Figure 6c is the $\Delta\rho$ plot for which the ion and *complete* six-water network served as the two reference fragments. This analysis, when compared with the fully fragment-based $\Delta\rho$ analysis (Figure 6b), separated the water–water H-bonding effects from the role of the metal ion. This comparison demonstrated that

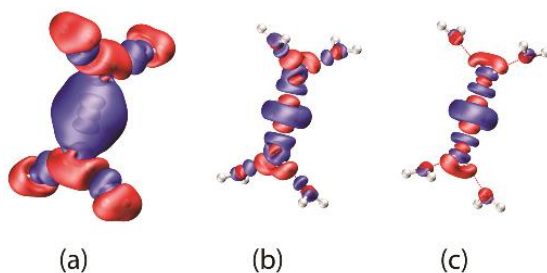


Figure 6. Total electron density difference upon complexation in isomer 6C of $\text{Cu}^+(\text{H}_2\text{O})_6$. Panels a and b are relative to separate Cu^+ and H_2O fragments at isovalues $\Delta\rho = 0.001$ au and $\Delta\rho = 0.005$ au, respectively. Panel c is relative to Cu^+ and the collective $(\text{H}_2\text{O})_6$ group, at $\Delta\rho = 0.001$ au. Blue lobes correspond to an increase in density; red lobes correspond to a decrease in density.

the metal ion itself comprised much of the water-polarization effects, although a portion of the second-shell effects were purely water-based. This analysis also graphically illustrated the spatial extent of the metal ion's role—at least into the second solvation shell—in impacting the surrounding water network.

One final comment is warranted for the $n = 5, 6$ set of structures. In their lowest-energy forms, the binding energy of the last water molecule was computed to be 13.2 and 12.4 kcal/mol, respectively. The highest-frequency O–H stretches in the existing experimental spectra²⁴ were observed near 3750 cm^{-1} , which only corresponds to a 10.7 kcal/mol photon. Therefore, past infrared-dissociation experiments were either accessing a multiphoton-dissociation regime or were “skimming off” the higher-energy portion of the relatively hot ensemble. Therefore, new experiments involving clusters tagged with either rare gas atoms⁸³ or H_2/D_2 ⁸⁴ are encouraged for definitive structural assignments.

C. Evolution of Trends in $\text{Cu}^+(\text{H}_2\text{O})_{7-10}$. For $n = 7-10$, the total number of unique isomers obtained from the basin-hopping search was 143, 383, 269, and 344, respectively. The four lowest-energy forms for each cluster size are shown in Figure 7, and much of the discussion in this section will focus on these low-lying structures. Whereas the $n = 5, 6$ regime exhibited competition between two- and three-coordinate metal centers, this larger size window mainly showed competition between three- and four-coordinate isomers. Assignment of the lowest-energy isomer was often reliant upon ZPE corrections. At $n = 7$, for example, a four-coordinate isomer (7A) possessed the lowest electronic energy, but the three-coordinate isomer 7M exhibited the lowest ZPE-corrected structure. Furthermore, due to free-rotor entropic considerations, two-coordinate isomer 7AV (+0.6 kcal/mol) would likely contribute to the isomer ensemble at even slightly elevated temperatures. The low-energy forms of $n = 8$ include two three-coordinate and two four-coordinate structures. This size regime does show some structural oscillation, however. A four-coordinate species 9A was found to be lowest in energy, whereas particularly favorable ZPE corrections made three-coordinate isomers 10C and 10J slightly lower in energy than the more compact H-bond arrangements of 10A and 10B.

Somewhat unexpectedly, most of the low-energy isomers exhibited agglomeration of the solvating water molecules to one “side” of the coordinated metal ion. Even though second-shell binding of water molecules was established in section A to be especially favorable compared to typical single H-bonds in

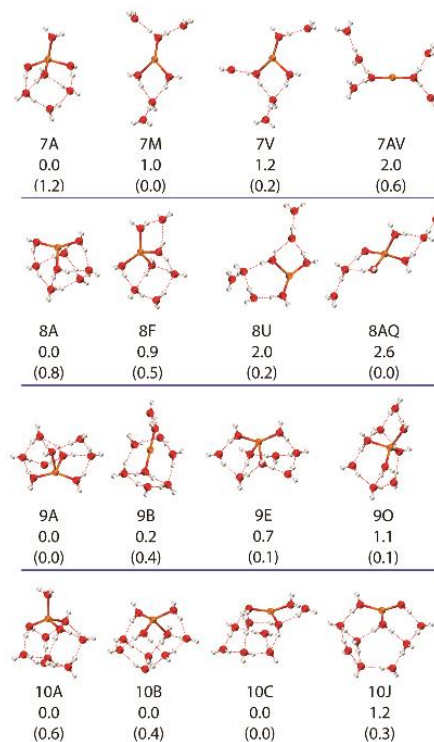


Figure 7. Representative low-energy isomers of $\text{Cu}^+(\text{H}_2\text{O})_{7-10}$ using MPW1K/aug-cc-pVDZ(O,H)/LANL2DZ(Cu). Relative energies are listed for each isomer, in kcal/mol; ZPE-corrected relative energies are listed in parentheses. Coordinates, energies, and frequencies for the full set of isomer structures may be found in the Supporting Information.

water, the ability to donate/accept multiple H-bonds within the solvating network evidently outcompetes this effect. This behavior resulted in low-energy isomers, such as 7A, in which a third solvation shell was stably formed while leaving a first-shell water ligand unsolvated. Similar one-sided behavior was also observed at $n = 9$ and 10. The Cu(I) ion exhibited a clear propensity for the cluster boundary, with the added possibility of a single dangling water ligand in stable clusters, such as 10A.

The electronic behavior of these larger clusters is depicted in the $\Delta\rho$ plots of Figure 8. The three-coordinate (7M, Figure

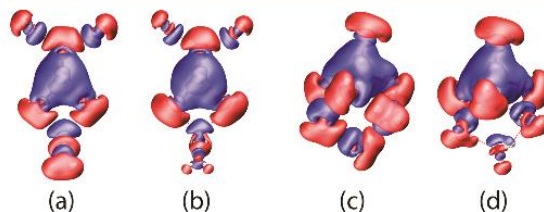


Figure 8. Total electron density difference upon complexation in isomers 7M (panels a and b) and 7A (panels c and d) of $\text{Cu}^+(\text{H}_2\text{O})_7$. Panels a and c are relative to separate Cu^+ and H_2O fragments at isovalue $\Delta\rho = 0.001$ au. Panels b and d are relative to Cu^+ and the collective $(\text{H}_2\text{O})_7$ group, at $\Delta\rho = 0.001$ au. Blue lobes correspond to an increase in density; red lobes correspond to a decrease in density.

8a,b) and four-coordinate (7A, Figure 8c,d) isomers of $n = 7$ displayed significant delocalization of the increased electron density (blue) in the vicinity of the ion, due to both polarization of the water molecules and hybridization of the metal center. The latter effect can be seen as the d void inside the main metal lobe in both structures. Through comparison of the two $\Delta\rho$ analyses, using each ion/water as reference fragments (panels a and c) and with the ion and collective water network as reference fragments (panels b and d), the role of the metal ion could be visualized. For both isomers, this comparison showed that the ion induced strong polarization in the coordination-sphere water molecules and, to a lesser degree, polarization of the first- and second-shell water molecules. The first-shell water network was found to be more polarized in the four-coordinate, (4+2+1)-type structure 7A than in the (3+3+1)-type structure 7M. Based on the bonding trends discussed above for the smaller clusters, the EDA results confirmed the increased role of electrostatics in these structures with higher coordination. For this analysis, the metal ion and the collective water network were used as two reference fragments. Because of the increased coordination, the total interaction was appreciably larger in 7A than in 7M. Although the charge-transfer component remained significant (20%), the electrostatic contribution dominated both interactions. The absolute electrostatic component expectedly increased (by about 15%) in the four-coordinate isomer. Yet the fractional contribution of electrostatics was nearly the same in both isomers (48% and 50%), which suggested that the fourth coordinated water still induced appreciable polarization. This effect was consistent with the observed $\Delta\rho$ plots.

These electronic properties also manifested as characteristic vibrational signatures that could potentially be confirmed experimentally. In particular, the O–H asymmetric stretch modes (Figure 9), which became mostly localized O–H stretches when strongly red-shifted, were indicative of the

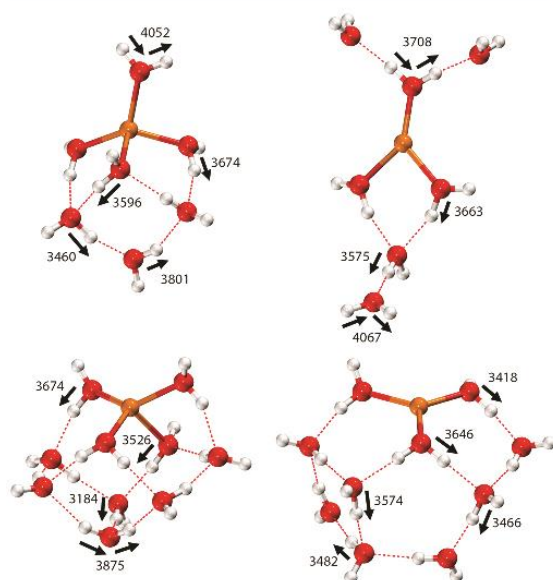


Figure 9. Representative asymmetric O–H stretch modes and corresponding harmonic frequencies (cm⁻¹) for isomers 7A (top left), 7M (top right), 10B (bottom left), and 10J (bottom right).

second-shell effects that strongly impacted binding motifs. In four-coordinate isomer 7A, for example, the H-bonded water molecules in the second shell exhibited particularly dramatic red shifts, with harmonic H-bond donor frequencies shifted to 3460 cm⁻¹, even though coordination-sphere asymmetric stretches ranged from 3596 to 4052 cm⁻¹. The effect was somewhat diminished in three-coordinate isomer 7M, with a 3575 cm⁻¹ stretch in the second shell. This result is counterintuitive from an anticooperativity standpoint, which would suggest that the effect of the ion should be more polarizing in the three-coordinate structure, but the density-difference maps in Figure 8 showed a propensity of the four-coordinate isomers to more strongly polarize second-shell water molecules. Although assigning a definitive source of this behavior is challenging, the partial chemical nature of the first-shell bonding appeared to cause nontrivial spectral shifts in neighboring water molecules. In fact, these shifts were exactly the water-network activation signatures that were originally conjectured to be present. Based on the results for isomers 10B and 10J (also shown in Figure 9), the effect extended to third-shell water molecules (10J, 3482 cm⁻¹) and also further shifted the bright, red-shifted transitions (10B, 3184 cm⁻¹). Therefore, even this nominally d¹⁰ noble metal ion is capable of partially activating the surrounding hydration network at least two shells beyond the primary coordination sphere.

D. Comparison to Monovalent, Hydrated Alkali Metal Cations. One remaining question concerns the nature of the water network alterations. Is, for example, the strong shift in vibrational frequencies just due to the dense charge of the cation, or do the aforementioned hybridization and charge-transfer effects contribute appreciably? To assess this question, the related isomers of simple alkali metal cations were examined. The K⁺ ion was examined as a d-orbital-free analogue of Cu⁺, although the Li⁺ ion, which was also examined, actually bears a nearly identical standard ionic radius for six-coordinate structures.⁸⁵ For both of these ions, selected isomers were reoptimized with the same level of theory (without the ECP for Li), and harmonic frequencies were computed. Structures and properties may be found in the Supporting Information.

For $n = 3$, where first- and second-shell effects became competitive for Cu⁺, neither Li⁺ nor K⁺ followed the same isomer energy ordering as Cu⁺. Because of the dominantly electrostatic interaction (53% for Li⁺, 64% for K⁺), the alkali analogues of Cu⁺ structure 3B (Figure 1) were found to be lower in electronic energy than 3A in both cases, by 7.0 kcal/mol for Li⁺ and by 0.9 kcal/mol for K⁺, in contrast to the behavior observed for Cu⁺. The structures were also more symmetric in the absence of the chemical bonding interactions. The three Li⁺...O interactions were equivalent at 1.898 Å in the analogue of 3B (with the water molecules equally canted out of the ion-oxygen plane), whereas the Cu⁺ version exhibited one Cu⁺–O bond that was more than 0.9 Å longer than the shortest, as well as one water molecule that was canted perpendicular to the plane of the other two. This asymmetry in the copper case was clearly indicative of the chemical interactions involved. The structures and energies, therefore, suggested that charge and size considerations alone are insufficient to explain the bonding behavior in hydrated Cu(I).

Differences between alkali metal cations and Cu⁺ were also observed in the computed harmonic vibrational frequencies for $n = 3$. Isomer 3A was examined, to assess the role of H-bonding effects to coordination-sphere water ligands. In the equivalent

analogues of this isomer, the H-bonded O–H stretches were 3661 cm^{-1} (K^+), 3439 cm^{-1} (Li^+), and 3335 cm^{-1} (Cu^+). The strong chemical interaction between Cu^+ and its first-shell water ligands was sufficient to red-shift the characteristic H-bonding stretch more than 100 cm^{-1} beyond the effect seen for Li^+ . This behavior is consistent with computed density-difference plots (Figure 10), which showed a marked difference in the nature of metal–ligand binding. The K^+ ion exhibited a relatively weak perturbation to the water electron density. The Li^+ ion's effect was much stronger, on par with changes observed for Cu^+ , but the behavior in the vicinity of the metal was qualitatively different.

The spectral behavior of these alternative ions in larger clusters was found to be much more consistent with the $\text{Cu}(\text{I})$ analogues, however. For example, the Li^+ equivalent of four-coordinate isomer 7A exhibited a most strongly red-shifted O–H stretch of 3461 cm^{-1} , in almost perfect congruence with the 3460 cm^{-1} stretch for Cu^+ (Figure 9). The remaining frequencies were also similar, and the normal modes were qualitatively similar in the two complexes. The Li^+ equivalent of isomer 7M exhibited O–H stretches that were only $20\text{--}40\text{ cm}^{-1}$ to the blue of the Cu^+ version. As the ion became four-coordinate, the electrostatic effects apparently became more consistent between the two ions. The differences were mainly contained to the relative energy ordering of the isomers. Isomers 7A and 7M were the lowest-energy $\text{Cu}(\text{I})$ forms without and with ZPE corrections, respectively; the equivalent Li^+ isomers were $+0.23\text{ kcal/mol}$ (electronic) and $+3.79\text{ kcal/mol}$ (ZPE-corrected) higher in energy than the equivalent of four-coordinate isomer 7H. Therefore, for the larger clusters, the alkali cations preferred more centrally solvated, symmetric structures, whereas Cu^+ clusters preferred asymmetric, edge-bound structures. When in the same structure, however, the spectral signatures were found to be similar.

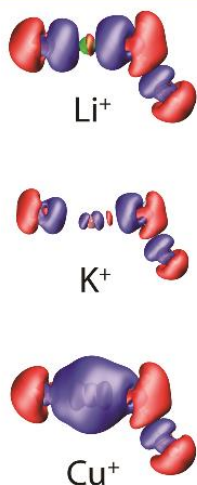


Figure 10. Total electron density difference upon complexation for the 3A-equivalent isomers of $\text{Li}^+(\text{H}_2\text{O})_3$, $\text{K}^+(\text{H}_2\text{O})_3$, and $\text{Cu}^+(\text{H}_2\text{O})_3$. All density differences are computed relative to individual ion/water fragments. The isovalue is $\Delta\rho = 0.001\text{ au}$ in all panels. Blue lobes correspond to an increase in density; red lobes correspond to a decrease in density.

CONCLUSIONS

Through a reasonably exhaustive computational search of the available isomer space of $\text{Cu}^+(\text{H}_2\text{O})_{1-10}$, yielding hundreds of new isomers, new trends in $\text{Cu}(\text{I})$ hydration behavior were observed. In particular, the well-known propensity to form two-coordinate structures for $n = 1$ and 2 continues for $n = 3, 4$, due to strong polarization of the coordination-sphere water ligands that can, in turn, form strong hydrogen bonds to second-shell water molecules. This effect outweighs the largely electrostatic interaction responsible for expanding the coordination sphere.

At $n = 5, 6$, however, these two effects become comparable in energy, and both two- and three-coordinate isomers were observed at low energies. For $n = 7\text{--}10$, the expanded solvation shells' H-bonding was not fully able to compete with the strong electrostatic attraction of the ion, and three- and four-coordinate structures became low-energy forms in this size regime.

Interestingly, the ion (in its three- and four-coordinate forms) exhibited a propensity to prefer the cluster boundary. The source of this preferentially “one-sided” H-bonding remains an open question. Whether the effect simply stems from a drive to complete H-bonding networks or from an as-yet unascrbed symmetry-breaking of the metal ion remains unclear. An examination of the structural progression in yet-larger clusters, where more complete H-bonding environments around the coordinated metal would likely be available, would be required to definitively answer this question.

Finally, vibrational frequencies were used in concert with corresponding electronic analyses to highlight both the strength and “depth” of the metal ion's perturbation to the water network. The computed results indicated that the strength of the impact to O–H stretch frequencies was *greater* in the largest clusters and was also highly sensitive to isomer structure. More importantly, the same signatures suggested that even this nominally simple metal ion can nontrivially affect the O–H bonds of water molecules at least three shells away from the ion. This result holds special consequence for water-oxidation catalysis, and future investigations will examine the strength of water network perturbation *required* for successful water-splitting catalysts. Ions with more oxidizing potential, including higher oxidation states of copper,^{86–91} will also be examined in this context.

ASSOCIATED CONTENT

Supporting Information

The Supporting Information is available free of charge on the ACS Publications website at DOI: 10.1021/acs.jpca.6b10346.

Tables of benchmark energies for $n = 1$ and $n = 2$; basin-hopping convergence summary; Cartesian coordinates, energies, and frequencies for all unique isomers (PDF)

AUTHOR INFORMATION

Corresponding Author

*Author to whom correspondence should be addressed. Electronic mail address: ryan.steele@utah.edu.

ORCID

Ryan P. Steele: 0000-0002-3292-9805

Notes

The authors declare no competing financial interest.

ACKNOWLEDGMENTS

This material is based upon work supported by the National Science Foundation CAREER under CHE-1452596. The support and resources from the Center for High-Performance Computing at the University of Utah are gratefully acknowledged. This work also used the Extreme Science and Engineering Discovery Environment (XSEDE), which is supported by National Science Foundation grant number ACI-1053575.

REFERENCES

- (1) Chen, Z.; Meyer, T. J. Copper(Ii) Catalysis of Water Oxidation. *Angew. Chem., Int. Ed.* **2013**, *52* (2), 700–703.
- (2) Roscioli, J. R.; Diken, E. G.; Johnson, M. A.; Horvath, S.; McCoy, A. B. Prying Apart a Water Molecule with Anionic H-Bonding: A Comparative Spectroscopic Study of the X-H₂O (X = Oh, O, F, Cl, and Br) Binary Complexes in the 600–3800 Cm⁻¹ Region. *J. Phys. Chem. A* **2006**, *110* (15), 4943–4952.
- (3) Martell, D. J.; Joshi, C. P.; Gaballa, A.; Santiago, A. G.; Chen, T.-Y.; Jung, W.; Helmann, J. D.; Chen, P. Metalloregulator Cues Biases Rna Polymerase's Kinetic Sampling of Dead-End or Open Complex to Repress or Activate Transcription. *Proc. Natl. Acad. Sci. U. S. A.* **2015**, *112* (44), 13467–13472.
- (4) Rensing, C.; Grass, G. Escherichia Coli Mechanisms of Copper Homeostasis in a Changing Environment. *FEMS Microbiology Reviews* **2003**, *27* (2–3), 197–213.
- (5) Lutsenko, S.; Gupta, A.; Burkhead, J. L.; Zuzel, V. Cellular Multitasking: The Dual Role of Human Cu-Atases in Cofactor Delivery and Intracellular Copper Balance. *Arch. Biochem. Biophys.* **2008**, *476* (1), 22–32.
- (6) Li, S.; Ahmed, L.; Zhang, R.; Pan, Y.; Matsunami, H.; Burger, J. L.; Block, E.; Batista, V. S.; Zhuang, H. Smelling Sulfur: Copper and Silver Regulate the Response of Human Odorant Receptor Or2t11 to Low-Molecular-Weight Thiols. *J. Am. Chem. Soc.* **2016**, *138*, 13281.
- (7) Du, J.; Chen, Z.; Ye, S.; Wiley, B. J.; Meyer, T. J. Copper as a Robust and Transparent Electrocatalyst for Water Oxidation. *Angew. Chem., Int. Ed.* **2015**, *54* (7), 2073–2078.
- (8) Zhang, M.-T.; Chen, Z.; Kang, P.; Meyer, T. J. Electrocatalytic Water Oxidation with a Copper(Ii) Polypeptide Complex. *J. Am. Chem. Soc.* **2013**, *135* (6), 2048–2051.
- (9) Barnett, S. M.; Goldberg, K. I.; Mayer, J. M. A Soluble Copper–Bipyridine Water-Oxidation Electrocatalyst. *Nat. Chem.* **2012**, *4* (6), 498–502.
- (10) Bard, A. J. Inner-Sphere Heterogeneous Electrode Reactions. Electrocatalysis and Photocatalysis: The Challenge. *J. Am. Chem. Soc.* **2010**, *132* (22), 7559–7567.
- (11) Talbot, J. J.; Cheng, X.; Herr, J. D.; Steele, R. P. Vibrational Signatures of Electronic Properties in Oxidized Water: Unraveling the Anomalous Spectrum of the Water Dimer Cation. *J. Am. Chem. Soc.* **2016**, *138* (36), 11936–11945.
- (12) Herr, J. D.; Talbot, J.; Steele, R. P. Structural Progression in Clusters of Ionized Water, (H₂O)_N = 1–5+. *J. Phys. Chem. A* **2015**, *119* (4), 752–766.
- (13) Herr, J. D.; Steele, R. P. Ion–Radical Pair Separation in Larger Oxidized Water Clusters, (H₂O)_N = 6–21. *J. Phys. Chem. A* **2016**, *120* (36), 7225–7239.
- (14) Mizuse, K.; Kuo, J.-L.; Fujii, A. Structural Trends of Ionized Water Networks: Infrared Spectroscopy of Water Cluster Radical Cations (H₂O)_N+ (N = 3–11). *Chem. Sci.* **2011**, *2* (5), 868–876.
- (15) Mizuse, K.; Fujii, A. Characterization of a Solvent-Separated Ion–Radical Pair in Cationized Water Networks: Infrared Photodissociation and Ar-Attachment Experiments for Water Cluster Radical Cations (H₂O)_N+ (N = 3–8). *J. Phys. Chem. A* **2013**, *117* (5), 929–938.
- (16) Lu, E.-P.; Pan, P.-R.; Li, Y.-C.; Tsai, M.-K.; Kuo, J.-L. Structural Evolution and Solvation of the Oh Radical in Ionized Water Radical Cations (H₂O)_N+, N = 5–8. *Phys. Chem. Chem. Phys.* **2014**, *16* (35), 18888–18895.
- (17) Do, H.; Besley, N. A. Structure and Bonding in Ionized Water Clusters. *J. Phys. Chem. A* **2013**, *117* (25), 5385–5391.
- (18) Marsalek, O.; Elles, C. G.; Pieniazek, P. A.; Pluhařová, E.; VandeVondele, J.; Bradforth, S. E.; Jungwirth, P. Chasing Charge Localization and Chemical Reactivity Following Photoionization in Liquid Water. *J. Chem. Phys.* **2011**, *135* (22), 224510.
- (19) Dalleska, N. F.; Honma, K.; Sunderlin, L. S.; Armentrout, P. B. Solvation of Transition Metal Ions by Water. Sequential Binding Energies of M+(H₂O)_X (X = 1–4) for M = Ti to Cu Determined by Collision-Induced Dissociation. *J. Am. Chem. Soc.* **1994**, *116* (8), 3519–3528.
- (20) Magnera, T. F.; David, D. E.; Michl, J. Gas-Phase Water and Hydroxyl Binding Energies for Monopositive First-Row Transition Metal Ions. *J. Am. Chem. Soc.* **1989**, *111* (11), 4100–4101.
- (21) Magnera, T. F.; David, D. E.; Stulik, D.; Orth, R. G.; Jonkman, H. T.; Michl, J. Production of Hydrated Metal Ions by Fast Ion or Atom Beam Sputtering. Collision-Induced Dissociation and Successive Hydration Energies of Gaseous Copper+ with 1–4 Water Molecules. *J. Am. Chem. Soc.* **1989**, *111* (14), 5036–5043.
- (22) Feller, D.; Glendening, E. D.; de Jong, W. A. Structures and Binding Enthalpies of M+(H₂O)_N Clusters, M = Cu, Ag, Au. *J. Chem. Phys.* **1999**, *110* (3), 1475–1491.
- (23) Iino, T.; Ohashi, K.; Mune, Y.; Inokuchi, Y.; Judai, K.; Nishi, N.; Sekiya, H. Infrared Photodissociation Spectra and Solvation Structures of Cu+(H₂O)_N (N = 1–4). *Chem. Phys. Lett.* **2006**, *427* (1–3), 24–28.
- (24) Iino, T.; Ohashi, K.; Inoue, K.; Judai, K.; Nishi, N.; Sekiya, H. Infrared Spectroscopy of Cu+(H₂O)_N and Ag+(H₂O)_N: Coordination and Solvation of Noble-Metal Ions. *J. Chem. Phys.* **2007**, *126* (19), 194302.
- (25) Blumberger, J.; Bernasconi, L.; Tavernelli, I.; Vuilleumier, R.; Sprik, M. Electronic Structure and Solvation of Copper and Silver Ions: A Theoretical Picture of a Model Aqueous Redox Reaction. *J. Am. Chem. Soc.* **2004**, *126* (12), 3928–3938.
- (26) El-Nahas, A. M.; Tajima, N.; Hirao, K. Binding Energies and Electronic Structures of Cu+(Oh₂)_N and Cu+(Nh₃)_N (N = 1–4): Anomaly of the Two Ligand Cu+ Complexes. *J. Mol. Struct.: THEOCHEM* **1999**, *469* (1–3), 201–213.
- (27) Hoyau, S.; Ohanessian, G. Complexation of Small Organic Molecules by Cu+. *Chem. Phys. Lett.* **1997**, *280* (3–4), 266–272.
- (28) Burda, J. V.; Pavelka, M.; Šimánek, M. Theoretical Model of Copper Cu(I)/Cu(II) Hydration. Dft and Ab Initio Quantum Chemical Study. *J. Mol. Struct.: THEOCHEM* **2004**, *683* (1–3), 183–193.
- (29) Bauschlicher, C. W.; Langhoff, S. R.; Partridge, H. The Binding Energies of Cu+(H₂O)_N and Cu+(Nh₃)_N (N = 1–4). *J. Chem. Phys.* **1991**, *94* (3), 2068–2072.
- (30) Rosi, M.; Bauschlicher, C. W. The Binding Energies of One and Two Water Molecules to the First Transition-Row Metal Positive Ions. *J. Chem. Phys.* **1990**, *92* (3), 1876–1878.
- (31) Curtiss, L. A.; Jurgens, R. Nonadditivity of Interaction in Hydrated Copper(1+) and Copper(2+) Clusters. *J. Phys. Chem.* **1990**, *94* (14), 5509–5513.
- (32) Koizumi, A.; Tachikawa, M.; Shiga, M. Quantum Fluctuation and Vibrational Dynamics of Aqueous Cu+ and Ag+ Clusters. *Chem. Phys.* **2013**, *419*, 44–49.
- (33) Song, X.; Zhao, Y.; Zhang, G.; Zhang, P. Theoretical Study on Structures, Binding Energies and Vibrational Spectra of M+(H₂O)₂ar (M = Cu, Ag, Au). *Comput. Theor. Chem.* **2011**, *963* (2–3), 290–293.
- (34) Carnegie, P. D.; McCoy, A. B.; Duncan, M. A. Ir Spectroscopy and Theory of Cu+(H₂O)_{Ar}2 and Cu+(D₂O)_{Ar}2 in the O–H (O–D) Stretching Region: Fundamentals and Combination Bands. *J. Phys. Chem. A* **2009**, *113* (17), 4849–4854.
- (35) Schneider, W. F.; Hass, K. C.; Ramprasad, R.; Adams, J. B. Cluster Models of Cu Binding and Co and No Adsorption in Cu-Exchanged Zeolites. *J. Phys. Chem.* **1996**, *100* (15), 6032–6046.

- (36) Day, P. N.; Jensen, J. H.; Gordon, M. S.; Webb, S. P.; Stevens, W. J.; Krauss, M.; Garmer, D.; Basch, H.; Cohen, D. An Effective Fragment Method for Modeling Solvent Effects in Quantum Mechanical Calculations. *J. Chem. Phys.* **1996**, *105* (5), 1968–1986.
- (37) Petersen, C. P.; Gordon, M. S. Solvation of Sodium Chloride: An Effective Fragment Study of NaCl(H₂O)_N. *J. Phys. Chem. A* **1999**, *103* (21), 4162–4166.
- (38) Gordon, M. S.; Freitag, M. A.; Bandyopadhyay, P.; Jensen, J. H.; Kairys, V.; Stevens, W. J. The Effective Fragment Potential Method: A Qm-Based Mm Approach to Modeling Environmental Effects in Chemistry. *J. Phys. Chem. A* **2001**, *105* (2), 293–307.
- (39) Miller, Y.; Thomas, J. L.; Kemp, D. D.; Finlayson-Pitts, B. J.; Gordon, M. S.; Tobias, D. J.; Gerber, R. B. Structure of Large Nitrate–Water Clusters at Ambient Temperatures: Simulations with Effective Fragment Potentials and Force Fields with Implications for Atmospheric Chemistry. *J. Phys. Chem. A* **2009**, *113* (46), 12805–12814.
- (40) Richard, R. M.; Herbert, J. M. Many-Body Expansion with Overlapping Fragments: Analysis of Two Approaches. *J. Chem. Theory Comput.* **2013**, *9* (3), 1408–1416.
- (41) Richard, R. M.; Lao, K. U.; Herbert, J. M. Aiming for Benchmark Accuracy with the Many-Body Expansion. *Acc. Chem. Res.* **2014**, *47*, 2828.
- (42) Lao, K. U.; Herbert, J. M. Accurate and Efficient Quantum Chemistry Calculations for Noncovalent Interactions in Many-Body Systems: The Xspt Family of Methods. *J. Phys. Chem. A* **2015**, *119* (2), 235–252.
- (43) Matsuda, A.; Mori, H. Theoretical Study on the Hydration Structure of Divalent Radium Ion Using Fragment Molecular Orbital–Molecular Dynamics (Fmo–Md) Simulation. *J. Solution Chem.* **2014**, *43* (9), 1669–1675.
- (44) Pruitt, S. R.; Brorsen, K. R.; Gordon, M. S. Ab Initio Investigation of the Aqueous Solvation of the Nitrate Ion. *Phys. Chem. Chem. Phys.* **2015**, *17* (40), 27027–27034.
- (45) Bajaj, P.; Götz, A. W.; Paesani, F. Toward Chemical Accuracy in the Description of Ion–Water Interactions through Many-Body Representations. I. Halide–Water Dimer Potential Energy Surfaces. *J. Chem. Theory Comput.* **2016**, *12* (6), 2698–2705.
- (46) Riera, M.; Gotz, A. W.; Paesani, F. The I-Tm Model for Ab Initio-Based Ion–Water Interaction Potentials. II. Alkali Metal Ion–Water Potential Energy Functions. *Phys. Chem. Chem. Phys.* **2016**, *18*, 30334–30343.
- (47) Cizek, J. On the Correlation Problem in Atomic and Molecular Systems. Calculation of Wavefunction Components in Ursell-Type Expansion Using Quantum-Field Theoretical Methods. *J. Chem. Phys.* **1966**, *45* (11), 4256–4266.
- (48) Bartlett, R. J.; Musial, M. Coupled-Cluster Theory in Quantum Chemistry. *Rev. Mod. Phys.* **2007**, *79* (1), 291–352.
- (49) Møller, C.; Plesset, M. S. Note on an Approximation Treatment for Many-Electron Systems. *Phys. Rev.* **1934**, *46* (7), 618–622.
- (50) Adamo, C.; Barone, V. Exchange Functionals with Improved Long-Range Behavior and Adiabatic Connection Methods without Adjustable Parameters: The Mpw and Mpw1pw Models. *J. Chem. Phys.* **1998**, *108* (2), 664–675.
- (51) Lynch, B. J.; Fast, P. L.; Harris, M.; Truhlar, D. G. Adiabatic Connection for Kinetics. *J. Phys. Chem. A* **2000**, *104* (21), 4811–4815.
- (52) Becke, A. D. Density-Functional Thermochemistry. Iii. The Role of Exact Exchange. *J. Chem. Phys.* **1993**, *98* (7), 5648–5652.
- (53) Stephens, P. J.; Devlin, F. J.; Chabalowski, C. F.; Frisch, M. J. Ab Initio Calculation of Vibrational Absorption and Circular Dichroism Spectra Using Density Functional Force Fields. *J. Phys. Chem.* **1994**, *98* (45), 11623–11627.
- (54) Yanai, T.; Tew, D. P.; Handy, N. C. A New Hybrid Exchange–Correlation Functional Using the Coulomb-Attenuating Method (Cam-B3lyp). *Chem. Phys. Lett.* **2004**, *393* (1–3), 51–57.
- (55) Gill, P. M. W.; Johnson, B. G.; Pople, J. A. A Standard Grid for Density Functional Calculations. *Chem. Phys. Lett.* **1993**, *209* (5–6), 506–512.
- (56) Hehre, W. J.; Stewart, R. F.; Pople, J. A. Self-Consistent Molecular-Orbital Methods. I. Use of Gaussian Expansions of Slater-Type Atomic Orbitals. *J. Chem. Phys.* **1969**, *51* (6), 2657–2664.
- (57) Hehre, W. J.; Ditchfield, R.; Pople, J. A. Self-Consistent Molecular Orbital Methods. Xii. Further Extensions of Gaussian-Type Basis Sets for Use in Molecular Orbital Studies of Organic Molecules. *J. Chem. Phys.* **1972**, *56* (5), 2257–2261.
- (58) Hariharan, P. C.; Pople, J. A. The Influence of Polarization Functions on Molecular Orbital Hydrogenation Energies. *Theoret. Chim. Acta* **1973**, *28* (3), 213–222.
- (59) Krishnan, R.; Binkley, J. S.; Seeger, R.; Pople, J. A. Self-Consistent Molecular Orbital Methods. Xx. A Basis Set for Correlated Wave Functions. *J. Chem. Phys.* **1980**, *72* (1), 650–654.
- (60) Dunning, T. H. Gaussian Basis Sets for Use in Correlated Molecular Calculations. I. The Atoms Boron through Neon and Hydrogen. *J. Chem. Phys.* **1989**, *90* (2), 1007–1023.
- (61) Kendall, R. A.; Dunning, T. H.; Harrison, R. J. Electron Affinities of the First-Row Atoms Revisited. Systematic Basis Sets and Wave Functions. *J. Chem. Phys.* **1992**, *96* (9), 6796–6806.
- (62) Hay, P. J.; Wadt, W. R. Ab Initio Effective Core Potentials for Molecular Calculations. Potentials for the Transition Metal Atoms Sc to Hg. *J. Chem. Phys.* **1985**, *82* (1), 270–283.
- (63) Roy, L. E.; Hay, P. J.; Martin, R. L. Revised Basis Sets for the Lanl Effective Core Potentials. *J. Chem. Theory Comput.* **2008**, *4* (7), 1029–1031.
- (64) Ehlers, A. W.; Böhme, M.; Dapprich, S.; Gobbi, A.; Höllwarth, A.; Jonas, V.; Köhler, K. F.; Stegmann, R.; Veldkamp, A.; Frenking, G. A Set of F-Polarization Functions for Pseudo-Potential Basis Sets of the Transition Metals Sc, Cu, Y, Ag and La, Au. *Chem. Phys. Lett.* **1993**, *208* (1), 111–114.
- (65) Stevens, W. J.; Basch, H.; Krauss, M. Compact Effective Potentials and Efficient Shared-Exponent Basis Sets for the First- and Second-Row Atoms. *J. Chem. Phys.* **1984**, *81* (12), 6026–6033.
- (66) Bergner, A.; Dolg, M.; Küchle, W.; Stoll, H.; Preuß, H. Ab Initio Energy-Adjusted Pseudopotentials for Elements of Groups 13–17. *Mol. Phys.* **1993**, *80* (6), 1431–1441.
- (67) Shao, Y.; Gan, Z.; Epifanovsky, E.; Gilbert, A. T. B.; Wormit, M.; Kussmann, J.; Lange, A. W.; Behn, A.; Deng, J.; Feng, X.; et al. Advances in Molecular Quantum Chemistry Contained in the Q-Chem 4 Program Package. *Mol. Phys.* **2015**, *113* (2), 184–215.
- (68) Humphrey, W.; Dalke, A.; Schulten, K. Vmd: Visual Molecular Dynamics. *J. Mol. Graphics* **1996**, *14* (1), 33–38.
- (69) Wales, D. J.; Doye, J. P. K. Global Optimization by Basin-Hopping and the Lowest Energy Structures of Lennard-Jones Clusters Containing up to 110 Atoms. *J. Phys. Chem. A* **1997**, *101* (28), 5111–5116.
- (70) Metropolis, N.; Ulam, S. The Monte Carlo Method. *J. Am. Stat. Assoc.* **1949**, *44* (247), 335–341.
- (71) Cobar, E. A.; Khaliullin, R. Z.; Bergman, R. G.; Head-Gordon, M. Theoretical Study of the Rhenium–Alkane Interaction in Transition Metal–Alkane Σ -Complexes. *Proc. Natl. Acad. Sci. U. S. A.* **2007**, *104* (17), 6963–6968.
- (72) Khaliullin, R. Z.; Cobar, E. A.; Lochan, R. C.; Bell, A. T.; Head-Gordon, M. Unravelling the Origin of Intermolecular Interactions Using Absolutely Localized Molecular Orbitals. *J. Phys. Chem. A* **2007**, *111* (36), 8753–8765.
- (73) Khaliullin, R. Z.; Bell, A. T.; Head-Gordon, M. Analysis of Charge Transfer Effects in Molecular Complexes Based on Absolutely Localized Molecular Orbitals. *J. Chem. Phys.* **2008**, *128* (18), 184112.
- (74) Lochan, R. C.; Khaliullin, R. Z.; Head-Gordon, M. Interaction of Molecular Hydrogen with Open Transition Metal Centers for Enhanced Binding in Metal–Organic Frameworks: A Computational Study. *Inorg. Chem.* **2008**, *47* (10), 4032–4044.
- (75) Becke, A. D. Density-Functional Exchange-Energy Approximation with Correct Asymptotic Behavior. *Phys. Rev. A: At, Mol, Opt. Phys.* **1988**, *38* (6), 3098–3100.
- (76) Lee, C.; Yang, W.; Parr, R. G. Development of the Colle-Salvetti Correlation-Energy Formula into a Functional of the Electron Density. *Phys. Rev. B: Condens. Matter Mater. Phys.* **1988**, *37* (2), 785–789.

- (77) Ke, H.; van der Linde, C.; Lisy, J. M. Insights into Gas-Phase Structural Conformers of Hydrated Rubidium and Cesium Cations, $M+(H_2O)_N$ ($M = Rb, Cs; N = 3-5$), Using Infrared Photodissociation Spectroscopy. *J. Phys. Chem. A* **2014**, *118* (8), 1363–1373.
- (78) Bandyopadhyay, B.; Reishus, K. N.; Duncan, M. A. Infrared Spectroscopy of Solvation in Small $Zn+(H_2O)_N$ Complexes. *J. Phys. Chem. A* **2013**, *117* (33), 7794–7803.
- (79) Rodriguez, O.; Lisy, J. M. Revisiting $Li+(H_2O)_3-4$ Clusters: Evidence of High-Energy Conformers from Infrared Spectra. *J. Phys. Chem. Lett.* **2011**, *2* (12), 1444–1448.
- (80) Feller, D.; Glendening, E. D.; Kendall, R. A.; Peterson, K. A. An Extended Basis Set Abinitio Study of $Li+(H_2O)_N$, $N = 1-6$. *J. Chem. Phys.* **1994**, *100* (7), 4981–4997.
- (81) Relph, R. A.; Guasco, T. L.; Elliott, B. M.; Kamrath, M. Z.; McCoy, A. B.; Steele, R. P.; Schofield, D. P.; Jordan, K. D.; Viggiano, A. A.; Ferguson, E. E.; et al. How the Shape of an H-Bonded Network Controls Proton-Coupled Water Activation in H₂O⁺ Formation. *Science* **2010**, *327* (5963), 308–312.
- (82) Li, J.-W.; Morita, M.; Takahashi, K.; Kuo, J.-L. Features in Vibrational Spectra Induced by Ar-Tagging for $H_3O^+Ar_m$, $m = 0-3$. *J. Phys. Chem. A* **2015**, *119* (44), 10887–10892.
- (83) Posey, L. A.; Johnson, M. A. Photochemistry of Hydrated Electron Clusters $(H_2O)_-N$ ($15 \leq N \leq 40$) at 1064 Nm: Size Dependent Competition between Photofragmentation and Photodetachment. *J. Chem. Phys.* **1988**, *89* (8), 4807–4814.
- (84) Kamrath, M. Z.; Garand, E.; Jordan, P. A.; Leavitt, C. M.; Wolk, A. B.; Van Stipdonk, M. J.; Miller, S. J.; Johnson, M. A. Vibrational Characterization of Simple Peptides Using Cryogenic Infrared Photodissociation of H₂-Tagged, Mass-Selected Ions. *J. Am. Chem. Soc.* **2011**, *133* (16), 6440–6448.
- (85) Shannon, R. Revised Effective Ionic Radii and Systematic Studies of Interatomic Distances in Halides and Chalcogenides. *Acta Crystallogr., Sect. A: Cryst. Phys., Diffraction, Theor. Gen. Crystallogr.* **1976**, *32* (5), 751–767.
- (86) Marsh, B. M.; Voss, J. M.; Zhou, J.; Garand, E. Coordination Structure and Charge Transfer in Microsolvated Transition Metal Hydroxide Clusters $[M(OH)]+(H_2O)_1-4$. *Phys. Chem. Chem. Phys.* **2015**, *17* (35), 23195–23206.
- (87) Sweeney, A. F.; O'Brien, J. T.; Williams, E. R.; Armentrout, P. B. Structural Elucidation of Hydrated $CuOH^+$ Complexes Using Ion Action Spectroscopy and Theoretical Modeling. *Int. J. Mass Spectrom.* **2015**, *378*, 270–280.
- (88) Sweeney, A. F.; Armentrout, P. B. Guided Ion Beam Studies of the Collision-Induced Dissociation of $CuOH+(H_2O)_N$ ($N = 1-4$): Comprehensive Thermodynamic Data for Copper Ion Hydration. *J. Phys. Chem. A* **2014**, *118* (44), 10210–10222.
- (89) Marsh, B. M.; Zhou, J.; Garand, E. Vibrational Spectroscopy of Small Hydrated $CuOH^+$ Clusters. *J. Phys. Chem. A* **2014**, *118* (11), 2063–2071.
- (90) Armentrout, P.; Sweeney, A. Hydrated Copper Ion Chemistry: Guided Ion Beam and Computational Investigation of $Cu_2+(H_2O)_N$ ($N = 7-10$) Complexes. *Eur. Mass Spectrom.* **2015**, *21* (3), 497–516.
- (91) Stace, A. J.; Walker, N. R.; Firth, S. $[Cu-(H_2O)_N]^{2+}$ Clusters: The First Evidence of Aqueous $Cu(I)$ in the Gas Phase. *J. Am. Chem. Soc.* **1997**, *119* (42), 10239–10240.

CHAPTER 5

ACCELERATING *AB INITIO* MOLECULAR DYNAMICS SIMULATIONS BY LINEAR PREDICTION METHODS

Reprinted from Herr, J. D.; Steele, R. P. Accelerating *Ab Initio* Molecular Dynamics Simulations by Linear Prediction Methods. *Chem. Phys. Lett.* **2016**, *661*, 42-47, Copyright (2016), with permission from Elsevier.



Contents lists available at ScienceDirect

Chemical Physics Letters

journal homepage: www.elsevier.com/locate/cplett

Editor's choice

Accelerating *ab initio* molecular dynamics simulations by linear prediction methods

Jonathan D. Herr, Ryan P. Steele*

Department of Chemistry, University of Utah, 315 South 1400 East, Salt Lake City, UT 84112, United States
 Henry Eyring Center for Theoretical Chemistry, University of Utah, 315 South 1400 East, Salt Lake City, UT 84112, United States

ARTICLE INFO

Article history:
 Received 31 July 2016
 In final form 19 August 2016
 Available online 21 August 2016

Keywords:
Ab initio molecular dynamics
 Fock extrapolation
 Linear prediction

ABSTRACT

Acceleration of *ab initio* molecular dynamics (AIMD) simulations can be reliably achieved by extrapolation of electronic data from previous timesteps. Existing techniques utilize polynomial least-squares regression to fit previous steps' Fock or density matrix elements. In this work, the recursive Burg 'linear prediction' technique is shown to be a viable alternative to polynomial regression, and the extrapolation-predicted Fock matrix elements were three orders of magnitude closer to converged elements. Accelerations of 1.8–3.4 \times were observed in test systems, and in all cases, linear prediction outperformed polynomial extrapolation. Importantly, these accelerations were achieved without reducing the MD integration timestep.

© 2016 Elsevier B.V. All rights reserved.

1. Introduction

Ab initio molecular dynamics (AIMD) simulation techniques employ 'on-the-fly' generation of quantum chemistry molecular forces to propagate classical molecular dynamics trajectories on the Born-Oppenheimer potential energy surface. The ability to accurately capture strong polarization, charge transfer, and bond-breaking/-making events motivates the use of such techniques in chemical simulations of real-time dynamics, equilibrium sampling, and spectroscopic response. However, the many-orders-of-magnitude cost increase of AIMD, relative to commonly used molecular mechanics force fields, makes such simulations a daunting computational challenge for complex molecular systems.

Density-functional theory [1] (DFT) is the most commonly used quantum chemistry method for large AIMD simulations, although Møller-Plesset perturbation theory [2] (MP2)-based simulations have also been performed. For Kohn-Sham DFT or the underlying Hartree-Fock (HF) calculation for MP2, a non-linear, self-consistent field (SCF) optimization procedure is solved iteratively [3], leading to an overall computational prefactor that is determined by the number of SCF cycles required for convergence to a chosen tolerance. Although advanced integral evaluation techniques [4,5] tackle the scaling of these simulations with respect to the size of the system, motivation remains to reduce the SCF-based

prefactor, particularly for molecular systems that are large, open-shell, and/or undergoing bond-rearrangement events.

The small timesteps required for AIMD trajectories (≤ 0.5 fs for hydrogen-containing systems) suggest that the bulk of the electronic structure has not appreciably changed between neighboring timesteps. Restarting the SCF procedure anew from a typically poor initial guess, therefore, would appear to be computationally wasteful. This notion has motivated two diverging routes to accelerating MD simulations.

One option is the *propagation* of electronic information to the next timestep. Extended-Lagrangian MD (ELMD) methods [6–8] accelerate—or altogether avoid—the SCF procedure by propagating Fock or density matrix information. Fidelity with the true Born-Oppenheimer surface is approximated through the extended-Lagrangian formalism. One often-cited advantage of this approach is the rigorous enforcement of total energy conservation. Tradeoffs include the need for typically smaller MD timesteps (thereby reducing the effectiveness of the computational acceleration), choice of a fictitious mass, and the potential for electronic 'lag' artifacts [8–10] that can appear in observables, such as vibrational spectra. More recent implementations [11–16] successfully bridge the ELMD-BOMD divide, although stable propagation of the electronic variables for reactive systems remains an area of active research. One of the clear advantages to time-reversibly propagating electronic information has been the demonstration by Niklasson that the SCF procedure does not need to be converged tightly—sometimes requiring only a single SCF step [13,15]—in order to produce energy-conserving trajectories.

* Corresponding author.
 E-mail address: ryan.steele@utah.edu (R.P. Steele).

The second option involves *extrapolation* of electronic information from previous timesteps. Motivated by the observation that Fock matrix elements, for example, are simple oscillatory functions of time, these approaches attempt to fit previous timesteps' information to a simple form that can be used as an improved initial guess for the SCF procedure [17–20]. This approach allows for longer timesteps while still reducing the number of requisite SCF cycles. In its simplest version, this approach uses the converged Fock matrix from the previous timestep as this initial guess, which is consistent with the intuitive notion that the electronic structure has not changed appreciably. However, as has been noted in previous analyses [18], such a choice quickly fails when loose SCF convergence settings are employed. The use of the previous step's Fock matrix introduces a hysteresis effect that leads to rather severe non-conservation of the energy. Over only short trajectories, the energy drift swamps the inherent energy fluctuations of the chosen integration scheme. While higher-order polynomials somewhat dampen this energy-conservation concern, its effects should eventually be borne out in long MD trajectories since the history-dependent guess renders the propagator formally non-symplectic. The practical cure to this pathology, of course, is to more tightly converge the SCF procedure. As will be shown below, this approach rectifies energy-drift concerns for very long trajectories (by AIMD standards), but it also necessarily leads to additional computational cost overhead.

The single SCF cycle performed in the 'propagation' approach could potentially lead to unstable electronic states for slow-to-converge SCF cases, such as open-shell ions or systems near bond-arrangement events, and these cases require additional testing in the literature. Because of our interest in these difficult systems [21], the present analysis focuses solely on the 'extrapolation' approach, with the intent of improving existing acceleration techniques within tight SCF convergence settings. An investigation into whether the behavior observed in the present analysis can be combined with rigorously time-reversible propagators is reserved for future studies.

Existing Fock extrapolation techniques employ a polynomial least-squares regression (PLSR) of N previous timesteps' information, to a polynomial of a chosen order O . A recent analysis [22] has shown that an optimal N may exist, at least for a given timestep and chemical system, although no assessment of O -dependence was performed. Nonetheless, past studies have shown that with only a handful of previous steps' data, roughly 2-fold reductions in the number of Fock builds can be achieved. Extension to MP2 simulations, in both the SCF and gradient response terms, has also been demonstrated [23].

While this standard PLSR approach is appropriate for accurately fitting the data within the chosen time window, it is decidedly *not* optimal for extrapolating information outside of this window. Given that the Fock data throughout an MD trajectory is locally oscillatory (with some slight noise, stemming from incomplete convergence) and globally stochastic, techniques that are well-suited to signal prediction were conjectured to be a better choice. In particular, so-called *linear prediction* techniques—not to be confused with linear PLSR extrapolation ($O = 1$)—are designed to accurately represent exactly this type of behavior. This study presents an implementation of the Burg Linear Prediction (BLP) algorithm for Fock extrapolation, as well as rigorous tests of its efficacy and efficiency for accelerating AIMD simulations.

2. Methods

The basic components of the BLP algorithm are presented in this section, including a discussion of the distinguishing features of the BLP and PLSR approaches. This presentation is followed by a

description of the techniques used to assess the methods throughout the remainder of the study.

2.1. Burg Linear Prediction

The BLP algorithm [24,25], in an extrapolated AIMD context, fits N previous timesteps' atomic-orbital (AO) basis Fock matrix elements to a *recursive series* with L coefficients forward [f] in time:

$$\tilde{F}_{\mu\nu}^{[f]}(t) = \sum_{i=1}^L c_i F_{\mu\nu}(t-i) \quad (1)$$

The Burg algorithm augments this simpler Levinson-Durbin recursion definition by also considering a fit to backward [b] predictions:

$$\tilde{F}_{\mu\nu}^{[b]}(t) = \sum_{i=1}^L c_i F_{\mu\nu}(t+i) \quad (2)$$

In this notation, the predicted element is denoted as \tilde{F} , and t acts as a timestep index, rather than a physical simulation time. In all analyses performed in this work, the timesteps were evenly spaced, although the LPB prescription is not restricted to this form. The coefficients are obtained using linear least-squares minimization of the *sum* of the forward and backward mean-square deviations, χ^2 , defined over the fitting length N as

$$\begin{aligned} \chi_{\mu\nu}^{2[f]} &= \sum_{t=L}^N [F_{\mu\nu}(t) - \tilde{F}_{\mu\nu}^{[f]}(t)]^2 \\ &= \sum_{t=L}^N \left[F_{\mu\nu}(t) - \left(\sum_{i=1}^L c_i F_{\mu\nu}(t-i) \right) \right]^2 \end{aligned} \quad (3)$$

$$\begin{aligned} \chi_{\mu\nu}^{2[b]} &= \sum_{t=L}^N [F_{\mu\nu}(t) - \tilde{F}_{\mu\nu}^{[b]}(t)]^2 \\ &= \sum_{t=L}^N \left[F_{\mu\nu}(t) - \left(\sum_{i=1}^L c_i F_{\mu\nu}(t+i) \right) \right]^2 \end{aligned} \quad (4)$$

This optimization of $\chi^2 = \chi^{2[f]} + \chi^{2[b]}$, rather than $\chi^{2[f]}$ alone, distinguishes BLP from simpler recursion approaches and introduces considerable stability to the method. Further algorithmic details can be found in standard numerical texts, including the one used in the present implementation [24].

The BLP algorithm, therefore, generates a weighted linear combination of existing Fock matrix elements. In this sense, it is superficially similar to a PLSR fit,

$$\tilde{F}_{\mu\nu}^{[f]}(t) = \sum_{i=0}^O c_i \cdot t^i \quad (5)$$

However, as will be shown below, the BLP algorithm was found to be much more powerful for extrapolation purposes. For sums of Fourier signals, for example, preliminary tests of this approach yielded nearly quantitative reproduction of the signal for thousands of extrapolated signal cycles, rather than the 1–2 that was afforded with PLSR. Of course, in an AIMD context, the fit will be recomputed at each timestep, meaning that the algorithm only needs to be accurate to the next timestep. Even in this regime, though, the BLP approach led to several-orders-of-magnitude reductions in error for values of this subsequent step.

The use of PLSR requires a choice of N and O , compactly notated in the remainder of this work as (N, O) extrapolation. Commonly used choices in previous studies [17,18] included (4,2) to (20,10) extrapolations. Since this approach is intended as an extrapolation, rather than a fit, increases in N or O do not necessarily yield better SCF guesses, and the optimal choice is often simulation-specific

[22]. For BLP, analogous choices must be made, and the notation will similarly be defined as an (N,L) extrapolation. In practice, fits to a larger number of data points N (10–100) were required in BLP than in PLSR, but the subsequent extrapolation behavior was also much less sensitive to these parameters, as will be shown below. For atom-centered basis sets, no appreciable overhead is incurred by either approach, compared to the overwhelming cost of computing *ab initio* energies and forces.

2.2. Numerical analyses

The guiding question to be addressed in this analysis was whether the BLP algorithm led to any appreciable reduction in the requisite number of SCF cycles for AIMD simulations. Micro-canonical AIMD simulations were mainly performed on two hydrogen-containing test systems, in order to address this issue. Small systems were selected in order to enable testing of the long-time energy conservation properties of these trajectories. A single water molecule, H_2O , represented the regime in which the SCF was already reasonably simple to converge. The lack of a large density of low-frequency vibrational modes actually made this case challenging for extrapolation techniques, however. The water dimer cation, $(\text{H}_2\text{O})_2^+$ (more accurately described as $\text{H}_3\text{O}^+ \cdots \text{OH}^+$), represented the difficult-to-converge regime. Past experience with this open-shell ion highlighted the challenge in converging its SCF—often requiring 20–50 cycles for even this small complex—and its use here serves as a small-molecule model of challenges encountered in larger systems. Subsequently, the larger diglycine molecule, $\text{C}_4\text{N}_2\text{O}_3\text{H}_8$, was examined, in order to ensure that results were not specific to these small water complexes. For testing purposes, most of the simulations employed the HF method with the 6-31G(d,p) basis set [26,27], although the conclusions are likely invariant to this choice. The dipeptide was tested with B3LYP-D [28–30]/cc-pVTZ [31]. All computations were performed in a development version of the Q-Chem 4.3 quantum chemistry software package [32].

Several auxiliary factors influence the cost and stability of extrapolated AIMD trajectories, including the extrapolation parameters, the MD integration timestep, and the degree of SCF convergence. Tests that varied parameters along all three of these axes were performed on the two small test complexes:

- (1) The influence of the number of BLP points (N) was examined by holding the number of coefficients (L) constant at 10 while increasing the number of points from 11 to 100, by multiples of 10. The L dependence was subsequently examined by holding the number of points constant at 100 and increasing the number of coefficients from 10 to 99, also by multiples of ten.
- (2) The behavior of the extrapolation schemes was also examined as a function of MD integration timestep, Δt . Two timesteps—10 a.u. (0.242 fs) and 20 a.u. (0.484 fs)—were examined in this analysis, which will hereafter be referred to as Δt_a and Δt_b , respectively. The Velocity Verlet integrator was used in all tests.
- (3) Dependence on the SCF convergence criterion was performed with a (100,30) BLP extrapolation using SCF convergence settings of $\{10^{-4}, 10^{-6}, 10^{-8}, 10^{-10}\}$ a.u. In these analyses, the convergence criterion was defined as either the RMS value of the DIIS [33,34] error vector or the maximum value of the energy-weighted GDM [35] orbital gradient, depending on the convergence algorithm employed.

The main metric of interest was the trajectory-averaged number of SCF cycles. In all cases, statistics were only generated after

the extrapolation period began. Also examined were the RMS total relative energy fluctuations, defined in this work as

$$\Delta = \log_{10} \left[\frac{\langle (E(t_i) - E(t_0))^2 \rangle^{1/2}}{E(t_0)} \right] \quad (6)$$

where the average was computed over the entire trajectory. In order to assess any energy non-conservation (drift), the energy fluctuations were also fit to a line, and the corrected fluctuations, Δ^{corr} , with this linear fit subtracted were also computed analogously to Eq. (6).

Comparison to non-extrapolated trajectories, with the same settings, was performed throughout. Initial conditions included equilibrium structures and momenta selected from a Maxwell-Boltzmann distribution at 300 K. Once selected, these initial conditions were fixed for all NVE trajectories in a given analysis, in order to provide an even-handed comparison of methods. The SCF-step analysis was performed on 5-ps trajectories (roughly 10,000–20,000 MD steps), and trajectory stability analyses were performed on 45-ps trajectories. In all cases, an integral drop tolerance [36,37] of 10^{-12} a.u. was employed.

3. Results

3.1. A demonstrative example

Before presenting statistical averages across the suite of tests, an explicit example was chosen to highlight the utility of the BLP approach. Using H_2O with Δt_b (20 a.u.), a selected single Fock matrix element was examined. This element was chosen as one that oscillated significantly on the O–H stretch timescale, although extrapolation behavior for all elements was found to be similar. Fig. 1(a) shows the computed value of this element across a 5000-step trajectory. A 100-step section of this trajectory is shown in Fig. 1(b), where the value of the extrapolated-guess Fock elements for BLP (100,30) and PLSR (16,8) methods are also shown. Visually, the difference between the two methods can be seen in panel (b). The BLP guess tightly followed the converged Fock result, whereas the PLSR showed more scatter about the converged value. To better quantify this difference, the deviation between the extrapolated guess and the converged Fock matrix element is shown in Fig. 1(c), across the trajectory (after extrapolation began). The BLP approach yielded guess values that were more than three orders of magnitude closer to the converged value, which suggested that this approach should lead to improved SCF performance.

3.2. Linear prediction parameters and timestep analysis

The results of the various (N,L) parameter sets for both small test systems are listed in Tables 1 and 2. The overall results in Table 1 indicate that BLP extrapolation provided appreciable reductions in the average number of SCF cycles. Including more previous data points in the extrapolation, when using $L = 10$ coefficients, generally increased the effectiveness of the extrapolation, although the results became essentially saturated near 50 points. At this setting, average SCF accelerations ranged from $1.8 \times (\text{H}_2\text{O}, \Delta t = 0.484 \text{ fs})$ to $3.2 \times ((\text{H}_2\text{O})_2^+, \Delta t = 0.242 \text{ fs})$. The extrapolation was, not surprisingly, less effective at the longer timestep, but cost reductions were still appreciable at this most aggressive integration setting. The cost reductions were considerably more impressive in the tough-to-converge water dimer cation case.

The results in Table 2 show that the coefficient dependence of BLP extrapolation, when the number of points is held fixed ($N = 100$), is rather small. Although each test exhibited an optimum

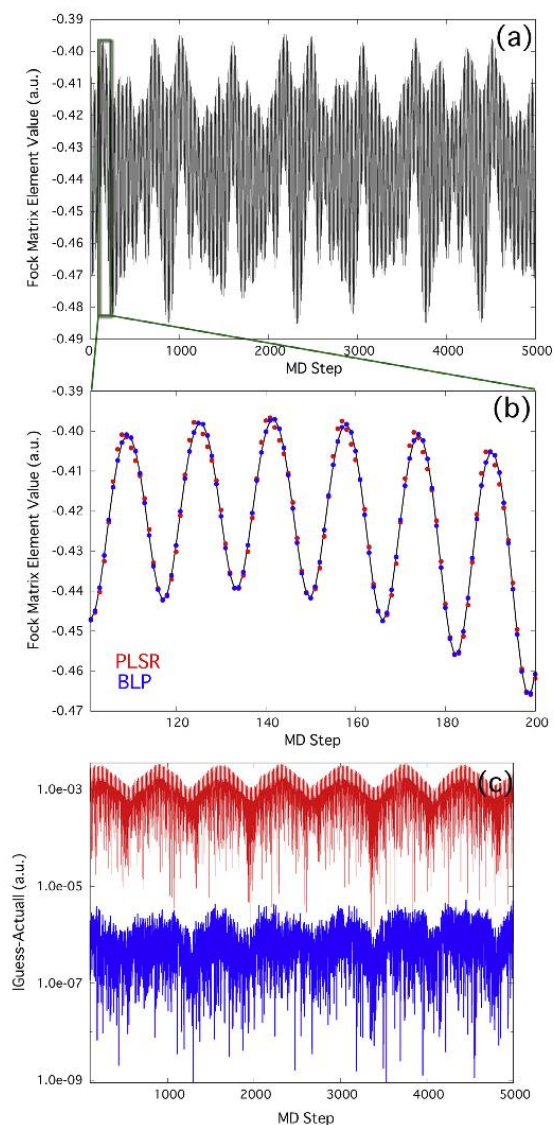


Fig. 1. Explicit Fock matrix element behavior for H_2O with $\Delta t = 20$ a.u. (a) Single Fock matrix element value across the trajectory. (b) 100-step close-up of converged Fock element, as well as PLSR (red) and BLP (blue) extrapolated guess Fock element values. (c) Absolute deviation between extrapolated guess values and converged values. Colors are consistent with (b). (For interpretation of the references to color in this figure legend, the reader is referred to the web version of this article.)

value of this parameter, the fluctuations in average SCF cycles as a function of this parameter were negligible compared to the magnitude of the overall reduction. This result, combined with the saturation shown in Table 1, was particularly encouraging since the acceleration appeared to be much less sensitive to the choice of extrapolation parameters than PLSR methods. For example, a (4,2) PLSR extrapolation for $(\text{H}_2\text{O})_2^+$ at $\Delta t = 10$ a.u. (0.242 fs) required an average of 18.18 SCF cycles. An alternative (16,8)

Table 1

SCF cycles, averaged over 5-ps AIMD trajectories with HF/6-31G(d,p). Shown are results with and without BLP extrapolation. Results for two integration timesteps are listed: $\Delta t_a = 0.242$ fs, $\Delta t_b = 0.484$ fs. SCF convergence was set to 10^{-8} a.u.

Extrapolation parameters		Average SCF cycles			
Points	Coefficients	H_2O		$(\text{H}_2\text{O})_2^+$	
		Δt_a	Δt_b	Δt_a	Δt_b
11	10	8.87	10.10	16.87	18.78
20	10	7.08	8.97	13.73	16.34
30	10	5.79	8.68	12.09	15.09
40	10	5.33	8.50	11.28	14.69
50	10	5.20	8.43	10.74	14.35
60	10	5.16	8.42	10.54	14.41
70	10	5.11	8.42	10.69	14.44
80	10	5.12	8.42	10.25	14.44
90	10	5.12	8.41	10.29	14.37
100	10	5.12	8.42	10.20	14.36
(No Extrapolation)		14.77	14.76	34.81	35.00

Table 2

SCF cycles, averaged over 5-ps AIMD trajectories with HF/6-31G(d,p). Shown are results with and without BLP extrapolation. Results for two integration timesteps are listed: $\Delta t_a = 0.242$ fs, $\Delta t_b = 0.484$ fs. SCF convergence was set to 10^{-8} a.u.

Extrapolation parameters		Average SCF cycles			
Points	Coefficients	H_2O		$(\text{H}_2\text{O})_2^+$	
		Δt_a	Δt_b	Δt_a	Δt_b
100	10	5.12	8.42	10.20	14.36
100	20	4.80	7.99	9.79	14.06
100	30	4.76	7.94	9.57	13.94
100	40	4.75	7.89	9.69	13.78
100	50	4.78	7.84	9.81	14.12
100	60	4.81	7.85	9.92	14.36
100	70	4.84	7.87	9.84	14.42
100	80	4.85	7.91	9.87	14.17
100	90	4.87	7.93	10.05	14.41
100	99	4.88	7.95	10.17	14.20
(No Extrapolation)		14.77	14.76	34.81	35.00

Table 3

SCF cycles, averaged over 5-ps AIMD trajectories with HF/6-31G(d,p). Shown are results with and without PLSR/BLP extrapolation for several SCF convergence criteria ($\text{Conv} = 10^{-n}$). Results for two integration timesteps are listed: $\Delta t_a = 0.242$ fs, $\Delta t_b = 0.484$ fs. The BLP results employed a (100,30) extrapolation throughout; the PLSR results used the optimal extrapolation, among (20,10), (16,8), (12,6), (8,4), and (4,2) extrapolation options, as a 'best case' comparison for each system.

System	Method	Average SCF cycles			
		Conv = 4	6	8	10
H_2O Δt_a	BLP	1.78	3.01	4.76	6.61
	PLSR	3.18	4.46	7.52	10.78
	None	9.00	11.80	14.77	17.70
H_2O Δt_b	BLP	2.46	4.93	7.84	11.13
	PLSR	4.53	7.56	10.82	14.23
	None	9.00	11.80	14.76	17.70
$(\text{H}_2\text{O})_2^+$ Δt_a	BLP	2.89	6.26	9.57	13.57
	PLSR	9.25	9.70	11.39	17.45
	None	24.75	30.58	34.81	42.17
$(\text{H}_2\text{O})_2^+$ Δt_b	BLP	4.79	9.02	13.78	18.01
	PLSR	10.01	12.21	18.10	22.91
	None	24.51	30.39	35.00	42.67

extrapolation improved this result to only 11.39 cycles. However, further increasing the order to a (20,10) extrapolation yielded 16.11 cycles. Therefore, once beyond low-order extrapolations, the BLP approach appeared to be sufficiently resilient to choice of parameters, and a roughly (100,30) extrapolation is recommended, based on this data.

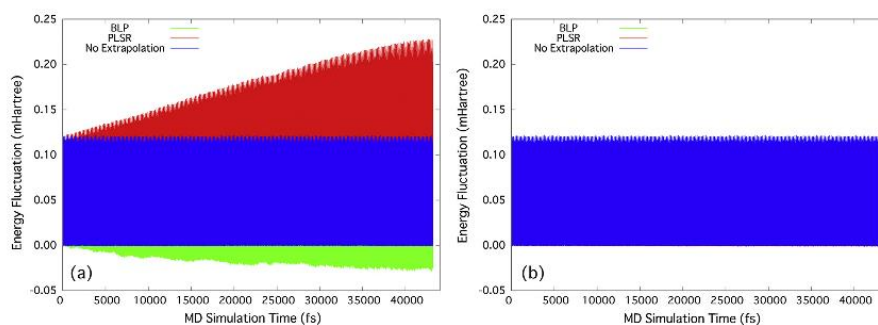


Fig. 2. Energy drift analysis for H₂O with $\Delta t = 20$ a.u. Shown are results for extrapolation-free trajectories (blue), BLP extrapolation (green), and PLSR (red). (a) Energy fluctuations with an SCF (DIIS) convergence of 10^{-5} a.u. In this panel, the extrapolated values drift, with roughly constant fluctuation magnitude relative to this drift (data behind the no-extrapolation results). (b) Energy fluctuations with an SCF convergence of 10^{-8} a.u. All data were nearly identical and overlap in this panel. (For interpretation of the references to color in this figure legend, the reader is referred to the web version of this article.)

Table 4

SCF cycles, averaged over 5-ps AIMD trajectories with HF/6-31G(d,p), $\Delta t = 20$ a.u., and SCF convergence of 10^{-8} a.u. Shown are results with and without PLSR/BLP extrapolation for canonical (NVT) and microcanonical (NVE) simulations. The former used a white-noise, Langevin thermostat. The BLP results employed a (100,30) extrapolation throughout; the PLSR results used the optimal extrapolation, among (20,10), (16,8), (12,6), (8,4), and (4,2) extrapolation options, as a 'best case' comparison for each system.

System	Method	Average SCF cycles	
		NVE	NVT
H ₂ O	BLP	7.84	10.36
	PLSR	10.82	10.86
	None	14.76	14.83
(H ₂ O) ₂ ⁺	BLP	13.78	21.07
	PLSR	18.10	21.34
	None	35.00	30.39

3.3. SCF convergence analysis

The number of requisite SCF cycles is naturally tied to the degree of convergence in AIMD simulations. The performance of Fock extrapolation techniques was analyzed at several convergence settings. Using a fixed (100,30) BLP extrapolation, the number of SCF cycles was shown to increase with convergence setting, as expected; results are shown in Table 3. In all cases, however, the BLP approach provided significant acceleration over both extrapolation-free trajectories, as well as PLSR. For the latter method, a crude optimization of the extrapolation order O (with N fixed at $2 \cdot O$) was performed, and the results shown in Table 3 represent the best-performing PLSR setting. Complete data tables can be found in the Supporting Information. The difference between the two extrapolation techniques was more pronounced at shorter timesteps, but BLP still provided non-negligible savings over PLSR at the longer of the two timesteps.

3.4. Energy conservation analysis

As mentioned in Section 1, any extrapolation of previous timestep data formally breaks time-reversibility in AIMD simulations. This behavior is clearly evident in the plot of energy fluctuations shown in Fig. 2(a), for which the SCF convergence setting (DIIS) was set to 10^{-5} a.u. and $\Delta t_b = 20$ a.u. Without extrapolation, the BOMD trajectory exhibited long-term stability. Energy fluctuations, on the order of 0.1 milliHartree, were exhibited, but no observable drift in the energy was found. Conversely, both PLSR and BLP exhibited drifts. By the end of the 45-ps trajectory, the

drift in the PLSR trajectory had surpassed the inherent fluctuations stemming from the velocity Verlet integrator. The drift in the BLP results was smaller but clearly still present.

Encouragingly, measurable drifts in all methods were removed with the SCF convergence tightened to 10^{-8} . In Fig. 2(b), all three methods overlapped, exhibiting equal energy fluctuation magnitudes ($\Delta = -4.058$, see Eq. (6)). The average slope of all three methods was $<10^{-11}$ Hartree/step, which was within the bounds of endpoint effects in the linear fit for this trajectory length. Therefore, tight SCF convergence can practically remove any energy-conservation concerns, even for relatively long trajectories. Of course, this tight tolerance also increases the number of SCF cycles. As was demonstrated in Table 3, BLP speedups are still appreciable in this tight convergence window. In particular, the required number of BLP SCF cycles was always lower at a convergence setting of 10^{-8} than for non-extrapolated trajectories at a setting of 10^{-4} .

3.5. Canonical sampling

One additional usage of AIMD is for the purpose of sampling thermal equilibrium ensembles. To our knowledge, no explicit analysis of the efficacy of extrapolation methods in this context was available in the literature. Therefore, the above tests were repeated in the NVT ensemble, using a white-noise Langevin thermostat (time constant = 100 fs). The average number of SCF cycles from these trajectories is compared in Table 4. For H₂O (Δt_b), the BLP extrapolation is less effective in this regime; the stochastic 'kicks' imparted by the thermostat increase the number of SCF cycles from 7.8 to 10.4 (14.8 without extrapolation). Similar trends were observed for (H₂O)₂⁺. These tests represent a worst-case scenario because the velocity alterations imparted by this very tightly coupled thermostat most strongly affect small systems. In larger systems, where energy can more easily redistribute naturally and where looser thermostat coupling can be employed, SCF behavior closer to the microcanonical result is anticipated.

3.6. Larger test system

The larger diglycine test system was also examined, using a B3LYP-D/cc-pVTZ potential. With an MD integration timestep of $\Delta t = 15$ a.u., a non-extrapolated BOMD trajectory required an average of 15.0 SCF cycles for convergence to 10^{-8} a.u. The PLSR extrapolation reduced this cost to an average of 6.9 cycles, whereas the BLP further reduced the cost to 5.0 cycles. Therefore, both approaches provided significant acceleration in this larger system, and BLP once again outperformed the PLSR approach. The fact that

BLP is also appropriate for DFT-based potentials and with large basis sets is particularly encouraging, given that promising new density functionals (particularly those with non-local components) often require large basis sets [38].

4. Conclusions

This study has presented an implementation of the Burg Linear Prediction algorithm for the purpose of enhancing Fock-extrapolated AIMD simulations. The BLP algorithm fits a recursive series to previous timesteps' Fock matrix data and is tailor-made for extrapolating (slightly noisy) oscillatory signals. This new approach was shown to be superior to existing polynomial least-squares regression techniques, in terms of reducing the number of requisite SCF cycles during AIMD trajectories. Like any extrapolation method, it still formally breaks time-reversal symmetry. However, this new method provides a route to accelerating tightly converged SCF-based dynamics, and tests of long trajectories showed no appreciable energy drift. Furthermore, the results were notably less sensitive to the choice of extrapolation parameters, which should make this new approach a reliable alternative across disparate chemical systems.

The BLP extrapolation typically uses more of the previous timesteps' data, which means that the extrapolation 'warmup' period is longer. For long trajectories, this difference is negligible. For shorter trajectories, the relative insensitivity of the method to extrapolation parameters suggests that the extrapolation could, in principle, actually begin after only a few steps (similar to polynomial extrapolation), and the traveling extrapolation window could be augmented until the full window is filled. This approach would also allow for on-the-fly saturation tests, in order to automatically determine this optimal window size.

Implementation of the BLP method in quantum chemistry programs is actually very similar to machinery used for polynomial regression, and our present implementation recycled much of the existing code. Based on the above results and this simple implementation, we expect that linear prediction-based extrapolation could become a direct replacement in existing AIMD codes.

Acknowledgements

This material is based on work supported by the United States National Science Foundation CAREER under CHE-1452596. The support and resources from the Center for High-Performance Computing at the University of Utah are gratefully acknowledged. This work also used the Extreme Science and Engineering Discovery Environment (XSEDE), which is supported by the National Science Foundation Grant Number ACI-1053575.

Appendix A. Supplementary material

Supplementary data associated with this article can be found, in the online version, at <http://dx.doi.org/10.1016/j.cplett.2016.08.050>.

References

- [1] D.S. Sholl, J.A. Steckel, *Density Functional Theory: A Practical Introduction*, Wiley-Interscience, 2009.

- [2] C. Møller, M.S. Plesset, *Phys. Rev.* 46 (1934) 618.
 [3] A. Szabo, N.S. Ostlund, *Modern Quantum Chemistry*, McGraw-Hill Inc, New York, 1989.
 [4] C.A. White, B.G. Johnson, P.M.W. Gill, M. Head-Gordon, *Chem. Phys. Lett.* 230 (1994) 8.
 [5] C. Ochsenfeld, J. Kussmann, D.S. Lambrecht, in: *Reviews in Computational Chemistry*, John Wiley & Sons, Inc., 2007, p. 1.
 [6] R. Car, M. Parrinello, *Phys. Rev. Lett.* 55 (1985) 2471.
 [7] H.B. Schlegel, J.M. Millam, S.S. Lyengar, G.A. Voth, A.D. Daniels, G.E. Scuseria, M. J. Frisch, *J. Chem. Phys.* 114 (2001) 9758.
 [8] J.M. Herbert, M. Head-Gordon, *J. Chem. Phys.* 121 (2004) 11542.
 [9] P. Tangney, S. Scandolo, *J. Chem. Phys.* 116 (2002) 14.
 [10] I.F.W. Kuo, C.J. Mundy, M.J. McGrath, J.I. Siepmann, J. VandeVondele, M. Sprik, J. Hutter, B. Chen, M.L. Klein, F. Mohamed, M. Krack, M. Parrinello, *J. Phys. Chem. B* 108 (2004) 12990.
 [11] A.M.N. Niklasson, C.J. Tymczak, M. Challacombe, *Phys. Rev. Lett.* 97 (2006) 123001.
 [12] M.J. Cawkwell, A.M.N. Niklasson, *J. Chem. Phys.* 137 (2012) 134105.
 [13] P. Souvatzis, A.M.N. Niklasson, *J. Chem. Phys.* 139 (2013) 214102.
 [14] A.M.N. Niklasson, M.J. Cawkwell, *J. Chem. Phys.* 141 (2014) 164123.
 [15] P. Souvatzis, A.M.N. Niklasson, *J. Chem. Phys.* 140 (2014) 044117.
 [16] T.D. Kühne, M. Krack, F.R. Mohamed, M. Parrinello, *Phys. Rev. Lett.* 98 (2007) 066401.
 [17] P. Pulay, G. Fogarasi, *Chem. Phys. Lett.* 386 (2004) 272.
 [18] J.M. Herbert, M. Head-Gordon, *Phys. Chem. Phys.* 7 (2005) 3269.
 [19] J. VandeVondele, M. Krack, F. Mohamed, M. Parrinello, T. Chassaing, J. Hutter, *Comput. Phys. Commun.* 167 (2005) 103.
 [20] T. Atsumi, H. Nakai, *J. Chem. Phys.* 128 (2008) 094101.
 [21] J.D. Herr, J. Talbot, R.P. Steele, *J. Phys. Chem. A* 119 (2015) 752.
 [22] J. Fang, X. Gao, H. Song, H. Wang, *J. Chem. Phys.* 144 (2016) 244103.
 [23] R.P. Steele, J.C. Tully, *Chem. Phys. Lett.* 500 (2010) 167.
 [24] W.H. Press, S.A. Teukosky, W.T. Vetterling, B.P. Flannery, *Numerical Recipes in C*, Cambridge University Press, 2002.
 [25] J.P. Burg, in: D.G. Childers (Ed.), *Modern Spectrum Analysis*, IEEE Press, 1978.
 [26] W.J. Hehre, R.F. Stewart, J.A. Pople, *J. Chem. Phys.* 51 (1969) 2657.
 [27] W.J. Hehre, R. Ditchfield, J.A. Pople, *J. Chem. Phys.* 56 (1972) 2257.
 [28] A.D. Becke, *J. Chem. Phys.* 98 (1993) 5648.
 [29] P.J. Stephens, F.J. Devlin, C.F. Chabalowski, M.J. Frisch, *J. Phys. Chem.* 98 (1994) 11623.
 [30] S. Grimme, *J. Comput. Chem.* 27 (2006) 1787.
 [31] T.H. Dunning, *J. Chem. Phys.* 90 (1989) 1007.
 [32] Y. Shao, Z. Gan, E. Epifanovsky, A.T.B. Gilbert, M. Wormit, J. Kussmann, A.W. Lange, A. Behn, J. Deng, X. Feng, D. Ghosh, M. Goldey, P.R. Horn, L.D. Jacobson, I. Kaliman, R.Z. Khaliullin, T. Kus, A. Landau, J. Liu, E.I. Proynov, Y.M. Rhee, R.M. Richard, M.A. Rohrdanz, R.P. Steele, E.J. Sundstrom, H.L. Woodcock, P.M. Zimmerman, D. Zuev, B. Albrecht, E. Alguire, B. Austin, G.J.O. Beran, Y.A. Bernard, E. Berquist, K. Brandhorst, K.B. Bravaya, S.T. Brown, D. Casanova, C.-M. Chang, Y. Chen, S.H. Chien, K.D. Closser, D.L. Crittenden, M. Diederichsen, R.A. DiStasio, H. Do, A.D. Dutoi, R.G. Edgar, S. Fatehi, L. Fusti-Molnar, A. Ghysels, A. Golubeva-Zadorozhnaya, J. Gomes, M.W.D. Hanson-Heine, P.H.P. Harbach, A. W. Hauser, E.G. Hohenstein, Z.C. Holden, T.-C. Jagau, H. Ji, B. Kaduk, K. Khistyayev, J. Kim, J. Kim, R.A. King, P. Klunzinger, D. Kosenkov, T. Kowalczyk, C. M. Krauter, K.U. Lao, A.D. Laurent, K.V. Lawler, S.V. Levchenko, C.Y. Lin, F. Liu, E. Livshits, R.C. Lochan, A. Luenser, P. Manohar, S.F. Manzer, S.-P. Mao, N. Mardirossian, A.V. Marenich, S.A. Maurer, N.J. Mayhall, E. Neuscamman, C.M. Oana, R. Olivares-Amaya, D.P. O'Neill, J.A. Parkhill, T.M. Perrine, R. Peverati, A. Prociuk, D.R. Rehn, E. Rosta, N.J. Russ, S.M. Sharada, S. Sharma, D.W. Small, A. Sodt, T. Stein, D. Stück, Y.-C. Su, A.J.W. Thom, T. Tsuchimochi, V. Vanovschi, L. Vogt, O. Vydrov, T. Wang, M.A. Watson, J. Wenzel, A. White, C.F. Williams, J. Yang, S. Yeganeh, S.R. Yost, Z.-Q. You, I.Y. Zhang, X. Zhang, Y. Zhao, B.R. Brooks, G.K.L. Chan, D.M. Chipman, C.J. Cramer, W.A. Goddard, M.S. Gordon, W.J. Hehre, A. Klamt, H.F. Schaefer, M.W. Schmidt, C.D. Sherrill, D.G. Truhlar, A. Warshel, X. Xu, A. Aspuru-Guzik, R. Baer, A.T. Bell, N.A. Besley, J.-D. Chai, A. Dreuw, B.D. Dunietz, T.R. Furlani, S.R. Gwaltney, C.-P. Hsu, Y. Jung, J. Kong, D.S. Lambrecht, W. Liang, C. Ochsenfeld, V.A. Rassolov, L.V. Slipchenko, J.E. Subotnik, T. Van Voorhis, J.M. Herbert, A.I. Krylov, P.M.W. Gill, M. Head-Gordon, *Mol. Phys.* 113 (2015) 184.
 [33] P. Pulay, *Chem. Phys. Lett.* 73 (1980) 393.
 [34] P. Pulay, *J. Comput. Chem.* 3 (1982) 556.
 [35] T. Van Voorhis, M. Head-Gordon, *Mol. Phys.* 100 (2002) 1713.
 [36] J. Almlöf, K. Faegri, K. Korsell, *J. Comput. Chem.* 3 (1982) 385.
 [37] M. Häser, R. Ahlrichs, *J. Comput. Chem.* 10 (1989) 104.
 [38] N. Mardirossian, M. Head-Gordon, *J. Chem. Theory Comput.* 9 (2013) 4453.

CHAPTER 6

ACCELERATING *AB INITIO* PATH INTEGRAL

SIMULATIONS VIA IMAGINARY

MULTIPLE-TIMESTEPPING

Reprinted with permission from Cheng, X.; Herr, J. D.; Steele, R. P. Accelerating *Ab Initio* Path Integral Simulations via Imaginary Multiple-Timestepping. *J. Chem. Theory Comput.* **2016**, *12* (4), 1627-1638. Copyright 2016 American Chemical Society.

Accelerating *Ab Initio* Path Integral Simulations via Imaginary Multiple-Timestepping

Xiaolu Cheng, Jonathan D. Herr, and Ryan P. Steele*

Department of Chemistry and Henry Eyring Center for Theoretical Chemistry, University of Utah, 315 South 1400 East, Salt Lake City, Utah 84112, United States

ABSTRACT: This work investigates the use of multiple-timestep schemes in imaginary time for computationally efficient *ab initio* equilibrium path integral simulations of quantum molecular motion. In the simplest formulation, only every n^{th} path integral replica is computed at the target level of electronic structure theory, whereas the remaining low-level replicas still account for nuclear motion quantum effects with a more computationally economical theory. Motivated by recent developments for multiple-timestep techniques in real-time classical molecular dynamics, both 1-electron (atomic-orbital basis set) and 2-electron (electron correlation) truncations are shown to be effective. Structural distributions and thermodynamic averages are tested for representative analytic potentials and *ab initio* molecular examples. Target quantum chemistry methods include density functional theory and second-order Møller–Plesset perturbation theory, although any level of theory is formally amenable to this framework. For a standard two-level splitting, computational speedups of 1.6–4.0x are observed when using a 4-fold reduction in time slices; an 8-fold reduction is feasible in some cases. Multitiered options further reduce computational requirements and suggest that quantum mechanical motion could potentially be obtained at a cost not significantly different from the cost of classical simulations.



INTRODUCTION

Path integral (PI) techniques^{1–4} provide a computationally efficient route for the simulation of quantum mechanical nuclear motion, including zero-point motion, tunneling, and thermal effects. By mapping quantum particles onto a chain of classical replicas, path integrals bypass the need for exponentially scaling eigenstate calculations and recast quantum equilibrium in a form that is amenable to Monte Carlo (MC)^{4–8} and molecular dynamics (MD)^{9,10} sampling techniques. Quantum averages, structural distributions, thermodynamics, and even approximate dynamics^{11–21} can be obtained from these simulations.

When combined with underlying electronic structure theory (EST) potential energy surfaces and forces, *ab initio* (AI) path integrals^{9,22–24} can achieve highly accurate quantum calculations that include the role of strong polarization and even bond-making/-breaking on the aforementioned quantities. Uniquely quantum properties of gas-phase clusters^{25–30} and condensed-phase systems^{31–35} have been obtained with such techniques. For computational efficiency reasons, AI-PIMD has most often been performed with density functional theory (DFT) potentials,²⁴ although examples of wave-function-based correlation methods, such as Møller–Plesset perturbation theory³⁶ (MPn) and coupled-cluster theory,^{37,38} have also been demonstrated.^{28,29,32,39,40} A straightforward parallelization over path integral replicas—typically on the order of 30 for room-temperature molecules—allows access to these simulations, albeit at the increased cost of additional computational resources.

Unfortunately, the use of accurate *ab initio* potentials, including electron correlation and large atom-centered or

plane-wave basis sets, nonetheless places large demands on computational time and resources. The trade-off of using crude EST, while still accounting for nuclear motion quantum effects, can dramatically alter distributions, tunneling dynamics, and thermodynamic averages. Spectroscopic studies, for example, have often shown the need for accurate EST in order to accurately reproduce structures and frequencies, and similar EST requirements should be transferable to zero-point and entropic contributions to thermodynamic quantities. Basis set superposition error (BSSE) further complicates matters for atom-centered basis sets. Eliminating this artifact from PIMD trajectories is challenging, especially for intramolecular BSSE,^{41–44} and enabling PIMD with large basis sets is a straightforward solution.

The aim of the present work is to investigate whether recent developments in multiple-timestep molecular dynamics (MTS-MD) algorithms^{45–49} can be used to alleviate some of the computational burden of path integral simulations. In MTS-MD, rapidly oscillating components of molecular forces are used to integrate classical equations of motion at small timesteps, whereas the more slowly oscillating components are employed at longer timesteps. In the often-encountered regime in which the latter components are the computational bottleneck, the effective increase in integration step size leads to concomitant increases in computational efficiency. Although such algorithms have historically been used for force field-based MD, we,^{50–52} and others,^{53–55} have shown that several options exist for *ab initio* MTS-MD, even though no spatial separability

Received: January 8, 2016

Published: March 11, 2016

of these potentials is available. In particular, force splittings based on electron correlation,⁵⁰ basis sets,⁵² and even two-electron integral evaluation^{51,55} can be used to accelerate AIMD simulations.

While these techniques could potentially be used to directly integrate AI-PIMD equations of motion, the role of the high-frequency bead motions (which are already analytically integrated with MTS techniques,⁵⁶ in order to avoid small timesteps) complicates this combination and will, therefore, be reserved for a separate analysis. In the present work, MTS techniques are instead used in “imaginary time”, wherein the path integral replicas are implemented at varying levels of electronic structure theory. This choice is motivated by known chemical considerations and has a simple physical justification. The degree of nonclassical behavior of a system can typically be assessed by its inherent frequencies and temperatures. The ratio $\frac{\hbar\omega}{k_B T}$ provides a rough lower bound, for example, for the minimum number of path integral replicas required for converged averages. In the OH^- ion, a simple HF/6-31G harmonic frequency calculation yields a fundamental transition of 3472 cm^{-1} , whereas a high-level CCSD/cc-pVQZ calculation yields 3688 cm^{-1} . This difference is sufficient to alter distributions and thermodynamic averages (0.3 kcal/mol zero-point energy difference), but the frequency of the difference potential $\omega_{\text{diff}} = \sqrt{\omega_{\text{high}}^2 - \omega_{\text{low}}^2} = 1244 \text{ cm}^{-1}$ suggests that roughly three times fewer beads would be required in order to converge this difference. Therefore, the methods presented and analyzed in this work seek to exploit this differential convergence behavior for computationally expedient path integral simulations.

This physical motivation was the basis for previous path integral contraction schemes, which were originally designed for analytic potentials. Termed “mixed time slicing”,⁵⁷ “ring-polymer contraction”,^{58–60} or “multilevel path integrals”,⁶¹ these schemes, which differ only slightly in implementation details, all essentially seek to perform the same task. The formulation used in this work follows our past study,⁵⁷ in which a direct Trotter splitting allows for an effective reduction in the number of beads for high-frequency components of the potential. Our previous assessment, which was based on a spatial partitioning of the potential, suggested that it was most efficient only for a small number of quantum degrees of freedom. However, this assessment appears to have been overly pessimistic since separability in nominally nonseparable *ab initio* methods has now been established through recent MTS-MD work. The present analysis, therefore, provides a natural marriage of these two concepts for accelerated quantum simulations. Namely, rather than a physical-space partitioning of the potential for imaginary-time integration, an alternative partitioning by either the level of electron correlation or the one-electron basis set is presented. This work investigates whether such separations are possible for AI-PI techniques and examines the efficiencies and limitations of this approach.

METHODS

The theory for imaginary multiple-timestep (iMTS) path integrals was largely depicted in our past work.⁵⁷ A brief sketch of the theory and details that are germane to the following analyses are presented below. The details of several numerical tests, which are designed to assess the behavior and limits of iMTS path integrals in an *ab initio* context, are also presented.

Imaginary Multiple-Timestep Path Integrals. The quantum partition function for a single particle of mass m in one spatial dimension x can be written as

$$Z = \int dx \langle x | e^{-\beta \hat{H}} | x \rangle = \int dx_1 \cdots dx_N \langle x_1 | e^{-\frac{\beta}{N} \hat{H}} | x_2 \rangle \cdots \langle x_N | e^{-\frac{\beta}{N} \hat{H}} | x_1 \rangle \quad (1)$$

where $\beta = \frac{1}{k_B T}$. The number of time slices N controls the degree of convergence when a high-temperature (NT) approximation to the density matrix elements is employed. For a generic Hamiltonian $\hat{H} = \hat{T} + \hat{V}$, a simple Trotter expansion^{62–64} $\exp(-\epsilon H) \approx \exp(-\epsilon T) \exp(-\epsilon V)$ yields a standard form for the matrix elements

$$\langle x_i | e^{-\frac{\beta}{N} \hat{H}} | x_{i+1} \rangle = \sqrt{\frac{Nm}{2\pi\beta\hbar^2}} e^{-\frac{Nm}{2\beta\hbar^2}(x_i - x_{i+1})^2} e^{-\frac{\beta}{N} V(x_{i+1})}$$

The harmonic coupling between neighboring time slices, combined with the cyclic nature of the overall trace in eq 1, leads to the “ring polymer” depiction of equilibrium path integrals, in which time slices are colloquially referred to as ring-polymer beads. The total expression for the partition function becomes

$$Z = \left(\frac{Nm}{2\pi\beta\hbar^2} \right)^{\frac{N}{2}} \int dx_1 \cdots dx_N e^{-\frac{\beta}{N} V_{\text{eff}}(x_1, \dots, x_N)} \quad (2)$$

where the effective quantum potential, now in N -dimensional space, is

$$V_{\text{eff}}(x_1, \dots, x_N) = \frac{N^2 m}{2\beta^2 \hbar^2} \sum_{i=1}^N (x_i - x_{i+1})^2 + \sum_{i=1}^N V(x_i) \quad (3)$$

If the potential can be written in terms of separable components, $V = V_1 + V_2$, then an alternative Trotter splitting can be performed, in analogy to the one used for classical MTS-MD.⁴⁸ Starting with a smaller number of time slices, $N_2 \leq N$, each density matrix becomes

$$\begin{aligned} \langle x_i | e^{-\frac{\beta}{N_2} \hat{H}} | x_{i+1} \rangle &\approx \langle x_i | e^{-\frac{\beta}{N_2} (\hat{T} + \hat{V}_1)} e^{-\frac{\beta}{N_2} \hat{V}_2} | x_{i+1} \rangle \\ &= \langle x_i | e^{-\frac{\beta}{N_2} (\hat{T} + \hat{V}_1)} | x_{i+1} \rangle e^{-\frac{\beta}{N_2} V_2(x_{i+1})} \end{aligned}$$

This Trotter division over N_2 (splitting out V_2) will hereafter be referred to as the “high-level” splitting, with the intent that $V = V_1 + V_2$ will become $V = V_{\text{low}} + \Delta V_{\text{high}}$ for *ab initio* potentials. At this stage, the V_1 -containing matrix element can then be further time-sliced according to N_1 , by subdividing this imaginary-time segment

$$\begin{aligned} \langle x_i | e^{-\frac{\beta}{N_1 N_2} (\hat{T} + \hat{V}_1)} | x_{i+1} \rangle e^{-\frac{\beta}{N_2} V_2(x_{i+1})} \\ = \int dx_i^{(1)} \cdots dx_i^{(N_1-1)} \langle x_i | e^{-\frac{\beta}{N_1 N_2} (\hat{T} + \hat{V}_1)} | x_i^{(1)} \rangle \cdots \\ \langle x_i^{(N_1-1)} | e^{-\frac{\beta}{N_1 N_2} (\hat{T} + \hat{V}_1)} | x_{i+1} \rangle e^{-\frac{\beta}{N_2} V_2(x_{i+1})} \end{aligned}$$

These matrix elements can subsequently be obtained by the same manipulations as above to produce the total “multiple-timestep” partition function. The governing expression is the same as in eq 2, with a modified effective potential

$$V_{\text{eff}}(x_1, \dots, x_N) = \frac{N^2 m}{2\beta^2 \hbar^2} \sum_{i=1}^N (x_i - x_{i+1})^2 + \left[\sum_{i=1}^N V_1(x_i) + N_1 \sum_{i=1}^{N_1} V_2(x_{(N_1, i)}) \right] \quad (4)$$

This effective potential requires V_1 for all of the $N = N_1 N_2$ beads and the V_2 component on every bead multiple of N_1 ; the harmonic coupling terms remain unchanged. As such, the ring polymer effective potential has adopted an MTS form when moving through time slices/beads. The qualitative interpretation of this result is also conceptually simple. The method assumes that V_2 does not appreciably change until the next high-level bead is encountered. This change should be comparable to the same change seen in V_1 between low-level beads. Therefore, the V_2 effect can be distributed across the N_1 beads of the low-level segment using a constant value. A schematic representation of this two-level Trotter splitting is shown in Figure 1.

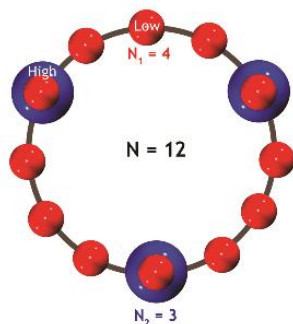


Figure 1. Schematic depiction of iMTS path integrals for a single quantum particle with 12 total beads and 3 high-level beads.

In the context of *ab initio* path integrals, the lone remaining task is the choice of V_1 and V_2 . Based on the aforementioned, recent MTS-MD studies, several options are available. The present analyses focus on splittings based on (a) electron correlation ($V_1 = V_{\text{HF}}$ and $V_2 = \Delta V_{\text{corr}}$) or (b) one-electron basis sets ($V_1 = V_{\text{small}}$ and $V_2 = \Delta V_{\text{large}}$). The aim of this work is

not to explore all possibilities and limitations since many of these aspects have been addressed in previous MD studies. Instead, we simply aim to assess whether concepts discovered in these past studies are transferable to path integral simulations.

Design of Numerical Experiments. A series of model potentials and target molecular complexes have been devised, in order to assess the performance of iMTS *ab initio* path integrals.

Analytic Models. The first set of tests employs only analytic potential functions, which have been designed to mimic common *ab initio* behavior and examine limiting regimes of this approach. While the aim of this methodology is to accelerate on-the-fly PIMD, these reference analytical potentials provide a framework with which the *ab initio* results can be interpreted. Accordingly, models 1A and 1B employ a pair of harmonic potentials for low/high “levels of theory” with controllable frequencies. The force constants and reduced mass are chosen to correspond to the harmonic frequency of H_2 (4400 cm^{-1}), which serves as an upper frequency bound for molecular systems. In model 1A, the low-level potential is an analogous harmonic potential, centered at the same equilibrium bond length, but with a 400 cm^{-1} reduction in fundamental harmonic frequency. While this difference may appear modest, it would lead to a ZPE difference comparable to $k_B T$ for this system, and the frequency difference is also appreciably larger than the difference between H_2 harmonic frequencies using HF/3-21G and CCSD/cc-pVQZ, for example. This parametrization, therefore, serves as a reasonably stringent test of the methodology for chemical systems. The two potentials, along with their difference potential ΔV , are shown in the first panel of Figure 2.

No variational principle applies to computed harmonic frequencies, and the possibility also exists that the target potential exhibits a smaller force constant than its low-level partner. Model 1B, therefore, uses the same harmonic potentials as were used in 1A but with the identity of the potentials reversed. Accordingly, the ΔV function is an *inverted* harmonic oscillator (center panel of Figure 2). The role of this inverted potential in modifying the convergence behavior of iMTS path integral simulations will be assessed, using both position distributions and thermodynamic averages as metrics.

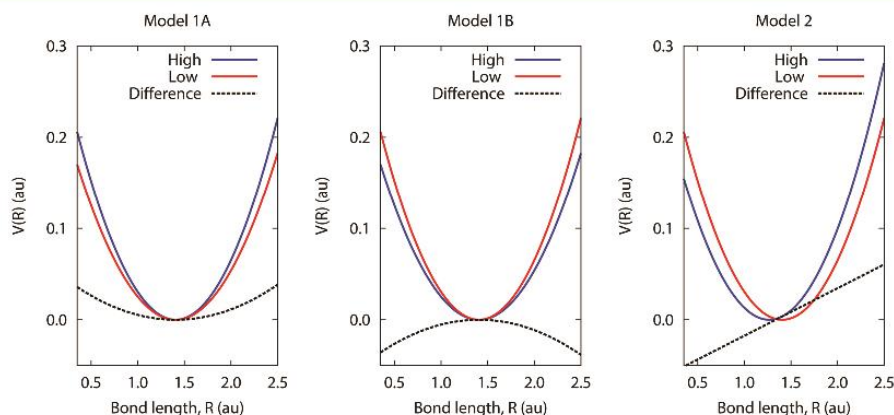


Figure 2. Representative harmonic model potentials for H_2 used in iMTS tests. Shown are low- and high-level potentials, along with difference potentials ΔV .

Estimators for these averages require brief comment. The desire for target-level quantities superficially suggests that averaging should be performed only over the high-level beads. However, such averages would not stem from proper estimators, as has been discussed in detail in related contexts.⁶⁵ Instead, *all* beads make a contribution to the averages, including the low-level beads. For average positions and distributions, estimates are computed no differently than they would be for the entire ring polymer in a standard simulation. For energies,⁷ the new effective quantum potential (eq 4) replaces the original effective potential for proper estimators.

Model 2 provides an assessment of the case in which low- and high-level potentials exhibit a change in geometry. The same 4400 cm^{-1} oscillator is used, with a 10% (0.14 Bohr) extension of the equilibrium position. In this case, the difference potential is a linear function. Bond distributions will once again guide the analysis.

For all three analytic models, the iMTS algorithm has been implemented with PIMC, PIMD, and grid-based PIMM.⁶⁶ Results will be presented for PIMC simulations at 300 K, using 10^7 sampling points. For each ring polymer size N , Lévy-flight sampling⁶⁷ parameters were chosen to maximize the mean-square displacement of the ring polymer throughout the sampling. Primitive and centroid-virial estimators^{67,68} were employed for average energies.

Ab Initio Tests. In order to explore iMTS behavior in a common *ab initio* regime, analyses were first performed on a single water molecule, using the B3LYP hybrid density functional^{69,70} with the 6-311G** target basis set.^{71–74} Since MTS partitioning based on these basis sets has already been shown to be effective for MD,⁵² the 6-31G basis set was used for the low-level potential in this test. The PIMD algorithm with a white-noise Langevin thermostat^{56,75} (time constant = 100 fs) was used for sampling at 300 K. All sampling was performed “on-the-fly”, using a development version of the Q-Chem quantum chemistry software package.⁷⁶ Analytic propagation of the harmonic coupling terms⁵⁶ was performed, and a timestep of 0.40 fs was used for the bare-potential integration. A total of 16 ps of sampling was performed after equilibration of the 32 total beads. A variable number of high-level beads was examined.

One of the potential virtues of the iMTS algorithm is to aid in the enabling of simulations using methods beyond DFT. In past MTS-MD analyses, for example, a splitting into Hartree–Fock and MP2 components was shown to be feasible and reliable.⁷⁷ Combining the two approaches is also possible, by using small-basis HF with target-basis MP2.⁵² This latter approach effectively eliminated the overhead of the low-level steps. To examine this regime, the hydrated chloride ion complex, $\text{Cl}^- \cdots \text{H}_2\text{O}$, was used as a model. In this hydrogen-bonded complex, the strong perturbation to the O–H bond manifests as unique spectroscopic signatures;⁷⁸ this perturbation is also sensitive to both basis set and electron correlation. Therefore, the HF/6-31G level of theory was used as the low-level potential, whereas MP2/cc-pVTZ, within the frozen-core and resolution-of-the-identity^{79–83} (RI) approximations, was chosen as the target level. Since the equilibrium structure and bond distributions are sensitive to this level of theory, reproduction of target structural distributions will be the metric of interest throughout. For this test, 3.2 ps of sampling was performed, using 32 total beads at 300 K.

Timings. A final pair of tests was performed for the purpose of assessing timings. For this analysis, the B3LYP/6-31G**

regime was examined with the water octamer, $(\text{H}_2\text{O})_8$, test system. The 6-31G basis set pairing was used as the low-level method, and timings were averaged over short trajectories, again with 32 beads at 300 K. A similar analysis was performed for the protonated glycine⁸⁴ complex (GlyH^+), $\text{C}_2\text{H}_6\text{NO}_2^+$ using RI-MP2/cc-pVTZ as the target level of theory. The main timing question to be investigated is whether the fractional reduction in high-level beads directly leads to equivalent time savings, or whether the additional low-level overhead tempers this advantage.

Some of this overhead can be addressed by exploiting the fact that the low- and high-level energies/forces are computed at the same molecular structure for the high-level beads. Two simple acceleration techniques were used previously^{52,77} for MTS-MD and are also applicable for iMTS path integrals. For basis set partitionings, an improved SCF guess can be obtained by projecting the low-level molecular orbitals into the high-level basis set, using techniques first developed for dual-basis SCF algorithms.^{85–91} For multiple-timestepping based on a Hartree–Fock/electron correlation splitting, the SCF information need not be recomputed for the correlation piece (although some minor additional overhead in the gradient is necessary). Both of these additional improvements have been implemented in the iMTS-PIMD code in Q-Chem. Neither of these (admittedly modest) improvements is possible in the alternative ring-polymer contraction scheme of refs 58–60, due to the fact that the high-level computations are performed at different positions than those of the low-level beads.

3-Tier Tests. The splitting of the ring polymer into two tiers is not unique. Sequential Trotter splitting of the density matrix elements, according to diminishing-frequency contributions to the underlying potential, would provide the possibility to “bootstrap” the quantum chemistry accuracy, at a cost that is potentially comparable to classical MD alone. In order to examine this possibility, three 1D potential energy curves were fit to *ab initio* data for the NeH^+ complex. The role of tagging rare-gas atoms is of interest in modern cryogenic ion spectroscopy experiments,^{92–95} and the interaction between these species is also sensitive to the quantum chemistry level of theory. In the present case, 12th-order polynomial curves were fit to coupled-cluster singles and doubles (CCSD) energies, using the 6-31G (low), cc-pVDZ⁹⁶ (middle), and cc-pVQZ (high) basis sets. The curves and corresponding properties are shown in Figure 3. A 3-level iMTS-PIMC code was used to sample distributions and averages, using sampling parameters analogous to those used in the previous analytic models.

RESULTS

Model 1A. Path integral position distributions for model 1A are shown in Figure 4. In Figure 4(a), the quantum and classical distributions are compared, for both low- and high-level potentials. At room temperature, quantum effects are appreciable ($\frac{\hbar\omega}{k_B T} \approx 20$) and notably broaden the distribution.

In Figure 4(b)–(c), only the top of the quantum distribution is examined, in order to highlight differences. The use of only a single high-level ring polymer bead [Figure 4(b)] results in a distribution that is closer to the target distribution than the low, but some error remains. Conversely, the use of 8 high-level beads (32 total) is in good agreement with the target distribution, which is consistent with the analysis of difference frequencies presented earlier.

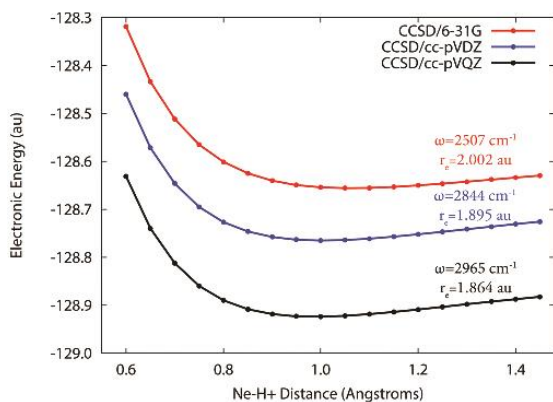


Figure 3. Coupled-cluster potential energy curves used for 3-tier iMTS tests. Indicated for each curve are the harmonic frequency (ω) and equilibrium (r_e) bond length.

Thermodynamic averages for this model are also consistent with this behavior. The average energy (Figure 5), for example, exhibits typical convergence behavior with standard PIMC, and the quantum $\langle E \rangle$ is an order of magnitude larger than the corresponding classical value. The iMTS-PIMC results, on the other hand, are nearly converged—recovering 95% of the classical-quantum difference—with only a single high-level bead. Convergence is also much more rapid with respect to the number of high-level beads, suggesting that the low-level “background” beads indeed provide a suitably shallower potential for the high-level beads to converge. This result is particularly encouraging for path integral computations of accurate thermodynamic data. Similar behavior is observed for structural averages, including $\langle x^2 \rangle$ (not shown).

Model 1B. In spite of the successes observed for model 1A, the inverted-potential properties of ΔV in model 1B provide a cautionary tale. The iMTS-PIMC distributions, as well as those

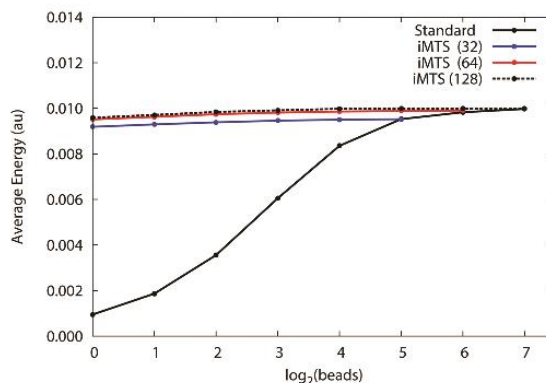


Figure 5. Convergence behavior of average energies for model 1A using PIMC at 300 K. The iMTS results are plotted as a function of the number of high-level beads. The iMTS numbering in the legend signifies the total number of beads.

of their low- and high-level counterparts, are shown in Figure 6. With 8 high-level beads [Figure 6(b)], the results are once again in nearly quantitative agreement with target-level distributions. However, when using a small number of high-level beads, the results are notably worse than low-level quantities [Figure 6(a)]. The PIMC results show significant noise away from equilibrium, and results from a PIMM simulation on a large grid (not shown) indicate that the distribution actually blows up at large distances.

The source of this divergent behavior stems from the high-level correction term in the iMTS formalism, $e^{-\frac{\beta}{N} \langle N, \Delta V \rangle}$, which is a growing exponential for this model potential. At low temperature and a converged number of low-level beads, the harmonic distribution obeys $\rho(x) \propto e^{-\frac{m\omega}{\hbar} x^2}$. With the high-level iMTS correction, this distribution is modified to $\rho(x) \propto e^{-\frac{m}{\hbar} (\omega_1 + \frac{\beta}{2N_2} (\omega_2^2 - \omega_1^2)) x^2}$. Therefore, if $\omega_1 + \frac{\beta}{2N_2} (\omega_2^2 - \omega_1^2) < 0$,

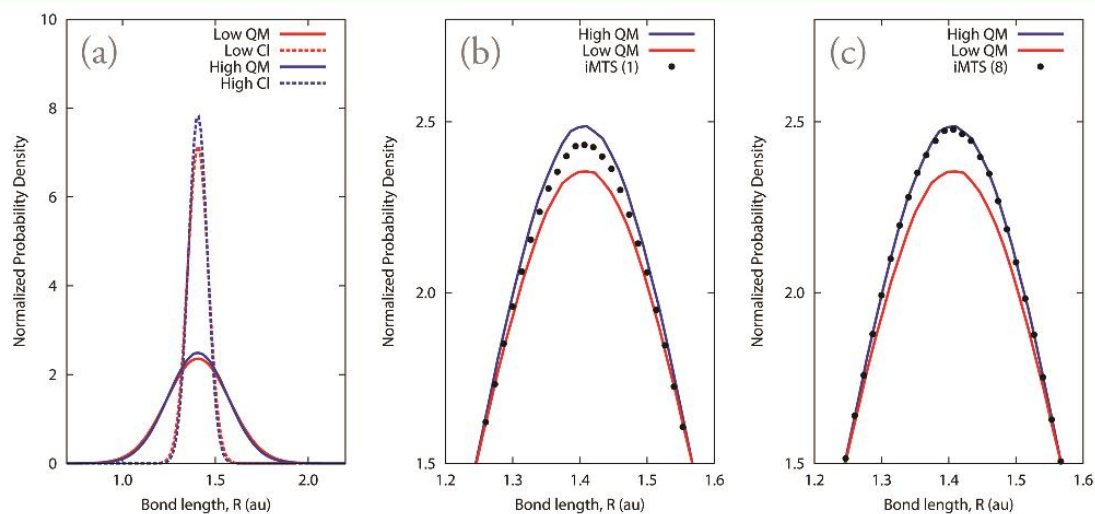


Figure 4. Histogrammed bond distributions for model 1A using PIMC at 300 K. Panels (b) and (c) are zoomed in to the peak of the quantum distributions. “QM” corresponds to quantum mechanical distributions, and “CI” corresponds to classical distributions. The numbering scheme for iMTS results signifies the number of high-level beads.

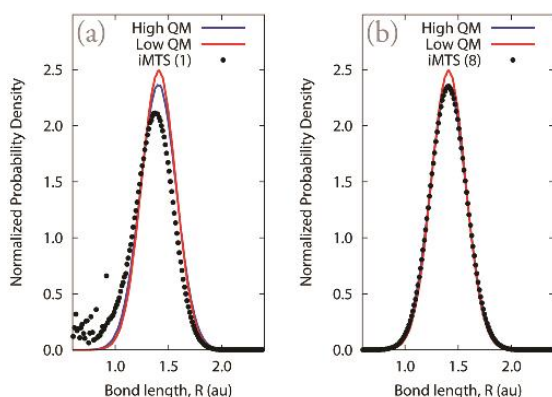


Figure 6. Histogrammed bond distributions for model 1B using PIMC at 300 K. The numbering scheme for iMTS results signifies the number of high-level beads.

the distribution will diverge at large displacements. This expression sets a rough bound on the number of high-level beads required to avoid divergence: $N_2 > \frac{\beta(\omega_1^2 - \omega_2^2)}{2\omega_1}$. For the 4400/4000 cm^{-1} pairing in this model, $N_2 \geq 2$ at 300 K. Practically speaking, this result simply suggests that the difference potential must be sufficiently converged in order to obtain reliable results. However, the cautionary lesson of this demonstration is that the iMTS results do not necessarily smoothly interpolate the low- and high-level results when the target frequency is lower than the low-level frequency. Introduction of a sign function, as has been previously used for nonadiabatic path integrals^{97,98} and some higher-order path integrals,⁹⁹ could potentially alleviate some of these pathologies, but in this work, a sufficient number of beads is chosen instead since converged properties are of interest anyway.

With these caveats in mind, assessment of the $\langle E \rangle$ and $\langle x^2 \rangle$ results for model 1B (Figure 7) is now straightforward. At very small high-bead numbers, the results are quite poor. However, with at least 4 high-level beads, iMTS results notably outperform the standard path integral algorithms and rapidly converge toward target-level results. A 4- or 8-fold reduction in target-level time slices would be sufficient for converged quantum averages. Interestingly, for high-accuracy quantum

simulations, the error in truncating 64 high-level beads to 8 with iMTS is comparable to truncating 64 total beads to 32 in standard path integrals.

Model 2. The bond-displacement model allows for the quantification of effects due to molecular structure changes among levels of electronic structure theory. Shown in Figure 8 are results for a 10% bond elongation at the target level. As was seen for model 1B, results with very small high-level bead numbers should be used with caution. The source of this error once again stems from the sign of the difference potential, which, in this instance, only adopts negative values on one side of equilibrium. However, for at least 8 high-level beads, the results are in near-quantitative agreement with target distributions, even for this relatively large structural change.

Water with B3LYP/6-311G.** Using an *ab initio* implementation of iMTS-PIMD, room-temperature path integral results for a single water molecule with B3LYP/6-311G** are shown in Figure 9. The low-level 6-31G results are appreciably different, in both the O–H bond and H–O–H angle distributions, whereas iMTS-PIMD results with only 4 high-level beads accurately reproduce the shifts exhibited by the target structural distributions. These results are consistent with the 127–195 cm^{-1} discrepancies in O–H stretch frequencies between the two quantum chemistry methods. The bend frequencies are actually closer in value (17 cm^{-1} difference), but the equilibrium structures exhibit larger angular deviations, leading to slightly more discrepancy in the angular results. Analogous distributions with 8 high-level beads (not shown) remove the remaining visual error in the angular distribution.

Hydrated Chloride Ion with RI-MP2/cc-pVTZ. Structural distributions for the case of wave-function-based electron correlation methods are shown in Figures 10 and 11. Even when using relatively crude electronic structure as the low level of theory (HF/6-31G), 8 high-level beads are sufficient to recover structural properties at the target level (RI-MP2/cc-pVTZ). The two O–H bond distributions in Figure 10 show that the low level of theory, which lacks polarization functions and electron correlation, incorrectly depicts the bonds as nearly identical, in spite of the nontrivial perturbation to the complex by the ion. The high level of theory instead shows an elongated O–H bond pointing toward the ion that is also appreciably anharmonic. (This behavior is confirmed by spectroscopic studies.⁷⁸) The iMTS simulations reproduce this bond

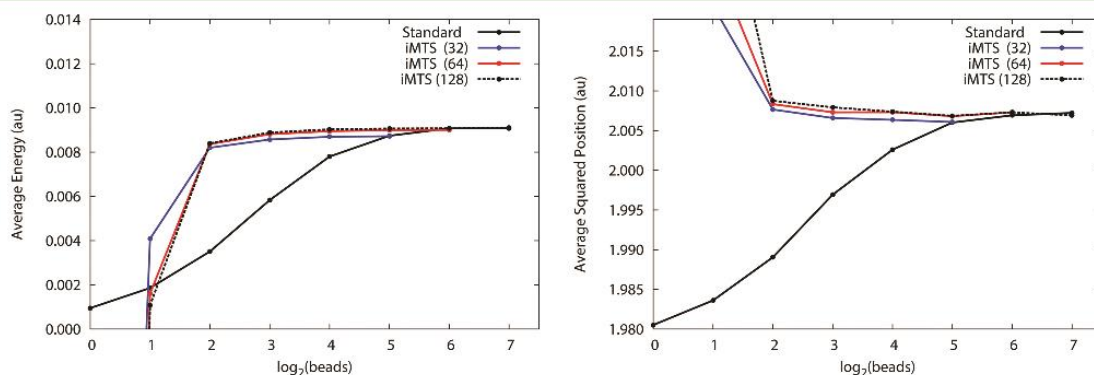


Figure 7. Convergence behavior of average energies (left) and squared positions (right) for model 1B using PIMC at 300 K. The iMTS results are plotted as a function of the number of high-level beads. The iMTS numbering in the legend signifies the total number of beads.

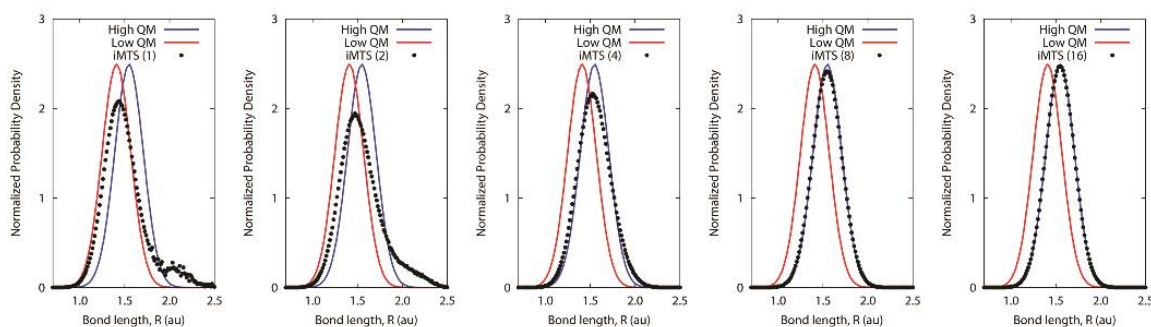


Figure 8. Histogrammed bond distributions for model 2 using PIMC at 300 K. The numbering scheme for iMTS results signifies the number of high-level beads.

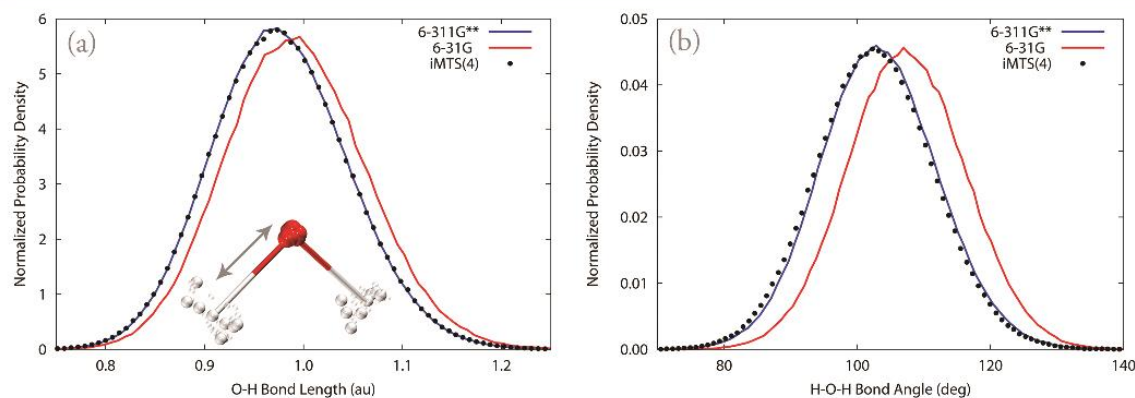


Figure 9. Structural distributions for H_2O using PIMD at 300 K with the B3LYP density functional. The inset in panel (a) shows a snapshot from the trajectory, in which high-level beads are depicted larger than the low-level beads.

distribution behavior within the resolution of the rather limited sampling.

Similar consistency is observed in the angular distributions, shown in Figure 11. The H–O–H angle within the water molecule changes appreciably at the higher level of the theory (more so than the bond lengths discussed above), and the iMTS results recover this shift. The O–H...Cl angle participating in the hydrogen bond is most sensitive to level of theory, and the bimodal distribution suggests that some shuttling of the hydrogen bond occurs during the low-frequency rocking motion of the water molecule. The iMTS results once again recover the target-level distribution to within the error bars (not shown) afforded by the sampling. Therefore, even with the rather drastic jump from HF/6-31G to RI-MP2/cc-pVTZ, adequate reproduction of target-level structural quantities can be obtained.

Ab Initio Timing Tests. Timing data for short trajectories of $(H_2O)_8$ with B3LYP/6-31G** [B3LYP/6-31G] and $GlyH^+$ with RI-MP2/cc-pVTZ [HF/6-31G] are presented in Tables 1 and 2, respectively. The timing data for DFT is broken down into energy and force information, as well as low- and high-level timings for iMTS. All data is presented as serial CPU time per PIMD step per bead, averaged over the entire ring polymer.

The DFT timings for the water cluster (Table 1) indicate that iMTS provides some speedup, although the savings are tempered by the overhead cost of the low-level method. The reduction in high-level beads alone would lead to a formal 4-

fold speedup, whereas the reduction in basis set alone (using all 32 beads) would instead lead to a 2.4-fold speedup. The actual observed speedup is a factor of 1.6, which is consistent with a weighted average of the low- and high-level cost contributions. The iMTS method recovers 61% of the computational cost difference between low- and high-level methods alone. Due to the use of the basis-projected SCF guess, the high-level beads' cost in iMTS is actually slightly lower than in the reference trajectory. The average number of high-level SCF cycles is reduced from 9.8 in standard 6-31G** PIMD to 8.1 in iMTS-PIMD, and this modest reduction in cycles leads to a roughly 10% additional reduction in high-level SCF cost. Similar overall behavior has been observed previously for MTS-AIMD, and based on these past analyses, extension to larger systems would move the timings closer to the theoretical 4-fold speedup.

Relative cost savings are more promising for the RI-MP2 tests on $GlyH^+$ (Table 2). Here, the cost difference between low- and high-level reference methods is more dramatic (167x) and leads to relative speedups that almost perfectly reproduce theoretical speedups (4.0x) for iMTS. The slight cost reduction in the high-level SCF from basis projection offsets the entire remnant overhead of the remaining low-level beads. Therefore, in this higher-accuracy regime, the reduction in bead number leads directly to nearly equivalent reduction in overall cost.

Three-Tiered iMTS. The multiple-tiered extension of the iMTS algorithm has been implemented for the $Ne-H^+$ CCSD potentials shown in the Methods section. Once again using

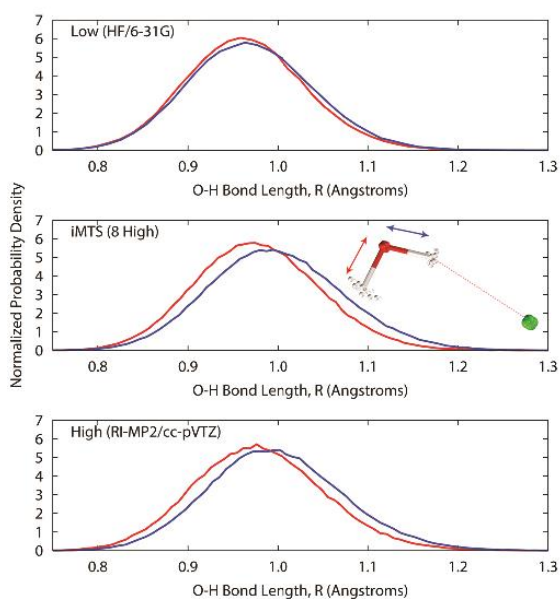


Figure 10. Histogrammed O–H bond distributions for $\text{Cl}^- \cdots \text{H}_2\text{O}$ using PIMD at 300 K. The blue and red curves correspond to the two inequivalent O–H bond distributions in the water moiety. Arrows in the inset of the middle panel distinguish these two bonds.

PIMC at 300 K with 32 total beads, distributions for the reference potentials and the iMTS algorithm are shown in Figure 12. The reference distributions reflect the bond contraction and harmonic frequency increase as the basis set size is increased. The incremental change, as expected, is larger with cc-pVDZ than with cc-pVQZ.

With three Trotter splittings involved, the number of possible bead-number combinations becomes quite large. Rather than a pedantic survey of all possible combinations, only one bead-number trio is shown in Figure 12, which is representative of time slicing that borders on convergence. For this splitting, only 2 target-level beads are used, in combination 8 midlevel beads (4 per high level) and 32 total beads (4 per middle level). The bond distribution does show some minor

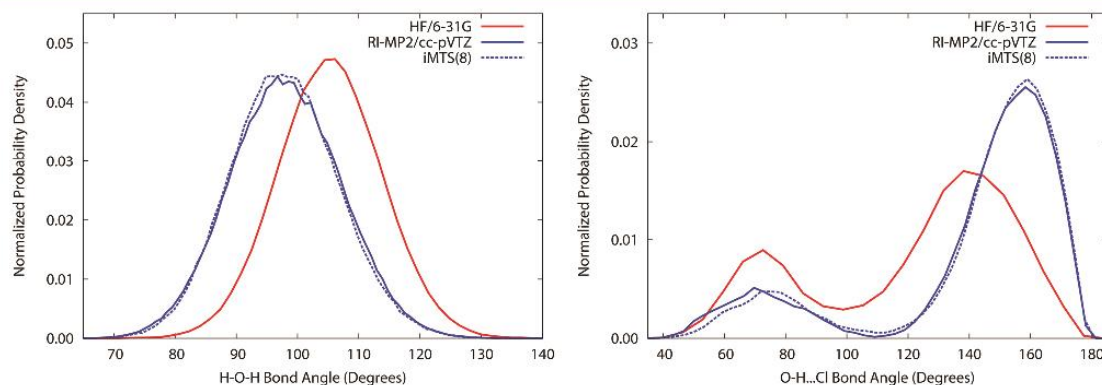


Figure 11. Histogrammed angle distributions for $\text{Cl}^- \cdots \text{H}_2\text{O}$ using PIMD at 300 K. The numbering in iMTS results signifies the number of high-level beads (32 total beads are used throughout).

Table 1. Computational Cost Analysis for $(\text{H}_2\text{O})_8$ Using B3LYP/6-31G**

basis set	$\langle \text{timings} \rangle^a$			speedup	% cost recovery ^b
	energy	force	total		
6-31G	16.6	2.9	19.5	2.4	
iMTS(8)	16.4/33.5	2.8/9.9	30.0	1.6	61%
6-31G**	36.8	9.6	46.5		

^aSerial CPU sec per PIMD step per bead. For MTS entries, low/target values are shown. ^bPercent recovery of differential cost by iMTS, compared to low- and high-level methods alone.

Table 2. Computational Cost Analysis for GlyH^+ Using RI-MP2/cc-pVTZ

method	$\langle \text{timings} \rangle^a$	speedup	% cost recovery ^b
HF/6-31G	1.7	166.7	
iMTS(8)	69.7	4.0	75%
RI-MP2/cc-pVTZ	278.7		

^aSerial CPU sec per PIMD step per bead. ^bPercent recovery of differential cost by iMTS, compared to low- and high-level methods alone.

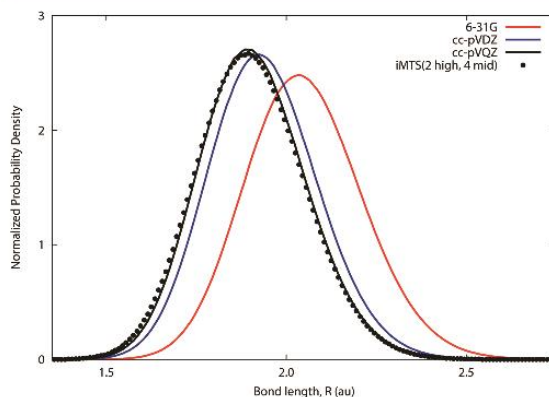


Figure 12. Histogrammed CCSD bond distributions for Ne-H^+ using 3-tiered iMTS-PIMC at 300 K. For all simulations, 32 total beads are used. In the iMTS results, 2 high-level beads are used, with 4 midlevel beads per high-level bead (8 total).

discrepancy with the reference distribution; however, the errors are much smaller than using either of the lower-level potentials alone. Encouragingly, this three-tiered distribution is in almost perfect agreement with a two-tiered iMTS simulation using only the mid- and high-level potentials; no appreciable degradation, due to the low-level method, is observed. This result suggests that any remnant overhead from the lower-level beads can be effectively eliminated by this multitiered approach. (The quartic scaling of many EST methods with respect to basis set size dictates that this overhead should rapidly decrease upon moving some beads to lower levels.) In the limit that convergence of the quantum chemistry method is sought, the need for only a single high-level bead, with little extant overhead, is likely. In other words, the cost of a quantum path integral simulation should approach the cost of a classical AIMD calculation when high-accuracy quantum chemistry methods (correlation and/or basis sets) are employed.

DISCUSSION AND CONCLUSIONS

The results of the previous analyses confirm that iMTS-based path integrals provide a sufficiently accurate alternative to standard path integral implementations, while providing cost savings that approach the reduction in the number of time slices. This reduction can be roughly 4- to 8-fold, depending on the potentials chosen. These results are entirely consistent with results observed for classical, real-time MTS-MD, which suggests that the original transferability premise of MTS concepts to imaginary-time path integrals was, in fact, valid.

Based on the preceding tests and timings, the recommended basis set pairings for HF and DFT remain unchanged from past MTS-MD analyses, although an exhaustive survey of these pairings was not performed here. In particular, 6-31G serves as a sufficient low-level basis set for simulations using 6-31G** or 6-311G** as the target basis set, provided that roughly a 4-fold reduction in high-level beads is utilized. For MP2 simulations with triple- ζ -quality basis sets, the low-level basis set may also be 6-31G, and even HF typically serves as a sufficient low-level partner. Some cost trade-off likely exists in these choices. A more accurate low-level potential would introduce larger low-level overhead but may also allow for more aggressive truncation in the number of time slices. The details of this trade-off are almost certainly system-dependent, but the rough guidelines presented here serve as reference points for chemical systems.

Nearly all path integral routines, including the Q-Chem code used in this work, exploit the straightforward parallel-computing implementation of these methods. Apart from a computationally trivial harmonic coupling term, the time slices (beads) require independent energy and force calculations, and parallelization over this time slicing is extremely efficient. Further subparallelization (or multithreading) of the underlying electronic structure is also possible. All timings presented in this work have focused on serial cost, for the sake of direct comparison among methods and avoidance of quantum chemistry parallel efficiency corrections. The only unique implementation consideration for iMTS is that the cost of each bead's energy/force is no longer roughly equivalent. Straightforward dynamic load balancing, however, should be able to handle these tasks without undue impact on the parallel efficiency. Of course, a reasonable critique of this approach is that the parallel end-user time would remain essentially unchanged, compared to a standard path integral simulation. However, a reduction in required computer resources

(comparable to the reduction in beads) would still be attained, and this freeing of resources could, for example, instead be used to more quickly or accurately converge the path integral sampling.

The reduction in necessary time slices observed in this work is comparable to similar quantities in higher-order path integral implementations.^{64,65,100–104} Unlike in these alternative approaches, however, no gradient term is present in the effective potential, which means that neither second derivatives nor reweighted sampling are required in order to perform the PIMD integration. In some sense, the present iMTS algorithm is, itself, a reweighted sampling approach, but two factors tame the known pitfalls of such sampling.¹⁰⁵ First, the paired potentials are chosen with some care, such that appreciable overlap remains between the low- and high-level distributions. If this property was not present, too many beads would be required anyway at the high level of theory. Second, the choice of multiple-timestepping in imaginary time means that the harmonic coupling between neighboring time slices serves to keep the low- and high-level beads from drifting to qualitatively different regions of the potential energy surface.

Finally, the potential ability to “stack” multiple tiers of iMTS is particularly encouraging, for several reasons. In the medium-accuracy EST regime, multiple tiers allow for the convergence of quantum motion properties using very crude low levels of theory. In the high-accuracy EST regime, multiple tiers provide the opportunity to systematically improve the underlying quantum chemistry method until only a single bead remains at the target level. Lastly, low-temperature path integral simulations would particularly benefit from such tiered approaches since more opportunity is available to further subdivide the large number of time slices required for convergence at these temperatures. The present analysis has shown that these possibilities are promising, based on models of *ab initio* data. Future studies will explore these latter approaches for larger molecular complexes.

AUTHOR INFORMATION

Corresponding Author

*E-mail: ryan.steele@utah.edu.

Author Contributions

X.C. and J.D.H. contributed equally to this work.

Notes

The authors declare no competing financial interest.

ACKNOWLEDGMENTS

This material is based upon work supported by the National Science Foundation CAREER under CHE-1452596. The support and resources from the Center for High-Performance Computing at the University of Utah are gratefully acknowledged. This work also used the Extreme Science and Engineering Discovery Environment (XSEDE), which is supported by National Science Foundation grant number ACI-1053575.

REFERENCES

- (1) Feynman, R. P.; Hibbs, A. R. *Quantum Mechanics and Path Integrals*; McGraw-Hill: New York, 1965.
- (2) Chandler, D.; Wolynes, P. G. Exploiting the Isomorphism between Quantum Theory and Classical Statistical Mechanics of Polyatomic Fluids. *J. Chem. Phys.* **1981**, *74*, 4078–4095.

- (3) Kleinert, H. *Path Integrals in Quantum Mechanics, Statistics, Polymer Physics, and Financial Markets*, 4th ed.; World Scientific Publishing Co. Pte. Ltd.: Singapore, 2006.
- (4) Berne, B. J.; Thirumalai, D. On the Simulation of Quantum Systems: Path Integral Methods. *Annu. Rev. Phys. Chem.* **1986**, *37*, 401–424.
- (5) Barker, J. A. A Quantum-Statistical Monte Carlo Method: Path Integrals with Boundary Conditions. *J. Chem. Phys.* **1979**, *70*, 2914–2918.
- (6) Herman, M. F.; Bruskin, E. J.; Berne, B. J. On Path Integral Monte Carlo Simulations. *J. Chem. Phys.* **1982**, *76*, 5150–5155.
- (7) Cao, J.; Berne, B. J. On Energy Estimators in Path Integral Monte Carlo Simulations: Dependence of Accuracy on Algorithm. *J. Chem. Phys.* **1989**, *91*, 6359–6366.
- (8) Sprik, M.; Klein, M. L.; Chandler, D. Staging: A Sampling Technique for the Monte Carlo Evaluation of Path Integrals. *Phys. Rev. B: Condens. Matter Mater. Phys.* **1985**, *31*, 4234–4244.
- (9) Parrinello, M.; Rahman, A. Study of an F Center in Molten KCl. *J. Chem. Phys.* **1984**, *80*, 860–867.
- (10) Tuckerman, M. E.; Berne, B. J.; Martyna, G. J.; Klein, M. L. Efficient Molecular Dynamics and Hybrid Monte Carlo Algorithms for Path Integrals. *J. Chem. Phys.* **1993**, *99*, 2796–2808.
- (11) Cao, J.; Voth, G. A. The Formulation of Quantum Statistical Mechanics Based on the Feynman Path Centroid Density. II. Dynamical Properties. *J. Chem. Phys.* **1994**, *100*, 5106–5117.
- (12) Jang, S.; Voth, G. A. A Derivation of Centroid Molecular Dynamics and Other Approximate Time Evolution Methods for Path Integral Centroid Variables. *J. Chem. Phys.* **1999**, *111*, 2371–2384.
- (13) Pavese, M.; Berard, D. R.; Voth, G. A. Ab Initio Centroid Molecular Dynamics: A Fully Quantum Method for Condensed-Phase Dynamics Simulations. *Chem. Phys. Lett.* **1999**, *300*, 93–98.
- (14) Ohta, Y.; Ohta, K.; Kinugawa, K. Ab Initio Centroid Path Integral Molecular Dynamics: Application to Vibrational Dynamics of Diatomic Molecular Systems. *J. Chem. Phys.* **2004**, *120*, 312–320.
- (15) Craig, I. R.; Manolopoulos, D. E. A Refined Ring Polymer Molecular Dynamics Theory of Chemical Reaction Rates. *J. Chem. Phys.* **2005**, *123*, 034102–10.
- (16) Craig, I. R.; Manolopoulos, D. E. Chemical Reaction Rates from Ring Polymer Molecular Dynamics. *J. Chem. Phys.* **2005**, *122*, 084106–12.
- (17) Collepardo-Guevara, R.; Craig, I. R.; Manolopoulos, D. E. Proton Transfer in a Polar Solvent from Ring Polymer Reaction Rate Theory. *J. Chem. Phys.* **2008**, *128*, 144502.
- (18) Perez, A.; Tuckerman, M. E.; Muser, M. H. A Comparative Study of the Centroid and Ring-Polymer Molecular Dynamics Methods for Approximating Quantum Time Correlation Functions from Path Integrals. *J. Chem. Phys.* **2009**, *130*, 184105–13.
- (19) Polyakov, E. A.; Lyubartsev, A. P.; Vorontsov-Velyaminov, P. N. Centroid Molecular Dynamics: Comparison with Exact Results for Model Systems. *J. Chem. Phys.* **2010**, *133*, 194103–14.
- (20) Habershon, S.; Manolopoulos, D. E.; Markland, T. E.; Miller, T. F. Ring-Polymer Molecular Dynamics: Quantum Effects in Chemical Dynamics from Classical Trajectories in an Extended Phase Space. *Annu. Rev. Phys. Chem.* **2013**, *64*, 387–413.
- (21) Witt, A.; Ivanov, S. D.; Shiga, M.; Forbert, H.; Marx, D. On the Applicability of Centroid and Ring Polymer Path Integral Molecular Dynamics for Vibrational Spectroscopy. *J. Chem. Phys.* **2009**, *130*, 194510.
- (22) Marx, D.; Parrinello, M. Ab Initio Path Integral Molecular Dynamics: Basic Ideas. *J. Chem. Phys.* **1996**, *104*, 4077–4082.
- (23) Shiga, M.; Tachikawa, M.; Miura, S. A Unified Scheme for Ab Initio Molecular Orbital Theory and Path Integral Molecular Dynamics. *J. Chem. Phys.* **2001**, *115*, 9149–9159.
- (24) Tuckerman, M. E.; Marx, D.; Klein, M. L.; Parrinello, M. Efficient and General Algorithms for Path Integral Car–Parrinello Molecular Dynamics. *J. Chem. Phys.* **1996**, *104*, 5579–5588.
- (25) Ishibashi, H.; Hayashi, A.; Shiga, M.; Tachikawa, M. Geometric Isotope Effect on the N2h7+ Cation and N2h5– Anion by Ab Initio Path Integral Molecular Dynamics Simulation. *ChemPhysChem* **2008**, *9*, 383–387.
- (26) Kakizaki, A.; Takayanagi, T.; Shiga, M. Path Integral Molecular Dynamics Calculations of the and Clusters on an Ab Initio Potential Energy Surface. *Chem. Phys. Lett.* **2007**, *449*, 28–32.
- (27) Hayashi, A.; Shiga, M.; Tachikawa, M. H/d Isotope Effect on the Dihydrogen Bond by Ab Initio Path Integral Molecular Dynamics Simulation. *Mol. Simul.* **2007**, *33*, 185–188.
- (28) Kaczmarek, A.; Shiga, M.; Marx, D. Quantum Effects on Vibrational and Electronic Spectra of Hydrazine Studied by “on-the-Fly” Ab Initio Ring Polymer Molecular Dynamics†. *J. Phys. Chem. A* **2009**, *113*, 1985–1994.
- (29) Suzuki, K.; Shiga, M.; Tachikawa, M. Temperature and Isotope Effects on Water Cluster Ions with Path Integral Molecular Dynamics Based on the Fourth Order Trotter Expansion. *J. Chem. Phys.* **2008**, *129*, 144310.
- (30) Durlak, P.; Berski, S.; Latajka, Z. Car-Parrinello and Path Integral Molecular Dynamics Study of the Hydrogen Bond in the Acetic Acid Dimer in the Gas Phase. *J. Mol. Model.* **2011**, *17*, 2995–3004.
- (31) Durlak, P.; Latajka, Z. Car-Parrinello and Path Integral Molecular Dynamics Study of the Intramolecular Hydrogen Bonds in the Crystals of Benzoylacetone and Dideuterobenzoylacetone. *Phys. Chem. Chem. Phys.* **2014**, *16*, 23026–23037.
- (32) Durlak, P.; Latajka, Z. Car–Parrinello and Path Integral Molecular Dynamics Study of the Intramolecular Hydrogen Bond in the Novel Class of Anionic H-Chelates: 6-Nitro-2,3-Dipyrrol-2-Ylquinoline Anion. *Chem. Phys. Lett.* **2009**, *480*, 173–177.
- (33) Hayes, R. L.; Paddison, S. J.; Tuckerman, M. E. Proton Transport in Triflic Acid Hydrates Studied Via Path Integral Car–Parrinello Molecular Dynamics. *J. Phys. Chem. B* **2009**, *113*, 16574–16589.
- (34) Marx, D.; Tuckerman, M. E.; Hutter, J.; Parrinello, M. The Nature of the Hydrated Excess Proton in Water. *Nature* **1999**, *397*, 601–604.
- (35) Chen, J.; Li, X.-Z.; Zhang, Q.; Probert, M. I. J.; Pickard, C. J.; Needs, R. J.; Michaelides, A.; Wang, E. Quantum Simulation of Low-Temperature Metallic Liquid Hydrogen. *Nat. Commun.* **2013**, *4*, 4.
- (36) Møller, C.; Plesset, M. S. Note on an Approximation Treatment for Many-Electron Systems. *Phys. Rev.* **1934**, *46*, 618–622.
- (37) Cizek, J. On the Correlation Problem in Atomic and Molecular Systems. Calculation of Wavefunction Components in Ursell-Type Expansion Using Quantum-Field Theoretical Methods. *J. Chem. Phys.* **1966**, *45*, 4256–4266.
- (38) Bartlett, R. J.; Musiał, M. Coupled-Cluster Theory in Quantum Chemistry. *Rev. Mod. Phys.* **2007**, *79*, 291–352.
- (39) Fujita, T.; Tanaka, S.; Fujiwara, T.; Kusa, M.-A.; Mochizuki, Y.; Shiga, M. Ab Initio Path Integral Monte Carlo Simulations for Water Trimer with Electron Correlation Effects. *Comput. Theor. Chem.* **2012**, *997*, 7–13.
- (40) Sugimoto, M.; Shiga, M.; Tachikawa, M. Nuclear Quantum Effect on the Dissociation Energies of Cationic Hydrogen Clusters. *Comput. Theor. Chem.* **2011**, *975*, 31–37.
- (41) Jensen, F. The Magnitude of Intramolecular Basis Set Superposition Error. *Chem. Phys. Lett.* **1996**, *261*, 633–636.
- (42) Brandenburg, J. G.; Alessio, M.; Civalleri, B.; Peintinger, M. F.; Bredow, T.; Grimme, S. Geometrical Correction for the Inter- and Intramolecular Basis Set Superposition Error in Periodic Density Functional Theory Calculations. *J. Phys. Chem. A* **2013**, *117*, 9282–9292.
- (43) Asturiol, D.; Duran, M.; Salvador, P. Intramolecular Basis Set Superposition Error Effects on the Planarity of Benzene and Other Aromatic Molecules: A Solution to the Problem. *J. Chem. Phys.* **2008**, *128*, 144108.
- (44) Valdés, H.; Klusák, V.; Pitoňák, M.; Exner, O.; Starý, I.; Hobza, P.; Rulišek, L. Evaluation of the Intramolecular Basis Set Superposition Error in the Calculations of Larger Molecules: [N]Helicenes and Phe-Gly-Phe Tripeptide. *J. Comput. Chem.* **2008**, *29*, 861–870.

- (45) Tuckerman, M. E.; Martyna, G. J.; Berne, B. J. Molecular Dynamics Algorithm for Condensed Systems with Multiple Time Scales. *J. Chem. Phys.* **1990**, *93*, 1287–1291.
- (46) Tuckerman, M. E.; Berne, B. J.; Martyna, G. J. Molecular Dynamics Algorithm for Multiple Time Scales: Systems with Long Range Forces. *J. Chem. Phys.* **1991**, *94*, 6811–6815.
- (47) Tuckerman, M. E.; Berne, B. J.; Rossi, A. Molecular Dynamics Algorithm for Multiple Time Scales: Systems with Disparate Masses. *J. Chem. Phys.* **1991**, *94*, 1465–1469.
- (48) Tuckerman, M.; Berne, B. J.; Martyna, G. J. Reversible Multiple Time Scale Molecular Dynamics. *J. Chem. Phys.* **1992**, *97*, 1990–2001.
- (49) Streett, W. B.; Tildesley, D. J.; Saville, G. Multiple Time-Step Methods in Molecular Dynamics. *Mol. Phys.* **1978**, *35*, 639–648.
- (50) Steele, R. P. Communication: Multiple-Timestep Ab Initio Molecular Dynamics with Electron Correlation. *J. Chem. Phys.* **2013**, *139*, 011102.
- (51) Fatehi, S.; Steele, R. P. Multiple-Time Step Ab Initio Molecular Dynamics Based on Two-Electron Integral Screening. *J. Chem. Theory Comput.* **2015**, *11*, 884–898.
- (52) Steele, R. P. Multiple-Timestep Ab Initio Molecular Dynamics Using an Atomic Basis Set Partitioning. *J. Phys. Chem. A* **2015**, *119*, 12119.
- (53) Gibson, D. A.; Carter, E. A. Time-Reversible Multiple Time Scale Ab Initio Molecular Dynamics. *J. Phys. Chem.* **1993**, *97*, 13429–13434.
- (54) Tuckerman, M. E.; Parrinello, M. Integrating the Car–Parrinello Equations. I. Basic Integration Techniques. *J. Chem. Phys.* **1994**, *101*, 1302–1315.
- (55) Luehr, N.; Markland, T. E.; Martínez, T. J. Multiple Time Step Integrators in Ab Initio Molecular Dynamics. *J. Chem. Phys.* **2014**, *140*, 084116.
- (56) Ceriotti, M.; Parrinello, M.; Markland, T. E.; Manolopoulos, D. E. Efficient Stochastic Thermostatting of Path Integral Molecular Dynamics. *J. Chem. Phys.* **2010**, *133*, 124104–13.
- (57) Steele, R. P.; Zwickl, J.; Shushkov, P.; Tully, J. C. Mixed Time Slicing in Path Integral Simulations. *J. Chem. Phys.* **2011**, *134*, 074112–14.
- (58) Markland, T. E.; Manolopoulos, D. E. A Refined Ring Polymer Contraction Scheme for Systems with Electrostatic Interactions. *Chem. Phys. Lett.* **2008**, *464*, 256–261.
- (59) Markland, T. E.; Manolopoulos, D. E. An Efficient Ring Polymer Contraction Scheme for Imaginary Time Path Integral Simulations. *J. Chem. Phys.* **2008**, *129*, 024105–10.
- (60) Fanourgakis, G. S.; Markland, T. E.; Manolopoulos, D. E. A Fast Path Integral Method for Polarizable Force Fields. *J. Chem. Phys.* **2009**, *131*, 094102–10.
- (61) Geng, H. Y. Accelerating Ab Initio Path Integral Molecular Dynamics with Multilevel Sampling of Potential Surface. *J. Comput. Phys.* **2015**, *283*, 299–311.
- (62) Trotter, H. F. On the Products of Semi-Groups of Operators. *Proc. Am. Math. Soc.* **1959**, *10*, 545–551.
- (63) De Raedt, H.; De Raedt, B. Applications of the Generalized Trotter Formula. *Phys. Rev. A: At., Mol., Opt. Phys.* **1983**, *28*, 3575–3580.
- (64) Li, X.-P.; Broughton, J. Q. High-Order Correction to the Trotter Expansion for Use in Computer Simulation. *J. Chem. Phys.* **1987**, *86*, 5094–5100.
- (65) Perez, A.; Tuckerman, M. E. Improving the Convergence of Closed and Open Path Integral Molecular Dynamics Via Higher Order Trotter Factorization Schemes. *J. Chem. Phys.* **2011**, *135*, 064104–17.
- (66) Thirumalai, D.; Bruskin, E. J.; Berne, B. J. An Iterative Scheme for the Evaluation of Discretized Path Integrals. *J. Chem. Phys.* **1983**, *79*, 5063–5069.
- (67) Krauth, W. *Statistical Mechanics: Algorithms and Computations*, 1st ed.; Oxford University Press: USA, 2006.
- (68) Janke, W.; Sauer, T. Optimal Energy Estimation in Path-Integral Monte Carlo Simulations. *J. Chem. Phys.* **1997**, *107*, 5821–5839.
- (69) Becke, A. D. Density-Functional Thermochemistry. Iii. The Role of Exact Exchange. *J. Chem. Phys.* **1993**, *98*, 5648–5652.
- (70) Stephens, P. J.; Devlin, F. J.; Chabalowski, C. F.; Frisch, M. J. Ab Initio Calculation of Vibrational Absorption and Circular Dichroism Spectra Using Density Functional Force Fields. *J. Phys. Chem.* **1994**, *98*, 11623–11627.
- (71) Hehre, W. J.; Stewart, R. F.; Pople, J. A. Self-Consistent Molecular-Orbital Methods. I. Use of Gaussian Expansions of Slater-Type Atomic Orbitals. *J. Chem. Phys.* **1969**, *51*, 2657–2664.
- (72) Hehre, W. J.; Ditchfield, R.; Pople, J. A. Self-Consistent Molecular Orbital Methods. Xii. Further Extensions of Gaussian-Type Basis Sets for Use in Molecular Orbital Studies of Organic Molecules. *J. Chem. Phys.* **1972**, *56*, 2257–2261.
- (73) Hariharan, P. C.; Pople, J. A. The Influence of Polarization Functions on Molecular Orbital Hydrogenation Energies. *Theoret. Chim. Acta* **1973**, *28*, 213–222.
- (74) Krishnan, R.; Binkley, J. S.; Seeger, R.; Pople, J. A. Self-Consistent Molecular Orbital Methods. Xx. A Basis Set for Correlated Wave Functions. *J. Chem. Phys.* **1980**, *72*, 650–654.
- (75) Bussi, G.; Parrinello, M. Accurate Sampling Using Langevin Dynamics. *Phys. Rev. E* **2007**, *75*, 056707.
- (76) Shao, Y.; Gan, Z.; Epifanovsky, E.; Gilbert, A. T. B.; Wormit, M.; Kussmann, J.; Lange, A. W.; Behn, A.; Deng, J.; Feng, X.; et al. Advances in Molecular Quantum Chemistry Contained in the Q-Chem 4 Program Package. *Mol. Phys.* **2015**, *113*, 184–215.
- (77) Steele, R. P. Communication: Multiple-Timestep Ab Initio Molecular Dynamics with Electron Correlation. *J. Chem. Phys.* **2013**, *139*, 011102–4.
- (78) Roscioli, J. R.; Diken, E. G.; Johnson, M. A.; Horvath, S.; McCoy, A. B. Prying Apart a Water Molecule with Anionic H-Bonding: A Comparative Spectroscopic Study of the X-H₂O (X = Oh, O, F, Cl, and Br) Binary Complexes in the 600–3800 Cm⁻¹ Region. *J. Phys. Chem. A* **2006**, *110*, 4943–4952.
- (79) Feyerhagen, M.; Fitzgerald, G.; Komornicki, A. Use of Approximate Integrals in Ab Initio Theory. An Application in Mp2 Energy Calculations. *Chem. Phys. Lett.* **1993**, *208*, 359–363.
- (80) Eichkorn, K.; Treutler, O.; Öhm, H.; Häser, M.; Ahlrichs, R. Auxiliary Basis Sets to Approximate Coulomb Potentials. *Chem. Phys. Lett.* **1995**, *240*, 283–290.
- (81) Weigend, F.; Häser, M.; Patzelt, H.; Ahlrichs, R. Ri-Mp2: Optimized Auxiliary Basis Sets and Demonstration of Efficiency. *Chem. Phys. Lett.* **1998**, *294*, 143–152.
- (82) Jung, Y.; Sodt, A.; Gill, P. M. W.; Head-Gordon, M. Auxiliary Basis Expansions for Large-Scale Electronic Structure Calculations. *Proc. Natl. Acad. Sci. U. S. A.* **2005**, *102*, 6692–6697.
- (83) DiStasio, R. A.; Steele, R. P.; Rhee, Y. M.; Shao, Y.; Head-Gordon, M. An Improved Algorithm for Analytical Gradient Evaluation in Resolution-of-the-Identity Second-Order Møller-Plesset Perturbation Theory: Application to Alanine Tetrapeptide Conformational Analysis. *J. Comput. Chem.* **2007**, *28*, 839–856.
- (84) Wu, R.; McMahon, T. B. Protonation Sites and Conformations of Peptides of Glycine (Gly1–5h+) by Impd Spectroscopy. *J. Phys. Chem. B* **2009**, *113*, 8767–8775.
- (85) Steele, R. P.; DiStasio, J. R. A.; Shao, Y.; Kong, J.; Head-Gordon, M. Dual-Basis Second-Order M[O-Slash]ller-Plesset Perturbation Theory: A Reduced-Cost Reference for Correlation Calculations. *J. Chem. Phys.* **2006**, *125*, 074108–11.
- (86) Steele, R. P.; Shao, Y.; DiStasio, R. A.; Head-Gordon, M. Dual-Basis Analytic Gradients. I. Self-Consistent Field Theory. *J. Phys. Chem. A* **2006**, *110*, 13915–13922.
- (87) Steele, R. P.; Head-Gordon, M. Dual-Basis Self-Consistent Field Methods: 6-31g* Calculations with a Minimal 6–4g Primary Basis. *Mol. Phys.* **2007**, *105*, 2455–2473.
- (88) Steele, R. P.; DiStasio, R. A.; Head-Gordon, M. Non-Covalent Interactions with Dual-Basis Methods: Pairings for Augmented Basis Sets. *J. Chem. Theory Comput.* **2009**, *5*, 1560–1572.
- (89) Steele, R. P.; Head-Gordon, M.; Tully, J. C. Ab Initio Molecular Dynamics with Dual Basis Set Methods. *J. Phys. Chem. A* **2010**, *114*, 11853–11860.

- (90) Wolinski, K.; Pulay, P. Second-Order Møller–Plesset Calculations with Dual Basis Sets. *J. Chem. Phys.* **2003**, *118*, 9497–9503.
- (91) Liang; Head-Gordon, M. Approaching the Basis Set Limit in Density Functional Theory Calculations Using Dual Basis Sets without Diagonalization†. *J. Phys. Chem. A* **2004**, *108*, 3206–3210.
- (92) Gerardi, H. K.; Gardenier, G. H.; Viswanathan, U.; Auerbach, S. M.; Johnson, M. A. Vibrational Predissociation Spectroscopy and Theory of Ar-Tagged, Protonated Imidazole (Im) Im1–3h+·Ar Clusters. *Chem. Phys. Lett.* **2011**, *501*, 172–178.
- (93) McCunn, L. R.; Roscioli, J. R.; Elliott, B. M.; Johnson, M. A.; McCoy, A. B. Why Does Argon Bind to Deuterium? Isotope Effects and Structures of Ar-H So 2 + Complexes. *J. Phys. Chem. A* **2008**, *112*, 6074–6078.
- (94) Posey, L. A.; Johnson, M. A. Photochemistry of Hydrated Electron Clusters (H₂O)_N (15 ≤ N ≤ 40) at 1064 Nm: Size Dependent Competition between Photofragmentation and Photo-detachment. *J. Chem. Phys.* **1988**, *89*, 4807–4814.
- (95) Hernandez, F. J.; Brice, J. T.; Leavitt, C. M.; Liang, T.; Raston, P. L.; Pino, G. A.; Doublerly, G. E. Mid-Infrared Signatures of Hydroxyl Containing Water Clusters: Infrared Laser Stark Spectroscopy of Oh–H₂O and Oh(D₂O)_N (N = 1–3). *J. Chem. Phys.* **2015**, *143*, 164304.
- (96) Dunning, T. H. Gaussian Basis Sets for Use in Correlated Molecular Calculations. I. The Atoms Boron through Neon and Hydrogen. *J. Chem. Phys.* **1989**, *90*, 1007–1023.
- (97) Schmidt, J. R.; Tully, J. C. Path-Integral Simulations Beyond the Adiabatic Approximation. *J. Chem. Phys.* **2007**, *127*, 094103.
- (98) Ananth, N.; Miller, T. F. Exact Quantum Statistics for Electronically Nonadiabatic Systems Using Continuous Path Variables. *J. Chem. Phys.* **2010**, *133*, 234103.
- (99) Zillich, R. E.; Mayrhofer, J. M.; Chin, S. A. Extrapolated High-Order Propagators for Path Integral Monte Carlo Simulations. *J. Chem. Phys.* **2010**, *132*, 044103.
- (100) Chin, S. A. Symplectic Integrators from Composite Operator Factorizations. *Phys. Lett. A* **1997**, *226*, 344–348.
- (101) Chin, S. A. Structure of Positive Decompositions of Exponential Operators. *Phys. Rev. E* **2005**, *71*, 016703.
- (102) Zillich, R. E.; Mayrhofer, J. M.; Chin, S. A. Extrapolated High-Order Propagators for Path Integral Monte Carlo Simulations. *J. Chem. Phys.* **2010**, *132*, 044103–7.
- (103) Brualla, L.; Sakkos, K.; Boronat, J.; Casulleras, J. Higher Order and Infinite Trotter-Number Extrapolations in Path Integral Monte Carlo. *J. Chem. Phys.* **2004**, *121*, 636–643.
- (104) Suzuki, K.; Tachikawa, M.; Shiga, M. Efficient Ab Initio Path Integral Hybrid Monte Carlo Based on the Fourth-Order Trotter Expansion: Application to Fluoride Ion-Water Cluster. *J. Chem. Phys.* **2010**, *132*, 144108.
- (105) Ceriotti, M.; Brain, G. A. R.; Riordan, O.; Manolopoulos, D. E. The Inefficiency of Re-Weighted Sampling and the Curse of System Size in High-Order Path Integration. *Proc. R. Soc. London, Ser. A* **2012**, *468*, 2–17.

CHAPTER 7

CONCLUSION

7.1 Summary of Research and Future Prospects

This series of computational studies collectively formed a bottom-up analysis of water oxidation and the underlying driving forces present within cationic water systems. The purpose was to investigate aspects of water oxidation and catalysis that have not been previously explained and offer insight for the inner-sphere workings of WOCs. The properties and characteristics of bare, cationic water clusters were first investigated. Key structural changes, including separation of the ion-radical contact pair, were observed as the number of water molecules was increased. These changes were later seen to be exacerbated in clusters containing multiple solvation shells. Cationic water cluster vibrational spectra were generated computationally and decomposed in order to explain anomalous peaks, as well as determine signatures of water clusters activated for oxidation. Following the bare water-cluster study, an investigation was conducted into how transition metal cations, specifically a copper (I) cation, perturb neutral water clusters, compared to the cationic water-cluster benchmarks. This model was utilized not only as a precursor to full homogenous WOC studies, but also to understand how a species containing available d orbitals interacts with solvating water molecules. The solvated copper (I) analysis unveiled many non-intuitive covalent, electrostatic, and hydrogen bonding “balancing acts” observed to be occurring in the hydrated transition-

metal clusters. Lastly, 2 methods were developed to reduce the computational overhead required to perform classical and quantum dynamics on reactive systems, including larger oxidized water clusters. These dynamical routines provide new tools for understanding the thermodynamics and quantum driving forces of reactive systems. Importantly, the acceleration methods did not incur significantly more error than already occurs from numerical integration methods. Because of the generality of the methods, they will hopefully have an impact on the MD community beyond the timescale of this thesis.

The future of this research program is to begin to study a bona fide homogeneous catalyst to understand its interactions with solvating waters and determine how they differ from what was observed from the fundamental studies presented in this document. A triglycylglycine macrocyclic copper (II) WOC has been preliminarily studied and represents the initial step past this research program.¹ This catalyst is comprised of cheap and readily available elements, is created by a simple self-assembling mechanism, and is fairly stable in oxidative working conditions.² These properties are what made this molecule highly attractive for further investigation. Several details of the inner-sphere redox chemistry remain speculative; however, the present study has begun to probe the system from an electronic structure prospective and will try to carve out the unknowns within the mechanism and offer molecular-level connections between observed electrochemical data and the determined catalysis cycle. Information on bare water oxidation will also be utilized to determine how to further stabilize this catalyst under working conditions as well as improve its capability of decreasing water-splitting activation energies.

This study is the culmination of 4.5 years of research into WOC and MD acceleration. The information and discussions contained within this document will not drive the overnight commercial adoption of renewable fuel sources. These fundamental studies lay the proverbial groundwork for an electronic-level understanding of how water loses an electron. From the beginning, this study was meant to generate the data and understanding of what is required to make informed decisions on what determines the viability a potential WOC candidate. It is hoped that with the fundamental understanding of water oxidation and MD acceleration methods developed throughout this study, maybe current society will be one step closer to a renewable and green energy economy.

7.2 References

1. Zhang, M.-T.; Chen, Z.; Kang, P.; Meyer, T. J. Electrocatalytic Water Oxidation with a Copper(II) Polypeptide Complex. *J. Am. Chem. Soc.* **2013**, *135* (6), 2048-2051.
2. Murariu, M. ESI-MS Study of Self-Assembly-Formed Tetraglycine Macrocyclic Ligand Complex of Cu(II). *Int. J. Mass Spectrom.* **2013**, *351*, 12-22.